

125<sup>th</sup>

ISSN 2712-8172

# MAGAZINE OF CIVIL ENGINEERING



**Magazine of Civil Engineering**

ISSN 2712-8172

Online peer-reviewed open-access scientific journal in the field of Civil and Construction Engineering

**Founder and Publisher:** Peter the Great St. Petersburg Polytechnic University

This journal is registered by the Federal Service for Supervision of Communications, Information Technology, and Mass Media (ROSKOMNADZOR) in 2020. Certificate EI No. FS77-77906 issued February 19, 2020.

**Periodicity:** 8 issues per year

Publication in the journal is open and free for all authors and readers.

**Indexing:** Scopus, Web of Science (ESCI, RSCI), DOAJ, Compendex, Google Academia, Index Copernicus, ProQuest, Ulrich's Serials Analysis System, CNKI

**Corresponding address:** 29 Polytechnicheskaya st., Saint Petersburg, 195251, Russia

**Chief science editor:**

D.Sc., Galina L. Kozinets

**Deputy chief science editors:**

D.Sc., Sergey V. Korniyenko

**Executive editor:** Ekaterina A. Linnik

**Translator, editor:** Irina Ye. Lebedeva

**Proofreader:** Philipp Chrysanthos S. Bastian

**DT publishing specialist:**

Anastasiya A. Kononova

**Contacts:**

E-mail: [mce@spbstu.ru](mailto:mce@spbstu.ru)

Web: <http://www.engstroy.spbstu.ru>

---

Date of issue: 07.04.2025

© Peter the Great St. Petersburg Polytechnic University. All rights reserved.

© Coverpicture – Polina A. Ivanova

**Editorial board:**

T. Awwad, PhD, professor, Damascus University, Syrian Arab Republic

A.I. Belostotsky, D.Sc., professor, StaDyO Research & Engineering Centre, Russia

A.I. Borovkov, PhD, professor, Peter the Great St. Petersburg Polytechnic University, Russia

M. Veljkovic, PhD, professor, Delft University of Technology, The Netherlands

R.D. Garg, PhD, professor, Indian Institute of Technology Roorkee (IIT Roorkee), India

M. Garifullin, PhD, postdoctoral researcher, Tampere University, Finland

T. Gries, Dr.-Ing., professor, RWTH Aachen University, Germany

T.A. Datsyuk, D.Sc., professor, Saint-Petersburg State University of Architecture and Civil Engineering, Russia

V.V. Elistratov, D.Sc., professor, Peter the Great St. Petersburg Polytechnic University, Russia

O.N. Zaitsev, D.Sc., professor, Southwest State University, Russia

T. Kärki, Dr.-Ing., professor, Lappeenranta University of Technology, Russia

G.L. Kozinets, D.Sc., professor, Peter the Great St. Petersburg Polytechnic University, Russia

D.V. Kozlov, D.Sc., professor, National Research Moscow State Civil Engineering University, Russia

S.V. Korniyenko, D.Sc., professor, Volgograd State Technical University, Russia

Yu.G. Lazarev, D.Sc., professor, Peter the Great St. Petersburg Polytechnic University, Russia

M.M. Muhammadiev, D.Sc., professor, Tashkent State Technical University, Republic of Uzbekistan

H. Pasternak, Dr.-Ing.habil., professor, Brandenburgische Technische Universität, Germany

F. Rögner, Dr.-Ing., professor, Technology Arts Science TH Köln, Germany

V.V. Sergeev, D.Sc., professor, Peter the Great St. Petersburg Polytechnic University, Russia

T.Z. Sultanov, D.Sc., professor, Tashkent Institute of Irrigation and Agricultural Mechanization Engineers, Republic of Uzbekistan

A.M. Sychova, D.Sc., professor, Military Space Academy named after A.F. Mozhaysky, Russia

M.G. Tyagunov, D.Sc., professor, National Research University "Moscow Power Engineering Institute", Russia

M.P. Fedorov, D.Sc., professor, Peter the Great St. Petersburg Polytechnic University, Russia

D. Heck, Dr.-Ing., professor, Graz University of Technology, Austria

P. Cao, D.Sc., professor, Jilin University, China

A.G. Shashkin, D.Sc., PI Georekonstruktsiya, LLC, Russia

B.M. Yazyev, D.Sc., professor, Don State Technical University, Russia

**Contents**

Kolosova, N.B., Kolosov, E.S., Ptukhina, I.S., Rineyskaya, A.A. Reconstruction of a moss layer in permafrost conditions	13401
To, P., Pham, N.T. Application of various binders in soil stabilisation for road batter protection	13402
Shitikova, M.V., Smirnov, V.A. Analysis of rheological model parameters for various foamed vibration-damping materials	13403
Dashevsky, V.P., Kondratieva, V.I., Rzhimsky, R.V., Ronzhin, A.L. Detection of unauthorized connections to storm drains based on passive radio frequency identification technology	13404
Zagorodnyuk, L.H., Sytov, G.A., Bogdanov, V.N., Kudyakow, A.I. Granular aggregate for fill mortars using blast furnace slag	13405
Chepurnenko, A., Yazyev, B., Al-Zgul, S., Tyurina, V. Simplified finite element model for rectangular CFST columns strength calculation under eccentric compression	13406
Beketova, M.S., Nuguzhinov, Zh., Travush, V.I., Vatin, N.I., Akhmediyev, S.K., Kurokhtina, I.A., Shagiyeva, R.A., Mikhailov, V.F., Khabidolda, O. Bending of orthotropic scalene triangle plates: finite difference modeling	13407
Al-Omari, A.A., Al-Dabbagh A. A model study of axially loaded micropiles in layered soils	13408
Hasanzadeh, A., Hematibahar, M., Vatin, N.I., Kharun, M. An investigation on the nonlinear dynamic behavior of reinforced concrete shear wall under seismic loading	13409
Al-Salamy, H.A., Al-Naddaf, M.A., Almuhanha, R.A. Experimental study on the behavior of multilayer geosynthetic-reinforced sandy embankments	13410



Research article

UDC 624.139.53

DOI: 10.34910/MCE.134.1



## Reconstruction of a moss layer in permafrost conditions

N.B. Kolosova<sup>1</sup> , E.S. Kolosov<sup>1</sup>, I.S. Ptukhina<sup>1</sup>, A.A. Rineyskaya<sup>2</sup>

<sup>1</sup> Peter the Great St. Petersburg Polytechnic University, St. Petersburg, Russian Federation

<sup>2</sup> Enigma-S, LLC, St. Petersburg, Russian Federation

✉ [kolosova\\_nb@spbstu.ru](mailto:kolosova_nb@spbstu.ru)

**Keywords:** moss layer, pipeline, permafrost conditions, secondary use, permafrost soils, underground oil pipeline

**Abstract.** The object of research in this work is the relationship between the feasibility of secondary use the moss layer and the thermal characteristics of an oil pipeline, which was laid underground in permafrost conditions. The purpose of the work is to determine the expediency of the secondary use of the moss layer with underground laying of the pipeline in the permafrost conditions. The choice of the object and purpose of the study is motivated by the intensive development of territories with permafrost soils, by the relevance of problems related to the construction and operation of the energy transport system, by its impact on the ecological development of the permafrost zone and by the need for further research aimed at solving these problems. The following tasks were formulated to achieve this goal: a) to determine the main thermal factor affecting the expediency of the secondary use of the moss layer; b) to consider the possibility of restoring the moss layer at various permafrost soils; c) to determine the feasibility of restoring the moss layer for underground laying pipeline with various types of energy resources; d) to determine the economic component of the secondary use of the moss layer. The equivalent of the Zapolyarye–Purpe Oil pipeline theoretical model of the underground oil pipeline is presented in this work for research. The inexpediency of the secondary use of the moss layer in the underground laying of the oil and gas pipeline is justified by the thermal and economic characteristics of the soil. Future considerations of this topic are related to the study of the economic indicators of underground pipelines in conditions of multi-layered permafrost soils.

**Citation:** Kolosova, N.B., Kolosov, E.S., Ptukhina, I.S., Rineyskaya, A.A. Reconstruction of a moss layer in permafrost conditions. Magazine of Civil Engineering. 2025. 18(2). Article no. 13402. DOI: 10.34910/MCE.134.1

### 1. Introduction

The object of research in this work is the relationship between the expediency of secondary use the moss layer and the thermal characteristics of the oil pipeline, which is laid underground and transports energy resources in permafrost conditions.

The choice of the research object is caused by the intensive development of territories with permafrost soils, the relevance of problems connected with the construction and maintenance the energy transport system, its impact on the ecological development of the permafrost zone, and the need for further research aimed at solving these problems.

In developing the topic of this work, the authors pay attention to the following facts.

It is known that there are three methods of laying pipelines in the world experience. These are underground, land, and aboveground methods [1–4]. Each of them has advantages and disadvantages.



However, there are often situations in our lives when only underground pipeline laying is possible. Herewith, it's impossible to avoid a negative impact on the environment.

According to the authors, one of the main issues is the study of the feasibility of restoring the moss layer on the surface of the soil that has been developed because the use of moss layer restoration technology in permafrost conditions will require significant additional financial and time resources [2, 4].

Analysis of the scientific literature has shown that the choice of the most effective technology for underground pipeline laying in permafrost conditions is a serious problem. It requires a comprehensive analysis, which is aimed not only at solving technical problems but at the impact of the construction process on the ecosystem also [5–9].

During the search of effective technologies for underground laying of pipelines, some authors [10–18] describe various factors and approaches to finding optimal technical solutions during the installation and operation of pipelines in permafrost distribution areas. However, these works are experimental in nature and do not reflect the relationship between pipeline laying technology and its effect on the temperature condition of permafrost soils. There is no information about the necessity of the secondary use moss layer here.

On the other hand, some authors [19–26] describe the relationship between various physical and mechanical properties of frozen soil and negative phenomena occurring in array of permafrost soils (frosty heaving, formation soil cracks, etc.).

These are theoretical works. They do not reflect the relationship between the technological operations during the construction of the pipeline (restoration the moss layer) and the process of thawing frozen soil.

As the analysis of scientific literature shows, some authors have conducted researches, which were related with the influence of the moss layer and the temperature mode of permafrost soils [27–30]. However, we have here the observation of the soils temperature mode with moss layer during long-term operation. There is not analysis of the expediency of restoring the moss layer during pipeline construction.

Thus, a review of the scientific literature has showed the lack of solution to the problem of the relationship between the secondary use of moss and the thermal parameters of permafrost soils during underground pipeline laying. And the purpose of the research has been obviously.

The purpose of the study is to determine the expediency of the secondary use moss layer during the underground laying of the pipeline in permafrost conditions.

We need to solve the following tasks in order to achieve the goal:

- to determine the basic thermal factor defining the expediency secondary use of the moss layer;
- to consider the possibility of restoring the moss layer with different types of permafrost soil;
- to determine the expediency of restoring moss layer for underground laying of pipeline with various types of fuels;
- to determine the economic effect of the secondary use moss layer.

## *2. Model and Methods*

### **Research model**

When the authors determined the design of the model for study, they relied on researches that were conducted in the field of interaction pipeline – frozen soil system [10, 11, 17, 19].

In the issue, it was decided to consider the model for study as the theoretical model of the oil pipeline, which was installed underground by analogy with the well-known Zapolyarye–Purpe Oil pipeline [15, 16]. Oil with a temperature of 60 °C was used as the transported raw material.

Design scheme of research model is shown in Fig. 1.



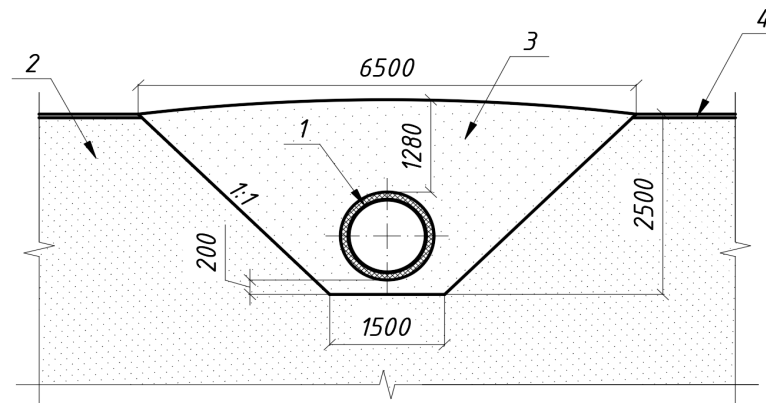


**Figure 1. The researched model of the underground oil pipeline: 1 – oil pipeline, 2 – the studied permafrost soil, 3 – the soil of backfill (imported sand), 4 – moss layer.**

The study of the feasibility of restoring the moss layer during underground pipeline laying in permafrost conditions was carried out using the calculation method in the PLAXIS 2D software package. Temperature fields and soil thawing indicators were determined in August of the first year operation of the pipeline. The temperature of 11.1 °C was assumed to be the edge condition on the ground surface. This temperature was determined on the basis of the technical report engineering and geological surveys of the Ust-Mom city Sakha Republic.

The main characteristics of frozen soils, backfilling soil, and moss layer were adopted on the basis of normative documents of the Russian Federation, technical reports of engineering, geological surveys and are presented in Tables 1, 2 and 3.

**Table 1. Main characteristics of the moss layer.**

Name title	Value
Laver thickness, mm	50
Density, kg/m <sup>3</sup>	231
Specific heat, J/kg·°C	6170
Heat conductivity factor, W/m·°C	0.15

The pipeline is modeled as a steel pipe in a polyurethane foam shell construction with a diameter of 1020 mm. The wall thickness of the oil pipeline was determined by the methodology which was described in the normative document.

The formula for determining the thickness of the shell construction is presented below:

$$\delta = \frac{n \cdot p \cdot D_n}{2 \cdot (R_1 + n \cdot p)},$$

where  $n$  is load reliability factor;  $p$  is operating (standard) pressure, MPa;  $D_n$  is outside diameter of the pipeline, cm;  $R_1$  is calculated compression resistance, MPa.

As a result, the thickness of the oil pipeline was accepted at 12 mm, and the thickness of the polyurethane shell construction was accepted at 100 mm.

Imported sandy soil with the characteristics given in Table 2 was considered as a backfilling soil.

**Table 2. The main characteristics of the backfilling soil.**

Name title	Value
Density, kg/m <sup>3</sup>	2000
Elasticity modulus, MPa	40
Angle of internal friction, deg	40
Specific cohesion, kPa	1
Specific heat, J/kg·°C	835
Heat conductivity factor, W/m·°C	2.22



Sandy loam, loam, and clay, which are most often found in permafrost conditions, were considered as the studied soil. The characteristics of these soils are presented in Table 3.

**Table 3. Main characteristics of permafrost soils.**

Name title	Type of soil		
	Soft sandy loam	Soft plastic loam	Plastic frozen sandy light clay
Densitv. $\alpha/\text{cm}^3$	1.82	1.82	1.67
Solid particles density, $q/\text{cm}^3$	2.7	2.71	2.73
Poisson number	0.3	0.34	0.35
Relative density, $kq/\text{m}^3$	1820	1820	1670
Angle of internal friction, deg	18	15	14
Total water content, %	23	26	30.6
Airspace ratio	0.82	0.88	1.128
Index of plasticity	0.06	0.09	0.208
Modulus of deformation, MPa	8	7	3.19
Specific cohesion, kPa	9	15	36
Total ice content, %	34	39	2.7
Ground freezing point, $^{\circ}\text{C}$	-0.67	-0.68	-0.25
Yearly average temperature at a depth of 10 m, $^{\circ}\text{C}$	-7	-7	-7
Specific heat, $\text{J}/\text{kg}\cdot^{\circ}\text{C}$	850	950	950
Volumetric heat capacity of frozen soil, $\text{kcal}/\text{m}^3\cdot^{\circ}\text{C}$	487	535	667
Heat conduction coefficient of thawed soil/ frozen soil, $\text{kcal}/\text{m}\cdot\text{hr}\cdot^{\circ}\text{C}$	1.69/1.92	1.45/1.65	1.14/1.36

To maximize the approximation of the computational model in the PLAXIS 2D PC with real conditions, the monthly values of atmospheric temperature in Ust-Moma of the Sakha Republic were taken by authors. These values ranged from  $14.8^{\circ}\text{C}$  (July) to  $-44.9^{\circ}\text{C}$  (January) [16].

The research task has been to determine the modification the thermal parameters of the pipeline-soil system.

### 3. Results and Discussion

During the modeling process, the distribution of these indicators was obtained for the oil pipeline of the pipe-ground system. The oil pipeline was installed underground in permafrost soils: sandy loam, loam, and clay.

Despite the numerous available factors affecting the thermal condition of the oil pipeline-soil system, the authors have accepted the depth of thawing and the width of the thawing halo effect as the studied factor, which determines the feasibility of restoring the moss layer during underground laying of the oil pipeline.

According to the authors, these indicators can cause negative natural hazards (frost heaving, soil slaking, etc.) and lead to loss bearing capacity of frozen soils and, as a result, to loss stability of the oil pipeline itself [10, 14].

During the study the theoretical model of the underground oil pipeline, which was installed in various soils with an existing moss layer, the authors obtained temperature fields where the depth of thawing and the width of the thawing halo were determined (Figs. 2–4). (The white contour line corresponds to a temperature equal to  $0^{\circ}\text{C}$ .)



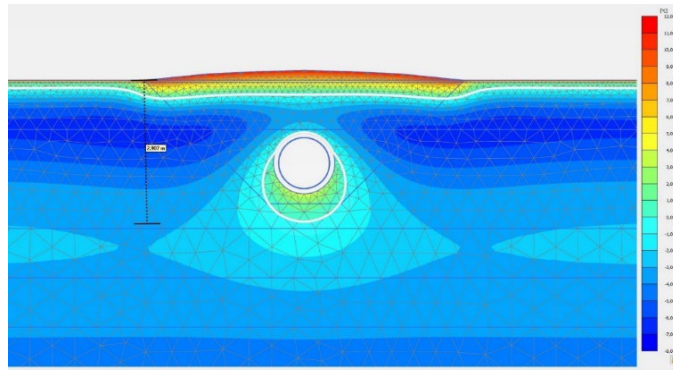


**Figure 2. Thermal parameters of the oil pipeline in the conditions of frozen sandy loam (the thawing depth is 2.907 m, the halo width is 1.55 m).**

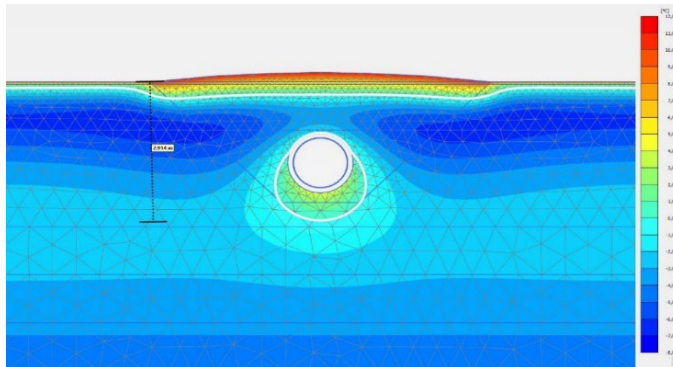


**Figure 3. Thermal parameters of the oil pipeline in the conditions of frozen loam (the thawing depth is 2.914 m, the halo width is 1.67 m).**

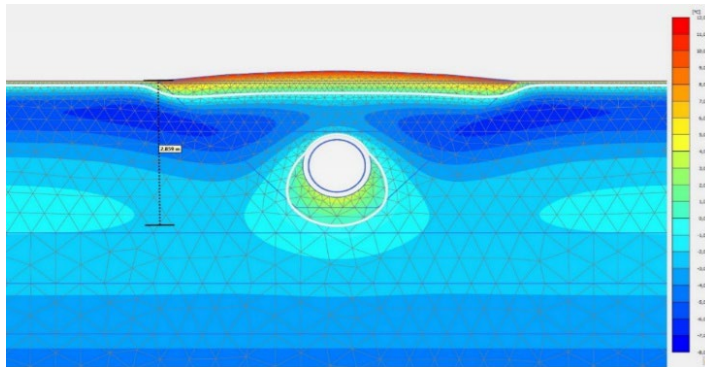


**Figure 4. Thermal parameters of the oil pipeline in the conditions of frozen clay (the thawing depth is 2.859 m, the halo width is 1.73 m).**

Then, the authors conducted a study and analysis the thermal parameters of the oil pipeline temperature fields with a restored moss layer in different soils. This research allowed us to have question answered about the expediency of restoring the moss layer of the underground oil pipeline (Figs. 5–7).

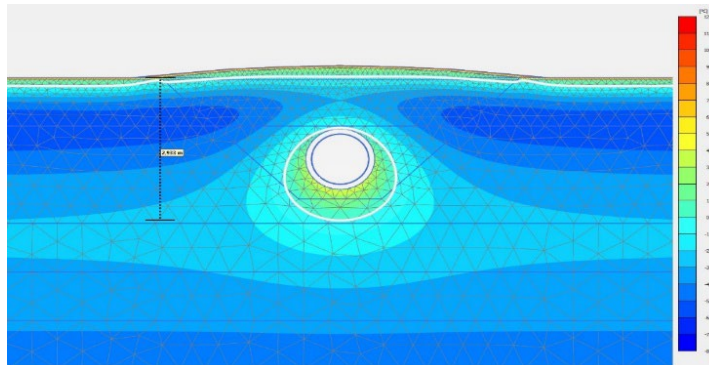


**Figure 5. Thermal parameters of the oil pipeline with the restored moss layer in the conditions of frozen sandy loam (the thawing depth is 2.933 m, the thawing halo width is 1.91 m).**



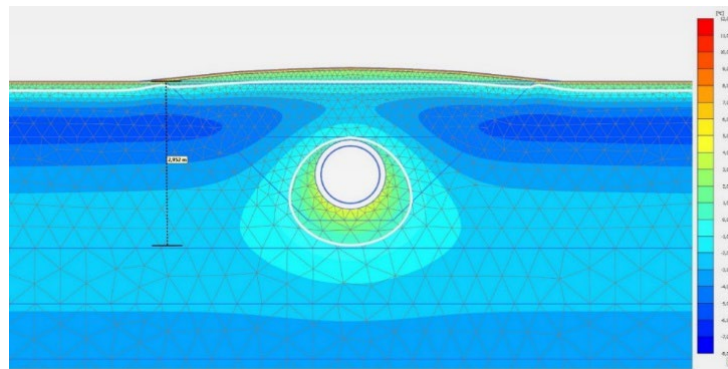


**Figure 6. Thermal parameters of the oil pipeline with a restored moss layer in the conditions of frozen loam (the thawing depth is 2.952 m, the thawing halo width is 2.01 m).**

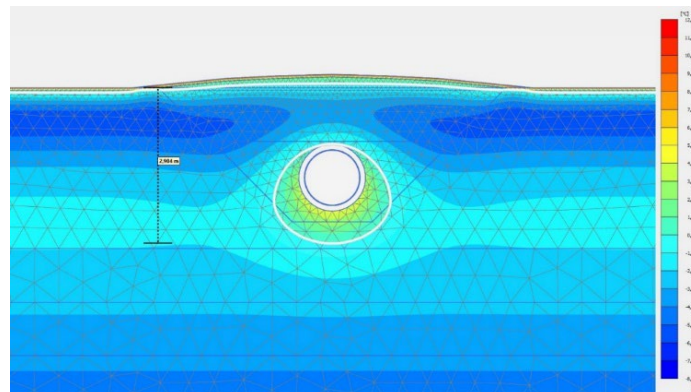


**Figure 7. Thermal parameters of the oil pipeline with a restored moss layer in the frozen clay conditions (the thawing depth is 2.904 m, the thawing halo width is 2.08 m).**

The authors obtained the following results when comparing the temperature fields of an underground oil pipeline with an undisturbed moss layer and an oil pipeline with a restored moss layer (secondary use):

- the depth of thawing during the secondary use of moss for all soils increased slightly (for frozen sandy loam by 0.9 %, for frozen loam by 1.3 %, for frozen clay by 1.6 %);
- the width of the thawing halo during the secondary use of moss for all soils increased significantly (for frozen sandy loam by 23.2 %, for frozen loam by 20.4 %, for frozen clay by 20.2 %);
- during the secondary use of moss, the horizontal propagation of the heat front around the oil pipeline is clearly traced.

The same research was conducted by the authors regarding the laying of the underground gas pipeline. And, here the results of the study were similar, with the only difference that the depth of thawing here is maximized up 4.2 %, and the width of the thawing halo is maximized up 41.2 %.

## 4. Conclusions

Thus, analyzing the obtained results, it is obvious that the secondary use of the moss layer in underground construction of the pipelines is impractical:

- the presence and growth of the horizontal component of the temperature fluctuation can cause substantial damage with longitudinal and transverse deformations, pipeline floating-up and negative effect of frost heaving;
- it is necessary to take into account the practical significance of the obtained result. Such as the additional economic costs of restoring the moss layer and the cost of associated works and equipment.

Thus, the cost of restoring one square meter of moss layer after underground laying of the pipeline is on the average 18870 rubles (the cost of loading moss, transporting it from the storage site to the installation site, renting equipment, and value added tax do not include this value).

In the future, the authors plan to continue the research work of the pipeline-permafrost system both in terms of temperature effects and in terms of the economic component of laying pipeline in permafrost conditions.



## References

1. Semenova, D.P. Laying pipelines in permafrost conditions. Current research. 2020. 6(9). Pp. 16–20. URL: <https://apni.ru/article/544-prokladka-truboprovodov-v-usloviyakh-vech-merz>
2. Mutalova, L.M., Mustafin, F.M. Improving the method of laying oil pipelines in areas of frozen soils. Transportation and storage of petroleum products and hydrocarbon raw materials. 2021. 4. Pp. 56–59. DOI: 10.24412/0131-4270-2021-4-56-59
3. Kolokolova, N.A., Harris, N.A. About choice the method of laying pipelines in permafrost areas. Transportation and storage of petroleum products and hydrocarbon raw materials. 2013. 1. Pp. 13–17. URL: <https://journal-thnp.ru/soderzhanie/arhiv-nomerov-za-2013/zhurnal-tkhn-1-2013.html>
4. Vvedensky, V.R., Gendler, S.G., Titova, T.S. Environmental impact of the tunnel construction. Magazine of Civil Engineering. 2018. 79(3). Pp. 140–149. DOI: 10.18720/MCE.79.15
5. Duvillard, P.A., Ravanel, L., Marcer, M., Schoeneich, P. Recent evolution of damage to infrastructure on permafrost in the French Alps. Regional Environmental Change. 2019. 19. Pp. 1281–1293. DOI: 10.1007/s10113-019-01465-z
6. Kaushik, S., Ravanel, L., Magnin, F., Trouve, E., Cusicanqui, D. Effects of topographic and meteorological parameters on the surface area loss of ice aprons in the Mont Blanc massif (European Alps). Cryosphere. 2022. 16(10). Pp. 4251–4271. DOI: 10.5194/tc-16-4251-2022
7. Ades, M., Adler, R., Aldred, F., Riddle, D.B., Veasey, S.W. et al. Global Climate. State of the Climate in 2021. Bulletin of the American Meteorological Society. 2022. 103(8). Pp. S11–S142. DOI: 10.1175/2022BAMSStateoftheClimate.1
8. Kaushik, S., Ravanel, L., Magnin, F., Trouve, E., Cusicanqui, D. Distribution and evolution of ice aprons in a changing climate in the mont-blanc massif (Western European ALPS). International Archives of the Photogrammetry, Remote Sensing and Spatial Information Sciences – ISPRS Archives. 2021. 43(B3-2021). Pp. 469–475. DOI: 10.5194/isprs-archives-XLIII-B3-2021-469-2021
9. Blunden, J., Boyer, T., Dunn, R.J.H., Zhang, P., Zhu, Z., Miętus, M. State of the Climate in 2021. Bulletin of the American Meteorological Society. 2022. 103(8). Pp. S1–S465. DOI: 10.1175/2022BAMSStateoftheClimate.1
10. Surikov, V.I., Ibragimov, E.R., Gunar, A.Y. Technique of route selection and technical solutions for main pipelines laying in permafrost areas. Science & Technologies: Oil and Oil Products Pipeline Transportation. 2018. 3(8). Pp. 254–263. DOI: 10.28999/2541-9595-2018-8-3-254-263
11. Shamilov, H.S., Karimov, R.M., Gumerov, A.K., Valeev, A.R., Tashbulatov, R.R. Optimization of design solutions for laying trunk pipelines in conditions of insular and intermittent permafrost soil. Science & Technologies: Oil and Oil Products Pipeline Transportation. 2021. 2(11). Pp. 136–144. DOI: 10.28999/2541-9595-2021-11-2-136-144
12. Ivanov, V.A., Sokolov, S.M., Ogudova, E.V. Methods of increasing efficiency and maintainability of pipeline systems. IOP Conference Series: Materials Science and Engineering. 2018. 357. Article no. 012016. DOI: 10.1088/1757-899X/357/1/012016
13. Petrov, A.M., Vakhrushev, S.I. The optimal set of machines for laying oil pipeline in deep soils. Modern technologies in construction: theory and practice. 2020. 2. Pp. 170–175.
14. Voronov, A.G., Lisin, Yu.V., Neganov, D.A., Zorin, N.E., Korotkevich, P.V. Information and analytical support of planning the replacement sections of the linear part main oil pipelines. Science & Technologies: Oil and Oil Products Pipeline Transportation. 2022. 12(1). Pp. 18–33. DOI: 10.28999/2541-9595-2022-12-1-18-33
15. Rineyskaya, A.A., Kolosov, E.S. Determination of the optimal method of laying oil trunk pipelines in terms of temperature interactions with frozen soils base. Proceedings of Russian Conference Science Week Institute of Civil Engineering. 2022. Pp. 225–228.
16. Kolosov, E.S., Kolosova, N.B. The depth of thawing as a factor of determining the method of laying oil pipeline in permafrost areas. Proceedings of International Scientific and Practical Conference Dedicated to Memory of G.S. Gryaznov. Tyumen, 2024. Pp. 224–229.
17. Bakhtizin, R.N., Sultanmagomedov, S.M., Sultanmagomedov, T.S., etc. Experimental studies resistance of frozen soil to longitudinal movements of the pipeline with changes temperature and wetness. Science and technology of pipeline transportation of oil and petroleum products. 2020. 10(3). Pp. 243–251. DOI: 10.28999/2541-9595-2020-10-3-243-251
18. Kolosov, E., Kolosova, N. Research on the relationship between the building displacements, thickness and soil type under seismic conditions. IOP Conference Series: Materials Science and Engineering. 2019. 698(2). Article no. 022045. DOI: 10.1088/1757-899X/698/2/022045
19. Andreeva, I.A., Efimova, T.O. On the Qualitative Study of Phase Portraits for Some Categories of Polynomial Dynamic Systems. Studies of Systems, Decision and Control. 2022. 418. Cyber-Physical Systems: Modeling and Industrial Application. Pp. 39–50. DOI: 10.1007/978-3-030-95120-7\_4
20. Chao, G., Lu, Z. Frost heaving of foundation pit for seasonal permafrost areas. Magazine of Civil Engineering. 2019. 86(2). Pp. 61–71. DOI: 10.18720/MCE.86.6
21. Yamamoto, Y., Springman, S.M. Three-and four-point bending tests on artificial frozen soil samples at temperatures close to 0 C. Cold Regions Science and Technology. 2017. 134. Pp. 20–32. DOI: 10.1016/j.coldregions.2016.11.003
22. Kozinetc, G.L., Kozinetc, P.V. The calculation of the dynamic characteristics of the spillway of the dam. Magazine of Civil Engineering. 2022. 113(5). Article no. 11312. DOI: 10.34910/MCE.113.12
23. Kozinetc, G., Kaarki, T., Barabanshchikov, Y., Lahtela, V., Zotov, D. Power Mechanical properties of sustainable wooden structures reinforced with Basalt Fiber Reinforced Polymer. Magazine of Civil Engineering. 2020. 100(8). Article no. 10012. DOI: 10.18720/MCE.100.12
24. Zhang, D., Liu, E., Liu, X., Zhang, G., Yin, X., Song, B. Investigation on the Nonlinear Strength Properties and Damage Statistical Constitutive Model for Frozen Sandy Soils. Advances in Materials Science and Engineering. 2018. Article no. 4620101. DOI: 10.1155/2018/4620101
25. Ming, F., Li, D., Zhang, M., Zhang, Y. A novel method for estimating the elastic modulus of frozen soil. Cold Regions Science and Technology. 2017. 141. Pp. 1–7. DOI: 10.1016/j.coldregions.2017.05.005
26. Yang, Y., Gao, F., Cheng, H., Lai, Y., Zhang, X. Researches on the Constitutive Models of Artificial Frozen Silt in Underground Engineering. Advances in Materials Science and Engineering. 2014. Article no. 902164. DOI: 10.1155/2014/902164
27. Harris, N.A., Rusakov, A.I. Degree accounting of anthropogenic impact underground pipelines on the thermal conductivity of frozen soils. Oil and gas business. 2020. 6(18). Pp. 99–106.



28. Marcer, M., Duvillard, P.-A., Tomaškovičová, S., Revil, A. Ingeman-Nielsen, T. Modelling present and future rock wall permafrost distribution in the Sisimiut mountain area, West Greenland. *Cryosphere*. 2024. 18(4). Pp. 1753–1771. DOI: 10.5194/tc-18-1753-2024
29. Tishkov, A.A., Osokin, N.I., Sosnovsky, A.V. The Impact of Moss Synusia on the Active Layer of Arctic Soil and Subsoil. *Proceedings of Russian Academy of Sciences. The Geographical Series*. 2013. 3. Pp. 39–46. DOI: 10.15356/0373-2444-2013-3-39-46
30. Glazov, P.M., Loshagina, Yu.A., Shmatova, A.G., Gnedenko, A.E., Tishkov, A.A. Kolguev Island as an object of biota monitoring in the western sector of Russian Arctic. *Arctic: Ecology and Economy*. 2024. 14(2). Pp. 261–273. DOI: 10.25283/2223-4594-2024-2-261-273

***Information about the authors:***

***Natalya Kolosova,***

ORCID: <https://orcid.org/0000-0002-7937-3269>

E-mail: [kolosova\\_nb@spbstu.ru](mailto:kolosova_nb@spbstu.ru)

***Evgeni Kolosov,***

E-mail: [eskol1978@yandex.ru](mailto:eskol1978@yandex.ru)

***Irina Ptukhina, PhD in Technical Sciences***

E-mail: [irena\\_ptah@mail.ru](mailto:irena_ptah@mail.ru)

***Anastasiya Rineyskaya,***

E-mail: [aaarin@mail.ru](mailto:aaarin@mail.ru)

*Received 18.11.2024. Approved after reviewing 09.03.2025. Accepted 21.03.2025.*





Research article

UDC 624.131.4

DOI: 10.34910/MCE.134.2



## Application of various binders in soil stabilisation for road batter protection

P. To<sup>1</sup> , N.T. Pham<sup>2</sup>  

<sup>1</sup> College of Science and Engineering, James Cook University, Douglas, Towns-ville, Queensland, Australia

<sup>2</sup> Thuyloi University, Dong Da, Hanoi, Vietnam

 [thinhtls@tlu.edu.vn](mailto:thinhtls@tlu.edu.vn)

**Keywords:** soil stabilisation, road batter, flood protection, lime, tripple blends, gypsum, binder

**Abstract.** The study investigates the use of various binders for soil stabilization to enhance road batter protection under extreme hydraulic conditions. Flash floods and high-velocity water flows in rural areas often lead to significant erosion, posing challenges for infrastructure sustainability. This research aimed to identify cost-effective and efficient binder combinations suitable for protecting soil surfaces against severe erosion. Disturbed soil samples were mixed with agricultural lime, gypsum, and triple blends at varying proportions and subjected to controlled weathering and flume tests at velocities of up to 2 m/s. The results revealed that triple blends, at proportions of 2 % and 3 %, demonstrated the most effective erosion resistance, with unconfined compressive strengths exceeding 1 MPa. In contrast, gypsum showed limited efficacy due to uneven binding distribution. The study concludes that optimal binder selection and application can significantly reduce erosion susceptibility, offering a sustainable solution for rural infrastructure protection.

**Citation:** To, P., Pham, N.T. Application of various binders in soil stabilisation for road batter protection. Magazine of Civil Engineering. 2025. 18(2). Article no. 13402. DOI: 10.34910/MCE.134.2

### 1. Introduction

Soil erosion is a common problem for transportation infrastructure projects, mainly road embankment slopes, causing significant damage due to flash floods. Strong water flow can lead to erosion, damaging the embankment and underlying soil layers and resulting in road surface cracks and subsidence [1]. While using concrete for slope protection is effective, it is costly, especially for traffic projects in rural areas with low traffic density and limited budgets. Therefore, finding cost-effective alternative solutions is essential. This study uses binders to stabilize the soil and protect the road embankment, contributing to enhanced sustainability and safety for the transportation system.

The traditional binders used in soil stabilization include Portland cement, lime, and fly ash, which have been extensively studied for their effectiveness in enhancing soil strength and stiffness. For instance, Tsai et al. highlighted that adding fiber-mixed binders can significantly improve the compaction and California Bearing Ratio (CBR) characteristics of sandy clay, demonstrating the potential of composite binders in soil stabilization [2]. Similarly, Lindh and Lemenkova emphasized that different soil types require specific stabilizers; coarse-grained soils benefit from Portland cement and fly ash, while fine-grained soils are more effectively stabilized with lime or a combination of lime and cement [3]. This distinction is crucial for engineers when selecting appropriate binders for specific soil types. In addition to traditional binders, alternative materials have gained attention due to their environmental benefits and effectiveness. For example, Du et al. explored using a phosphate-based binder for stabilizing soils contaminated with heavy metals, demonstrating that such binders can reduce leaching and enhance soil strength [4]. This approach



aligns with the growing trend of using waste materials and by-products in soil stabilization, improving soil properties, and addressing environmental concerns related to waste disposal [5]. Integrating alternative binders, such as ground granulated blast furnace slag (GGBS) and fly ash, has enhanced the mechanical properties of stabilized soils while reducing the carbon footprint associated with traditional cement production [6]. Their dosage and the water-binder ratio also influence the effectiveness of binders in soil stabilization. Lindh's research indicated that the water-binder ratio significantly affects stabilized soils' strength and seismic behavior, suggesting that careful control of this parameter is essential for achieving desired stabilization outcomes [7]. Moreover, Pham et al. found that increasing the binder leads to higher unconfined compressive strength (UCS) and reduced permeability in stabilized clayey soils, underscoring the importance of optimizing binder content for effective stabilization [8]. This optimization process is critical, as excessive binder use can lead to economic inefficiencies and environmental impacts. The application methods for binders also vary, with techniques such as deep soil mixing (DSM) and dry soil mixing commonly employed. Timoney et al. described the dry soil mixing method, where binders are injected in powder form into the soil, effectively enhancing the geotechnical properties of organic soils [9]. This method is particularly advantageous in areas with high moisture content, as it minimizes water-related issues during stabilization. Additionally, biopolymer binders, such as xanthan gum, have emerged as a promising alternative, offering unique properties such as high viscosity and hydrophilicity, which can improve soil stability and reduce erosion [10, 11]. The interaction between binders and soil also plays a significant role in determining the effectiveness of stabilization. The chemical reactions that occur during the hydration of binders, particularly with calcium silicate and alumina, contribute to the increased strength and durability of the stabilized soil [12]. Furthermore, using admixtures, such as sodium chloride as a cement accelerator, has enhanced the early strength gain of stabilized peat, indicating that the choice of binder and its additives can significantly influence stabilization outcomes [13]. Environmental considerations are increasingly influencing the selection of binders for soil stabilization. Alkali-activated binders and geopolymers have been explored as a sustainable alternative to traditional cement, offering similar or improved performance while reducing environmental impacts [14, 15]. The decision-making model proposed by Rocha et al. emphasizes the importance of minimizing costs and environmental impacts when selecting binders for soil stabilization, reflecting a broader trend toward sustainable engineering practices [16–18].

Although extensive research has been done on using binders for soil stabilization, studies focusing on protecting road embankment slopes, particularly in rural areas, are still lacking. Moreover, selecting the appropriate binder must be based on the specific factors of each project, including soil type, climatic conditions, technical requirements, and budget [19, 20]. This study is conducted within a confidential project in Queensland, where cost-effective and efficient solutions are sought to protect embankment slopes from erosion. The results of the survey will provide valuable information for selecting and applying binders in slope protection, contributing to the effectiveness and sustainability of the project.

## 2. Materials and Methods

### 2.1. Soil Preparation

So as to investigate the effect of binders, soil must be tested under controllable conditions in the laboratory. The Department of Transport and Main Road (DTMR) sampled the soil. Then, it was mixed with various binders at the DTMR laboratory. Four binders were selected based on commercial availability: agricultural lime, gypsum, triple blend, and emulsion (residual bitumen). However, the emulsion was eliminated due to environmental concerns. The triple blend comprises 30 % general-purpose cement, 30 % fly ash, and 40 % hydrated lime.

The main effect of binder is to build a C-S-H binding force, which comes from Calcium, Silicon, and Hydrogen. The binders contribute Calcium (Table 1), while the soil has over 50 % mass of  $\text{SiO}_2$ . Hydrogen is available in the soil's moisture content.

**Table 1. Calcium component in binders.**

Binder	Calcium (% mass)
Agricultural lime	37–40 %
Gypsum	27–31 %
Triple blend	35–46 %

A previous study on lime showed that 3.25 % of lime could significantly prevent erosion at a ratio of 3.75 %, and erosion is negligible at a ratio of 5.25 % of lime [20]. Due to economic constraints, the binders were mixed at lower different ratios. Agricultural lime and gypsum were mixed at 0.5 %, 1.5 %, and 2.5 % of mass. Meanwhile, the triple blend was mixed at 1 %, 2 %, and 3 %, thanks to its availability.



After that, the mixtures were molded in acrylic boxes with a plastic tamper and 3D printed to the appropriate size (Fig. 1). A compaction by layer may be required to reach the desired relative density of 97 %. The box's width was selected after the maximum power of the pump so that it could supply water at the velocity of 2 m/s over the sample in the flume test. The length and the depth were deterred from a previous erosion study so that the soil sample was thick enough for the developed erosion [20].

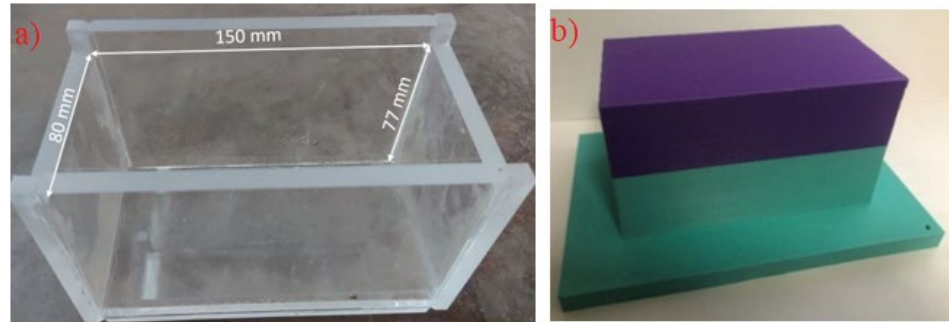


**Figure 1. Sample mold: (a) acrylic box and (b) plastic tamper.**

Before testing, samples were exposed to the weather for 5 weeks (Fig. 2). This sun bath simulates the weather effect on the ground surface. As a result, the top surface was dried and more susceptible to erosion. Ambient temperature varied from 22 °C to 38 °C, and humidity varied widely from 20 % to 80 %. However, no significant surface crack was observed.



**Figure 2. Samples in sun exposure.**

## 2.2. Laboratory Testing

**Flume test.** After the preparation, samples were tested with strong overflow of 0.5, 1.0, and 2.0 m/s. DTMR required the velocity for various probabilities of flood [21, 22]. These velocities already accounted for a heavy safety factor since actual flow may have a higher thickness, which results in a lower velocity at the flow bed. TUFLOW and ANSYS simulation can derive a detailed estimation [23 - 25].

The surface erosion apparatus was 3D printed in 5 pieces and assembled with a seal (Fig. 3). To reduce turbulence, the apparatus employed a laminator at the upstream side. The downstream side is empty to minimize backflow due to clogging.

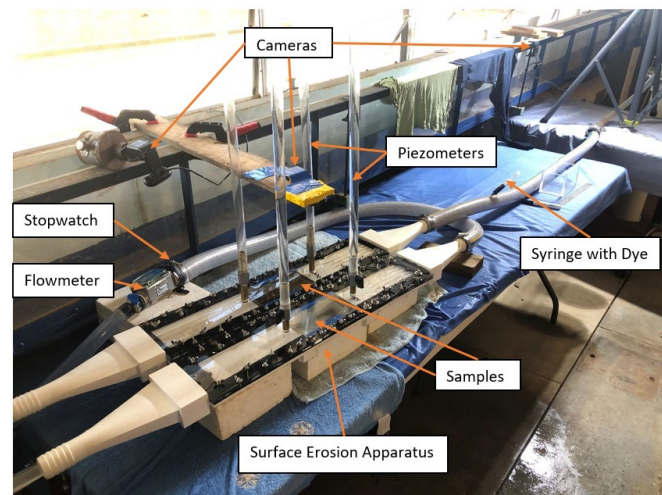


**Figure 1. Flume test setup.**



However, a trial showed that monitored water pressures still changed very quickly. Sometimes, the value at the upstream side is lower than at the downstream. Although there was a recommendation to use more sensitive sensors [9]. The sensing rate of the employed Wika A-10 and the recording rate of the DT85 data logger were already milliseconds. Hence, a decision was made to go in the opposite direction. 3 m piezometers were attached to reduce the fluctuation. The water heads still fluctuated but at a very slow rate, and the pressure at the upstream side was consistently more significant than the pressure at the downstream.

Four high-resolution webcams controlled by authorial software monitored the flume test. These cameras monitored a flow meter, a timer, samples, and the piezometers. The test on each sample was run continuously for 24 hours.

**Data processing.** After testing, samples were dried with a heat gun until no water was visible at the surface (Fig. 4a). Then, the surface was obtained with an EinScan Surface Light scanner. This portable scanner could help scan tricky corners. However, there were still several mesh failures, which must be patched (Fig. 4b). The surface data was transformed into a com-putable mesh with Shining 3D and Fusion 360 (Fig. 4c). After that, the eroded volume and erosion depth were computed. The average eroded depth,  $D$ , is calculated as  $D = \text{Volume loss}/\text{Sample Area}$ .

However, the actual depth may vary by location. Hence, erosion depth at various distances from the edge of the sample was also measured.

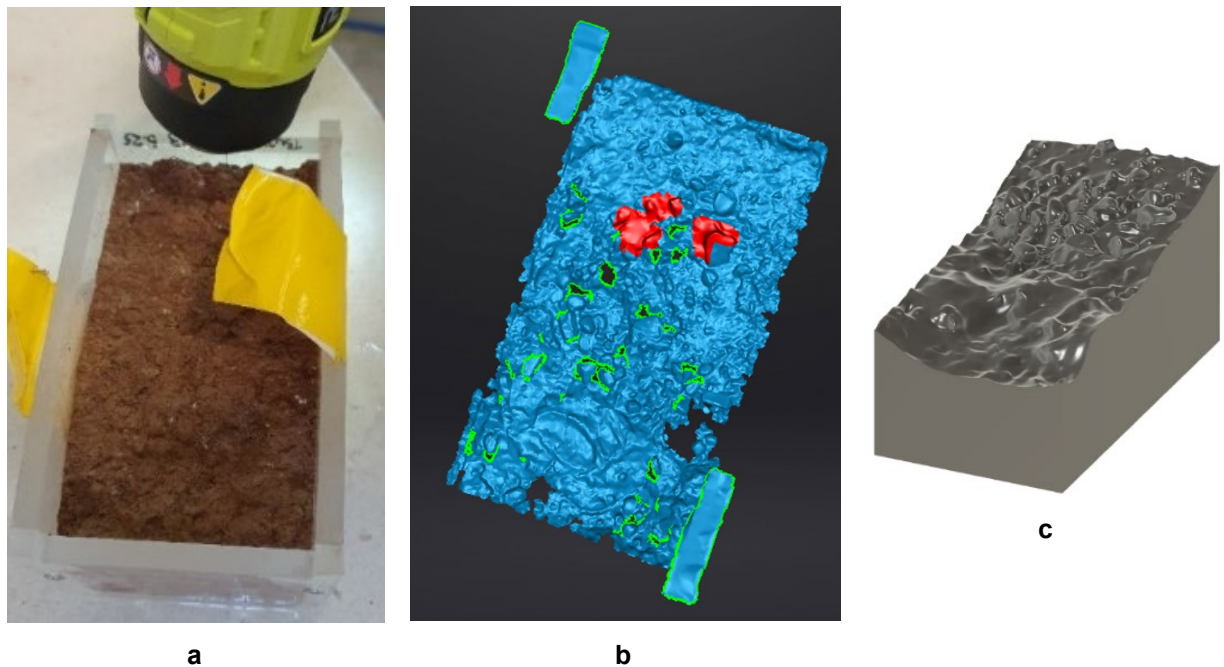


**Figure 4. Surface scan: (a) sample drying after the test, (b) scanned topography, and (c) remaining volume.**

### 3. Results and Discussion

A summary of test results is presented in Table 2. Gypsum has no effect on erosion protection with the given mass proportions. In contrast, it increased the eroded volume to the maximum. This may be caused by the fact that gypsum provided some binding force, but it was not distributed well due to the low mass proportions. Hence, some agglomerates were formed. However, there was not enough binding force globally. These agglomerates suffered more drag force and were more susceptible to erosion. This explanation may also be proper for the sample with a low proportion of agricultural lime and triple blend. Binders had a negative effect when a low proportion of binder could form ag-glomerates but could not bind the whole soil mass.

**Table 2. Eroded volume ( $\text{cm}^3$ ).**

V (m/s)	No binder	Agricultural lime			Gypsum			Triple blend		
		0.5 %	1.5 %	2.5 %	0.5 %	1.5 %	2.5 %	1 %	2 %	3 %
0.5	89.70	122.6	131.3	136.7	180.3	210.1	197.0	232.2	17.9	18.6
1.0	230.64	254.7	221.1	230.4	406.2	420.0	398.8	502.5	37.6	51.6
2.0	620.40	676.8	924.0	357.6	924.0	924.0	924.0	671.6	53.8	39.3



Agricultural lime showed some effect of treatment. However, the efficacy of the tested proportions was not yet satisfactory. The test of the sample with 1.5 % lime and 2.0 m/s flow was an interesting case when some gravels enhanced the erosion. Meanwhile, the triple blend showed good efficacy at proportions of 2 % and 3 % by mass.

Notably, the eroded volume may differ from the computed value due to the erosion (Fig. 5). After a significant erosion, the sample surface might not be exposed to strong flow anymore. Hence, it would have less shear stress. However, the turbulence might increase the direct impact on the surface. As a sequence, the everyday stress would increase. A previous study proposed to extrude the sample 1 mm into the flow to keep the flat surface [25]. This might not entirely reflect the surface erosion because the top layer might be peeled off by everyday stress from the intense flow rather than the shear stress. In addition, it may also cause some destruction at the boundary due to the sample extrusion. To illustrate the impact, the profile of eroded surfaces was built from 4 key points, the midpoints of sample quadrants (Fig. 6).

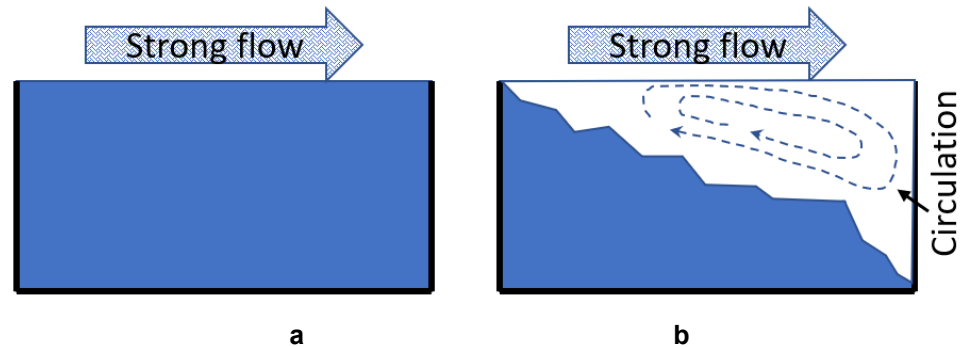


Figure 5. Flow pattern on tested specimen: (a) before the erosion and (b) after the erosion.

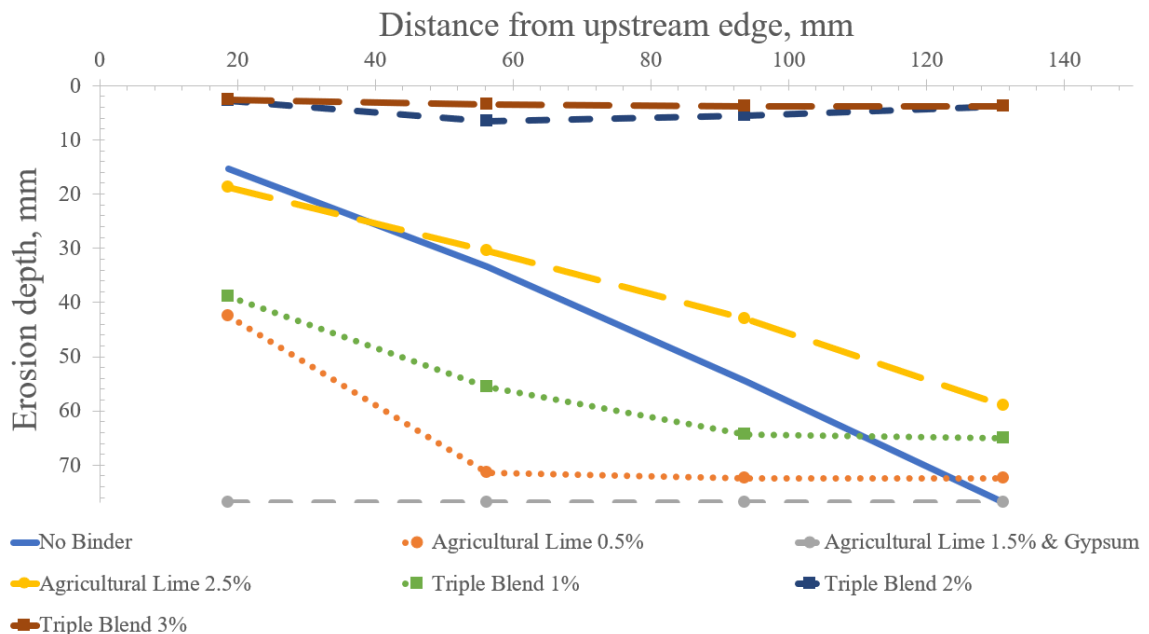
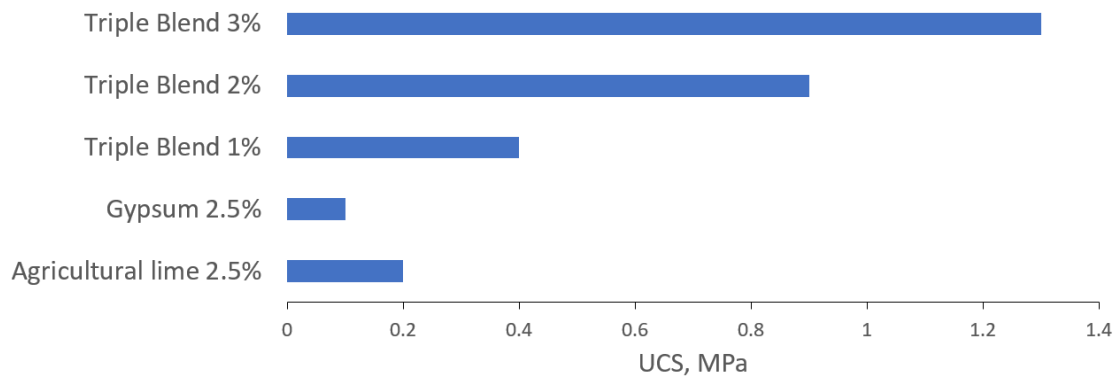


Figure 6. Surface profiles after tests with the 2 m/s flow.

The graph shows that samples with 0.5 % agricultural lime and 1 % triple blend suffered damage from everyday stress rather than shear stress. Hence, the surface was not straight but leveled off after a distance.

In contrast, samples with 2 % and 3 % of triple blends showed adequate protection. Indeed, the strong over-flow peeled off only the weathered top layer. These samples were damaged by shear stress rather than everyday stress. UCS tests were undertaken to see how strong the samples were bound. The direct link between erosion protection and UCS seemed obvious (Fig. 7). Although the strength requirement depends on the flow velocity of the flood, samples with a 3 % triple blend had UCS over 1 MPa, which stepped into the zone of very weak rock.





**Figure 7. Unconfined compressive strength of samples with binders.**

#### 4. Conclusion

The paper presents a study on the impact of various binders on soil erosion susceptibility. Some striking discoveries have been concluded:

- If the proportion of the binder is not high enough, the binder may negatively impact erosion protection due to the formation of agglomeration.
- Samples with 2 % and 3 % of triple blends seem to have adequate protection as only the weathered top layer was eroded. Note that this layer was dried during the curing process.
- UCS of roughly 1 MPa can be a good sign for an effective binder.

Future studies may focus on the impact of everyday stress during the erosion.

#### References

1. Ayoob, N.S., Abid, S.R., Hilo, A.N., Daek, Y.H. Water-impact abrasion of self-compacting concrete. *Magazine of Civil Engineering*. 2020. 96 (4). Pp. 60–69. DOI: 10.18720/MCE.96.5
2. Tsai, K., Chan, C., Tan, P. Compaction and CBR Characteristics of Sandy Clay Stabilised with Fibre-Mixed Binder. *International Journal of Engineering & Technology*. 2019. 7(4.14). Pp. 343–347. DOI: 10.14419/ijet.v7i4.14.27671
3. Lindh, P., Lemenkova, P. Laboratory Experiments on Soil Stabilization to Enhance Strength Parameters for Road Pavement. *Transport and Telecommunication Journal*. 2023. 24(1). Pp. 73–82. DOI: 10.2478/tjt-2023-0008
4. Du, Y., Wei, M., Reddy, K., Jin, F., Hao, W., Liu, Z. New phosphate-based binder for stabilization of soils contaminated with heavy metals: Leaching, strength and microstructure characterization. *Journal of Environmental Management*. 2014. 146. Pp. 179–188. DOI: 10.1016/j.jenvman.2014.07.035
5. Teing, T., Huat, B., Shukla, S., Anggraini, V., Nahazanan, H. Effects of alkali-activated waste binder in soil stabilization. *International Journal of Geomate*. 2019. 17(59). Pp. 82–89. DOI: 10.21660/2019.59.8161
6. Lindh, P., Lemenkova, P. Effects of GGBS and Fly Ash in Binders on Soil Stabilization for Road Construction. *Romanian Journal of Transport Infrastructure*. 2022. 11(2). Pp. 1–13. DOI: 10.2478/rjti-2022-0010
7. Lindh, P. Effects of Water-Binder Ratio on Strength and Seismic Behavior of Stabilized Soil from Kongshavn, Port of Oslo. *Sustainability*. 2023. 15(15). Article no. 12016. DOI: 10.3390/su151512016
8. Pham, V., Oh, E., Ong, D. Effects of binder types and other significant variables on the unconfined compressive strength of chemical-stabilized clayey soil using gene-expression programming. *Neural Computing and Applications*. 2022. 34(11). Pp. 9103–9121. DOI: 10.1007/s00521-022-06931-0
9. Timoney, M., McCabe, B., Bell, A. Experiences of dry soil mixing in highly organic soils. *Proceedings of the Institution of Civil Engineers – Ground Improvement*. 2012. 165(1). Pp. 3–14. DOI: 10.1680/grim.2012.165.1.3
10. Babatunde, Q., Byun, Y. Soil Stabilization Using Zein Biopolymer. *Sustainability*. 2023. 15(3). Article no. 2075. DOI: 10.3390/su15032075
11. Jiang, T., Zhao, J., Zhang, J. Splitting tensile strength and microstructure of xanthan gum-treated loess. *Scientific Reports*. 2022. 12(1). Article no. 9921. DOI: 10.1038/s41598-022-14058-4
12. Lindh, P., Lemenkova, P. Impact of Strength-Enhancing Admixtures on Stabilization of Expansive Soil by Addition of Alternative Binders. *Civil and Environmental Engineering*. 2022. 18(2). Pp. 726–735. DOI: 10.2478/cee-2022-0067
13. Wong, L., Hashim, R., Ali, F. Unconfined compressive strength characteristics of stabilized peat. *Scientific Research and Essays*. 2011. 6(9). Pp. 1915–1921. DOI: 10.5897/sre10.060
14. Abdeldjoud, L., Asadi, A., Huat, B., Jaafar, M., Dheyab, W., Elkhebu, A. Effect of curing temperature on the development of hard structure of alkali-activated soil. *International Journal of Geomate*. 2019. 17(60). Pp. 117–123. DOI: 10.21660/2019.60.8160
15. Du, Y., Feng, Y., Xia, W. Assessment of feasibility of using an innovative binder to solidify/stabilize site soils contaminated by mixed zinc and chloride. *Japanese Geotechnical Society Special Publication*. 2020. 8(10). Pp. 398–403. DOI: 10.3208/jgssp.v08.c29
16. Rocha, C., Bittar, E., Samaniego, R., Consoli, N. Decision-Making Model for Soil Stabilization: Minimizing Cost and Environmental Impacts. *Journal of Materials in Civil Engineering*. 2021. 33(2). Article no. 06020024. DOI: 10.1061/(asce)mt.1943-5533.0003551
17. Alex, J., Ayikkara, K. Stabilization of lateritic soil for masonry applications. *Magazine of Civil Engineering*. 2021. 1(101). Article no. 10109. DOI: 10.34910/MCE.101.9



18. El-Nadoury, W. Production of sustainable concrete using sawdust. Magazine of Civil Engineering. 2021. 2021. 105(5). Article no. 10507. DOI: 10.34910/MCE.105.7
19. Jegandan, S., Liska, M., Osman, A. A., Al-Tabbaa, A. Sustainable binders for soil stabilisation. Proceedings of the Institution of Civil Engineers – Ground Improvement. 2010. 163(1). Pp. 53–61. DOI: 10.1680/grim.2010.163.1.53
20. Pallanza, A., To, P., Matheson, M. Lime stabilised road batters: A laboratory simulation of site flood conditions using a customised erosion apparatus and sample digitisation. Transportation Geotechnics. 2023. 40. Article no. 100975. DOI: 10.1016/j.trgeo.2023.100975
21. J. Schubert, K. Mach, & B. Sanders, "National-scale flood hazard data unfit for urban risk management", Earth's Future, vol. 12, no. 7, 2024. <https://doi.org/10.1029/2024ef004549>
22. T. Mawasha and W. Britz, "Hydrological impacts of land use - land cover change on urban flood hazard: a case study of the Jukskei river in Alexandra Township, Johannesburg, South Africa", South African Journal of Geomatics, vol. 10, no. 2, pp. 139-162, 2022. <https://doi.org/10.4314/sajg.v10i2.11>
23. J. Ma, J. Chen, Z. Cui, W. Zhou, R. Chen, & C. Wang, "Reconstruction of catastrophic outburst floods of the Diexi ancient landslide-dammed lake in the upper Minjiang river, Eastern Tibetan Plateau", Natural Hazards, vol. 112, no. 2, pp. 1191-1221, 2022. <https://doi.org/10.1007/s11069-022-05223-z>
24. S. Islam and İ. Demir, "A novel methodology for enhancing flood risk communication: the nines of safety", 2024. <https://doi.org/10.31223/x58h5z>
25. Briaud, J.L., Ting, F.C.K., Chen, H.C., Cao, Y., Han, S.W., Kwak, K.W. Erosion Function Apparatus for Scour Rate Predictions. Journal of Geotechnical and Geoenvironmental Engineering. 2001. 127(2). Pp. 105–113. DOI: 10.1061/(ASCE)1090-0241(2001)127:2(105)

**Information about the authors:**

**Peter To,**

E-mail: [peter.to@jcu.edu.au](mailto:peter.to@jcu.edu.au)

**Ngoc Thinh Pham,**

ORCID: <https://orcid.org/0000-0002-4928-6236>

E-mail: [thinhtls@tlu.edu.vn](mailto:thinhtls@tlu.edu.vn)

*Received 24.12.2024. Approved after reviewing 11.03.2025. Accepted 11.03.2025.*





Research article

UDC 534.1

DOI: 10.34910/MCE.134.3



## Analysis of rheological model parameters for various foamed vibration-damping materials

M.V. Shitikova  , V.A. Smirnov 

Moscow State University of Civil Engineering (National Research University), Moscow, Russian Federation

✉ [shitikova@vmail.ru](mailto:shitikova@vmail.ru)

**Keywords:** viscoelastic materials, fractional derivatives, resonance testing, dynamic modulus, loss factor, material density, pore structure, polyurethane foam, damping properties, rheological modeling

**Abstract.** The study presents an experimental and analytical investigation of foamed polyurethane viscoelastic materials with varying density and pore structures, focusing on their dynamic mechanical behavior relevant for vibration damping applications. Samples with distinct pore configurations (open, closed, and combined) and varying densities (165–380 kg/m<sup>3</sup>) were subjected to resonance-based dynamic tests under static loads of 2, 5, and 10 kPa. The dynamic modulus of elasticity and damping characteristics, including loss factor, fractional damping parameters, and relaxation times, were determined. Results indicated that damping properties are strongly influenced by material density and internal pore structure, with closed-pore materials exhibiting lower damping capacities compared to materials with open or combined pores. A Fractional Standard Linear Solid (FSLs) model was effectively utilized to characterize the observed nonlinear viscoelastic behaviors, successfully correlating experimental data through parameter identification methods. The findings confirm that increased density generally enhances the dynamic modulus while reducing damping capacity, whereas pore structure significantly affects the material's dynamic response. These insights validate fractional derivative models as efficient predictive tools, facilitating the optimized design of viscoelastic isolation systems for engineering structures.

**Funding:** This research has been supported by the Ministry of Science and High Education of the Russian Federation, Project No.07-03-2023-132 (FZGM-2023-0006).

**Citation:** Shitikova, M.V., Smirnov, V.A. Analysis of rheological model parameters for various foamed vibration-damping materials. Magazine of Civil Engineering. 2025. 18(2). Article no. 13403. DOI: 10.34910/MCE.134.3

### 1. Introduction

Viscoelastic materials have been widely employed in numerous branches of science and engineering to address critical issues such as reducing dynamic impacts on supporting structures, vibration and seismic isolation of buildings and technical systems, and modifying the dynamic stiffness of structural elements. In these applications, understanding the dynamic behavior of the viscoelastic elements is indispensable for ensuring the reliability and efficiency of isolation and damping systems. Such behavior is inherently rate-dependent, as the stiffness and damping characteristics of elastomers and polymeric foams generally exhibit considerable sensitivity to strain rate, frequency, and amplitude of excitation. Consequently, formulating accurate constitutive models becomes pivotal in designing vibration and seismic isolation systems with predictable performance over their entire service life.

A broad spectrum of rheological models has been proposed to capture the complex time- and frequency-dependent behavior of viscoelastic materials, ranging from simple two-parameter models, such as the Kelvin–Voigt or Maxwell models, to sophisticated multi-element generalized models containing



multiple chains of springs and dashpots [1]. However, classical integer-order models can fail to capture certain real-world behaviors, especially when damping mechanisms arise from multiple or overlapping relaxation processes. Furthermore, simplified models sometimes yield unphysical predictions. For instance, Kelvin–Voigt-type models may exhibit artificially high or even unbounded loss factors under specific parametric conditions. On the other hand, highly parameterized multi-element frameworks, such as the Mooney–Rivlin model with eleven or more parameters, demand extensive experimental campaigns, making them impractical for many engineering contexts.

Recent studies emphasize that these challenges can often be addressed by leveraging fractional calculus, which introduces fractional-order derivatives into standard viscoelastic models. Fractional operators enable more flexible representation of material memory effects than their integer-order counterparts [2, 3]. Such models, including the Fractional Kelvin–Voigt, Fractional Maxwell, and Fractional Standard Linear Solid (FSLs) models, can reconcile high modeling accuracy with comparatively fewer model parameters [4]. Moreover, numerical advancements in solving fractional differential equations [5] further encourage the use of fractional derivatives in practical applications.

Early applications of fractional viscoelastic models in structural mechanics have demonstrated promising results. Studies on beams, plates, and shells resting on fractional viscoelastic foundations [6–9] have shown that incorporating fractional damping provides excellent agreement between experimental data and theoretical predictions for a wide range of frequencies. Furthermore, fractional operator models have found utility in seismology, where they can represent constant- $Q$  (quality factor) seismic waves more effectively than classical integer-order approaches [10, 11]. These successes align with other experimental validations in the literature: for instance, fractional models have demonstrated high fidelity in capturing the creep and recovery behavior of asphalt mixtures [12], the rheological response of fiber-reinforced rubber concrete [13], large-amplitude vibrations in metallic and polymeric systems [14], and viscoelasticity in polyethylene [15, 16], silicone [17, 18], and various rubber compounds [19].

Notably, fractional derivative-based methodologies have facilitated accurate and efficient identification of viscoelastic parameters. Bedard and Chevalier [20] proposed a parametric identification technique to determine fractional exponents and relaxation moduli from limited experimental datasets. Similarly, Espindola et al. [21] and Guo et al. [22] extended these approaches to thermoplastics and polymeric acoustic foams, revealing that fractional damping parameters often remain within a relatively narrow range under typical operational conditions, thus enabling simpler yet robust models. In these studies, the deviation between model predictions and experimental data was reported to be significantly lower compared to classical models – often below 5 % across a wide frequency range.

Despite the recognized advantages, an ongoing challenge in fractional derivative modeling pertains to the identification of fractional parameters from experimental data, which can be especially sensitive to measurement noise, excitation frequencies, and other test conditions [5]. Recent investigations [13] demonstrated that the fractional exponent for fiber-reinforced rubber concrete could be identified by comparing analytical solutions of the FSLs model with experimental resonance data, obtaining an excellent agreement (errors consistently under 4 % in the measured stiffness loss). Similar conclusions were made for other polymeric and hyperelastic materials, highlighting how fractional damping exponents effectively characterize time-dependent material behavior in both the low- and high-frequency regimes [17, 18, 20–22].

Driven by these findings, the present study focuses on foamed polyurethane vibration-damping materials with combined pore structures and varying densities, aiming to elucidate the role of fractional parameters in their dynamic response. By performing a series of resonance tests, the mechanical properties – dynamic modulus of elasticity and loss factor – are obtained under a range of static preloads and dynamic excitations. These datasets serve as inputs to a FSLs model, whose parameters are systematically identified via nonlinear least squares optimization. Emphasis is placed on capturing both stiffness and damping variations across different densities and pore structures, thereby highlighting the nuanced influence of foam microstructure on global vibrational performance.

This paper presents a comprehensive experimental and analytical framework – encompassing test setup, data acquisition, and model parameter identification – to ensure reliable quantification of viscoelastic behavior. The insights gained herein extend the applicability of fractional operator modeling to a broader class of vibration-damping materials, contributing to advanced design strategies for high-efficiency passive isolation and noise control systems. The following sections detail the experimental methodology, describe the fractional-derivative-based approach to parameter identification, and discuss the implications of the results for future research and practical applications in vibration and seismic isolation.



## 2. Method

### 2.1. Materials with Different Stiffness

Let us first consider the behavior of vibration-damping materials, widely used in various fields of engineering and construction, made on the basis of foamed polyurethanes with different combination of closed and open pores, as well as with different densities.

For a comparative evaluation of the behavior of materials under dynamic impact a series of samples (type s.1.1–s.1.4 in Fig. 1 a–d) with combined pore structure and increasing density, as well as materials with approximately the same density but different structure: type s.2.1 with closed pores (Fig. 1 e) and type s.1.4 (Fig. 1 d) are considered.

These materials, due to their foam structure, have pronounced nonlinear characteristics. When the applied compression load increases, the stiffness of the material in the range of its operation decreases, which is due to the structural features of "collapse" of open pores and "pumping" of sealed air, and, having reached the limit value, begins to increase.

The internal structure of the samples (slice fixation) of the materials is shown in Fig. 1. The images were obtained using an optical microscope with 50x – 100x magnification. For materials of types s.1.1–s.1.4 it could be noted that the increase in density occurs with a simultaneous increase in the number of internal pores and a decrease in their size – the spread between large and small pores decreases and their total diameter becomes more and more constant.

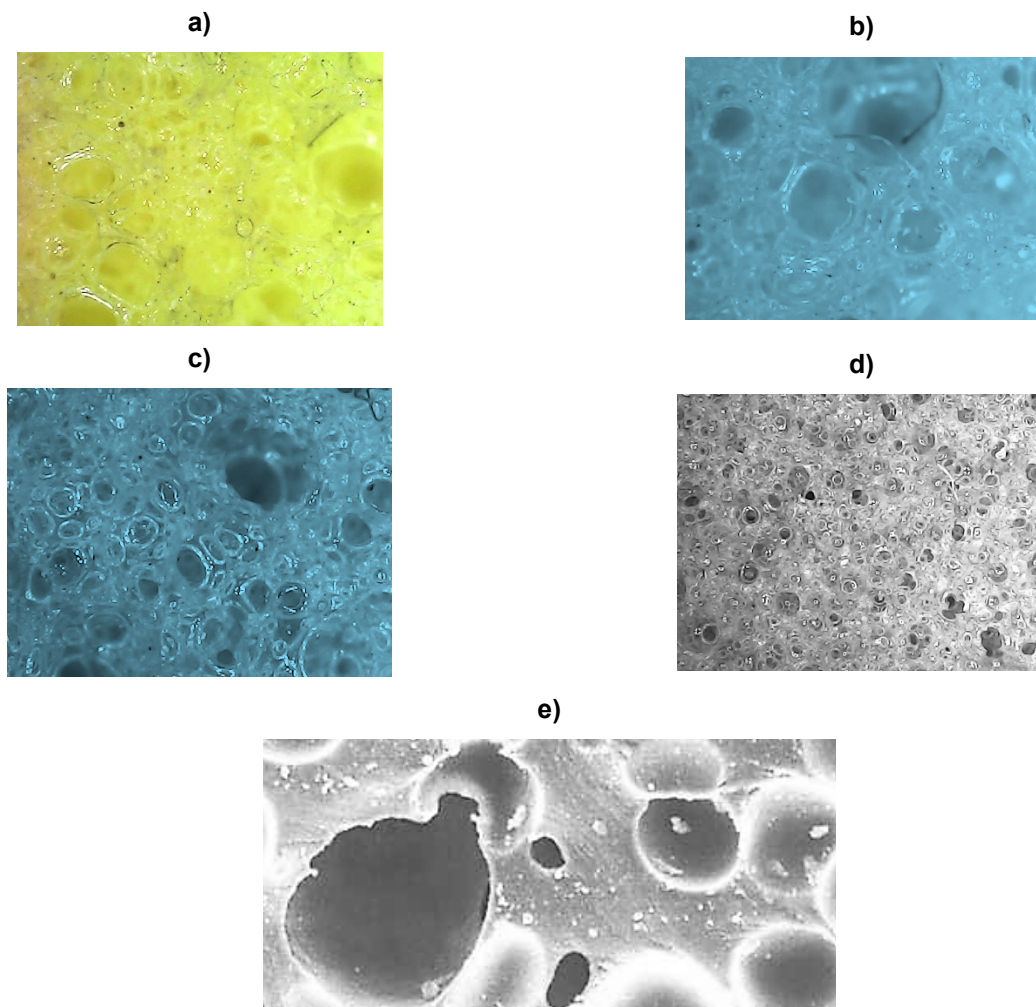


**Figure 1. Internal porous structure of material samples: a) type s.1.1; b) type s.1.2; c) type s.1.3; d) type s.1.4; e) type s.2.1.**

### 2.2. Materials with Different Damping

We also consider the behavior of vibration-damping materials based on polyurethane foam, used as a vibration-damping layer of vibration isolation systems for buildings and structures, machine foundations and high-precision equipment.

Two series of materials of approximately the same stiffness but with different structural features are considered for comparative evaluation of materials behavior under dynamic influence:

- type d.1 – material with closed pores, which has the most elastic properties;
- type d.2 – material with communicating pores, it has high damping, its properties are close to those of viscous liquids;
- type d.3 – material with combined pore structure, it combines the properties of materials of types d.1 and d.2.

These materials, due to their foamed structure, have pronounced nonlinear characteristics. When the applied compression load increases, the stiffness of the material in the range of its operation decreases, which is due to the structural features of "collapse" of open pores and "pumping" of sealed air, and, having reached the limit value, begins to increase.

### 2.3. Experimental Method

To determine the mechanical characteristics of the materials under study, a series of dynamic tests were carried out using the resonance method on a stand developed in accordance with GOST 16297-80, the general scheme of which is shown in Fig. 2. Experimental studies were carried out for samples in the form of square plates with dimensions of  $100 \times 100 \times 25$  mm. The sample of vibration-damping material 3 was installed on the stage 2 of electrodynamic vibro-exciter 1 and loaded with steel cylinders (masses) 4, providing constant loads on the sample of 2, 5 and 10 kPa.

Tests were conducted when the sample was subjected to broadband (white) noise. The perturbation signal was set by the oscillation generator RFT 03004 7, which through the amplifier RFT LV-102 8 was connected to the vibration exciter ESE-201 type 1. During the tests, the accelerations of the moving part of the electrodynamic vibration exciter (base) 5' – function  $z(t)$ , as well as the response of the system 5 – function  $x(t)$  were recorded by single-axis accelerometers PCB and multichannel measuring system LCARD LTR-24-2.

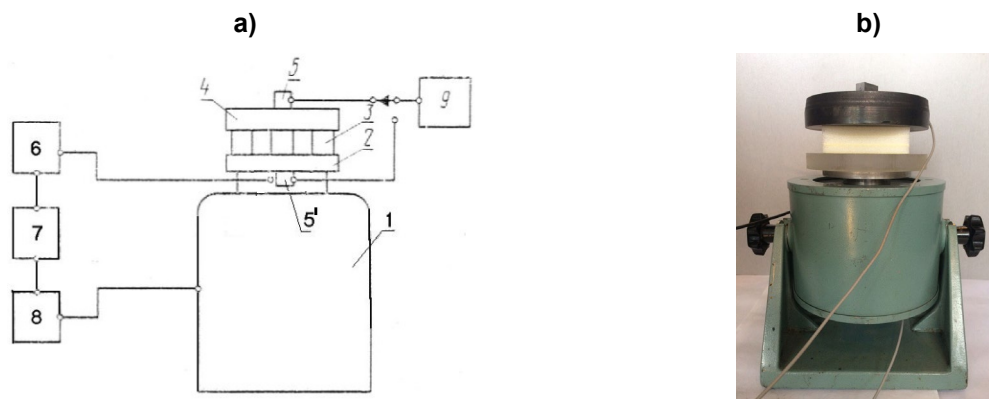


**Figure 2. Test bench for dynamic tests by resonance method:**  
a) schematic diagram of the test bench; b) photo of the shaker.

According to the results of dynamic tests by the resonance method, the measured accelerograms of base vibration  $\ddot{z}(t)$  and mass  $\ddot{x}(t)$  were processed to obtain the spectral characteristics of  $\ddot{z}(\omega)$  and  $\ddot{x}(\omega)$ . The transfer function  $\text{Tr}(\omega)$  is defined as the ratio of the spectral characteristics of the vibration accelerations obtained at the mass to the spectral characteristics of the vibration accelerations recorded at the base:

$$\text{Tr}(\omega) = \left| \frac{\ddot{x}(\omega)}{\ddot{z}(\omega)} \right|, \quad (1)$$

where  $\omega$  is the frequency of external kinematic influence, Hz.

Fig. 3 shows experimentally obtained curves of the transfer function modulus  $\text{Tr}(\omega)$  for the object of study in the frequency range of 1–500 Hz at a constant load on the sample of 5 kPa.

Note that for materials with combined pores of types s.1.1–s.1.4, shown by the dashed line, with increasing density, an increase in the resonance frequency of oscillations from 26 Hz (for type s.1.1) to



53 Hz (for type s.1.4) is observed. At the same time, the amplitude of the transfer function modulus at the resonance frequency remains approximately constant and varies in the range of 3–4. The materials of types s.1.4 and s.2.1, having comparable density but different structure, show differences in the region of the resonance frequency of the system: the material with closed pores (type s.2.1) has a lower resonance frequency (44 Hz vs. 53 Hz) and a much larger (3 times) amplitude of the resonance peak.

The dynamic modulus of elasticity of the material could be determined in accordance with GOST 16297-80 using the formula:

$$E_{dyn} = \frac{4\pi^2 \omega_0^2 M l}{S}, \quad (2)$$

where  $\omega_0$  is the resonant frequency of the system, Hz;  $M$  is the mass of the load, kg;  $l$  is the height (thickness) of the sample under load, m; and  $S$  is the area of the tested sample, m<sup>2</sup>.

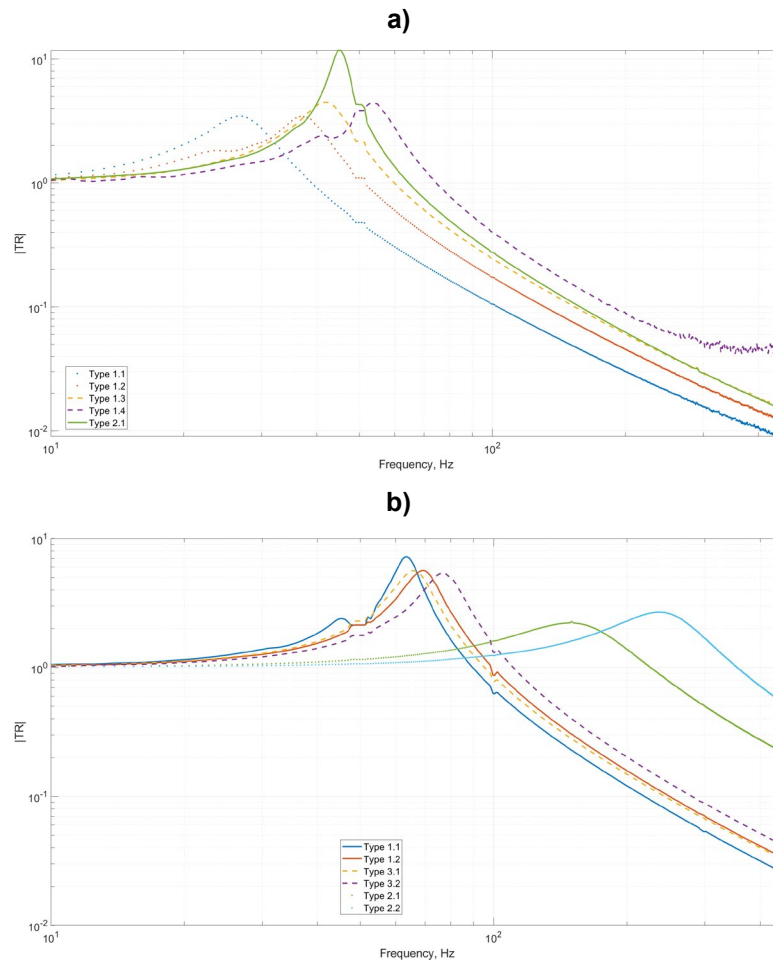


**Figure 3. Modulus curves of the transfer function for the considered materials at a constant load of 5 kPa: a) for materials with different stiffness, and b) for materials with different damping.**

The resonant frequency has been determined as the frequency corresponding to the maximum peak on the transfer function graph.

The loss factor has been evaluated by the width of the resonance peak [23], as shown in Fig. 4. In this case, points A and B on the graph correspond to the frequencies at which the amplitude of accelerations is  $\sqrt{2}$  times smaller than the maximum amplitude achieved at the resonant frequency.

Considering the introduced notations, the formula for the loss factor will be as follows:

$$\eta = \frac{\omega_2 - \omega_1}{\omega_0}. \quad (3)$$

Table 1 shows the obtained mechanical characteristics of the investigated materials.

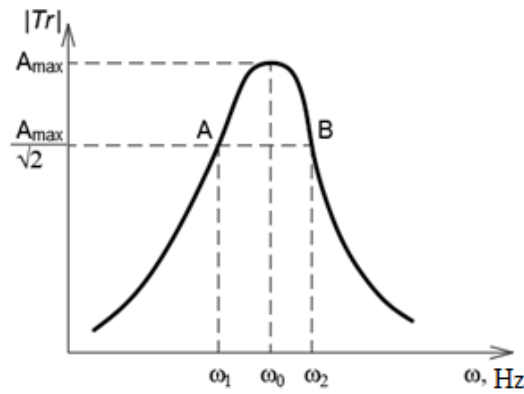


**Figure 4. Schematic of resonance peak width determination.**

**Table 1. Dynamic parameters of the object of study.**

Material identification		Density, kg/m <sup>3</sup>	Load, kPa	$E_{dyn}$ , MPa	$\eta$
Materials with different stiffness	Type s.1.1	165	2	0.428	0.440
			5	0.333	0.420
			10	0.179	0.670
	Type s.1.2	190	2	0.657	0.299
			5	0.659	0.324
			10	0.572	0.600
	Type s.1.3	210	2	0.637	0.423
			5	0.846	0.281
			10	0.782	0.343
	Type s.1.4	380	2	1.129	0.250
			5	1.275	0.237
			10	1.176	0.399
Materials with different damping	Type s.2.1	350	2	0.909	0.172
			5	0.969	0.155
			10	0.952	0.192
	Type d.1.1	343	2	0.788	0.221
			5	1.000	0.130
			10	1.050	0.079
	Type d.1.2	467	2	0.827	0.402
			5	1.190	0.187
			10	1.450	0.164
	Type d.2.1	353	2	3.070	0.664
			5	5.560	0.600
			10	6.690	0.620
	Type d.2.2	572	2	7.280	0.581
			5	13.640	0.483
			10	16.150	0.491
	Type d.3.1	280	2	0.724	0.288
			5	1.070	0.194
			10	1.260	0.177
	Type d.3.2	381	2	1.060	0.319
			5	1.459	0.198
			10	1.650	0.148

Materials belonging to type s.1 & d.1 have a combination of open and closed pores and have pronounced viscoelastic properties with a relatively small loss factor value. It can be noted that with increasing density, the dynamic modulus of elasticity increases, and the loss factor decreases. Materials



with a structure with closed pores (type s.2.1) have more pronounced elastic properties, as evidenced by rather low values of the loss factor compared to other samples.

## 2.4. Rheological Material Models

For mathematical description of viscoelastic characteristics of the considered materials, we would adopt the standard linear solid model with fractional derivative, the rheological model of which is presented in Fig. 5 in two modifications: Zener–Rzhanitsyn (Fig. 5 a) and Poyting–Thomson–Ishlinsky (Fig. 5 b). Both variants are described by the following equation [3]:

$$\sigma + \tau_\varepsilon^\gamma D^\gamma \sigma = E_0 \left( \varepsilon + \tau_\sigma^\gamma D^\gamma \varepsilon \right), \quad (4)$$

where  $\sigma$  is the stress in the element, N/mm<sup>2</sup>;  $\varepsilon$  is the strain of the viscoelastic element;  $\tau_\sigma$  and  $\tau_\varepsilon$  are the creep and relaxation times, respectively, s;  $E_0$  and  $E_\infty$  are the relaxed and instantaneous elastic moduli, respectively, N/mm<sup>2</sup>.

The fractional derivative in the Riemann–Liouville representation is defined as

$$D^\gamma x(t) = \frac{d}{dt} \int_0^t \frac{x(t-u) du}{\Gamma(1-\gamma) u^\gamma}, \quad (5)$$

where  $\Gamma(1-\gamma)$  is the Gamma-function.

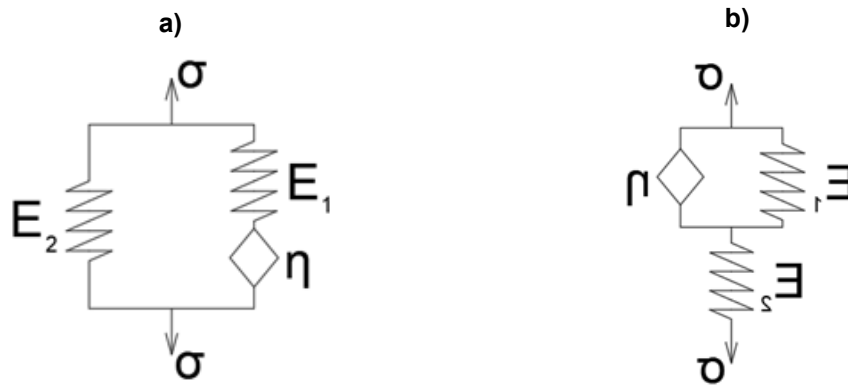


**Figure 5. Standard linear solid model: a) Zener–Rzhanitsyn representation, and b) Poyting–Thomson–Ishlinsky representation.**

Further we will use the standard linear solid model in the Zener–Rzhanitsyn representation, consisting of an elastic element with modulus  $E_2$ , N/mm<sup>2</sup>, connected in parallel with a fractional analog of a Maxwell element involving an elastic element with modulus  $E_1$ , N/mm<sup>2</sup>, and a viscous element  $\eta$ .

Parameters of this model entering in equation (4) are described by the following relationships [3]:

$$E_0 = E_2, \quad E_\infty = \frac{E_1 E_2}{E_1 + E_2},$$

$$\tau_\varepsilon^\gamma = \frac{\eta}{E_1}, \quad \tau_\sigma^\gamma = \frac{E_1 + E_2}{E_1 E_2} \eta, \quad \left( \frac{\tau_\varepsilon}{\tau_\sigma} \right)^\gamma = \frac{E_0}{E_\infty}. \quad (6)$$

Let us consider the mechanical model corresponding to the experimental studies performed in Section 2.

The relationship between the stiffness parameters  $k_1$ ,  $k_2$  and viscosity coefficient  $c$  of the mechanical model (Fig. 6) and the rheological model parameters  $E_1$ ,  $E_2$  and  $\eta$  (Fig. 5 a) is the following:

$$k_1 = \frac{S}{l} E_1, \quad k_2 = \frac{S}{l} E_2, \quad c = \frac{S}{l} \eta, \quad (7)$$

where  $S$  and  $l$  are the area and height (thickness) of the rectangular material specimen under load.

In this case, the damper will be described by the relation  $c = \tau_\varepsilon^\gamma k_1$ , where  $\gamma$  is the fractional parameter ( $0 \leq \gamma \leq 1$ ). When  $\gamma \rightarrow 0$ , the material has purely elastic behavior, and when  $\gamma \rightarrow 1$ , it has purely viscous behavior. In fact, every material has some combination of elastic and viscous properties.

The transfer function (1) for a single-mass system with a viscoelastic element described by equation (4), in the case of a kinematic perturbation of the base  $\ddot{z}(t) = \ddot{Z}_0 e^{i\omega t}$  will take the following form:

$$\text{Tr}_{sls} = \frac{\ddot{x}}{\ddot{z}} = \frac{1 + (N\tau_\varepsilon)^\gamma (i\omega)^\gamma}{1 + (N\tau_\varepsilon)^\gamma (i\omega)^\gamma - \left(\frac{\omega}{\omega_0}\right)^2 (1 + \tau_\varepsilon^\gamma (i\omega)^\gamma)}, \quad (8)$$

where  $\omega_0 = \sqrt{\frac{k}{m}}$ ,  $i = \sqrt{-1}$ ,  $N = \frac{\tau_\sigma}{\tau_\varepsilon}$ .

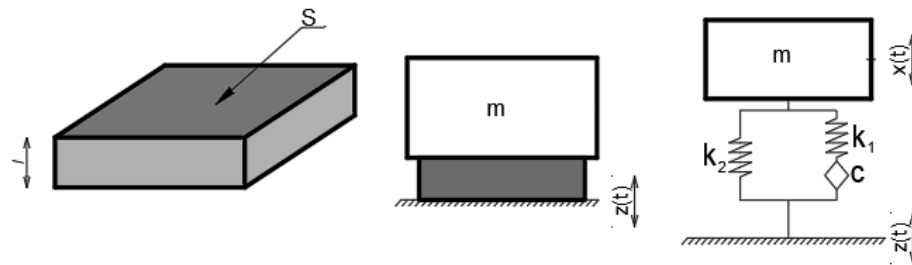


Figure 6. Single-mass oscillating system with a viscoelastic foundation.

### 3. Results and Discussion

To describe the material behavior by the standard linear solid model with fractional derivative, it is necessary to know 5 parameters:  $E_0$ ,  $E_\infty$ ,  $\tau_\varepsilon$ ,  $\tau_\sigma$ ,  $\gamma$ , in so doing 4 of them to be determined, and the 5<sup>th</sup> one could be obtained using relations (6).

The experimentally obtained transfer functions  $\text{Tr}(\omega)$  (1) was approximated by the curve described by the analytical solution (8) for the oscillating system shown in Fig. 6. The optimization problem was solved in the MATLAB program Optimization Toolbox by the nonlinear least squares method using the *lsqcurvefit* function. The natural frequency  $\omega_0$  obtained from the experimental results was set as an initial approximation.

Fig. 7 shows a graphical representation of the result of approximation of the experimental data for material type 2.1 at a load of 2 kPa. Dots indicate experimental data, solid red line refers to the approximated curve, red dotted line are lower and upper 95 % confidence interval.

The results of approximation of the rheological model parameters of the considered materials according to the performed tests are presented in Table 2.



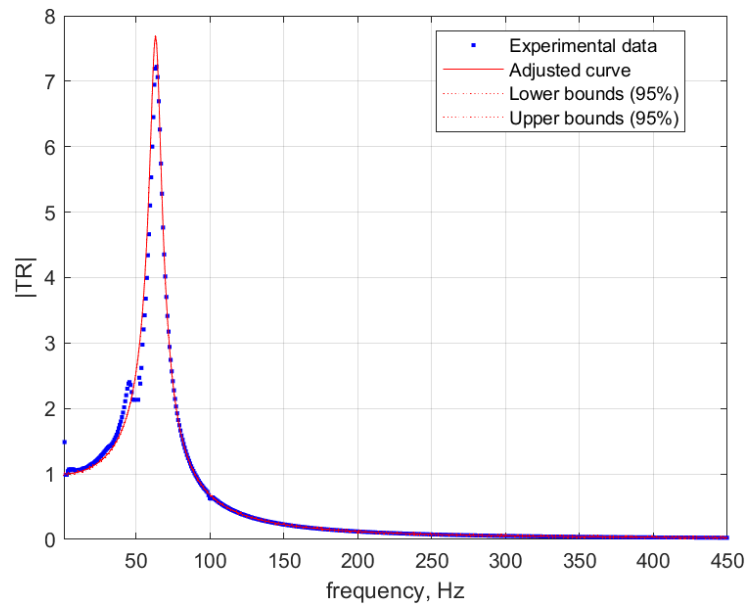


**Figure 7. Result of approximation of the transfer function modulus obtained from the results of tests of material type s.2.1 at a load of 2 kPa.**

**Table 2. Approximation results.**

Material identification	Density, kg/m <sup>3</sup>	Load, kPa	Approximation results			
			$N$	$\gamma$	$\tau_\varepsilon$ , s	$\omega_0$ , Hz
Materials with different stiffness	Type s.1.1	2	288.14	0.83	$8.3791 \cdot 10^{-9}$	42.64
		5	58.71	0.68	$5.94618 \cdot 10^{-8}$	24.73
		10	42.86	0.95	$4.82423 \cdot 10^{-6}$	14.80
	Type s.1.2	2	343.73	0.91	$1.09781 \cdot 10^{-8}$	56.00
		5	19.47	0.73	$1.01912 \cdot 10^{-6}$	34.01
		10	320.43	0.82	$6.89688 \cdot 10^{-9}$	22.27
	Type s.1.3	2	118.49	0.79	$3.06985 \cdot 10^{-8}$	54.14
		5	25.03	0.89	$3.28268 \cdot 10^{-6}$	41.29
		10	56.68	0.85	$4.3767 \cdot 10^{-7}$	27.43
	Type s.1.4	2	38.73	1.00	$1.77606 \cdot 10^{-6}$	79.69
		5	156.45	1.00	$1.78484 \cdot 10^{-7}$	53.03
		10	43.95	0.86	$5.2626 \cdot 10^{-7}$	36.74
	Type s.2.1	2	26.84	1.00	$3.14728 \cdot 10^{-6}$	68.40
		5	17.89	0.88	$2.75135 \cdot 10^{-6}$	44.99
		10	8.85	1.00	$4.12621 \cdot 10^{-5}$	31.64
Material identification	Density, kg/m <sup>3</sup>	Load, kPa	Approximation results			
			$N$	$\gamma$	$\tau_\varepsilon$ , s	$\omega_0$ , Hz
Materials with different damping	Type d.1.1	2	793.082	0.624	$1.659 \cdot 10^{-6}$	83.21
		5	434.170	0.890	$3.713 \cdot 10^{-6}$	62.28
		10	101.443	0.920	$1.597 \cdot 10^{-5}$	45.86
	Type d.1.2	2	9334.457	0.639	$4.117 \cdot 10^{-7}$	80.40
		5	14363.697	0.773	$1.296 \cdot 10^{-7}$	67.26
		10	15202.664	0.802	$8.908 \cdot 10^{-8}$	52.42
	Type d.2.1	2	18633.192	0.757	$1.865 \cdot 10^{-7}$	165.39
		5	38750.896	0.678	$1.211 \cdot 10^{-7}$	130.24
		10	42758.908	0.682	$1.445 \cdot 10^{-7}$	100.41
	Type d.2.2	2	5.861	0.806	$7.042 \cdot 10^{-4}$	233.32
		5	2849.600	0.544	$1.060 \cdot 10^{-6}$	193.56
		10	26344.363	0.671	$1.036 \cdot 10^{-7}$	161.13

Material identification	Density, kg/m <sup>3</sup>	Load, kPa	Approximation results			
			$N$	$\gamma$	$\tau_e, s$	$\omega_0, \text{Hz}$
Type d.3.1	280	2	266.839	0.588	$1.256 \cdot 10^{-5}$	77.50
		5	4178.858	0.721	$4.445 \cdot 10^{-7}$	63.81
		10	23061.408	0.770	$7.956 \cdot 10^{-8}$	48.46
Type d.3.2	381	2	7520.506	0.487	$4.618 \cdot 10^{-7}$	86.73
		5	6735.431	0.752	$2.565 \cdot 10^{-7}$	74.08
		10	1223.899	0.749	$1.284 \cdot 10^{-6}$	56.31

The scheme for determining the parameters of the rheological material model proposed in this work is shown in the diagram below (Fig. 8).

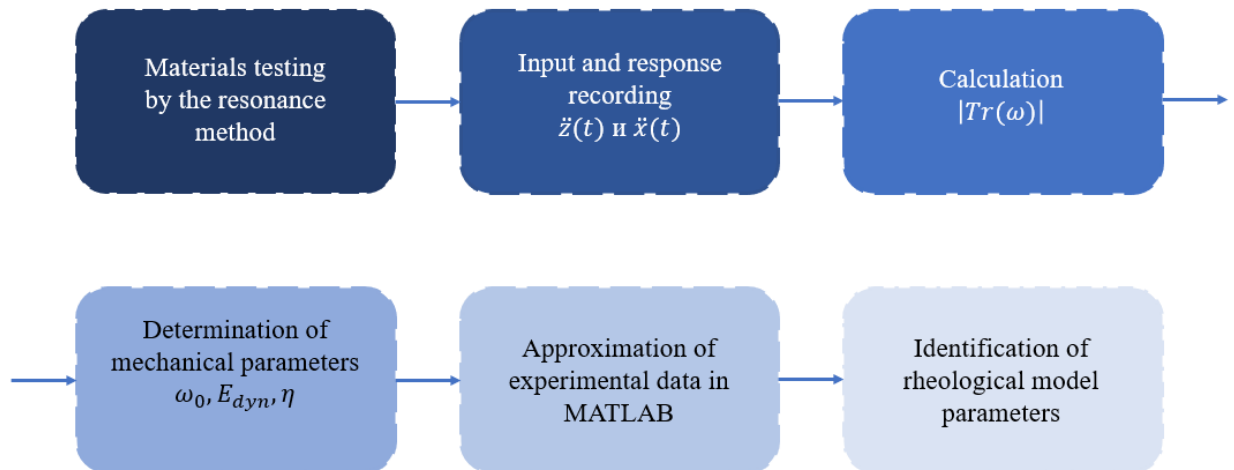


**Figure 8. Diagram of identification of parameters of the rheological model of the materials under study.**

Let us note several peculiarities of the behavior of the considered vibration-damping materials.

As can be seen from the test results presented in Table 2 and Fig. 9, with increasing load on each of the samples, there is a decrease in the natural frequency of vibrations of the system, which corresponds to the physical concept of the behavior of foamed materials. The increase in the resonance frequency is proportional to the increase in the density of the samples.

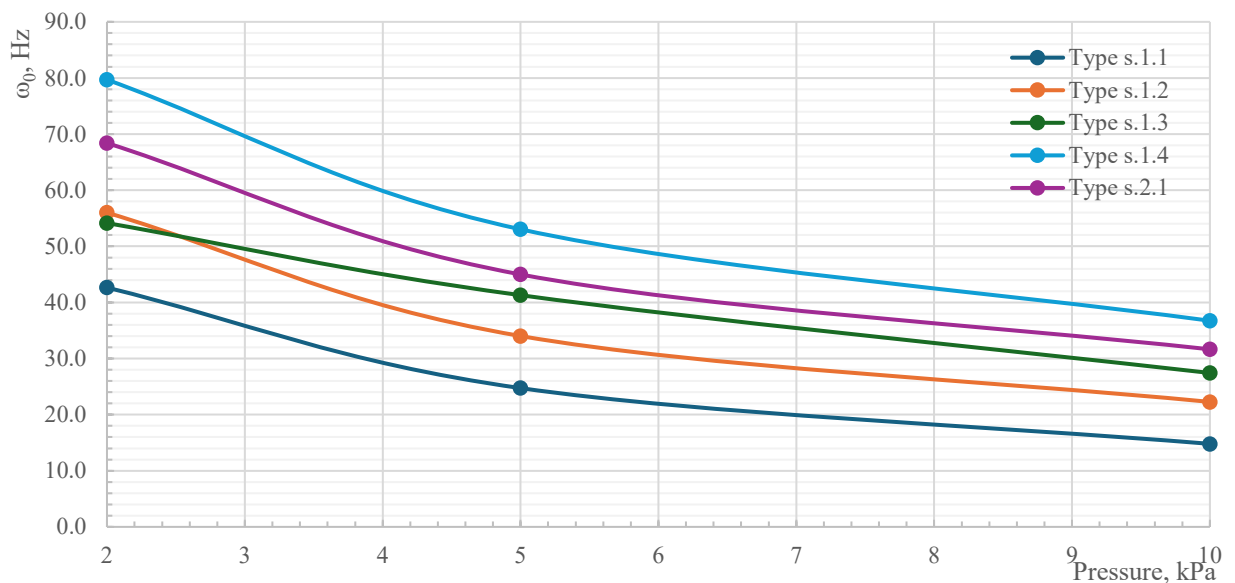


**Figure 9. Dependence between natural frequency  $\omega_0$  and acting load on the specimen for materials with different stiffness.**



The dependence of the fractional parameter on the magnitude of the acting load on the specimen for the tested materials is shown in Fig. 10.

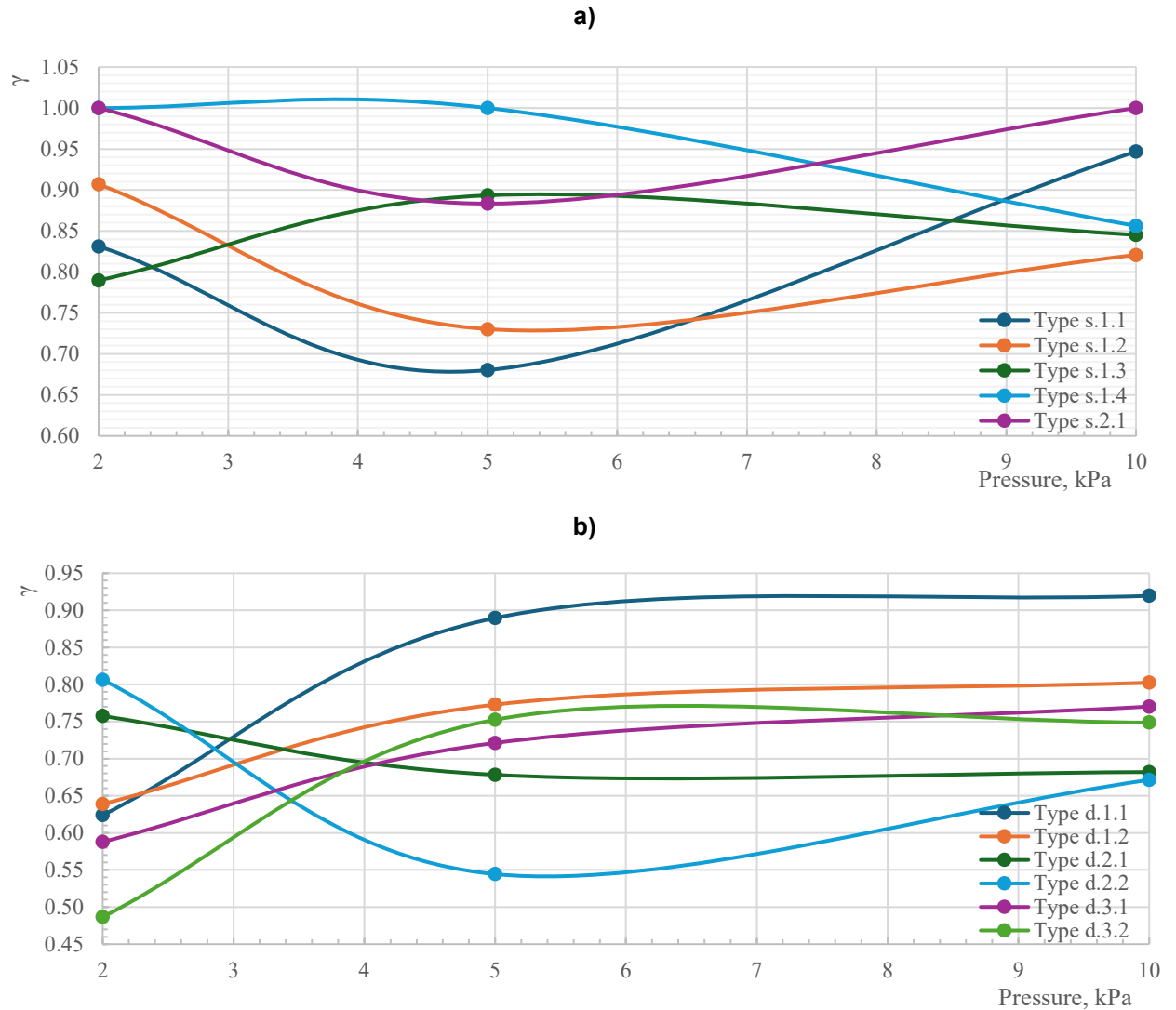


**Figure 10. Dependence of the fractional parameter on the sample load:**  
**a) for materials with different stiffness, and b) for materials with different damping.**

According to the test results, it should be noted that the fractional parameter for all materials is higher than 0.65. This means that the selected materials have predominantly viscous properties.

The nature of the change in the fractional parameter with increasing applied load on the specimen manifests itself in different ways. For example, for soft materials of types s.1.1 and s.1.2 (density 165–190 kg/m<sup>3</sup>), the fractional parameter initially decreases from 0.85–0.9 to 0.7–0.75, exhibiting more elastic properties, after which it increases to 0.8–0.95, i.e. the specimen starts behaving more viscous. Samples with higher density – types s.1.3 and s.1.4 (density 210–380 kg/m<sup>3</sup>), on the contrary, demonstrate at these values of loads from 2 to 10 kPa a decrease in ductile properties and an increase in elastic ones: the fractional parameter decreases from 0.8–1 to 0.85. That can be related to the change in the structure of the material with combined pores – at compression there is a gradual "collapse" of open communicating pores, pore gas pressure increases, and gas redistribution between internal pores occurs. Gas pumping between the pores is like the work of an ideal viscous damper. Further increases in load and compression strain result in the operation of only closed pores, thus it is worth noting that for denser materials this state is not achieved within the experiment described in Section 2.

The relaxation times determined from the approximation of the experimental data are shown in Fig. 11.

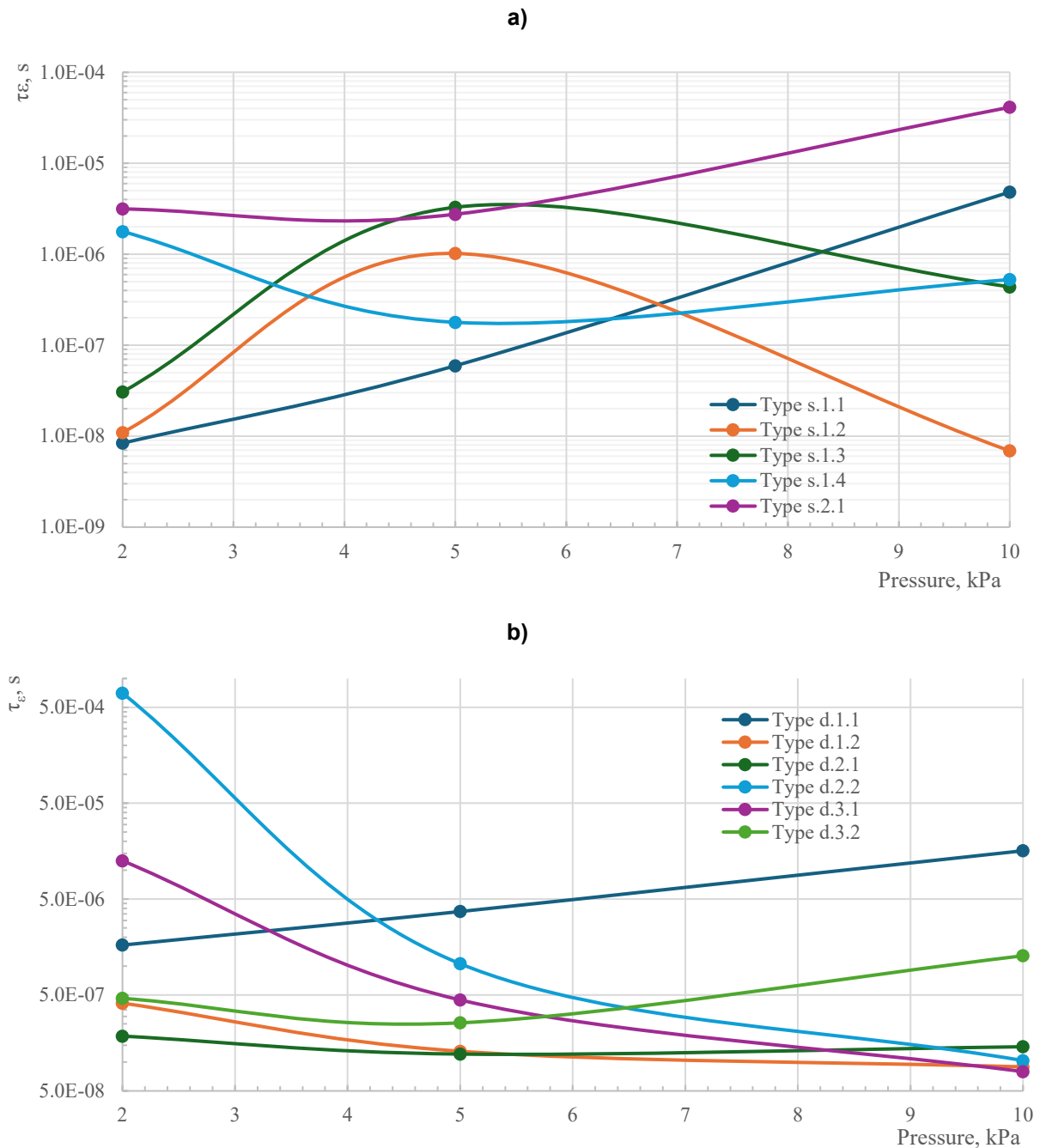


**Figure 11. Dependence of relaxation time for samples on load:  
a) for materials with different stiffness, and b) for materials with different damping.**

It can be noted that the lower the loss coefficient of the material, the shorter will be its relaxation time. At the same time, the relaxation time depends on the acting load on the sample, which is associated with the features of internal damping, including the elasticity of gas in the pores and its pumping between the communicating pores.

The variation of the parameter  $N$ , equal to the ratio of creep and relaxation times, depending on the load on the specimen is shown in Fig. 12.

The character of behavior of the parameter  $N$  coincides with the character of behavior of the fractional parameter  $\gamma$ . In this case, the more the "viscous" part of the vibration-damping material works, the smaller the parameter  $N$  is.



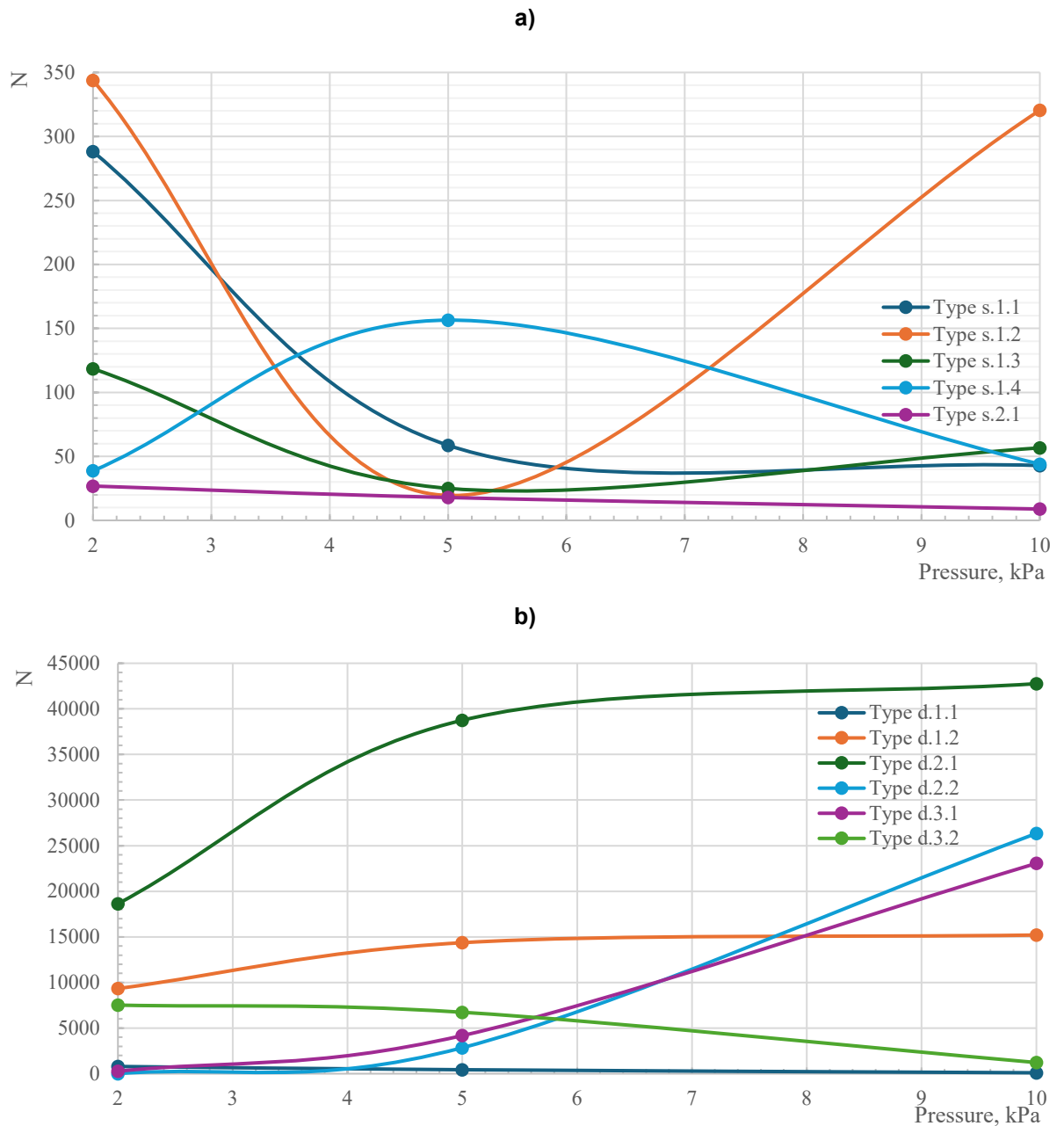


**Figure 12. Dependence of the parameter  $N$  on the sample load:**  
**a) for materials with different stiffness, and b) for materials with different damping.**

Our findings align with previous research indicating that fractional derivative models effectively capture the viscoelastic behavior of materials with fewer parameters compared to classical models. For instance, a study on solid propellants demonstrated that a three-branch fractional Maxwell model provided a satisfactory agreement with experimental data, highlighting the efficiency of fractional models in describing viscoelastic behaviors [24].

Additionally, the dynamic mechanical analysis of polyurethane foams has been explored in prior studies. One investigation utilized harmonic vibration tests to analyze the dynamic stiffness function of polyurethane foams, revealing insights into their damping effects and frequency response characteristics [25]. Another study emphasized the importance of considering dynamic properties, noting that while static tests are commonly used, the behavior of polyurethane foams under dynamic conditions is crucial for applications such as automotive seating [26].

The simplicity and practicality of the resonance method employed in our study are noteworthy. This approach does not require extensive resources or sophisticated instrumentation, making it accessible for a wide range of applications. The approximation of the experimentally obtained transfer function, with careful selection of initial parameters, resulted in physically meaningful material characteristics.

## 4. Conclusion

In this paper, we investigated the viscoelastic behavior of foamed polyurethane vibration-damping materials featuring combined porous structures, widely utilized in various engineering and construction applications. To quantify the mechanical characteristics of these materials, dynamic resonance tests were performed, enabling identification of parameters within a FLS model. The fractional-derivative approach proved highly effective in modeling complex viscoelastic behavior with fewer parameters compared to classical integer-order models.

Our experimental results explicitly demonstrated the significant influence of both material density and pore structure on damping properties:

- For materials with densities ranging from 165 to 380 kg/m<sup>3</sup>, an increase in density resulted in higher dynamic moduli of elasticity – from 0.428 MPa to 1.275 MPa (under a load of 5 kPa) – and reduced loss factors from 0.420 to 0.237, indicating a clear inverse relationship between density and damping capacity.
- The pore structure notably influenced damping performance: closed-pore materials exhibited lower loss factors (0.155 at 5 kPa for type s.2.1) compared to open or combined structures, confirming their predominantly elastic behavior.
- The fractional parameter  $\gamma$ , characterizing material viscoelasticity, was found consistently greater than 0.65, confirming predominantly viscous behavior across tested materials. However,  $\gamma$  varied nonlinearly with applied load and density, capturing the transition between elastic-dominated and viscous-dominated behaviors clearly.
- Relaxation times and the parameter  $N$  (ratio of creep to relaxation time) also correlated significantly with applied load and material structure, highlighting the complexity of internal damping mechanisms related to gas redistribution among communicating pores.

Overall, our findings emphasize the necessity of fractional-derivative modeling to accurately predict the dynamic behavior of foamed polyurethane materials. The resonance-based testing approach provided reliable data for fractional parameter identification, underscoring its practical applicability without requiring extensive instrumentation. Future research directions should consider broader ranges of material densities and structural variations to further refine fractional models and enhance their predictive capabilities for advanced vibration and seismic isolation applications.

This study contributes significantly to the expanding field of fractional calculus applications in mechanics of viscoelastic materials, bridging theoretical fractional-order models and practical experimental validation. Specifically, the investigation enhances the existing understanding of how fractional-derivative-based rheological models effectively represent complex viscoelastic behavior of foamed polymeric materials used extensively in structural and vibration isolation contexts. Unlike classical integer-order models, fractional-derivative models capture both elastic and viscous responses with greater fidelity while reducing parameter complexity. The quantification and explicit identification of viscoelastic parameters, presented in this research, underscore the pronounced dependency of damping properties on density and pore structure, providing clear quantitative relationships valuable for material selection and system optimization. Furthermore, this study showcases the applicability and robustness of fractional derivative models for accurately predicting dynamic properties, contributing to the advancement of methods that effectively address real-world engineering challenges in vibration and seismic isolation.

## References

1. Shitikova, M.V., Krusser, A.I. Models of Viscoelastic Materials: A Review on Historical Development and Formulation. *Advanced Structured Materials*. 2022. 175. Pp. 285–326. DOI: 10.1007/978-3-031-04548-6\_14
2. Rossikhin, Yu.A., Shitikova, M.V. Fractional calculus in structural mechanics. *Applications in Engineering, Life and Social Sciences. Part A*. 2019. 7. Pp. 159–192. DOI: 10.1515/9783110571905-009
3. Shitikova, M.V. Fractional operator viscoelastic models in dynamic problems of mechanics of solids: a review. *Mechanics of Solids*. 2022. 57(1). Pp. 1–33. DOI: 10.3103/S0025654422010022
4. Rossikhin, Yu.A., Shitikova, M.V. Application of Fractional Calculus for Analysis of Nonlinear Damped Vibrations of Suspension Bridges. *Journal of Engineering Mechanics*. 1998. 124(9). Pp. 1029–1036. DOI: 10.1061/(ASCE)0733-9399(1998)124:9(1029)
5. Diethelm, K. Numerical methods for the fractional differential equations of viscoelasticity. *Encyclopedia of Continuum Mechanics*. Springer. Berlin. Heidelberg, 2020. Pp. 1927–1938. DOI: 10.1007/978-3-662-55771-6\_89
6. Kou, L., Bai, Y. Dynamic response of rectangular plates on two-parameter viscoelastic foundation with fractional derivatives. *Journal of Vibration and Shock*. 2014. 33(8). Pp. 141–147.
7. Hosseinkhani, A., Younesian, D., Farhangdoust, S. Dynamic Analysis of a Plate on the Generalized Foundation with Fractional Damping Subjected to Random Excitation. *Mathematical Problems in Engineering*. 2018. 2018. Article no. 3908371. DOI: 10.1155/2018/3908371
8. Zhang, C., Zhu, H., Shi, B., Liu, L. Theoretical investigation of interaction between a rectangular plate and fractional viscoelastic foundation. *Journal of Rock Mechanics and Geotechnical Engineering*. 2014. 6(4). Pp. 373–379. DOI: 10.1016/j.jrmge.2014.04.007



9. Zhu, H.-H., Liu, L., Ye, X. Response of a loaded rectangular plate on fractional derivative viscoelastic foundation. *Journal of Basic Science and Engineering*. 2011. 19(2). Pp. 271–278. DOI: 10.3969/j.issn.1005-0930.2011.02.011
10. El-Misiery, A.E.M., Ahmed, E. On a fractional model for earthquakes. *Applied Mathematics and Computation*. 2006. 173(1). Pp. 231–242. DOI: 10.1016/j.amc.2005.10.011
11. Carcione, J.M., Cavalline, F., Mainardi, F., Hanyga, A., Zhang, Z.Z. Time-domain Modeling of Constant-Q Seismic Waves Using Fractional Derivatives. *Pure and Applied Geophysics*. 2002. 159. Pp. 1719–1736. DOI: 10.1007/s00024-002-8705-z
12. Celauro, C., Fecarotti, C., Pirrotta, A., Collop, A. Experimental validation of a fractional model for creep/recovery testing of asphalt mixtures. *Construction and Building Materials*. 2012. 36. Pp. 458–466. DOI: 10.1016/j.conbuildmat.2012.04.028
13. Popov, I.I., Shitikova, M.V., Levchenko, A.V., Zhukov, A.D. Experimental identification of the fractional parameter of the fractional derivative standard linear solid model for fiber-reinforced rubber concrete. *Mechanics of Advanced Materials and Structures*. 2024. 31(17). Pp. 4131–4139. DOI: 10.1080/15376494.2023.2191600
14. Amabili, M. Nonlinear damping in large-amplitude vibrations: modelling and experiments. *Nonlinear Dynamics*. 2018. 93. Pp. 5–18. DOI: 10.1007/s11071-017-3889-z
15. Alotta, G., Barrera, O., Pegg, E.C. Viscoelastic material models for more accurate polyethylene wear estimation. *The Journal of Strain Analysis for Engineering Design*. 2018. 53(5). Pp. 302–312. DOI: 10.1177/0309324718765512
16. Ciniello, A.P.D., Bavastri, C.A., Pereira, J.T. Identifying mechanical properties of viscoelastic materials in time domain using the fractional Zener model. *Latin American Journal of Solids and Structures*. 2016. 14(1). Pp. 131–152. DOI: 10.1590/1679-78252814
17. Shabani, M., Jahani, K., Di Paola, M., Sadeghi, M.H. Frequency domain identification of the fractional Kelvin-Voigt's parameters for viscoelastic materials. *Mechanics of Materials*. 2019. 137. Article no. 103099. DOI: 10.1016/j.mechmat.2019.103099
18. Amabili, M., Balasubramanian, P., Ferrari, G., Nonlinear vibrations and damping of fractional viscoelastic rectangular plates. *Nonlinear Dynamics*. 2021. 103(4). Pp. 3581–3609. DOI: 10.1007/s11071-020-05892-0
19. Santos, M. A procedure for the parametric identification of viscoelastic dampers accounting for preload. *Journal of the Brazilian Society of Mechanical Sciences and Engineering*. 2012. 34(2). Pp. 213–218. DOI: 10.1590/S1678-58782012000200013
20. Beda, T., Chevalier, Y. New Methods for Identifying Rheological Parameter for Fractional Derivative Modeling of Viscoelastic Behavior. *Mechanics of Time-Dependent Materials*. 2004. 8. Pp. 105–118. DOI: 10.1023/B:MTDM.0000027671.75739.10
21. Espindola, R.L., Silva Neto, J.L., Lopes, F.J. A generalized fractional derivative approach to viscoelastic material properties measurement. *Applied Mathematics and Computation*. 2005. 164(2). Pp. 493–506. DOI: 10.1016/j.amc.2004.06.099
22. Guo, X., Yan, G., Benyahia, L., Sahraoui, S. Fitting stress relaxation experiments with fractional Zener model to predict high frequency moduli of polymeric acoustic foams. *Mechanics of Time-Dependent Materials*. 2016. 20(4). Pp. 523–533. DOI: 10.1007/s11043-016-9310-3
23. Nashif, A.D., Jones, D.I.G., Henderson, J.P. *Vibration Damping*. Wiley-Interscience. New York, 1985. 480 p.
24. Fang, C., Shen, X., He, K., Yin, C., Li, S., Chen, X., Sun, H. Application of fractional calculus methods to viscoelastic behaviours of solid propellants. *Philosophical Transactions of the Royal Society A*. 2020. 378(2172). Article no. 20190291. DOI: 10.1098/rsta.2019.0291
25. Duboeuf, O., Dupuis, R., Aubry, E., Lauth, M. Harmonic Vibration Test for the Analysis of the Dynamic Behaviour of Polyurethane Foams. *Dynamic Behavior of Materials*. 1. Springer. Cham, 2016. Pp. 61–67. DOI: 10.1007/978-3-319-22452-7\_10
26. Dossi, M., Moesen, M., Brennan, M., Vandenbroeck, J. Dynamic Comfort and Vibration Damping with Polyurethane Foams. 2016 Polyurethanes Technical Conference. Baltimore, 2016. Pp. 60–73.

#### **Information about the authors:**

**Marina Shitikova**, Doctor of Physics and Mathematics

ORCID: <https://orcid.org/0000-0003-2186-1881>

E-mail: [shitikova@vmail.ru](mailto:shitikova@vmail.ru)

**Vladimir Smirnov**, PhD in Technical Sciences

ORCID: <https://orcid.org/0000-0001-5679-9542>

E-mail: [SmirnovVA@mgsu.ru](mailto:SmirnovVA@mgsu.ru)

*Received 17.01.2025. Approved after reviewing 11.03.2025. Accepted 15.03.2025.*




Research article

UDC 004.6:621.396.6:628.1/.3

DOI: 10.34910/MCE.134.4



## Detection of unauthorized connections to storm drains based on passive radio frequency identification technology

V.P. Dashevsky<sup>1</sup>, V.I. Kondratieva<sup>2</sup>, R.V. Rzhimsky<sup>1</sup>, A.L. Ronzhin<sup>1</sup> 

<sup>1</sup> St. Petersburg Federal Research Center of the Russian Academy of Sciences, St. Petersburg, Russian Federation

<sup>2</sup> State Research Institute of Industrial Ecology, Moscow, Russian Federation

 [ronzhin@iias.spb.su](mailto:ronzhin@iias.spb.su)

**Keywords:** storm drains, wastewater, RFID, radio frequency identification, unauthorized connections, protection of water bodies, state environmental control, discharges from industrial enterprises.

**Abstract.** The paper presents the results of research on using radio frequency identification (RFID) technologies to prevent pollution by enabling early detection of industrial discharges. The goal of the study is to develop a method for detecting unauthorized connections to storm sewers using passive RFID technology. The authors justify the choice of passive RFID, based on the EPC Class 1 Gen2 standard (ISO/IEC 18000-63:2021(E)). The authors describe experiments to reliably detect RFID tags floating in protective casings on the water's surface by reader with the antenna positioned 0.5–1.5 m above the water. A key challenge is the difficulty in reading tags directly on the water's surface, as water shields and reflects the reader's electromagnetic waves. Additional tests were conducted to evaluate the impact of tag collisions on the accuracy and completeness of readings, as these collisions may cause missed tags when passing by the reader's antenna. The study confirms that passive RFID can address key challenges in detecting unauthorized storm sewer connections. RFID technology has the potential to improve the efficiency and accuracy of environmental monitoring, reduce control costs, and better protect water bodies from industrial pollution. The research is significant for advancing new methods and technologies in environmental protection and can be applied in state environmental control systems to identify and prevent unauthorized wastewater discharges from industrial facilities.

**Funding:** The study was funded by financial support for the implementation of the state assignment Reg. No. NIOKTR 1023102300002-4.

**Citation:** Dashevsky, V.P., Kondratieva, V.I., Rzhimsky, R.V., Ronzhin, A.L. Detection of unauthorized connections to storm drains based on passive radio frequency identification technology. Magazine of Civil Engineering. 2025. 18(2). Article no. 13404. DOI: 10.34910/MCE.134.4

### 1. Introduction

Radio frequency identification (RFID) is widely used for detecting various objects and processes across different fields. One promising application is the use of this technology to identify unauthorized wastewater discharges to storm drains. This is especially important for environmental protection, as pollution of water bodies by industrial wastewater is one of the most serious ecological issues of our time [1, 2]. Pollution caused by industrial wastewater can lead to severe health consequences for the population, such as poisoning, illness, and even death, as well as the death of aquatic flora and fauna, disrupting ecosystems and reducing biodiversity. The ecological damage can affect the economy, particularly sectors like agriculture, fisheries, and tourism [3–5]. Many water bodies also have cultural and social significance for local communities, and their pollution can destroy traditional ways of life and harm cultural heritage.

Therefore, continuous monitoring of water resources and measures to protect water bodies from pollution are essential for adhering to national and international environmental standards and agreements. An important task is the effective detection of unauthorized connections of wastewater to storm sewers, which requires the development of new methods and technologies.

The primary distinction between stormwater drainage systems and industrial or domestic wastewater systems lies in their treatment infrastructure. Stormwater systems are typically not equipped with significant treatment facilities and discharge directly into water bodies. In contrast, domestic and industrial wastewater systems include treatment facilities that process the effluent before release, and the users are required to pay for the treatment of their discharges. As a result, the diversion of pollutants into storm water systems to reduce treatment costs constitutes a violation that must be identified and prevented, making methods to detect unauthorized connections to storm water drains essential.

The following are well-known methods for detecting unauthorized connections, along with their respective advantages and disadvantages [2, 6]:

- Visual inspection and diagnostics (tele-diagnosis method). This method allows for direct observation of the internal parts of the sewer system, helping to identify visible anomalies and unregistered connections. It provides real-time, accurate data about the condition of pipes and infrastructure. However, this method is labor-intensive and often requires the use of specialized equipment, such as remote-controlled cameras, which make it rather expensive.
- Smoke tests. This method is effective in detecting unauthorized connections through visible smoke outlets. It is relatively easy to implement and provides immediate results. However, it can lead to false alarms if there are natural venting points or if the smoke disperses unpredictably.
- Dye injection tests. Dye tests are highly effective in identifying illegal connections, especially when monitoring specific wastewater flows. They provide clear, easily traceable evidence of contamination and help identify the source of the illegal discharge. However, dyes can trigger complaints from the public, as their presence in the water is often perceived as pollution. Additionally, the complete washout of the dye may take a long period, delaying the process of locating the illegal connection. Furthermore, the method may lead to false positives if the dye interacts with other substances in the sewer system, and it can cause temporary environmental disruption while the dye remains in the water.
- Water and wastewater analysis. This method allows for the precise identification of industrial pollutants, heavy metals, chemicals, and biological markers that are indicative of unauthorized wastewater discharges. It is highly reliable for detecting contamination even in small quantities. However, it requires sophisticated equipment and laboratory analysis, which can be costly and time-consuming. Moreover, it may not immediately identify the source of contamination unless extensive sampling is performed.

The RFID-based method of identifying of unauthorized connections presents several advantages. RFID tags are cost-effective, compact, and do not contribute to wastewater contamination, making them an environmentally sustainable solution for detecting unauthorized connections. Furthermore, the electronic product code (EPC) stored in the memory of RFID tag can contain information about the time and location of its drop into the sewer system. This enables efficient, parallel detection of multiple illegal connections across different locations without the need for sequential examination of potential connections.

The main goal of this work was to explore the potential of using RFID technologies to develop sensors capable of promptly identifying unauthorized discharges of untreated wastewater from industrial facilities into storm sewers in urban areas, with the aim of supporting state environmental monitoring and control efforts.

RFID technology is widely employed for the automatic identification and tracking of objects using radio frequency (RF) tags. Its broad applicability is attributed to several key characteristics, such as the ability to read tags contactlessly at a distance, function in low-visibility conditions regardless of object orientation, and simultaneously read multiple tags. Additionally, RFID offers high data processing speeds, making it an efficient solution for various applications. Contemporary RFID systems not only allow for reading information from tags but also enable writing to them. Devices known as readers are capable of modifying or reprogramming the contents of tag memory, significantly enhancing the flexibility and functionality of this technology [7, 8].

RFID technology is classified into two main types: passive and active. Passive RFID tags operate without an internal power source, drawing energy from the electromagnetic field generated by the reader. They have a relatively short reading range (typically up to several meters) but offer advantages, such as



durability, low cost, and an extended operational lifespan. Active RFID tags, in contrast, are equipped with an internal battery, enabling a significantly greater reading range (up to hundreds of meters) and additional functionalities. However, they are more expensive and have a finite lifespan due to battery depletion. They also have a risk of environmental contamination from hazardous chemical components. A review of RFID applications for animal tracking [9], based on data collected from 1970 to 2023, identified 70 patents for related devices. Of these, 40 patents were based on the use of passive RFID tags, while only 5 were based on active RFID tags. Thus, passive RFID tags emerge as the most suitable solution for the task of detecting unauthorized connections.

One of the significant challenges in RFID technology is the reduced efficiency of tag detection in dense environments, such as in water. Reading tags at long distances becomes significantly more difficult when the tags are submerged. The presence of water, especially in aquatic environments, introduces additional interference due to the absorption and scattering of radio waves, which diminishes the effective detection range. This is particularly true for ultra high frequency (UHF) RFID systems where the radio frequency waves are highly susceptible to attenuation by water. As a result, the range, at which tags can be read in aquatic environments, is substantially lower compared to air, limiting the ability to track or monitor objects over extended distances.

Despite the significantly reduced detection range of RFID tags in water, especially for UHF RFID [10], they can be used in aquatic environments for applications like fish tracking and underwater navigation. A study [11] demonstrated the use of two types of passive integrated transponder (PIT) tags, with implantation in different anatomical locations of fish. The study confirmed that RFID technology is functional in such conditions, although implantation can affect fish growth and survival. The use of a handheld reader and portable X-ray systems was employed to verify tag implantation and functionality. In [12], two types of antenna systems were described for the detection and abundance estimation of PIT-tagged fish in rivers: a raft-based antenna system and a shore-based floating antenna system. The raft-based system includes a  $4.0 \times 1.2$  m horizontal antenna for shallow river areas and a  $2.7 \times 1.2$  m vertical antenna for deep pools, while the shore-based system spans the entire width of the river, measuring  $14.6 \times 0.6$  m, providing more comprehensive coverage. Both systems faced challenges, such as detection efficiency, which varied depending on tag size, orientation, and the proximity of multiple antennas. Additional challenges in the aquatic environment included interference from metal objects affecting the magnetic field, tag collisions, and the detection of "ghost" tags – those lost due to predation or natural mortality. These limitations required careful system design to maximize detection probability and minimize interference.

In [13], RFID technology was applied for marine sediment tracking using low-frequency tags, including ABS plastic disc tags (30 mm in diameter) and cylindrical glass tags (32 mm in length, 4 mm in diameter). Key challenges in underwater RFID application include the attenuation of electromagnetic waves, which limits signal penetration and reading distance, particularly in saltwater. To address these issues, a waterproof antenna was developed, enabling tag reading at distances of up to 50 cm and depths of up to 5 m, along with wireless data transmission to simplify tracking.

In [14], the application of passive UHF RFID tags for detecting blockages and unauthorized connections in sewer systems was explored. A total of 12 types of UHF RFID tags and three antennas with different gains (8, 9, and 12 dBiC) were evaluated. Based on factors, such as cost, size, and maximum reading range, three types of tags were selected. The experiments revealed that tag sensitivity was influenced by their position relative to the reader antenna, the material of the casing, and the volume of air inside the casing. As a result, PLA plastic was chosen for the casing, with the internal area optimized for the selected tag types. Field tests were conducted using a 9 dBiC antenna due to its size and ease of installation. The optimal detection range was found to be between 0.6 and 3.5 m. The sensors demonstrated good resilience to flow conditions and solid waste in domestic wastewater. The study shows that UHF RFID sensors can provide a high-performance, reliable, and non-invasive method for real-time monitoring of sewer systems.

The primary objective of this study was to evaluate the feasibility of using EPC Class 1 Gen2 RFID technology with low-cost, commercially available RFID tags and to assess their performance in water-proximate environments, such as storm sewer systems. A key focus was the development of a method to encapsulate RFID tags in a lightweight, sealed, and radio-transparent casing, allowing them to function as sensors capable of transmitting data from a safe distance while protecting the reader equipment from water exposure. Additionally, the study aimed to investigate how the received signal power, measured by the reader's Received Signal Strength Indicator (RSSI), varies with the distance between the antenna and the water surface on which the sensor is placed.

## 2. Methods

The general scheme of passive RFID technology application for storm sewer monitoring includes the following steps. The sensor undergoes initial initialization, during which:

- The EPC of the embedded RFID tag is programmed, including information about the location and time of its drop into the sewer system.
- If necessary, the tag information is additionally logged into the monitoring journal for further analysis of the percentage of lost tags.

After completing the initial initialization, the tag is dropped into the discharge manhole, after which it begins to move through the sewer system pipeline with the water flow. Since RFID technology incorporates an anti-collision algorithm for tags, readers can simultaneously detect multiple tags, enabling parallel monitoring of several industrial facilities for unauthorized connections as shown in Fig. 1.

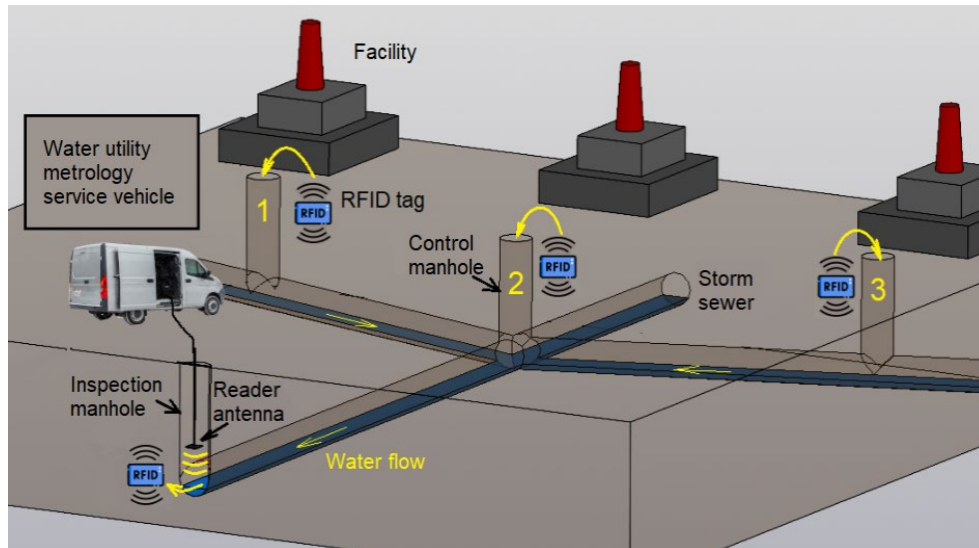


**Figure 1. General scheme of passive RFID technology application for inspecting the sewer pipeline.**

Multiple sensors can be dropped simultaneously into the control manholes of different facilities. After this, the reader antenna is lowered into the inspection manhole in such a way that the distance from the antenna to the water surface ranges from 0.5 to 1.5 m. Placing the antenna too close is undesirable for two reasons. First, the radiation pattern in close proximity to antenna body is still forming and may have areas with poor sensitivity, resulting in incomplete coverage of the water surface where a sensor might appear beneath it. Second, it has high risk of splashing, which could wet the antenna due to water flow and poor visibility inside the manhole. On the other hand, placing the antenna too far away will lead to significant signal attenuation, negatively affecting the detection quality of passing sensors.

The reader and its controlling computer (laptop) of the metrology service are located in the vehicle. The antenna is connected to the reader via a coax cable, the length of which allows the antenna to be lowered into the manhole at a distance of approximately  $1 \pm 0.5$  m from the water surface. This approach reduces the requirements for the reader's power and sensitivity and allows the use of less expensive tags for discharge into the manholes.

The experimental setup employed the ThingMagic M6-EU (UHF EPC GEN2) reader [15], capable of emitting a maximum power output of 1.4 W, which facilitates a reading range of up to 10–15 m in free space conditions. The reader was paired with the MT-242014/NRH/K antenna (865–870 MHz, 8.5 dBic RHCP), specifically optimized for extended reading distances. To mitigate potential signal attenuation due to cable losses, the antenna was connected to the reader using a 10-meter RG58 coaxial cable. This configuration accommodated the operational requirement of lowering the antenna into a manhole while maintaining an adequate distance from the measurement system.

The reader antenna is mounted beneath the ceiling of the room at an approximate height of 2.2 m above the floor. A support surface is positioned beneath the antenna at the maximum investigated distance of 150 cm. A plastic, radio-transparent container filled with water is then placed on this surface. The use of a radio-transparent container ensures that no interference is introduced to the reader's electromagnetic field. With the sensor floating on the water surface, measurements of the received signal are conducted. The experiment is subsequently repeated for the next distance. The distance between the antenna and the

tag is adjusted using spacer boxes, each 25 cm thick, which are stacked beneath the water container as shown in Fig. 2.

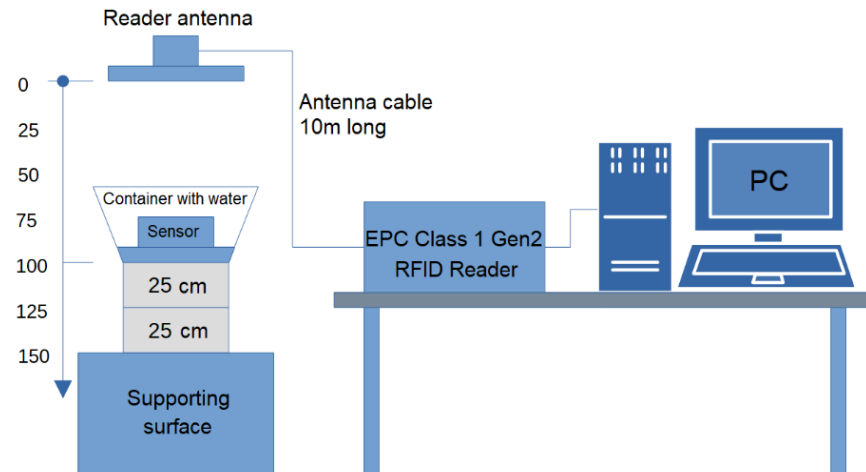
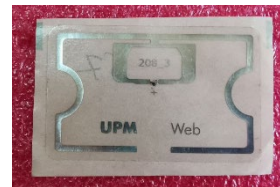


**Figure 2. Experiment for evaluating RFID tag read range in water.**

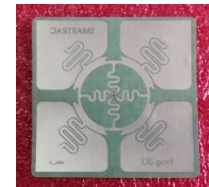
For the experiments, three types of RFID tags compliant with the EPC Class 1 Gen2 standard were applied (Fig. 3). These tags differ in antenna size and shape. The primary objective of employing multiple tag types was to investigate the relationship between the tag's reading range and orientation relative to the antenna's size and topology.



**a) NXP ISBC UCODE8,  
87 × 27 mm**



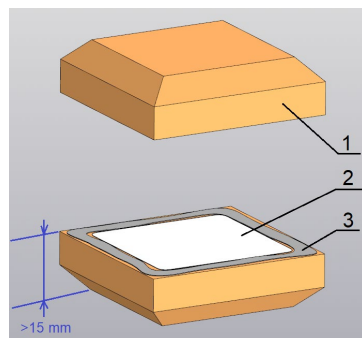
**b) Raftalac UPM  
Web, 54 × 34 mm**



**c) Raftalac Frog 3D,  
53 × 53 mm**

**Figure 3. RFID tags inlays of EPC Class 1 Gen2.**

The preliminary experiment with the provided RFID tags involved embedding them into a 3 mm thick plywood casing. The tags were successfully read in air; however, reading ceased after they were submerged in water. Two primary reasons account for this effect. Firstly, the distance between the tag and the main body of water was very small, around 1 mm. Secondly, plywood is highly susceptible to water absorption, as it readily wets and absorbs water into its porous wooden layers. Both factors lead to the blocking of the electromagnetic field, preventing the tag from receiving energy and interacting with the reader. Therefore, the casing had to be significantly improved for further work. Foamed polystyrene was chosen as the new casing material due to its substantially lower density compared to wood. Additionally, its low wettability prevents the formation of a continuous shielding water film on the casing surface. The thickness of the casing was increased to 40 mm to ensure the tag insert was sufficiently displaced from the water surface. An overall structure of the sensor, an encapsulated RFID tag, is shown in Fig. 4.



**a)**



**b)**

**Figure 4. Sensor construction: a) exploded view, b) placement on water.**



The RFID tag inlays (2) were glued into the protective casing (1), made of polystyrene, by forming an adhesive seam (3) around the perimeter of the inlay. Foamed polystyrene is easy to cut and glue, which reduces the cost of manufacturing tags for use in sewer systems. The bright orange color makes them highly visible in natural conditions.

The dimensions of the sensors exceeded the size of the inlays by approximately 10 mm on each side. For example, a tag with an NXP ISBC UCODE8 inlay measuring  $87 \times 27$  mm, when placed in the casing, had overall dimensions of  $110 \times 50 \times 40$  mm. Initial experiments with sensors encased in polystyrene demonstrated excellent results on water. Some tags were consistently read from distances of up to 2 m at the reader's maximum power. These sensors were subjected to a series of experiments to determine the conditions for stable tag reading at various reader power levels, as well as in scenarios involving potential collisions where multiple tags are simultaneously within the reader's field of view.

### 3. Results and Discussion

Two series of measurements were conducted during the experimental work. In the first series, a single tag was placed in the reader's field at a time (single-tag setup). In the second series, all three tags were placed simultaneously (multi-tag setup), but measurements were taken for a specific type of tag that was positioned optimally relative to the antenna, providing the highest received signal level.

Each series of experiments involved varying two parameters:

1. **Reader transmission power** was varied from +30 dBm to +10 dBm in increments of 5 dBm. Here, 0 dBm corresponds to a power of 1 mW, thus +30 dBm = 1 W, +20 dBm = 0.1 W, etc.
2. **Distance from the antenna to the sensor** was varied from 50 to 150 cm in increments of 25 cm.

To assess the reliability of tag reading, two characteristics were measured in each series:

1. **RSSI.** Measured in dBm, the RSSI values typically fall below  $-35$  dBm due to the weak reflected signal from the tag.
2. **Tag Read Rate.** This metric demonstrates the reliability of tag reading and the distance, at which signal degradation begins, leading to an increase in errors in the received signal.

**RSSI.** RSSI measures the power level of the signal received by the reader from the tag. It depends on the distance between the tag and reader, as well as environment like nearby metal, water, or other reflective surfaces. Since the reflected signal is typically weak, RSSI values are negative.

A high RSSI indicates a strong signal, high signal-to-noise ratio, and reliable communication, while a low RSSI suggests a weak signal and potential communication issues when the signal approaches noise levels.

RSSI analysis helps to diagnose and optimize RFID system performance. By identifying the signal level, at which tag reading becomes unstable or fails, and testing under various antenna and tag configurations, optimal reader and antenna placement can be determined. For fixed antenna setups, RSSI assists in defining optimal signal levels, guiding technical requirements for commercial readers in future measurement systems.

**Tag Read Rate.** The read rate parameter, measured in Hz, represents the number of tag detections per unit of time and is available through the reader's serial software. It is assumed that as the tag moves farther from the reader, signal errors increase, leading to a decrease in read rate and missed detections. By monitoring this parameter, one can determine the stable reception zone where tags are detected reliably, as well as the distance at which error rates reach 50 %.

In practice, readers typically accumulate tags over extended periods. The number of tag queries per inventory cycle in an EPC Class 1 Gen2 system depends on factors, such as channel access control and tag density. EPC Class Gen2 uses the ALOHA slotting algorithm to minimize collisions when multiple tags respond simultaneously. The reader initiates the inventory cycle by sending a Query command, which includes a Q parameter defining the number of time slots  $2^Q$ . Tags randomly choose a time slot, and if two tags select the same slot, a collision occurs, and the reader cannot receive valid responses. Tags not acknowledged in the current cycle are re-invited in the next cycle. This process repeats until all tags are identified. As cycles progress, tags choose different slots, reducing collision likelihood.

A single ALOHA slot [16, 17] takes about 400–600  $\mu$ s. While one-slot inventory is possible, it guarantees collisions of several tags. Therefore, Q values of 3 or 4 (8 or 16 slots) reduce the collision probability. Consequently, an elementary inventory cycle lasts approximately 9.6 ms ( $600 \mu\text{s} \times 16$ ). Typically, readers perform long inventory cycles (0.5–1.5 s), comprising 50 to 150 elementary cycles, and a tag is considered detected if it is identified at least once. This makes the read rate less informative, as

the likelihood of missing a tag after 50–150 attempts is almost zero, unless the tag moves out of range. As the tag moves further from the antenna, the RSSI decreases, but the read rate remains constant until it abruptly disappears. To improve the read rate's accuracy, inventory cycles should be shortened to single Query requests, though this is only available through the reader's API, not implemented in demonstration software we used. The results of reading tags in single-tag setup after processing are summarized in Table 1.

**Table 1. Measured RSSI from different tag types in a single-tag setup.**

Reader power (dBm)	Distance (cm)	RSSI (dBm)			Read rate (Hz)		
		Tag 01	Tag 02	Tag 03	Tag 01	Tag 02	Tag 03
+30	50	−54	−58	−45	19.70	19.97	19.91
	75	−57	−59	−44	20.09	19.90	19.90
	100	−59	−65	−47	20.10	19.95	19.90
	125	−63	−66	−54	19.99	19.96	19.99
	150	−67	−71	−57	19.96	19.92	19.87
+25	50	−54	−58	−45	20.15	20.06	19.90
	75	−58	−60	−48	20.11	20.05	20.04
	100	−60	−64	−52	20.11	20.05	19.99
	125	−64	−66	−57	20.10	20.10	20.08
	150	−69	−1	−60	20.10	–	19.97
+20	50	−52	−59	−44	19.72	19.32	19.45
	75	−60	−62	−51	19.44	19.55	19.36
	100	−62	–	−55	19.60	–	19.49
	125	−66	–	−60	19.54	–	19.34
	150	−70	–	−63	19.53	–	19.40
+15	50	−53	–	−47	16.19	–	16.22
	75	−62	–	−54	16.22	–	16.23
	100	−64	–	−57	16.24	–	16.23
	125	−70	–	–	16.24	–	–
	150	–	–	–	–	–	–
+10	50	−55	–	−50	19.94	–	20.25
	75	−62	–	–	20.27	–	–
	100	–	–	–	–	–	–
	125	–	–	–	–	–	–
	150	–	–	–	–	–	–

Notes: 1. A dash indicates that the tags could not be read under those conditions. 2. In the obtained data, for the reader power level of +15 dBm, a drop in the reading speed from about 20 to 16 times per second is observed. For the reader power level of +10 dBm, a speed recovery of about 20 times per second is observed. To assess the impact of tag collisions, all samples of three tags were simultaneously placed in a container with water.

In addition to testing the reading of a single tag, the system's performance with multiple tags is also of interest, as the tags can accumulate in the control zone of a sewer pipeline [18–21]. The reading process becomes more challenging due to the following two factors. First, tag collisions may occur during the inventory process, requiring the execution of an anti-collision algorithm. This introduces a delay, increasing the minimum required time a tag must remain in the field, thereby limiting the maximum read rate, particularly for a tag moving under an antenna with a narrow beamwidth. Second, tags draw energy from the reader's RF field, which imposes a load on the reader. As a result, in a multi-tag setup, there is a tendency for the read performance of individual tags to degrade. In addition, there are other negative factors associated with the aquatic environment, information security, dense and dynamic distribution of sensors in a wireless sensor network, which significantly complicates the operation of RF technologies [22–25]. To assess the impact of these effects, an experiment was conducted, in which all three tags were placed in a water container simultaneously.

The measurement results for multi-tag setup are presented in Table 2.

**Table 2. Measured RSSI from different tag types in a multi-tag setup (collision test).**

Reader power (dBm)	Distance (cm)	RSSI (dBm)					
		Tag 01		Tag 02		Tag 03	
		together	single <sup>1</sup>	together	single <sup>1</sup>	together	single <sup>1</sup>
+30	50	-55	-54	-59	-58	-47	-45
	75	-58	-57	-66	-59	-50	-44
	100	-63	-59	-68	-65	-49	-47
	125	-65	-63	-64	-66	-57	-54
	150	-68	-67	-66	-71	-65	-57
+25	50	-57	-54	-58	-58	-50	-45
	75	-63	-58	-64	-60	-56	-48
	100	-66	-60	-69	-64	-56	-52
	125	-66	-64	-67	-66	-61	-57
	150	-71	-69	- <sup>2</sup>	-	-64	-60
+20	50	-58	-52	-60	-59	-52	-44
	75	-60	-60	-	-62	-58	-51
	100	-63	-62	-	-	-57	-55
	125	-70	-66	-	-	-62	-60
	150	-74	-70	-	-	-	-63
+15	50	-60	-53	-	-	-55	-47
	75	-62	-62	-	-	-56	-54
	100	-70	-64	-	-	-61	-57
	125	-	-70	-	-	-	-
	150	-	-	-	-	-	-
+10	50	-63	-55	-	-	-	-50
	75	-	-62	-	-	-	-
	100	-	-	-	-	-	-
	125	-	-	-	-	-	-
	150	-	-	-	-	-	-

Notes: 1. These columns are copied from table with single-tag setup for reference. 2. A dash means that there was no response from the RFID tags.

The results of the experiment (see Tables 1 and 2) show that with sufficient reader radiation power, all types of tags are successfully read at the specified distances with sufficient speed. The water surface at frequencies in the 868 MHz range works as a thin metal screen. Tags whose antenna is located in the water column or directly on the water surface are shielded by water and are not read. Tags located above the water surface are read. Tags in a lightweight case, which provides a distance from the plane of the tag insert to the water surface of 15 mm, are read reliably.

For reliable tag reading at distances of 50–150 cm, high reader power is not required. The experiments showed that tags with large antennas can be read from any distance within this range with a reading power of 20 dBm or higher, which corresponds to a power of 100 mW. Therefore, a reader power range of 150–250 mW is recommended, as this margin will allow for future simplifications in antenna design, reduced antenna size, and lower antenna cost.

The measured data indicates that a power of 15 dBm is insufficient for reading tags at distances greater than 1 m, and this effect is not related to tag shielding by water. A similar behavior is observed for tag inlays without any enclosure. This is likely due to the fact that when the energy density of the field drops below a certain threshold, the energy received by the tag's antenna becomes insufficient to power the embedded chip, preventing it from processing incoming queries from the reader.

As can be seen from the data in Table 1, the last recorded RSSI value differs for different tags and reader power as the tag is moved away from the reader antenna. Thus, for tag type 01, the RSSI value drops to -70 dBm, and for tag type 02, the maximum RSSI changes from -71 to -62 dBm. It can be concluded that the reason for tag loss is not related to the sensitivity of the reader when receiving a signal, since in this case the maximum range would correspond to approximately the same RSSI level of -70 dBm, but to a decrease in the energy received by the tag chip from the incident electromagnetic wave. Starting



from a certain distance, the tag simply does not have enough energy, and it stops responding. From this point of view, the NXP UCODE8 tag is the most energy-efficient, it is capable of responding at the weakest signal. The Rafsec Frog 3D tag has a good antenna but a less energy-efficient chip compared to the NXP UCODE8. This is noticeable because its signal is about 10 dB higher, but the maximum range is shorter, apparently for the same reason, the lack of field energy to power up the tag embedded chip. However, a more powerful response signal is an advantage for less sensitive readers, and the Rafsec Frog 3D tag is more compact than the NXP UCODE8, 53 mm versus 87 mm.

During the experiments, it was found that the read rate of all tags approximately corresponds to the processing speed of the reader during its accumulative read process. Reading of a single tag occurs reliably 16–20 times per second and is practically independent of the distance. This can be explained by the characteristics of the reader's software implementation as described above.

Experimental data show that when several tags appear in the antenna field at the same time, the reader's radiation energy is distributed between several tags, causing the signal from them to weaken, which can be seen when comparing the data in Table 2. As can be seen from the data, the presence of three tags in the field of one antenna simultaneously reduces the reading range of each by about 25 cm. At the same time, two tags with the largest antennas retained readability at all distances at a power of 20 dBm and higher.

## 4. Conclusions

Based on an analysis of existing RFID technologies, passive RFID technology, specifically the EPC Class 1 Gen2 standard (ISO/IEC 18000-63:2021(E)), was selected to address the problem of detecting unauthorized wastewater connections to storm sewers. Experimental studies demonstrated the stable detection of encased RFID tags on water surfaces from a distance of 0.5–1.5 m, using a directional antenna connected to a serial RFID reader with its demo software. As a result of the study, a list of key technical characteristics of RFID tags was compiled, along with specifications for the RFID reader equipment, to ensure optimal performance in storm sewer conditions:

1. Passive RFID EPC Class 1 Gen2 technology can be used to track water flow at speeds of up to 8 m/s from a distance of 50 to 150 cm. For the territory of Russia, it is necessary to select equipment that supports the European frequency range of 868 MHz. To implement this technology, readers with a power output of 150 mW and a sensitivity of –70 dBm can be applied.
2. For use as sensors, tags that support an EPC length of 128 bits are optimal. A shorter length complicates the encoding of information about the place and time of tag reset, longer EPC lengths will slow down reading and will negatively affect the detection of tags in a fast flow of water in the event of possible collisions.
3. For stable reading across the full range of distances, NXP UCODE8 (antenna size 87 × 27 mm) and Rafsec Frog 3D (antenna size 53 × 53 mm) tags are appropriate, as their antennas provide sufficient power to the embedded chip. These dimensions are compatible with the required specifications for storm sewer pipes with diameters of 200 mm and above.
4. The technology works with tags from different manufacturers, which simplifies supply tasks. The cost of EPC Class 1 Gen2 RFID tags suitable for making sensors is about 20–25 rubles per piece, plus the cost of encapsulation in a lightweight non-wetting case made of foamed polystyrene or other lightweight radio-transparent material.
5. The reader must have the following external interfaces for connection to the control computer: Ethernet, RS-485. These two interfaces allow the implementation of control software in any operating system. In contrast, the use of a USB interface may require specific device drivers and additional system software to facilitate communication with the reader, potentially limiting the choice of operating systems.
6. The antenna can be connected to the reader via a long cable, extending to a distance of 10 m or more, thereby enabling the antenna to be positioned closer to the water surface within the storm drain inspection hatch.

Thus, RFID methods for detecting unauthorized connections to storm sewers have advantages, such as mobility, autonomy, the ability to simultaneously monitor multiple drains, high speed and efficiency of data reading, protected by error correction codes. The use of RFID methods for the rapid detection of unauthorized connections is a promising and important direction to ensure effective environmental control (supervision) of this type of violation of environmental legislation and sustainable development of cities and towns.

## References

1. Stepanov, S.V., Strelkov, A.K., Panfilova, O.N. Removal of heavy metals from wastewater with natural and modified sorbents. *Magazine of Civil Engineering*. 2022. 111(3). Article no. 11110. DOI: 10.34910/MCE.111.10
2. Il'ina, Kh.V., Gavrilova, N.M., Bondarenko, E.A., Andrianova, M.Ju., Chusov, A.N. Express-techniques of polluted suburban stream waters study. *Magazine of Civil Engineering*. 2017. 76(8). Pp. 241–254. DOI: 10.18720/MCE.76.21
3. Perevaryukha, A. Dynamic Model of Population Invasion with Depression Effect. *Informatics and Automation*. 2022. 3(21). Pp. 604–623. DOI: 10.15622/ia.21.3.6
4. Trofimova, I.V., Perevaryukha, A.Y., Manvelova, A.B. Adequacy of interpretation of monitoring data on biophysical processes in terms of the theory of bifurcations and chaotic dynamics. *Technical Physics Letters*. 2022. 48(12). Pp. 305–310. DOI: 10.1134/s1063785022110025
5. Dudakova, D., Anokhin, V., Dudakov, M., Ronzhin, A. On Theoretical Foundations of Aerolimnology: Study of Fresh Water Bodies and Coastal Territories Using Air Robot Equipment. *Informatics and Automation*. 2022. 6(21). Pp. 1359–1393. DOI: 10.15622/ia.21.6.10
6. Dashevsky, V.P., Rzhimsky, V.G., Ponomarenko, S.M. Detection of encapsulated radio frequency tags on water during sewer systems inspection. *News of the Kabardino-Balkarian Scientific Center of RAS*. 2024. 26(5). Pp. 29–39. DOI: 10.35330/1991-6639-2024-26-5-29-39
7. Herrojo, C., Paredes, F., Mata-Contreras, J., Martín, F. Chipless RFID: A Review and Recent Developments. *Sensors*. 2019. 19(15). Article no. 3385. DOI: 10.3390/s19153385
8. Rajanarayana, M., Sasikala, B., Geethavani, B. A Review on RFID Technology and Applications. *International Journal of Engineering and Computer Science*. 2018. 7(06). Pp. 24099–24105. DOI: 10.18535/ijecs/v7i6.12
9. Pereira, E. et al. RFID Technology for Animal Tracking: A Survey. *IEEE Journal of Radio Frequency Identification*. 2023. 7. Pp. 609–620. DOI: 10.1109/JRFID.2023.3334952
10. Reaz, M.I.B. Radio Frequency Identification from System to Applications. *InTech*, 2013. 460 p. DOI: 10.5772/46210
11. Peterson, D.P., Twibell, R.G., Piteo, M.S. Retention of passive integrated transponder tags in hatchery brook trout: Effect of tag size, implantation site, and double tagging. *Fisheries Management and Ecology*. 2023. 30(3). Pp. 240–256. DOI: 10.1111/fme.12616
12. Fetherman, E.R., Avila, B.W., Winkelman, D.L. Raft and Floating Radio Frequency Identification (RFID) Antenna Systems for Detecting and Estimating Abundance of PIT-tagged Fish in Rivers. *North American Journal of Fisheries Management*. 2014. 34(6). Pp. 1065–1077. DOI: 10.1080/02755947.2014.943859
13. Pozzebon, A., Bertoni, D. A wireless waterproof RFID reader for marine sediment localization and tracking. 2014 IEEE RFID Technology and Applications Conference (RFID-TA). Tampere, 2014. Pp. 187–192. DOI: 10.1109/rfid-ta.2014.6934225
14. Tatiparthi, S.R., De Costa, Y.G., Whittaker, C.N., Hu, S., Yuan, Z., Zhong, R.Y., Zhuang, W.-Q. Development of radio-frequency identification (RFID) sensors suitable for smart-monitoring applications in sewer systems. *Water Research*. 2021. 198. Article no. 117107. DOI: 10.1016/j.watres.2021.117107
15. MERCURY6: 4-Port Enterprise UHF RFID Reader. ThingMagic, 2010. URL: [https://www.barcode-uk.com/files/admin/product\\_groups/thingmagicmercury.pdf](https://www.barcode-uk.com/files/admin/product_groups/thingmagicmercury.pdf) (date of application: 12.05.2025).
16. ISO/IEC 18000-6:2013. Information technology – Radio frequency identification (RFID) for item management – Part 6: Parameters for air interface communications at 860 MHz to 960 MHz General. International Organization for Standardization. Geneva, 2018. URL: <https://www.iso.org/standard/59644.html> (date of application: 12.05.2025).
17. ISO/IEC 18000-63:2021. Information technology – Radio frequency identification for item management – Part 63: Parameters for air interface communications at 860 MHz to 960 MHz Type C. International Organization for Standardization. Geneva, 2021. URL: <https://www.iso.org/standard/78309.html> (date of application: 12.05.2025).
18. Kirillov, N.P., Dashevsky, V.P., Sokolov, B.V., Yusupov R.M. Perspective applications of radio frequency identification in libraries and museums. *SPIIRAS Proceedings*. 2008. 7. Pp. 48–53.
19. Polyakov, A.V., Dashevsky, V.P., Karpov, A.A., Kryuchkov, B.I., Usov, V.M. Application of RFID technologies for information support of cosmonauts aboard manned spacecraft when using medical packs and first aid kits. *Manned Space Flights*. 2016. 1(18). Pp. 104–117.
20. Dashevsky, V.P., Budkov, V.Yu. Network interface architecture SIM-SIM with power supply of distributed modules. *Information Technologies and Telecommunications*. 2017. 5(4). Pp. 25–35.
21. Styskin, M.M., Stepanov, P.V., Zheltov, S.Yu., Sokolov, B.V., Ronzhin, A.L. Means of optical and radio frequency identification in the technological process of automated control of mobile on-board equipment circulation. *Modeling, Optimization and Information Technology*. 2022;10(1). DOI: 10.26102/2310-6018/2022.36.1.003
22. Fedorova, T., Ryzhov, V., Safronov, K. The Use of Hybrid Communication Architecture in Underwater Wireless Sensor Networks to Enhance Their Lifetime and Efficiency. *Informatics and Automation*. 2024. 23(5). Pp. 1532–1570. DOI:10.15622/ia.23.5.10
23. Qiushi, S., Yang, H., Petrosian, O. Graph Attention Network Enhanced Power Allocation for Wireless Cellular System. *Informatics and Automation*. 2024. 23(1). Pp. 259–283. DOI:10.15622/ia.23.1.9
24. Le, V.N., Ronzhin, A.L. Methods and technical means of positioning and navigation of robots in the aquatic environment. *News of the Kabardino-Balkarian Scientific Center of RAS*. 2023. 6(116). Pp. 167–178. DOI: 10.35330/1991-6639-2023-6-116-167-178
25. Krishna, K.P.R., Thirumuru, R. A Balanced Intrusion Detection System for Wireless Sensor Networks in a Big Data Environment Using CNN-SVM Model. *Informatics and Automation*. 2023. 22(6). Pp. 1296–1322. DOI:10.15622/ia.22.6.2

**Information about the authors:**

**Vladimir Dashevsky**, PhD in Technical Sciences

E-mail: [vladimir.dashevsky@gmail.com](mailto:vladimir.dashevsky@gmail.com)

**Victoria Kondratieva**,

E-mail: [v.kondrateva@promeco-inst.ru](mailto:v.kondrateva@promeco-inst.ru)

**Vasily Rzhimsky**,

E-mail: [vladimir.dashevsky@strategic-it.ru](mailto:vladimir.dashevsky@strategic-it.ru)

**Andrey Ronzhin**, Doctor of Technical Sciences

E-mail: [ronzhin@iias.spb.su](mailto:ronzhin@iias.spb.su)

*Received 05.08.2024. Approved after reviewing 14.03.2025. Accepted 21.03.2025.*





Research article

UDC 691.5

DOI: 10.34910/MCE.134.5




## Granular aggregate for fill mortars using blast furnace slag

L.H. Zagorodnyuk<sup>1</sup> , G.A. Sytov<sup>1</sup>  , V.N. Bogdanov<sup>1</sup> , A.I. Kudyakow<sup>2</sup> 

<sup>1</sup> Belgorod State Technological University named after V.G. Shukhov, Belgorod, Russian Federation

<sup>2</sup> Tomsk State University of Architecture and Building, Tomsk, Russian Federation

 [sytov2024@icloud.com](mailto:sytov2024@icloud.com)

**Keywords:** granular aggregates, disc granulator, vortex jet mill, filling solutions.

**Abstract.** The technology of underground mining is one of the most promising areas of the mining industry. The use of technogenic waste, as well as unclaimed and substandard raw materials for the production of fill mortars in all over the world is an urgent problem in ecology and materials science. Research on obtaining the compositions of backfill mortars with different contents of blast furnace slag is presented. Mechanical activation of raw mixtures for granular aggregates was carried out in a vortex jet mill. A method for preparing raw material granules in a disc granulator has been developed. It has been established that when using a disc granulator, the following yield of aggregate fractions has been obtained: the number of fractions up to 8 mm is 30 %, fractions up to 6 mm – 27 %, fractions 2–4 mm – 43 %. It has been marked that granular aggregates using a slag fraction of 2.5 mm (composition 1) have the greatest strength of 3.73 MPa. When the fraction size increases up to 5 mm (composition 1), the strength of the granules decreases by 12.01 % and amounts to 3.33 MPa. The structure formation of solutions with different types of granular aggregates has its own characteristics, which are determined by the slag fraction, composition and water-binding ratio, as well as the condition of strength gain.

**Funding:** This work was realized in the framework of the Program “Priority 2030” on the base of the Belgorod State Technological University named after V.G. Shukhov. The work was realized using equipment of High Technology Center at BSTU named after V.G. Shukhov.

**Citation:** Zagorodnyuk, L.H., Sytov, G.A., Bogdanov, V.N., Kudyakow, A.I. Granular aggregate for fill mortars using blast furnace slag. Magazine of Civil Engineering. 2025. 18(2). Article no. 13505. DOI: 10.34910/MCE.135.5

### 1. Introduction

The object of the study is backfill mixtures that meet the operational characteristics for the effective backfill of mined-out spaces of mining enterprises.

The mining industry in the modern world is one of the main developing areas both in the Russian Federation and abroad. The extraction of iron ores and their processing leads to the formation of a fairly large number of by-products – slag, which must be disposed of, as they cause serious environmental problems, which is one of the important problems for the modern world [3].

Currently, many studies have been carried out on the possibility of using blast furnace slag in the production of building materials, including for use in the cement industry, this is due to the similarity of the chemical and mineralogical composition with Portland cement [1, 2, 4]. Blast furnace slag is crushed in efficient mills to achieve the required slag fraction, and then used as a mineral additive in the preparation of various types of cements and binder compositions [5, 6].

In backfill mining, filling compounds based on Portland cement are widely used as a binder and fine aggregate. At the same time, cement in filling mixtures is used in huge quantities, which leads to its overconsumption and affects the economic costs of iron ore mining and the maintenance of the mining complex [6–8]. Analysis of statistical data indicates that a significant share of the cost of the filling mixture belongs to Portland cement.

To prepare effective filling mixtures, it is necessary to have fine aggregates of a certain required granulometric composition, ensuring the rational use of the binder, guaranteeing the formation of high density and strength of filling mortars [12]. Unfortunately, in many regions of our country and abroad, where various mineral resources are mined, there are no effective fillers that ensure the formation of the necessary structure of backfill masses. When developing and using fill masses, you should take an individual approach to the geological features of the mined-out space, its condition, as well as the development and placement of fill mixtures, which requires additional technical, financial solutions and investments [9]. The main way to reduce the cost of production of backfill mortars is to obtain backfill mixtures with optimal technical and economic indicators, which requires the development of effective granular aggregates that ensure the rational use of Portland cement and the production of reliable and durable backfill mortars [10, 11, 13].

To date, there have been a number of scientific studies [14, 17, 18] related to the production of granular aggregates based on Portland cement and various technogenic raw materials.

It is noteworthy that in order to create cost-effective compositions of granular aggregates, it is necessary to select appropriate binder compositions [4, 7, 15].

The production of effective filling mixtures that meet the technological and physical-mechanical characteristics for filling mined-out voids for a mining enterprise is a very important task.

When developing various compositions of backfill masses to save material and technical resources, various mining enterprises use local and technogenic raw materials [16, 19, 20]. In many regions of our country and abroad, due to the peculiarities of the geological structure, there is a shortage of high-quality and fine aggregates. Therefore, in this regard, the development of granular aggregates with a certain composition that guarantees the production of high-quality and dense solutions and concretes for their intended purpose is relevant.

The goal of the research is to create effective backfill mixtures that meet the technological and physical-mechanical characteristics for backfilling mined-out voids for a mining enterprise.

The following tasks were solved within the framework of this study:

- Development of a composition with different dosages of slag in a percentage ratio from 85–95 %;
- Production of raw spherical granules by rolling in a plate granulator with a size of 2.5–10 mm;
- Analysis of the results of sieving the obtained granules using a plate granulator of fractions from 2–8 mm;
- Evaluation of the effectiveness of the application of physico-chemical characteristics of granular aggregates in fractions of 2.5, 5, 10 mm and strength indicators of granular aggregates with an increase in the size of fractions in the developed voids for mining enterprises.

## *2. Materials and Methods*

The production of granular aggregates involved the selection of compositions, the study of their properties, preparation of raw granules according to the proposed method, and the study of the properties of the resulting granular aggregates.

At the first stage, compositions with different dosages of slag were obtained.

When developing compositions for various granular aggregates, three compositions 1, 2, 3 were studied; for comparison, commercial Portland cement TsEM 0 Interstate Standard GOST 31108-2020 manufactured by Belgorod Cement CJSC was used; blast furnace slag of a fraction  $\leq 0.16$  mm from Severstal PJSC was used as a mineral additive [21–23].

The preparation of compositions 1, 2, 3 was carried out in a VSM-01 vortex jet mill by grinding to a specific surface of about 600 m<sup>2</sup>/kg.

**Table 1. Composition and specific surface.**

Code	Composition of the composition, %		Specific surface area before and after passing through VSM-01, m <sup>2</sup> /kg	
	PC	Slag	before grinding	after grinding
PC	100	–	305	–
1	5	95	325	604
2	10	90	310	590
3	15	85	290	576

During mechanical activation of compositions in a vortex jet mill, the specific surface area of compositions with different slag contents: 85, 90, 95 % changed, respectively, to 1.98, 1.9, 1.85 times.

Granulated aggregates from the given compositions were obtained in a disc granulator.

### 3. Results and Discussion

The laboratory installation is a cylindrical metal plate (bowl) with sides, to which a motor is attached, secured by a holder. The granulator is equipped with an inclination change device, a scraper device consisting of a combination of a non-powered scraper and a cleaning scraper, and is used to make balls (pellets) at the same time as bottom cleaning and edge cleaning to form balls. A general view of the laboratory granulator is shown in Figs. 1a, 1b.

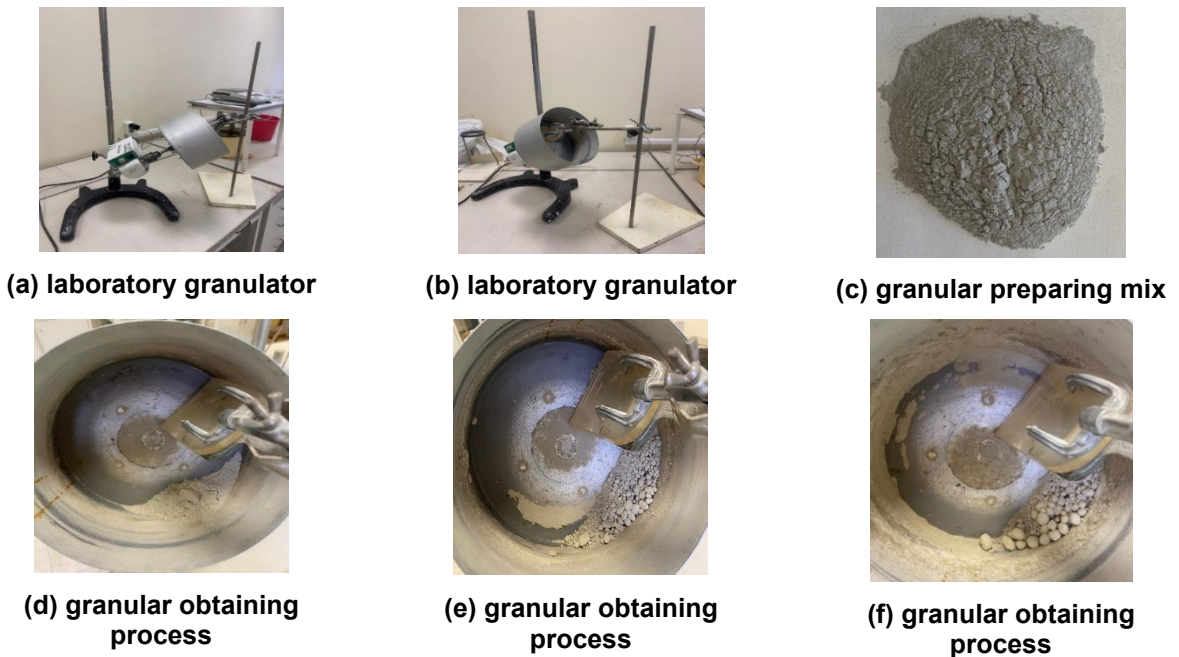


**Figure 1. General view of a laboratory granulator and stage-by-stage granular obtaining process.**

The production of raw material granules was carried out by the pelletizing method. Rolling involves a group of processes that are characterized by the movement of granulating powder over the surface of the device. The dry mix, located in a disc granulator, is irrigated with distilled water using a sprayer (Fig. 1c). At the same time, the surface of the powder in the disc granulator is moistened and, due to the rotation of the bowl, small granules begin to form, which, when in contact with the dry powder, increase in diameter. As the bowl rotates, the granules are further rolled to the required diameter (Figs. 1d, 1e, 1f).

In the granule pelletizing process, powder agglomeration is a crucial step essential for practical implementation. Continuous movement of the granular material facilitates both the formation and enlargement of granules, as well as their potential destruction due to fluctuations in humidity and variations in the adhesive properties of the material layers being rolled. The objective during agglomeration is to establish conditions conducive to the formation and preservation of granules with diverse diameters [24–27].

A typical pellet granulation setup involves a horizontally or slightly inclined rotating plate, onto which powder is fed, typically with a binding liquid. The wet particles undergo agglomeration and rolling to achieve



the desired density and size. However, deviations from optimal granule growth may occur due to individual granule connections or breakage, resulting in diminished granule quality.

As the plate rotates, a portion of the powder adheres to its walls and base, ascending to a certain height before descending. The ascent height and powder capture rate depend on various factors such as internal and external friction ratios, rotation speed, and unit filling level. During ascent, the granules move in tandem with the base, maintaining relative immobility until reaching a point where compression occurs, initiating rolling and subsequent granule enlargement. The process of rolling granules in a laboratory granulator occurs within 10 minutes until the required maximum diameter of 10 mm is reached.

When developing the technological basis for producing granular aggregates using mineral powders and binders, the hardening conditions of the resulting rounded particles are important, since binders harden differently under different conditions. The prepared granules hardened and gained strength under normal conditions (ambient temperature +20 °C and relative humidity 80–90 %).

Ready-made granular aggregates are fairly tightly compressed solid spherical particles ranging in size from 2.5 to 10 mm (Fig. 2).

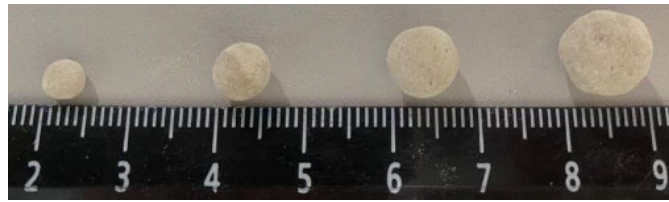


**Figure 2. Grained filling aggregates.**

Analysis of the results of sifting the resulting granules showed that when using a disc granulator, the highest content of the fraction up to 8 mm is obtained, which is 30 %, fractions up to 6 mm – 27 %, and the fraction from 2 to 4 mm is present in larger quantities in the amount of 43 % (Fig. 3).

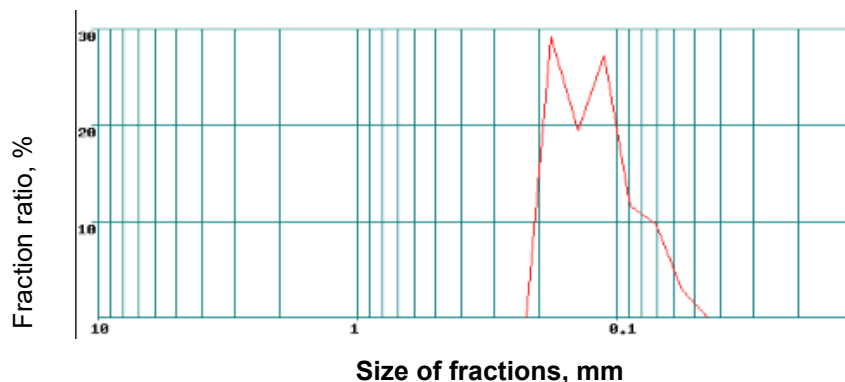


**Figure 3. Granulometric size grading.**

The Michaelis apparatus was used to determine the compressive strength of the resulting granules. The resulting granule of a certain fraction was placed between special clamping plates of the device, and the handle was twisted to tightly press the granule to the plates. Next, a bucket was placed on the hook and the shot began to be poured evenly until the moment when the bucket with shot set the lever in motion. Then the bucket of shot was weighed and the compressive strength of one granule was obtained in gc/mm<sup>2</sup>.

Testing of the resulting granules was carried out 28 days after complete hardening and drying. Granular aggregates obtained in a laboratory setup are shown in (Fig. 4).



**Figure 4. Granulated aggregate, obtained in a laboratory facility.**

The results of physical and mechanical tests of the obtained granular aggregates are shown in (Fig. 5).

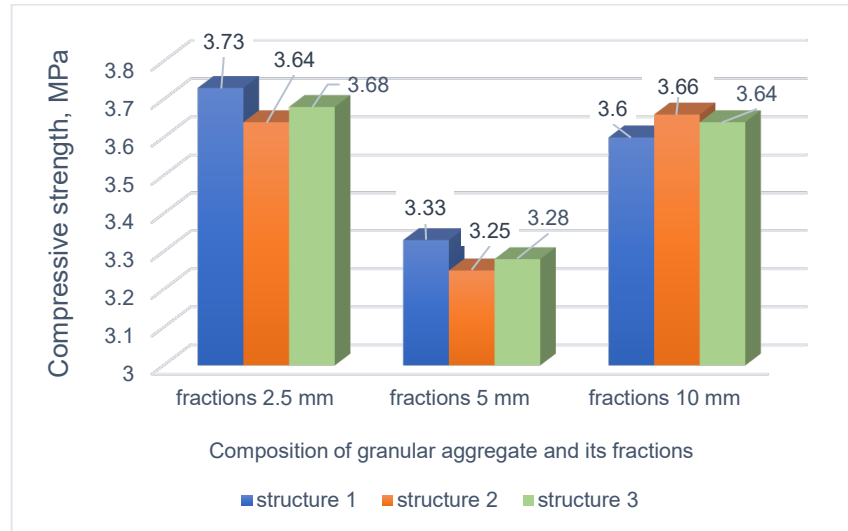


**Figure 5. Physico-mechanical characteristics of granular aggregates by fractions.2.5, 5, 10.**

Analysis of the results of physical and mechanical tests of granular aggregates showed that a certain technical effect was achieved. It has been established that granular aggregates using a slag fraction of 2.5 mm (composition 1) have the greatest strength of 3.73 MPa. When the fraction size increases to 5 mm (composition 1), the strength of the granules decreases by 12.01 % and amounts to 3.33 MPa relative to 2.5 mm granular aggregates. When the fraction size increases from 5 mm (composition 1) to 10 mm (composition 1), the strength increases by 8.11 % and amounts to 3.6 MPa.

In accordance with the stated goal of creating granular aggregates for backfill mortars, it was of interest to determine the strength characteristics of their various fractions in cement mortar. In this regard, cube samples were molded as follows: 1) prepare a cement mortar with  $W/C = 0.5$ ; 2) granular aggregates of different fractions with the same mass were weighed; 3) the mixture was mixed and placed in sample cubes, while granular aggregates in all forms occupied the maximum volume with their same mass. This type of molding was justified by the creation of such a macrostructure of cement stone with filler, in which the nature of the destruction of the samples will be realized with a gap in the places of grains of granular filler, that is, in the most weakened areas. Molded cubes  $3 \times 3 \times 3$  cm gained strength within 28 days under normal conditions.

During the research, 18 sample cubes were molded from 3 types of recipes. Laboratory tests of cube samples were carried out on a hydraulic press PGM-50MG4. Figs. 6, 7, 8 show destroyed samples of the compositions.



**Figure 6. Mortar sample chipping with granular aggregate 2.5 mm fractions.**



**Figure 7. Mortar sample chipping with granular aggregate 5 mm fractions.**



**Figure 8. Mortar sample chipping with granular aggregate 10 mm fractions.**

As a result of the study of chipped surfaces of the tested samples, a type of destruction was revealed, characterized by the predominant rupture of filler granules. It has been established that all granules in fracture zones have maximum diametrical dimensions; therefore, destruction occurs precisely at the radial distance from the contact zone of granules and cement stone.

It is important to take into account the porosity of granular aggregates and their features in the composition of the solution. Having carried out a comparative analysis of Figs. 6, 7, 8, it should be noted that the contact zones of granular aggregates (slag) and cement stone of the destroyed sample have clearly visible interface lines, when, as the diameter of the slag granules in the aggregates increases, these lines are blurred.

This suggests that the connection between granular aggregates and cement paste, due to an increase in the porosity of the former, increases, and therefore the optimal aggregate, from the point of view of the integrated operation of the entire composition of the mortar mixture, is an aggregate with a diameter of 2.5–10 mm. The size of the contact layer increases with decreasing binder content in the composition of the granular aggregate.

Thus, the process of structure formation of solutions with various types of granular aggregates has its own characteristics, which are determined by the use of slag of one or another fraction, the type of binder component and its percentage, water-binder ratio, conditions for strength development and other parameters.

In the study of granular slag aggregate in cement composites, when compared with carbon nanostructure in primary aluminum production, key parallels and differences in the relationship between structure and properties, interfacial interaction and optimization strategies are traced between them.

**Table 2. Similarities in Structural Behavior & Failure Mechanisms.**

Aspect	Slag-Cement Composites	Carbon Nanostructures in Aluminum
Interfacial Bonding	Weakest link is granule fracture (not ITZ); porosity improves adhesion.	Carbon nanostructures influence anode/cathode interfaces; poor bonding leads to inefficiencies [24].
Optimal Particle Size	2.5–10 mm slag granules maximize strength.	Nanoscale carbon (e.g., nanotubes) enhances conductivity but requires dispersion control [5].
Porosity Effects	Higher slag porosity improves mechanical anchoring.	Porous carbon anodes affect electrolysis efficiency and durability [17].
Failure Analysis	Radial cracks in granules dominate failure.	Carbon anode degradation due to microcracking/spalling [8].



**Table 3. Contrasts in Material Systems & Applications.**

Parameter	Slag-Cement Composites	Carbon in Aluminum Production
Primary Material	Industrial slag ( $\text{SiO}_2$ , $\text{CaO}$ , $\text{Al}_2\text{O}_3$ ).	Carbon (graphite, nanotubes) [14].
Key Interaction	Slag-cement chemical/physical bonding.	Carbon-electrolyte/oxide reactions [23].
Performance Goal	Mechanical strength, durability.	Electrical conductivity, thermal stability [13].
Destruction Mechanism	Granule fracture under tension/compression.	Anode erosion/corrosion via electrolysis [22].

Both studies highlight:

Interfacial Engineering:

- Slag porosity boosts cement bonding;
- Carbon nanostructures modify electrode interfaces.

Size-Dependent Properties:

- Slag granules (2.5–10 mm) optimize mortar strength;
- Nanocarbon size/shape affects aluminum electrolysis efficiency.

Process Optimization:

- Binder content, curing conditions;
- Carbon purity, electrolysis parameters.

### 3.1. Industrial Implications

Results using slag:

- Waste slag reuse in construction (circular economy);
- Guidelines for durable, low-cement composites.

## 4. Conclusion

In accordance with the set objective, the following results were obtained:

1. Granular fillers for cement slurries with different slag content were developed, which were obtained in a laboratory granulator.
2. A method for preparing raw material granules was developed. Studies have shown that the granulometric composition of the obtained granular fillers includes the highest content of fraction up to 8 mm, which is 30 % of the total volume of finished granules, fraction up to 6 mm is 27 %, and fraction from 2 to 4 mm is present in greater quantity in the amount of 43 %.

The obtained physical and mechanical results indicate that granules of fraction 2.5 mm (composition 1) have the highest strength of 3.73 MPa, which allows using them as granular fillers for cement slurries.

A study of the chipped surfaces of destroyed granules revealed their strong adhesion to the cement stone. The obtained granulated filler is of considerable interest for use in the development of mortars and fine-grained concrete in regions where high-quality fine fillers are not available.

## References

1. Zhao, Y., Soltani, A., Taheri, A., Karakus, M., Deng, A. The use of slag cement and fly ash to increase the strength when filling with cement paste. *Backfills. Minerals*. 2018. 9(1). Article no. 22. DOI: 10.3390/min9010022
2. Ageeva, M., Sopin, M., Lesovik, R., Bogusevic, G. Development of compositions of backfill mixtures. *Bulletin of BSTU named after V.G. Shukhov*. 2016. 1(12). Pp. 31–34. DOI: 10.12737/22641
3. Buryanov, A., Gal'ceva, N., Grunina, I. The use of pyrometallurgical industry wastes in the production of materials for laying excavation. *Bulletin of BSTU named after V.G. Shukhov*. 2019. 4(2). Pp. 21–26. DOI: 10.12737/article\_5c73bf50c6942.61479060
4. Zagorodnyuk, L.H., Ryzhikh, V.D., Sumskoy, D.A., Sinebok, D.A. Composite Binders Based on Dust of Electric Filters. *Lecture Notes in Civil Engineering*. 2021. Innovations and Technologies in Construction. BUILDINTECH BIT 2020. 95. Pp. 253–259. DOI: 10.1007/978-3-030-54652-6\_38
5. Li, J., Zhang, S., Wang, Q., Ni, W., Li, K., Fu, P., Hu, W., Li, Z. Feasibility of using fly ash-slag-based binder for mine backfilling and its associated leaching risks. *J Hazard Mater*. 2020.400. Article no. 123191. DOI: 10.1016/j.jhazmat.2020.123191

6. Lesovik, V., Zagorodnyuk, L., Ryzhikh, V., Lesovik, R., Fediuk, R., Vatin, N., Karelina, M. Granular Aggregates Based on Finely Dispersed Substandard Raw Materials. *Crystals*. 2021. 4(11). Article no. 369. DOI: 10.3390/cryst11040369
7. Zagorodnyuk, L.H., Ryzhikh, V.D., Syitov, G.A., Sumskoy, D.A. Construction and analysis of mathematical models of granular aggregates. *AIP Conference Proceedings*. 2023. 2758(1). Article no. 020001. DOI: 10.1063/5.0130752
8. Cantero, B., Bravo, M., de Brito, J., Sachs del Bosque, I.F., Medina, S. Thermal performance of concretes with recycled concrete powder as a partial replacement of cement and recycled CDW aggregate. *Applied Sciences*. 2020. 10(13). Article no. 4540. DOI: 10.3390/app10134540
9. Wu, J., Wen, M., Xu, J., Yu, P., Wang, Yu, Han, G. Particle Size Distribution of Cemented Rockfill Effects on Strata Stability in Filling Mining. *Minerals*. 2018. 8(9). Article no. 407. DOI: 10.3390/min8090407
10. Thomas, C., Cimentada, A.I., Cantero, B., Sos del Boscel, F., Polanco, J.A. Industrial prefabricated elements with low clinker content using recycled aggregates. *Applied Sciences*. 2020. 10(19). Article no. 6655. DOI: 10.3390/app10196655
11. Pichór, W., Kamiński, A., Szoldra, P., Frąc, M. Light cement mortars with the addition of granular foam glass and perlite waste. *Achievements in the field of civil engineering*. 2019. Article no. 1705490. DOI: 10.1155/2019/1705490
12. Zagorodnyuk, L.H., Lesovik, V.S., Sumskoy, D.A., Elistratkin, M.Yu., Makhortov, D.S. Peculiarities of binding composition production in vortex jet mill. 2018. *IOP Conference Series: Materials Science and Engineering*. 327(4). Article no. 042128. DOI: 10.1088/1757-899X/327/4/042128
13. Montanari, D., Agostini, A., Boni, M., Corti, G. The Use of Empirical Methods for Testing Granular Materials in Analogue Modelling. *Materials*. 2017. 10(6). Article no. 635. DOI: 10.3390/ma10060635
14. Jiang, H., Qi, Z., Yilmaz, E., Han, J., Qiu, J., Dong, C. The effectiveness of alkali-activated slag as an alternative binder on the machinability and compressive strength of cemented paste at an early age. *Construction and Building Materials*. 2019. 218. Pp. 689–700. DOI: 10.1016/j.conbuildmat.2019.05.162
15. Xiao, B., Yang, Z., Chen, D., Gao, Q. (2019). Impacts of Slag-Based-Binder Fineness on Strength in Mining Backfill. *SCIENTIA SINICA Technologica*. 2019. 49(4). Pp.402–410. DOI: 10.1360/n092018-00109
16. Zhang, S., Ren, F., Zhao, Yu, Yu, J., Guo, Z. The influence of stone waste on the properties of cemented grout filling with the use of alkali-activated slag as a binder has been studied. *Construction and Building Materials*. 2021. 283. Article no. 122686. DOI: 10.1016/j.conbuildmat.2021.122686
17. Day, X., Ren, L., Gu, Xi., Yilmaz, E., Fang, K., Jiang, H. Strength Analysis and Optimization of Alkali Activated Slag Backfills Through Response Surface Methodology. *Frontiers in Materials*. 2022. 9. Article no. 844608. DOI: 10.3389/fmats.2022.844608
18. Jiang, H., Han, J., Li, Y., Yilmaz, E., Sun, Q., Liu, J. The relationship between the speed of the ultrasonic pulse and the uniaxial compressive strength for filling cemented paste with alkali-activated slag. *Nondestructive Testing and Evaluation*. 2020. 35. Pp. 359–377. DOI: 10.1080/10589759.2019.1679140
19. Dudin, M.O., Vatin, N.I., Barabanshchikov, Y.G. Modeling a set of concrete strength in the program ELCUT at warming of monolithic structures by wire. *Magazine of Civil Engineering*. 2015. 54(2). Pp. 33–45. DOI: 10.5862/MCE.54.4
20. Amran, M., Onaizi, A.M., Fediuk, R., Vatin, N.I., Rashid, R.S.M., Abdelgader, H., Ozbakkaloglu, T. Self-Healing Concrete as a Prospective Construction Material: A Review. *Materials*. 2022. 15(9). Article no. 3214. DOI: 10.3390/ma15093214
21. Yelemessov, K., Sabirova, L.B., Martyushev, N.V., Malozyomov, B.V., Bakhmagambetova, G.B., Atanova, O.V. Modeling and Model Verification of the Stress-Strain State of Reinforced Polymer Concrete. *Materials*. 2023. 16(9). Article no. 3494. DOI: 10.3390/ma16093494
22. Rassokhin, A., Ponomarev, A., Karlina, A. Nanostructured high-performance concretes based on low-strength aggregates. *Magazine of Civil Engineering*. 2022. 110(2). Article no. 11015. DOI: 10.34910/MCE.110.15
23. Fastyskovsky, A.R., Martyushev, N.V., Musatova, A.I., Karlina, A.I. Feasibility demonstration of normative models for sheet-rolling shop productivity. *Message 2. Chernye Metally*. 2024. 3. Pp. 63–68. DOI: 10.17580/chm.2024.03.10
24. Kondrat'ev, V.V., Ershov, V.A., Shakhrai, S.G., Ivanov, N.A., Karlina, A.I. Formation and Utilization of Nanostructures Based on Carbon During Primary Aluminum Production. *Metallurgist*. 2016. 60(7–8). Pp. 877–882. DOI: 10.1007/s11015-016-0380-x
25. Rassokhin, A., Ponomarev, A., Shambina, S., Karlina, A. Different types of basalt fibers for disperse reinforcing of fine-grained concrete. *Magazine of Civil Engineering*. 2022. 109(1). Article no. 10913. DOI: 10.34910/MCE.109.13
26. Cherkasova, T.G., Cherkasova, E.V., Tikhomirova, A.V., Gilyazidinova, N.V., Gilyazidinova, N.V., Klyuev, R.V., Karlina, A.I., Skiba, V.Y. Study of Matrix and Rare Elements in Ash and Slag Waste of a Thermal Power Plant Concerning the Possibility of their Extraction. *Metallurgist*. 2022. 65(11–12). Pp. 1324–1330. DOI: 10.1007/s11015-022-01278-2
27. Klyuev, S.V., Klyuev, A.V., Vatin, N.I. Fiber concrete for the construction industry. *Magazine of Civil Engineering*. 2018. 84(8). Pp. 41–47. DOI: 10.18720/MCE.84.4

#### **Information about the authors:**

**Lilia Zagorodnyuk, Doctor in Technical Sciences**

ORCID: <https://orcid.org/0000-0001-9840-4414>

E-mail: [lh47@mail.ru](mailto:lh47@mail.ru)

**Gleb Sytov,**

ORCID: <https://orcid.org/0000-0002-8451-4716>

E-mail: [syto2024@icloud.com](mailto:sytov2024@icloud.com)

**Vsevolod Bogdanov,**

ORCID: <https://orcid.org/0009-0000-2353-1697>

E-mail: [Bogdanov\\_vsevolod@mail.ru](mailto:Bogdanov_vsevolod@mail.ru)

**Alexander Kudyakow**, *Doctor in Technical Sciences*

ORCID: <https://orcid.org/0000-0002-8927-6833>

E-mail: [Kudyakow@mail.tomsknet.ru](mailto:Kudyakow@mail.tomsknet.ru)

*Received 26.08.2024. Approved after reviewing 18.03.2025. Accepted 24.03.2025.*





Research article

UDC 624.04

DOI: 10.34910/MCE.134.6



## Simplified finite element model for rectangular CFST columns strength calculation under eccentric compression

A. Chepurnenko  , B. Yazyev  , S. Al-Zgul  , V. Tyurina 

*Don State Technical University, Rostov-on-Don, Russian Federation*

 [anton\\_chepurnenk@mail.ru](mailto:anton_chepurnenk@mail.ru)

**Keywords:** finite element method, numerical models, tubular steel structures, reinforced concrete, mechanical performance, compressive strength

**Abstract.** Concrete filled steel tubular (CFST) column is one of the most effective building structures types that combine high bearing capacity and economy. Three-dimensional nonlinear finite element analysis is the most common and reliable method for determining the bearing capacity of CFST columns. This approach is usually applied to individual elements and is not suitable for calculating buildings and structures with CFST elements as a single whole, due to high computational complexity. The purpose of the article is to develop a simplified model that allows reducing a three-dimensional problem of calculating a CFST column to a two-dimensional one. Rectangular CFST columns subjected to eccentric compression with eccentricity in two planes are considered. The problem dimension is reduced based on the hypothesis of plane sections. Rectangular elements are used for the concrete core and one-dimensional bar elements are used for the steel pipe. The developed model was verified by comparing calculation results with the results of three-dimensional finite element modeling in ANSYS. The maximum discrepancy between the results for stresses was 2.3 %. The model was also validated on experimental data for 38 samples presented in 3 different papers. The proposed model allows to significantly reduce the machine time costs when calculating CFST columns in a physically nonlinear formulation.

**Citation:** Chepurnenko, A., Yazyev, B., Al-Zgul, S., Tyurina, V. Simplified finite element model for rectangular CFST columns strength calculation under eccentric compression. Magazine of Civil Engineering. 2025. 18(2). Article no. 13406. DOI: 10.34910/MCE.134.6

### 1. Introduction

Concrete filled steel tubular (CFST) columns have attracted considerable attention in the construction industry due to their excellent mechanical properties, including high load-bearing capacity [1], ductility [2], and fire resistance [3]. The combined action of the steel tube and concrete core in the circumferential direction improves the compressive strength of concrete [4], making CFST columns a popular choice for high-rise buildings [5], bridges [6], and other unique structures. Accurate calculation of the CFST columns load-bearing capacity is essential to ensure the reliability of buildings and structures and optimize the design.

When calculating the bearing capacity of CFST structures, it is necessary to take into account the confinement effect of the concrete core by the steel pipe. Mander et al. [7] developed the model for confined concrete, which was adapted for CFST columns. This model was improved in the studies of Yu et al. [8] to take into account the nonlinear behavior of the confined concrete.

Numerical modeling, in particular finite element analysis (FEA), has become a powerful tool for predicting the load-bearing capacity of CFST columns [9]. This modeling can provide the detailed analysis of the structural behavior and the interaction between the steel tube and the concrete core [10]. The finite

element (FE) method allows for the consideration of complex stress-strain relationships for both steel and concrete [11], as well as the separation of the steel tube from the concrete core [12] and local buckling effects [13].

FEA of the CFST columns is usually performed in a three-dimensional setting. Ahmed et al. developed in paper [14] the 3D FE model to simulate the behavior of CFST columns of square cross-section strengthened with additional spiral reinforcement. The developed model accurately predicted the load-strain curves and failure modes. The article of authors Almasabha et al. [15] is devoted to three-dimensional modeling of CFST columns with circular cross-section under quasi-static axial compression. The emphasis in this work is on the scale effect, which has a great influence on the strength of large-diameter columns. In the article [16], three-dimensional FEA is used as a tool for studying the shear behavior of CFST columns. The developed FE models showed an average error of 12 % compared to the experimental results.

Parametric studies using nonlinear FEA allow to analyze the influence of various factors on the load-bearing capacity of CFST columns. Yadav and Chen [17] conducted a comprehensive parametric study for centrally compressed circular columns using the Abaqus software. Factors such as the diameter-to-thickness ratio of the steel pipe, the yield strength of the steel, the compressive strength of the concrete, and the slenderness coefficient of the column were considered. A similar problem was also considered in [18], but the friction coefficient between the concrete core and the steel shell was added to the factors listed above.

The authors of paper [19] studied self-stressing CFST columns using FE modeling in Abaqus. The initial self-stress value varied from 0 to 10 MPa. As a result of the parametric study, the calculation formula was proposed that allows taking into account the self-stress effect. In the paper [20], a comparative bearing capacity analysis of the round and square CFST columns with traditional reinforced concrete elements was performed. The comparison was carried out by means of laboratory experiments, as well as numerical experiments in Abaqus. The comparison results showed that the bearing capacity under axial compression for CFST columns is, on average, 1.5 times higher than that of reinforced concrete columns with the same consumption of concrete and steel.

The authors of work [21] compared the results of FE modeling with the provisions of various countries design codes for CFST columns. It was established that FEA provides more accurate results compared to empirical formulas.

Currently, machine learning methods are gaining increasing popularity in the task of predicting the bearing capacity of building structures, including CFST columns [22–24]. Unlike the theoretical and experimental approach with the selection of empirical formulas, machine learning methods allow taking into account complex nonlinear dependencies between parameters [25, 26]. However, to build reliable machine learning models, a large amount of data is required, which can only be obtained through laboratory and numerical experiments.

The conducted review shows that the FE method is the most common and effective method for determining the bearing capacity of CFST columns. At the same time, most publications are devoted to modeling the stress-strain state of individual CFST elements using three-dimensional FEA. Calculating CFST structures in a three-dimensional formulation taking into account physical nonlinearity requires large computational resources. This approach is not applicable for calculation of buildings and structures that include reinforced concrete elements as a single whole.

In [27], a simplified FE model was proposed that allows the three-dimensional problem of calculating a CFST column to be reduced to a two-dimensional problem based on the hypothesis of plane sections. This model was developed for columns of circular cross-section. The purpose of this work is to develop the proposed model for calculating rectangular CFST columns in the presence of the axial force eccentricity in two planes. Within the framework of the stated goal, the following tasks were formulated:

1. Obtaining resolving equations for determining the stress-strain state of a CFST element in a simplified two-dimensional formulation and developing a calculation algorithm.
2. Verification of the developed model by comparison with the results of three-dimensional FEA.
3. Validation of the developed model by comparison with the experimental results of other authors.

## 2. Methods

The calculation scheme of an eccentrically compressed CFST column with rectangular cross-section is shown in Fig. 1.

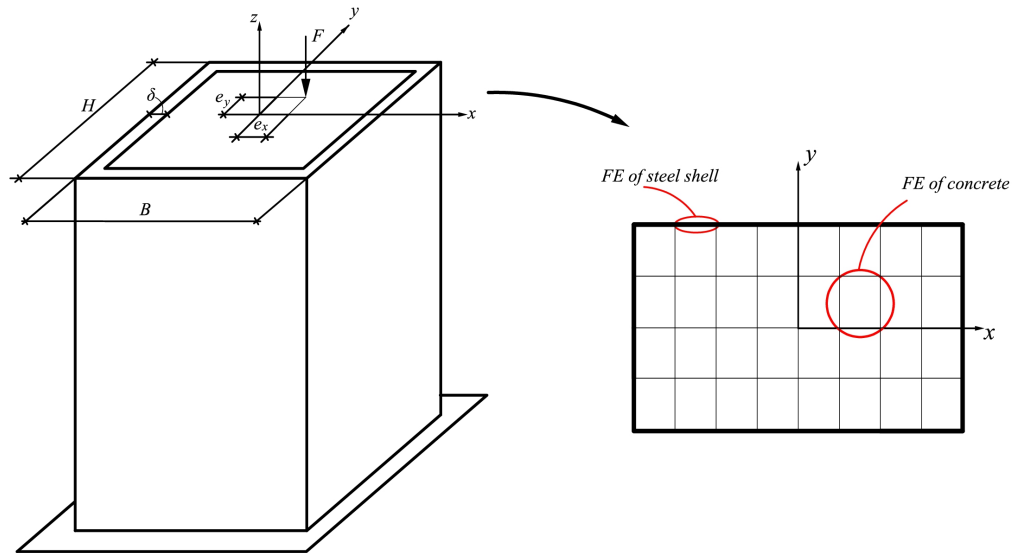


**Figure 1. Calculation scheme.**

Short CFST columns are considered, for which deflection does not lead to a noticeable increase in the bending moment. According to Russian design codes SR 266.1325800.2016, columns are considered short if their slenderness (the ratio of the calculated length to the radius of gyration of the reduced cross section) does not exceed 14.

When constructing the resolving equations for determining the stress-strain state of a CFST element, we will take into account the stresses  $\sigma_z$  in the direction of the column axis, as well as the stresses  $\sigma_x$ ,  $\sigma_y$  and  $\tau_{xy}$  in the plane of the cross section. Stresses  $\tau_{xz}$  and  $\tau_{yz}$  will be neglected. A simplified calculation method is based on the hypothesis of plane sections. In accordance with this method, the deformation along the  $z$  axis under the combined action of bending moments in two planes and axial forces can be represented as:

$$\varepsilon_z = \varepsilon_z^0 + y\chi_1 + x\chi_2. \quad (1)$$

The first term in formula (1) represents the axial deformation, the second and third terms include changes in element curvature  $\chi_1$  and  $\chi_2$ .

When using the plane sections hypothesis, local effects at the ends of the CFST element are neglected, assuming that the load is transmitted through a rigid stamp.

Let us obtain the relationship between the internal forces (axial force  $N$ , bending moments  $M_x$  and  $M_y$ ) and generalized deformations  $\varepsilon_z^0$ ,  $\chi_1$  and  $\chi_2$ . The physical equations for concrete, establishing the relationship between stresses and deformations, have the form:

$$\varepsilon_x = \frac{1}{E} \left( \sigma_x - \nu (\sigma_y + \sigma_z) \right) + \varepsilon_x^*; \quad (2)$$

$$\varepsilon_y = \frac{1}{E} \left( \sigma_y - \nu (\sigma_x + \sigma_z) \right) + \varepsilon_y^*; \quad (3)$$

$$\varepsilon_z = \frac{1}{E} \left( \sigma_z - \nu (\sigma_y + \sigma_x) \right) + \varepsilon_z^*; \quad (4)$$

$$\gamma_{xy} = \frac{2(1+\nu)}{E} \tau_{xy} + \gamma_{xy}^*, \quad (5)$$

where  $E$  is the concrete modulus of elasticity,  $\nu$  is the Poisson's ratio of concrete,  $\varepsilon_x^*$ ,  $\varepsilon_y^*$ ,  $\varepsilon_z^*$  and  $\gamma_{xy}^*$  are the additional terms that may include creep deformations, shrinkage, dilatation deformations, temperature deformations, etc.

Quantities  $\varepsilon_x^*$ ,  $\varepsilon_y^*$ ,  $\varepsilon_z^*$  and  $\gamma_{xy}^*$  will be referred hereinafter to forced deformations. To be able to take into account physical nonlinearity, the modulus of elasticity  $E$  in formulas (2)–(5) is taken as a function of coordinates  $x$  and  $y$ .

The stress  $\sigma_z$  can be expressed from (4) as:

$$\sigma_z = E(\varepsilon_z - \varepsilon_z^*) + \nu(\sigma_y + \sigma_x) = E(\varepsilon_z^0 + y\chi_1 + x\chi_2 - \varepsilon_z^*) + \nu(\sigma_y + \sigma_x). \quad (6)$$

The physical equations for a steel shell are written as:

$$\varepsilon_{s\theta} = \frac{1}{E_s}(\sigma_{s\theta} - \nu_s \sigma_{sz}); \quad (7)$$

$$\varepsilon_{sz} = \frac{1}{E_s}(\sigma_{sz} - \nu_s \sigma_{s\theta}), \quad (8)$$

where  $E_s$  and  $\nu_s$  are respectively, the modulus of elasticity and Poisson's ratio of steel.

Let us express from (7), (8) the stresses in the steel pipe through deformations:

$$\sigma_{sz} = \frac{E_s}{1 - \nu_s^2}(\varepsilon_{sz} + \nu_s \varepsilon_{s\theta}); \quad (9)$$

$$\sigma_{s\theta} = \frac{E_s}{1 - \nu_s^2}(\varepsilon_{s\theta} + \nu_s \varepsilon_{sz}). \quad (10)$$

It is assumed in the calculation that there is no slippage between the steel pipe and the concrete core. This hypothesis is usually fulfilled, since when designing CFST concrete columns, engineers strive to ensure a reliable connection between the steel pipe and the concrete core by welding on short periodic profile steel bars from the inside, or by using concrete on prestressing cement, which creates initial lateral compression stresses. Also, the support nodes are usually designed in such a way that the forces are transmitted simultaneously to the concrete core and the steel pipe.

From the condition of the concrete core and the steel shell joint work in  $z$  axis direction, deformation  $\varepsilon_{sz}$  at the point in the pipe with coordinates  $(x_s; y_s)$  can be written as:

$$\varepsilon_{sz} = \varepsilon_z^0 + y_s \chi_1 + x_s \chi_2. \quad (11)$$

Substitution of  $\varepsilon_{sz}$  from (11), as well as  $\varepsilon_{s\theta}$  from (7) into the equation (10) leads to the equation:

$$\sigma_{sz} = E_s \left( \varepsilon_z^0 + y_s \chi_1 + x_s \chi_2 \right) + \nu_s \sigma_{s\theta}. \quad (12)$$

Internal forces in a column represent the sum of the forces perceived by concrete and steel:

$$N = N_s + N_b = \int_{A_s} \sigma_{sz} dA + \int_{A_b} \sigma_z dA; \quad (13)$$

$$M_x = M_{sx} + M_{bx} = \int_{A_s} \sigma_{sz} y dA + \int_{A_b} \sigma_z y dA; \quad (14)$$

$$M_y = M_{sy} + M_{by} = \int_{A_s} \sigma_{sz} x dA + \int_{A_b} \sigma_z x dA, \quad (15)$$

where  $A_b$  and  $A_s$  are respectively the cross-sectional areas of the concrete core and the steel shell.

The relationships between generalized deformations  $\varepsilon_z^0$ ,  $\chi_1$ ,  $\chi_2$  and internal forces  $M_x$ ,  $M_y$ ,  $N$  can be obtained by substitution of (6) and (12) into (13)–(15):



$$\begin{Bmatrix} N \\ M_x \\ M_y \end{Bmatrix} = \begin{Bmatrix} N \\ N \cdot e_y \\ N \cdot e_x \end{Bmatrix} = \begin{bmatrix} EA & ES_x & ES_y \\ ES_x & EI_x & EI_{xy} \\ ES_y & EI_{xy} & EI_y \end{bmatrix} \begin{Bmatrix} \varepsilon_z^0 \\ \chi_1 \\ \chi_2 \end{Bmatrix} - \begin{Bmatrix} N^* \\ M_x^* \\ M_y^* \end{Bmatrix}, \quad (16)$$

where

$$EA = \int_{A_s} E_s(x, y) dA + \int_{A_b} E(x, y) dA; \quad (17)$$

$$ES_x = \int_{A_s} E_s(x, y) y dA + \int_{A_b} E(x, y) y dA; \quad (18)$$

$$ES_y = \int_{A_s} E_s(x, y) x dA + \int_{A_b} E(x, y) x dA; \quad (19)$$

$$EI_x = \int_{A_s} E_s(x, y) y^2 dA + \int_{A_b} E(x, y) y^2 dA; \quad (20)$$

$$EI_y = \int_{A_s} E_s(x, y) x^2 dA + \int_{A_b} E(x, y) x^2 dA; \quad (21)$$

$$EI_{xy} = \int_{A_s} E_s(x, y) xy dA + \int_{A_b} E(x, y) xy dA; \quad (22)$$

$$N^* = \int_{A_b} \left( E(x, y) \varepsilon_z^* + \nu (\sigma_x + \sigma_y) \right) dA + \nu_s \int_{A_s} \sigma_{s\theta} dA; \quad (23)$$

$$M_x^* = \int_{A_b} \left( E(x, y) \varepsilon_z^* + \nu (\sigma_x + \sigma_y) \right) y dA + \nu_s \int_{A_s} \sigma_{s\theta} y_s dA; \quad (24)$$

$$M_y^* = \int_{A_b} \left( E(x, y) \varepsilon_z^* + \nu (\sigma_x + \sigma_y) \right) x dA + \nu_s \int_{A_s} \sigma_{s\theta} x_s dA. \quad (25)$$

To determine the stresses acting in the plane of the cross section, the concrete core is divided into rectangular FEs, and the steel shell is modeled by one-dimensional bar elements (Fig. 2). Rounding of corners in rectangular bent-welded sections will be neglected.

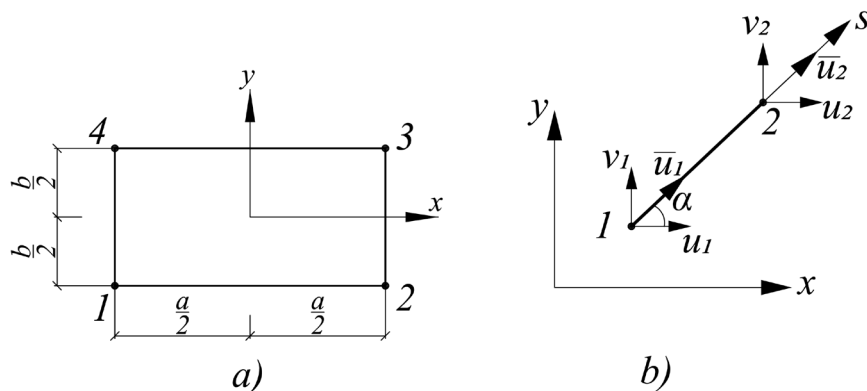


**Figure 2. Finite elements for determining the stress-strain state in the plane of the cross-section: a) finite element of the concrete core, b) finite element of the steel shell.**

The FE of the concrete core has 2 degrees of freedom at the node: displacements  $u$  and  $v$  in the plane of the cross section.

Approximation of displacements  $u$  and  $v$  is taken in the form:

$$u = \alpha_1 + \alpha_2 x + \alpha_3 y + \alpha_4 xy; \quad (26)$$

$$v = \beta_1 + \beta_2 x + \beta_3 y + \beta_4 xy. \quad (27)$$

Expressions (26), (27) in matrix form have the form:

$$\begin{Bmatrix} u \\ v \end{Bmatrix} = \begin{bmatrix} 1 & x & y & xy & 0 & 0 & 0 & 0 \\ 0 & 0 & 0 & 0 & 1 & x & y & xy \end{bmatrix} \{\alpha\}, \quad (28)$$

where  $\{\alpha\} = \{\alpha_1 \ \alpha_2 \ \alpha_3 \ \alpha_4 \ \beta_1 \ \beta_2 \ \beta_3 \ \beta_4\}^T$ .

The vector  $\{\alpha\}$  can be found by substituting the coordinates of the nodes into (28):

$$\begin{bmatrix} 1 & -\frac{a}{2} & -\frac{b}{2} & \frac{ab}{4} & 0 & 0 & 0 & 0 \\ 0 & 0 & 0 & 0 & 1 & -\frac{a}{2} & -\frac{b}{2} & \frac{ab}{4} \\ 1 & \frac{a}{2} & -\frac{b}{2} & -\frac{ab}{4} & 0 & 0 & 0 & 0 \\ 0 & 0 & 0 & 0 & 1 & \frac{a}{2} & -\frac{b}{2} & -\frac{ab}{4} \\ 1 & \frac{a}{2} & \frac{b}{2} & \frac{ab}{4} & 0 & 0 & 0 & 0 \\ 0 & 0 & 0 & 0 & 1 & \frac{a}{2} & \frac{b}{2} & \frac{ab}{4} \\ 1 & -\frac{a}{2} & \frac{b}{2} & -\frac{ab}{4} & 0 & 0 & 0 & 0 \\ 0 & 0 & 0 & 0 & 1 & -\frac{a}{2} & \frac{b}{2} & -\frac{ab}{4} \end{bmatrix} \{\alpha\} = [\Phi] \{\alpha\} = \{U\}, \quad (29)$$

where  $\{U\} = \{u_1 \ v_1 \ u_2 \ v_2 \ u_3 \ v_3 \ u_4 \ v_4\}^T$  is the vector of nodal displacements in the plane of the cross section.

The vector  $\{\alpha\}$  is expressed from (29) as:  $\{\alpha\} = [\Phi]^{-1} \{U\}$ . The matrix  $[\Phi]^{-1}$  has the form:

$$[\Phi]^{-1} = \begin{bmatrix} \frac{1}{4} & 0 & \frac{1}{4} & 0 & \frac{1}{4} & 0 & \frac{1}{4} & 0 \\ -\frac{1}{2a} & 0 & \frac{1}{2a} & 0 & \frac{1}{2a} & 0 & -\frac{1}{2a} & 0 \\ -\frac{1}{2b} & 0 & -\frac{1}{2b} & 0 & \frac{1}{2b} & 0 & \frac{1}{2b} & 0 \\ \frac{1}{ab} & 0 & -\frac{1}{ab} & 0 & \frac{1}{ab} & 0 & -\frac{1}{ab} & 0 \\ 0 & \frac{1}{4} & 0 & \frac{1}{4} & 0 & \frac{1}{4} & 0 & \frac{1}{4} \\ 0 & -\frac{1}{2a} & 0 & -\frac{1}{2a} & 0 & -\frac{1}{2a} & 0 & -\frac{1}{2a} \\ 0 & -\frac{1}{2b} & 0 & -\frac{1}{2b} & 0 & \frac{1}{2b} & 0 & \frac{1}{2b} \\ 0 & \frac{1}{ab} & 0 & -\frac{1}{ab} & 0 & \frac{1}{ab} & 0 & -\frac{1}{ab} \end{bmatrix}. \quad (30)$$

The deformation vector in the cross-sectional plane is determined as follows:

$$\{\varepsilon\} = \begin{Bmatrix} \frac{\partial u}{\partial x} \\ \frac{\partial v}{\partial y} \\ \frac{\partial u}{\partial y} + \frac{\partial v}{\partial x} \end{Bmatrix} = \begin{bmatrix} 0 & 1 & 0 & y & 0 & 0 & 0 & 0 \\ 0 & 0 & 0 & 0 & 0 & 0 & 1 & x \\ 0 & 0 & 1 & x & 0 & 1 & 0 & y \end{bmatrix} \{\alpha\} = \quad (31)$$

$$= \begin{bmatrix} 0 & 1 & 0 & y & 0 & 0 & 0 & 0 \\ 0 & 0 & 0 & 0 & 0 & 0 & 1 & x \\ 0 & 0 & 1 & x & 0 & 1 & 0 & y \end{bmatrix} [\Phi]^{-1} \{U\} = [B] \{U\},$$

where

$$[B] = \frac{1}{ab} \begin{bmatrix} y - \frac{b}{2} & 0 & \frac{b}{2} - y & 0 & \frac{b}{2} + y & 0 & -\frac{b}{2} - y & 0 \\ 0 & x - \frac{a}{2} & 0 & -\frac{a}{2} - x & 0 & \frac{a}{2} + x & 0 & \frac{a}{2} - x \\ x - \frac{a}{2} & y - \frac{b}{2} & -\frac{a}{2} - x & \frac{b}{2} - y & \frac{a}{2} + x & \frac{b}{2} + y & \frac{a}{2} - x & -\frac{b}{2} - y \end{bmatrix}. \quad (32)$$

Next, the relationships will be obtained that allow determining the stress-strain state in the plane of the column cross-section. To do this, the quantity  $\sigma_z$  should be excluded from equations (2)–(4). Substitution of the equation (6) into the equations in (2)–(3) leads to the following expressions:

$$\varepsilon_x = \frac{1}{E_1} (\sigma_x - \nu_1 \sigma_y) + \varepsilon_x^* - \nu (\varepsilon_z^0 + y\chi_1 + x\chi_2 - \varepsilon_z^*); \quad (33)$$

$$\varepsilon_y = \frac{1}{E_1} (\sigma_y - \nu_1 \sigma_x) + \varepsilon_y^* - \nu (\varepsilon_z^0 + y\chi_1 + x\chi_2 - \varepsilon_z^*), \quad (34)$$

where  $E_1 = E/(1-\nu)$ ,  $\nu_1 = \nu/(1-\nu)$ .

The equality in (5) can be represented as:

$$\gamma_{xy} = \frac{2(1+\nu_1)}{E_1} \tau_{xy} + \gamma_{xy}^*. \quad (35)$$

The stresses in the concrete core are expressed from (33)–(35) through the deformations in the form:

$$\sigma_x = \frac{E_1}{1-\nu_1^2} \left( \varepsilon_x + \nu_1 \varepsilon_y - (\varepsilon_x^* + \nu_1 \varepsilon_y^*) + \nu_1 (\varepsilon_z^0 + y\chi_1 + x\chi_2 - \varepsilon_z^*) \right); \quad (36)$$

$$\sigma_y = \frac{E_1}{1-\nu_1^2} \left( \varepsilon_y + \nu_1 \varepsilon_x - (\varepsilon_y^* + \nu_1 \varepsilon_x^*) + \nu_1 (\varepsilon_z^0 + y\chi_1 + x\chi_2 - \varepsilon_z^*) \right); \quad (37)$$

$$\tau_{xy} = \frac{E_1}{2(1+\nu_1)} (\gamma_{xy} - \gamma_{xy}^*). \quad (38)$$

Equalities (36)–(38) can be represented in matrix form:

$$\{\sigma\} = [D] \left( \{\varepsilon\} - \{\varepsilon^*\} \right) + \{\sigma_1\}, \quad (39)$$

$$\text{where } [D] = \frac{E_1}{1-\nu_1^2} \begin{bmatrix} 1 & \nu_1 & 0 \\ \nu_1 & 1 & 0 \\ 0 & 0 & \frac{1-\nu_1}{2} \end{bmatrix}, \quad \{\sigma\} = \begin{Bmatrix} \sigma_x \\ \sigma_y \\ \tau_{xy} \end{Bmatrix}, \quad \{\sigma\} = \begin{Bmatrix} \sigma_x \\ \sigma_y \\ \tau_{xy} \end{Bmatrix}, \quad \{\varepsilon\} = \begin{Bmatrix} \varepsilon_x \\ \varepsilon_y \\ \gamma_{xy} \end{Bmatrix}, \quad \{\varepsilon^*\} = \begin{Bmatrix} \varepsilon_x^* \\ \varepsilon_y^* \\ \gamma_{xy}^* \end{Bmatrix},$$

$$\{\sigma_1\} = \frac{E_1 \nu_1}{1-\nu_1^2} (\varepsilon_z^0 + y\chi_1 + x\chi_2 - \varepsilon_z^*) \begin{Bmatrix} 1 \\ 1 \\ 0 \end{Bmatrix}.$$

Formula (6) can be written as:

$$\sigma_z = E (\varepsilon_z^0 + y\chi_1 + x\chi_2 - \varepsilon_z^*) + \nu \{\sigma\}^T \begin{Bmatrix} 1 \\ 1 \\ 0 \end{Bmatrix}. \quad (40)$$

The resolving equations of the FE method for determining the stress-strain state in the plane of the cross section can be obtained based on the Lagrange variational principle. The potential strain energy of a CFST structure consists of the concrete core potential energy  $\Pi_b$  and the steel shell potential energy  $\Pi_s$ .

The value  $\Pi_b$  is determined by the formula:

$$\Pi_b = \frac{1}{2} \int_{A_b} (\sigma_x \varepsilon_x^{el} + \sigma_y \varepsilon_y^{el} + \tau_{xy} \gamma_{xy}^{el} + \sigma_z \varepsilon_z^{el}) dA. \quad (41)$$

The indices "el" in formula (41) correspond to elastic deformations. They are calculated as the difference between the total and forced deformations. The potential strain energy of the concrete core (41) can be represented as:

$$\Pi_b = \frac{1}{2} \int_{A_b} \sigma_z (\varepsilon_z^0 + y\chi_1 + x\chi_2 - \varepsilon_z^*) dA + \frac{1}{2} \int_{A_b} \{\sigma\}^T (\{\varepsilon\} - \{\varepsilon^*\}) dA. \quad (42)$$

The first integral in (42) can be represented in the following form:



$$\begin{aligned} \frac{1}{2} \int_{A_b} \sigma_z \left( \varepsilon_z^0 + y\chi_1 + x\chi_2 - \varepsilon_z^* \right) dA &= \frac{1}{2} \int_{A_b} E \left( \varepsilon_z^0 + y\chi_1 + x\chi_2 - \varepsilon_z^* \right)^2 dA + \\ &+ \frac{\nu}{2} \int_{A_b} \{\sigma\}^T \begin{Bmatrix} 1 \\ 1 \\ 0 \end{Bmatrix} \left( \varepsilon_z^0 + y\chi_1 + x\chi_2 - \varepsilon_z^* \right) dA. \end{aligned} \quad (43)$$

After differentiation with respect to the vector of nodal displacements  $\{U\}$  to find the minimum of the total energy, the first term in (43) vanishes. The second term in (43) can be written as:

$$\begin{aligned} &\frac{\nu}{2} \int_{A_b} \{\sigma\}^T \begin{Bmatrix} 1 \\ 1 \\ 0 \end{Bmatrix} \left( \varepsilon_z^0 + y\chi_1 + x\chi_2 - \varepsilon_z^* \right) dA = \\ &= \frac{\nu}{2} \int_{A_b} \left( \{\sigma_1\}^T + \left( \{\varepsilon\}^T - \{\varepsilon^*\}^T \right) [D] \right) \begin{Bmatrix} 1 \\ 1 \\ 0 \end{Bmatrix} \left( \varepsilon_z^0 + y\chi_1 + x\chi_2 - \varepsilon_z^* \right) dA = \\ &= \frac{\nu}{2} \left( \int_{A_b} \left( \{\sigma_1\}^T - \{\varepsilon^*\}^T [D] \right) \begin{Bmatrix} 1 \\ 1 \\ 0 \end{Bmatrix} \left( \varepsilon_z^0 + y\chi_1 + x\chi_2 - \varepsilon_z^* \right) dA + \right. \\ &\quad \left. + \int_{A_b} \{U\}^T [B]^T [D] \begin{Bmatrix} 1 \\ 1 \\ 0 \end{Bmatrix} \left( \varepsilon_z^0 + y\chi_1 + x\chi_2 - \varepsilon_z^* \right) dA \right). \end{aligned} \quad (44)$$

The first integral in (44) also vanishes when differentiated with respect to  $\{U\}$ . When calculating the second integral, the simplifying assumption is introduced that the forced deformation  $\varepsilon_z^*$  does not change within the FE. This hypothesis is justified if the FE mesh is dense enough. Taking into account the adopted simplification, the second integral in (43) is represented as:

$$\begin{aligned} &\frac{\nu}{2} \int_{A_b} \{U\}^T [B]^T [D] \begin{Bmatrix} 1 \\ 1 \\ 0 \end{Bmatrix} \left( \varepsilon_z^0 + y\chi_1 + x\chi_2 - \varepsilon_z^* \right) dA = \\ &= \frac{\nu}{2} \{U\}^T [B]^T [D] \begin{Bmatrix} 1 \\ 1 \\ 0 \end{Bmatrix} \left( \left( \varepsilon_z^0 - \varepsilon_z^* \right) A + \chi_1 \int_{A_b} y dA + \chi_2 \int_{A_b} x dA \right) = \\ &= \frac{1}{2} \{U\}^T [B]^T A_b \cdot \nu [D] \begin{Bmatrix} 1 \\ 1 \\ 0 \end{Bmatrix} \left( \varepsilon_z^0 + y_c \chi_1 + x_c \chi_2 - \varepsilon_z^* \right) = \\ &= \frac{1}{2} \{U\}^T [B]^T A_b \frac{E_1 \nu_1}{1 - \nu_1^2} \begin{Bmatrix} 1 \\ 1 \\ 0 \end{Bmatrix} \left( \varepsilon_z^0 + y_c \chi_1 + x_c \chi_2 - \varepsilon_z^* \right) = \frac{1}{2} \{U\}^T [B]^T A_b \{\sigma_1\}. \end{aligned} \quad (45)$$

Quantities  $x_c$  and  $y_c$  in formula (45) represent the coordinates of the FE center of gravity.

Let us further expand the second integral in (42):

$$\begin{aligned} \frac{1}{2} \int_{A_b} \{\sigma\}^T \{\varepsilon^{el}\} dA &= \frac{1}{2} \int_{A_b} \left[ \left( \{\varepsilon\}^T - \{\varepsilon^*\}^T \right) [D] + \{\sigma_1\}^T \right] \left( \{\varepsilon\} - \{\varepsilon^*\} \right) dA = \\ &= \frac{1}{2} \int_{A_b} \{\varepsilon\}^T [D] \{\varepsilon\} - 2 \{\varepsilon\}^T [D] \{\varepsilon^*\} + \{\varepsilon^*\}^T [D] \{\varepsilon^*\} + \{\sigma_1\}^T \{\varepsilon\} - \{\sigma_1\}^T \{\varepsilon^*\} dA. \end{aligned} \quad (46)$$

The terms  $\{\varepsilon^*\}^T [D] \{\varepsilon^*\}$  and  $\{\sigma_1\}^T \{\varepsilon^*\}$  vanish when differentiated with respect to the vector  $\{U\}$ . Let us separately expand the remaining terms:

$$\frac{1}{2} \int_{A_b} \{\varepsilon\}^T [D] \{\varepsilon\} dA = \frac{1}{2} \{U\}^T [B]^T [D] [B] A_b \{U\} = \frac{1}{2} \{U\}^T [K_b] \{U\}, \quad (47)$$

where  $[K_b] = [B]^T [D] [B] A_b$  is the stiffness matrix of the concrete core FE.

$$\frac{1}{2} \int_{A_b} \{\sigma_1\}^T \{\varepsilon\} dA = \frac{1}{2} \int_{A_b} \{\varepsilon\}^T \{\sigma_1\} dA = \frac{1}{2} \{U\}^T [B]^T \{\sigma_1\} A_b; \quad (48)$$

$$\int_{A_b} \{\varepsilon\}^T [D] \{\varepsilon^*\} dA = \{U\}^T [B]^T [D] \{\varepsilon^*\} A_b = \{U\}^T \{F^*\}. \quad (49)$$

Steel shell is assumed to operate under momentless stress conditions, i.e. the FEs of the steel shell have only translational degrees of freedom, and rotational degrees of freedom are neglected. This hypothesis is valid for all points except corner zones in the absence of corner rounding. Real rectangular pipes have corner rounding, so this hypothesis can be considered for all points of the pipe. A linear approximation is adopted for axial displacements  $u$  of the shell FE:

$$u(s) = u_1 + \frac{u_2 - u_1}{l} s. \quad (50)$$

The circumferential deformation of the steel pipe is determined as the derivative of the displacement:

$$\varepsilon_{s\theta} = \frac{du}{ds} = \left[ -\frac{1}{l} \frac{1}{l} \right] \begin{Bmatrix} u_1 \\ u_2 \end{Bmatrix} = [B_s] \{U_s\}. \quad (51)$$

The stresses in the steel shell can be written based on (9)–(11) as:

$$\sigma_{s\theta} = \frac{E_s}{1 - \nu_s^2} \left( \varepsilon_{s\theta} + \nu_s \left( \varepsilon_z^0 + y_s \chi_1 + x_s \chi_2 \right) \right); \quad (52)$$

$$\sigma_{sz} = \frac{E_s}{1 - \nu_s^2} \left( \varepsilon_z^0 + y_s \chi_1 + x_s \chi_2 + \nu_s \varepsilon_{s\theta} \right). \quad (53)$$

Coordinates  $x_s$  and  $y_s$  change within the FE, but for simplicity it is proposed to calculate them at the FE center of gravity. The potential strain energy of the steel shell FE is determined as follows:

$$\Pi_s = \frac{1}{2} \left( \delta \int_0^l \sigma_{s\theta} \varepsilon_{s\theta} ds + \delta \int_0^l \sigma_{sz} \varepsilon_{sz} ds \right). \quad (54)$$

Let us expand the first integral in (54):

$$\begin{aligned}
\int_0^l \sigma_{s\theta} \varepsilon_{s\theta} ds &= \frac{E_s}{1-\nu_s^2} \int_0^l \left( \{U_s\}^T [B_s]^T + \nu_s \left( \varepsilon_z^0 + y_s \chi_1 + x_s \chi_2 \right) \right) [B_s] \{U_s\} ds = \\
&= \frac{E_s l}{1-\nu_s^2} \{U_s\}^T [B_s]^T [B_s] \{U_s\} + \frac{E_s \nu_s l}{1-\nu_s^2} \left( \varepsilon_z^0 + y_s \chi_1 + x_s \chi_2 \right) [B_s] \{U_s\} = \\
&= \frac{1}{\delta} \left( \{U_s\}^T [K_s] \{U_s\} + \{U_s\}^T [B_s]^T \frac{E_s \nu_s l}{1-\nu_s^2} \left( \varepsilon_z^0 + y_s \chi_1 + x_s \chi_2 \right) \right),
\end{aligned} \quad (55)$$

where  $[K_s] = \frac{E_s \delta l}{1-\nu_s^2} [B_s]^T [B_s] = \frac{E_s \delta}{l(1-\nu_s^2)} \begin{bmatrix} 1 & -1 \\ -1 & 1 \end{bmatrix}$  is the stiffness matrix of the steel shell FE.

Next, we expand the second integral in (54):

$$\begin{aligned}
\int_0^l \sigma_{sz} \varepsilon_{sz} ds &= \frac{E_s}{1-\nu_s^2} \int_0^l \left( \varepsilon_z^0 + y_s \chi_1 + x_s \chi_2 + \nu_s \{U_s\}^T [B_s]^T \right) \left( \varepsilon_z^0 + y_s \chi_1 + x_s \chi_2 \right) ds = \\
&= \frac{E_s}{1-\nu_s^2} \left( \int_0^l \left( \varepsilon_z^0 + y_s \chi_1 + x_s \chi_2 \right)^2 ds + \nu_s \int_0^l \left( \varepsilon_z^0 + y_s \chi_1 + x_s \chi_2 \right) [B_s] \{U_s\} ds \right).
\end{aligned} \quad (56)$$

The first integral in (56) vanishes after differentiation with respect to the vector of nodal displacements  $\{U\}$ . The second integral in (56) can be written in the following form:

$$\frac{E_s \nu_s}{1-\nu_s^2} \int_0^l \left( \varepsilon_z^0 + y_s \chi_1 + x_s \chi_2 \right) [B_s] \{U_s\} ds = \{U_s\}^T [B_s]^T \frac{E_s \nu_s l}{1-\nu_s^2} \left( \varepsilon_z^0 + y_s \chi_1 + x_s \chi_2 \right). \quad (57)$$

The work of external loads on the column displacements in the  $xy$  plane is equal to zero. Consequently, the Lagrange functional for the problem under consideration is equivalent to the potential strain energy. Differentiation of the expression for the potential strain energy by the vector of nodal displacements  $\{U\}$  leads to the following system of equations:

$$[K] \{U\} + \{F_b\} + \{F_s\} - \{F^*\} = 0, \quad (58)$$

where  $[K] = [K_b] + [K_s]$ ,

$$\{F_b\} = [B]^T \{\sigma_1\} A_b = [B]^T A_b \frac{E_1 \nu_1}{1-\nu_1^2} \left( \varepsilon_z^0 + y_s \chi_1 + x_s \chi_2 - \varepsilon_z^* \right) \begin{Bmatrix} 1 \\ 0 \end{Bmatrix}; \quad (59)$$

$$\{F_s\} = [B_s]^T \frac{E_s \delta \nu_s l}{1-\nu_s^2} \left( \varepsilon_z^0 + y_s \chi_1 + x_s \chi_2 \right). \quad (60)$$

The vector  $\{F_s\}$  in (60), as well as the matrix  $[K_s]$  in (55) are written in the local coordinate system of the steel shell FE. When forming the system of equations of the FE method for the entire section, it is necessary to transform matrices and vectors from local coordinate systems to the global one using the formulas:

$$\{\bar{U}\} = [L] \{U\}; \quad (61)$$

$$[K] = [L]^T [\bar{K}] [L]; \quad (62)$$

$$\{F\} = [L]^T \{\bar{F}\}; \quad (63)$$

$$[L] = \begin{bmatrix} \cos \alpha & \sin \alpha & 0 & 0 \\ 0 & 0 & \cos \alpha & \sin \alpha \end{bmatrix}. \quad (64)$$

The bar above the vectors and matrices in formulas (61)–(63) corresponds to the local coordinate system.

To take into account the thickness of the pipe wall when calculating the stiffness in formulas (17)–(25), matrices  $[K_s]$  and vectors  $\{F_s\}$ , nodal coordinates of the steel shell are reduced to the middle of the wall thickness according to the formulas:

$$x_p = x_b \cdot \frac{B - \delta}{B_b}; \quad (65)$$

$$y_p = y_b \cdot \frac{H - \delta}{H_b}, \quad (66)$$

where  $x_b$  and  $y_b$  are the coordinates of the node on the contour of the concrete core,  $x_p$  and  $y_p$  are the coordinates of the node on the center line of the pipe wall,  $B_b$  and  $H_b$  are the dimensions of the concrete core.

The system of equations (58) allows to calculate the stresses  $\sigma_x$ ,  $\sigma_y$ ,  $\tau_{xy}$ , as well as  $\sigma_{s\theta}$  in the plane of the cross section using the values of generalized deformations  $\varepsilon_z^0$ ,  $\chi_1$  and  $\chi_2$ .

The equations of the concrete deformation theory of plasticity by G.A. Geniyev [28] are used as a model of the material for concrete. In these equations, the dilation effect is taken into account by introducing the value of dilation deformation  $\varepsilon_d$ . The value  $\varepsilon_d$  is determined by the formula:

$$\varepsilon_d = -\frac{g_0 \Gamma^2}{3}, \quad (67)$$

where  $g_0$  is the dilation modulus,  $\Gamma = \sqrt{\frac{2}{3} \sqrt{(\varepsilon_1 - \varepsilon_2)^2 + (\varepsilon_2 - \varepsilon_3)^2 + (\varepsilon_1 - \varepsilon_3)^2}}$  is the intensity of shear deformations.

Dilatational deformation can be considered a special case of forced deformation ( $\varepsilon_x^* = \varepsilon_y^* = \varepsilon_z^* = \varepsilon_d$ ,  $\gamma_{xy}^* = 0$ ). The adopted stress-strain diagram for steel is a diagram of ideal elastic-plastic material with the Huber–Mises–Hencky yield criterion.

The calculation taking into account physical nonlinearity is performed according to a scheme with a stepwise increase in load in the following sequence:

1. At the first step of loading, the modulus of elasticity of concrete and steel are taken equal to the initial values corresponding to the elastic work of the material. Dilatational deformations are absent at the first step.

$$2. \text{ Cross-section stiffness matrix } [D_1] = \begin{bmatrix} EA & ES_x & ES_y \\ ES_x & EI_x & EI_{xy} \\ ES_y & EI_{xy} & EI_y \end{bmatrix} \text{ and vector } \begin{Bmatrix} \Delta N^* \\ \Delta M_x^* \\ \Delta M_y^* \end{Bmatrix} \text{ are calculated}$$

using formulas (12).

3. The increments of generalized deformations are determined by the formula:



$$\{\Delta\varepsilon\} = \begin{Bmatrix} \Delta\varepsilon_z^0 \\ \Delta\chi_1 \\ \Delta\chi_2 \end{Bmatrix} = [D_1]^{-1} \cdot \{\Delta F\}, \quad (68)$$

$$\text{where } \{\Delta F\} = \begin{Bmatrix} \begin{Bmatrix} \Delta N \\ \Delta M_x \\ \Delta M_y \end{Bmatrix} + \begin{Bmatrix} \Delta N^* \\ \Delta M_x^* \\ \Delta M_y^* \end{Bmatrix} \end{Bmatrix}.$$

1. The stress-strain state in the plane of the cross section is determined based on the values of generalized deformations using the system of equations (58).
2. The tangential elastic moduli of concrete and steel are corrected based on the calculated stresses and deformations.
3. The corrected matrix  $[D_1']$  and the residual vector of forces  $\{\delta F\} = \{\Delta F\} - [D_1']\{\Delta\varepsilon\}$  are calculated.
4. Vector of additional deformations  $\{\delta\varepsilon\} = [D_1']^{-1}\{\delta F\}$  caused by the discrepancy of forces is determined.
5. The vector  $\{\Delta\varepsilon\}$  is corrected according to the formula  $\{\Delta\varepsilon\} := \{\Delta\varepsilon\} + \{\delta\varepsilon\}$ .
6. Steps 3–6 are repeated in approximations from the second to  $j_{\max}$ , where  $j_{\max}$  is the maximum number of iterations. Starting from the second iteration, convergence is controlled using the formula:

$$\frac{\|\{\delta\varepsilon_j\} - \{\delta\varepsilon_{j-1}\}\|}{\|\{\delta\varepsilon_j\}\|} \cdot 100\% < 0.1\%, \quad (69)$$

where  $\|\{a\}\| = \sqrt{\{a\}^T \{a\}}$  is the vector norm.

Each loading step ends with the calculation of total deformations and stresses, as well as recalculation of stiffness matrices.

The described calculation algorithm was implemented by the authors in the MATLAB environment.

### 3. Results and Discussion

At the first stage, the developed method was compared in an elastic setting with the results of a three-dimensional analysis in the ANSYS 2021R1 software package. The eccentrically compressed CFST column with the cross-sectional size of 300×200 mm, length of 2000 mm, and wall thickness of 5.73 mm was considered. A concentrated force  $F = 1$  kN was applied at the corner of the cross-section (Fig. 3). The column had a fixed support at the bottom. To eliminate local effects at the upper end caused by the action of the concentrated force, the 10 mm thick metal rigid plate was installed on top, which in ANSYS Workbench was set as “Surface Coating”. Surface Coating objects are the shell FEs whose nodes coincide with the nodes of volumetric FEs located on the surface of the concrete core. Stiffness behavior for the plate on the upper end was taken as “Membrane and Bending”. The steel pipe was also modeled with “Surface Coating” objects with stiffness behavior “Membrane Only”. This stiffness behaviour was adopted to eliminate local effects caused by bending moments at the corners of the rectangular tube. The concrete core was modeled using FEs in the form of parallelepipeds. The FE mesh size was taken to be 10 mm.

Since the steel pipe was defined by “Surface Coating” objects, then when modeling using the author's method, it was simply assumed that  $B = B_b$ ,  $H = H_b$ , and formulas (42) were not used.

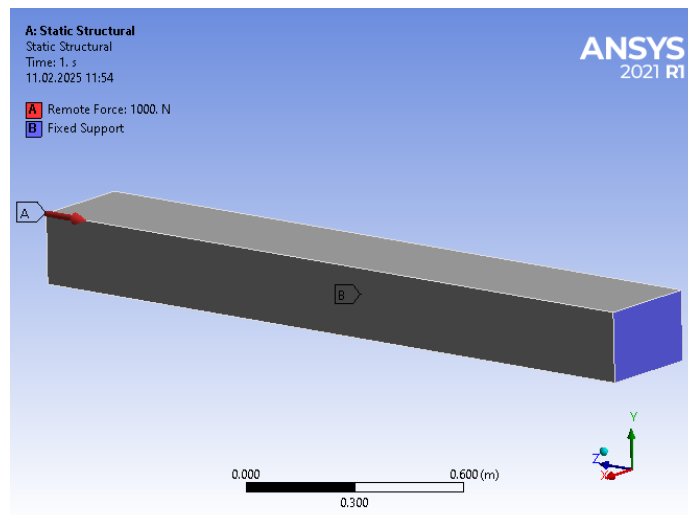


**Figure 3. Calculation scheme in ANSYS.**

Figs. 4, 5 show the stresses  $\sigma_z$  isofields for concrete in the middle section ( $z = L/2$ ), obtained as a result of three-dimensional modeling in ANSYS and using a simplified method proposed by the authors. The highest tensile stresses were 32.16 kPa when calculated in ANSYS and 32.58 kPa when calculated using the author's method. The highest compressive stresses were 52.08 kPa when calculated in ANSYS and 52.04 kPa when calculated using the author's method.

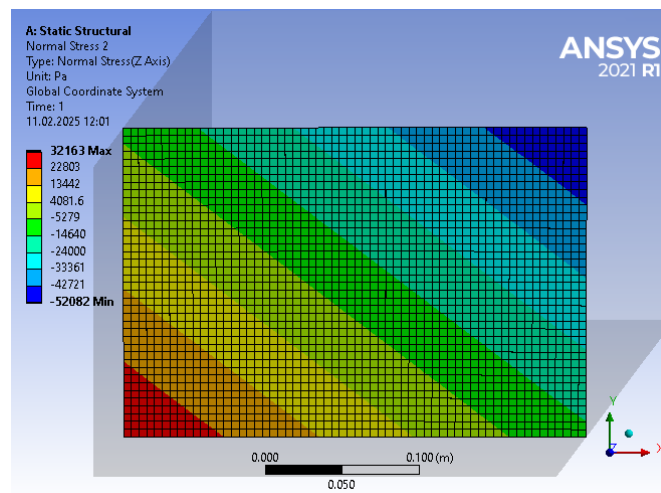


**Figure 4. Stress isofields  $\sigma_z$  (Pa) in ANSYS.**

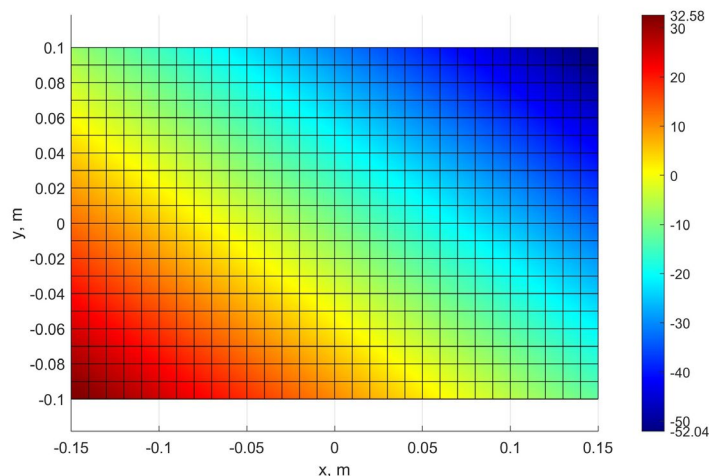


**Figure 5. Isofields of stresses  $\sigma_z$  (kPa), obtained using the author's method.**

Figs. 6, 7 show the stresses  $\sigma_x$  isofields in concrete obtained as a result of calculation in ANSYS and according to the author's method. Figs. 8, 9 are the same for stresses  $\sigma_y$ . The maximum stress  $\sigma_x$  value was 5.68 kPa in ANSYS and 5.81 kPa according to the author's method. The minimum stress  $\sigma_x$  value was -3.55 kPa in ANSYS and -3.54 kPa according to the author's method. The maximum and minimum stresses  $\sigma_y$  in the calculation with ANSYS coincided with the maximum and minimum stresses  $\sigma_x$ . When calculating according to the author's method, the maximum stress  $\sigma_y$  was 5.75 kPa, and the minimum was -3.49 kPa.

Thus, the greatest deviation of the calculation results using the author's method from the results in ANSYS is 2.3 %, and the average deviation is 0.5 %.

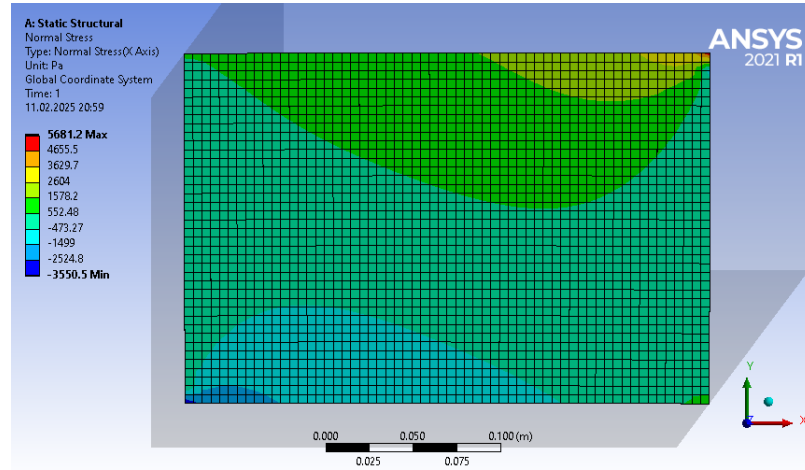


Figure 6. Isofields of stresses  $\sigma_x$  (Pa) in concrete core obtained in ANSYS.

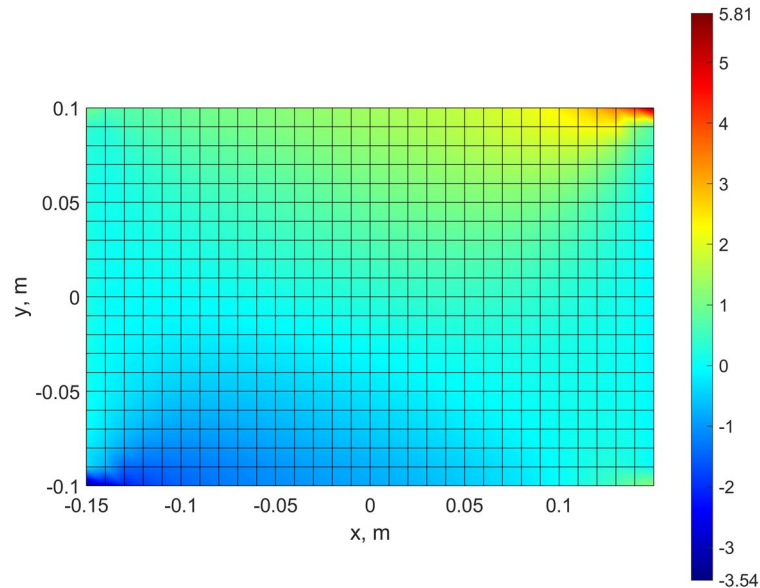


Figure 7. Isofields of stresses  $\sigma_x$  (kPa) in the concrete core, obtained using the author's method.

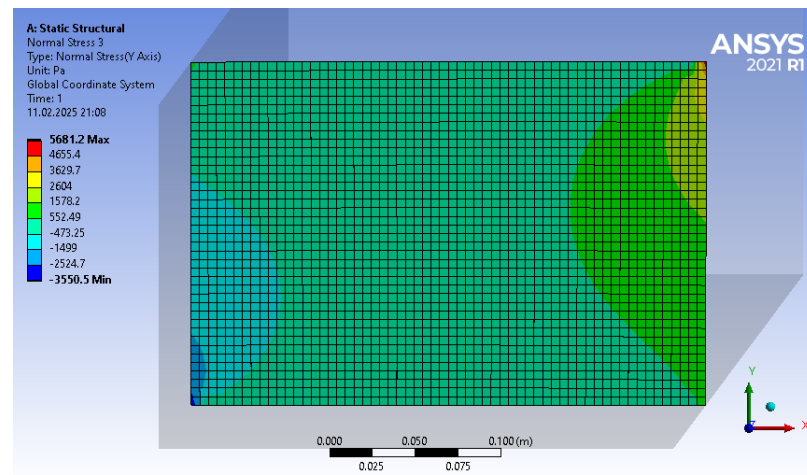


Figure 8. Isofields of stresses  $\sigma_y$  (Pa) in concrete core obtained in ANSYS.

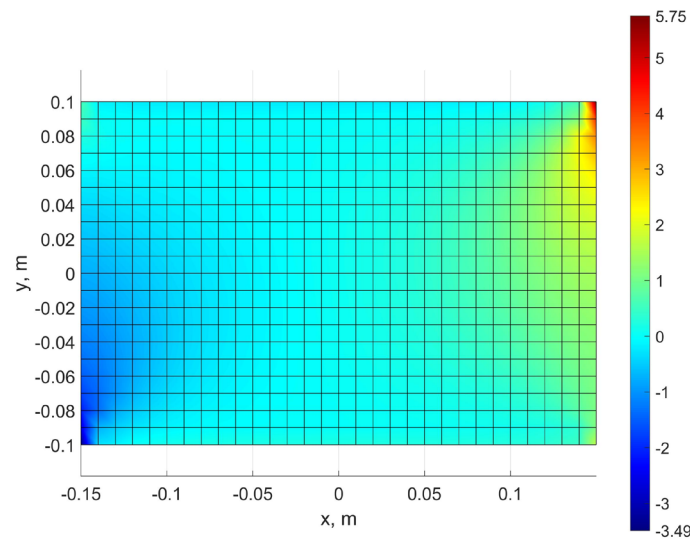


Figure 9. Isofields stresses  $\sigma_y$  (kPa) in the concrete core, obtained using the author's method.

The developed method was also tested on experimental data for 38 samples given in [29–31]. The experimental data included results for centrally compressed CFST columns, as well as for eccentrically compressed columns with eccentricity in one and two planes. Table 1 compares the calculation results according to the author's method in a physically nonlinear formulation with the experimental results. In this table,  $R_c$  is the compressive strength of concrete determined from tests of concrete cubes,  $N_{exp}$  and  $N_{calc}$  are respectively experimental and calculated values of the ultimate load.

**Table 1. Comparison of calculation results with experimental data.**

Sample	$B$ , mm	$H$ , mm	$t$ , mm	$R_c$ , MPa	$R_y$ , MPa	$e_x$ , mm	$e_y$ , mm	$N_{exp}$ , kN	$N_{calc}$ , kN
B. Uy, 2001 [29]									
HSS1	110	110	5	28	750	0	0	1836	1834
HSS2	110	110	5	28	750	0	0	1832	1834
HSS3	110	110	5	30	750	15	0	1555	1431
HSS4	110	110	5	30	750	30	0	1281	1153
HSS8	160	160	5	30	750	0	0	2868	2 806
HSS9	160	160	5	30	750	0	0	2922	2806
HSS10	160	160	5	30	750	25	0	2024	2105
HSS11	160	160	5	30	750	50	0	1979	1662
HSS14	210	210	5	32	750	0	0	3710	42 05
HSS15	210	210	5	32	750	0	0	3483	4205
HSS16	210	210	5	32	750	25	0	3106	3292
HSS17	210	210	5	32	750	50	0	2617	2669



Sample	$B$ , mm	$H$ , mm	$t$ , mm	$R_c$ , MPa	$R_y$ , MPa	$e_x$ , mm	$e_y$ , mm	$N_{exp}$ , kN	$N_{calc}$ , kN
Y. Yang et al., 2011 [30]									
Scfst-1	150	150	3	59.3	324	0	0	1618	1559
Scfst-2	150	150	3	59.3	324	15	0	1260	1260
Scfst-3	150	150	3	59.3	324	30	0	1244	1057
Scfst-4	150	150	3	59.3	324	15	15	1280	1195
Scfst-5	150	150	3	59.3	324	30	30	1193	925
Rcfst-1	180	120	3	59.3	324	0	0	1476	1517
Rcfst-2	180	120	3	59.3	324	36	0	1140	1020
Rcfst-3	180	120	3	59.3	324	18	12	1147	1160
Rcfst-4	180	120	3	59.3	324	36	24	939	900
X. Qu et al., 2013 [31]									
PYA-1	150	100	4.065	48.75	235	10	0	750	822
PYA-2	150	100	4.065	82.5	235	15	0	1040	1035
PYA-3	150	100	4.065	65	235	20	0	810	850
PYA-4	200	150	4.433	65	235	20	0	1750	1670
PYA-5	200	150	4.433	48.75	235	30	0	1250	1260
PYA-6	200	150	4.433	82.5	235	40	0	1400	1630
PYA-7	300	200	5.73	82.5	345	50	0	3450	3850
PYA-8	300	200	5.73	65	345	60	0	2650	3150
PYA-9	300	200	5.73	48.75	345	70	0	2445	2610
PYB-1	150	100	4.065	48.75	235	8.32	5.55	980	822
PYB-2	150	100	4.065	82.5	235	12.48	8.32	950	1039
PYB-3	150	100	4.065	65	235	16.64	11.09	980	838
PYB-4	200	150	4.433	65	235	16	12	1300	1683
PYB-5	200	150	4.433	48.75	235	24	18	1300	1275
PYB-6	200	150	4.433	82.5	235	32	24	1600	1588
PYB-7	300	200	5.73	82.5	345	38.41	32.01	3600	3740
PYB-8	300	200	5.73	65	345	46.09	38.41	2550	3020

The average value of the  $N_{calc}/N_{exp}$  ratio was 1.01, the maximum was 1.29, and the minimum was 0.78. The standard deviation was 0.11, and the coefficient of variation was 11 %.

#### 4. Conclusions

A simplified method for determining the bearing capacity of eccentrically compressed rectangular CFST columns in the presence of axial force eccentricities in two planes has been developed. The proposed method allows reducing the three-dimensional problem of determining the stress-strain state to a two-dimensional one, which ensures significant savings in machine time. This allows calculation in a physically nonlinear formulation not only for individual elements, but also for buildings that include CFST elements as a whole.

The verification of the developed method was performed by comparison with the results of FEA of the three-dimensional model in an elastic formulation in the ANSYS software package using volumetric FEs for concrete and shell FEs for a steel pipe. The maximum deviation of the results for stresses was 2.3 %. Validation of the developed method was performed using experimental data for 38 samples presented in three different works.

It should be noted that the proposed method does not allow for the slippage of concrete in the steel pipe, local stability loss of the pipe wall and the separation of the concrete core from the steel shell. The first two factors can be taken into account only when analyzing the column in a three-dimensional formulation, which is a very labor-intensive process and is not suitable for analyzing entire buildings. The third factor can be taken into account in the approach we propose. To implement this, the FEs of the steel pipe must be given a third bending degree of freedom, and one-way connections must be established between the nodes of the concrete and the steel shell that work only in compression. The development of the proposed model in this direction is a prospect for our further research.

## References

- Chen, Z., Ning, F., Song, C., Liang, Y. Study on axial compression bearing capacity of novel concrete-filled square steel tube columns. *Journal of Building Engineering*. 2022. 51. Article no. 104298. DOI: 10.1016/j.jobe.2022.104298
- Grzeszykowski, B., Szmigiera, E.D. Experimental Investigation on the Vertical Ductility of Rectangular CFST Columns Loaded Axially. *Materials*. 2022. 15(6). Article no. 2231. DOI: 10.3390/ma15062231
- Moradi, M.J., Daneshvar, K., Ghazi-Nader, D., Hajiloo, H. The prediction of fire performance of concrete-filled steel tubes (CFST) using artificial neural network. *Thin-Walled Structures*. 2021. 161. Article no. 107499. DOI: 10.1016/j.tws.2021.107499
- Ren, Z., Wang, D., Li, P. Axial compressive behaviour and confinement effect of round-ended rectangular CFST with different central angles. *Composite Structures*. 2022. 285. Article no. 115193. DOI: 10.1016/j.compstruct.2022.115193
- Remya, K.V., Prasad, R. Comparison of Seismic Performance of Different Irregular High Rise Structures with RCC and CFST Columns. *Lectures Notes in Civil Engineering*. 607. Proceedings of SECON'24 (SECON 2024). Pp. 623–644. DOI: 10.1007/978-3-031-70431-4\_45
- Jiao, C., Liu, W., Li, Y., Shi, W., Long, P. Experimental study of CFST embedded precast concrete bridge column-foundation connection with studs. *Soil Dynamics and Earthquake Engineering*. 2023. 168. Article no. 107826. DOI: 10.1016/j.soildyn.2023.107826
- Mander, J.B., Priestley, M.J., Park, R. Theoretical Stress-Strain Model for Confined Concrete. *Journal of Structural Engineering*. 1988. 114(8). Pp. 1804–1826. DOI: 10.1061/(ASCE)0733-9445(1988)114:8(1804)
- Yu, T.T.J.G., Teng, J.G., Wong, Y.L., Dong, S.L. Finite element modeling of confined concrete-I: Drucker-Prager type plasticity model. *Engineering Structures*. 2010. 32(3). Pp. 665–679. DOI: 10.1016/j.engstruct.2009.11.014
- Ding, F., Cao, Z., Lyu, F., Huang, S., Hu, M., Lin, Q. Practical design equations of the axial compressive capacity of circular CFST stub columns based on finite element model analysis incorporating constitutive models for high-strength materials. *Case Studies in Construction Materials*. 2022. 16. Article no. e01115. DOI: 10.1016/j.cscm.2022.e01115
- Sarir, P., Jiang, H., Asteris, P.G., Formisano, A., Armaghani, D.J. Iterative Finite Element Analysis of Concrete-Filled Steel Tube Columns Subjected to Axial Compression. *Buildings*. 2022. 12(12). Article no. 2071. DOI: 10.3390/buildings12122071
- Megahed, K., Mahmoud, N.S., Abd-Rabou, S.E.M. Finite Element Modeling for Concrete-Filled Steel Tube Stub Columns under Axial Compression. *International Journal of Steel Structures*. 2024. 24(5). Pp. 1229–1250. DOI: 10.1007/s13296-024-00896-7
- Wang, F.C., Xie, W.Q., Li, B., Han, L.H. Experimental study and design of bond behavior in concrete-filled steel tubes (CFST). *Engineering Structures*. 2022. 268. Article no. 114750. DOI: 10.1016/j.engstruct.2022.114750
- Wang, S., Wang, W., Xie, Z. Nonlinear cyclic behavior of steel tube in concrete-filled steel tube members including local buckling. *Thin-Walled Structures*. 2023. 191. Article no. 111055. DOI: 10.1016/j.tws.2023.111055
- Ahmed, M., Sheikh, M.N., Hadi, M.N., Liang, Q.Q. Nonlinear analysis of square spiral-confined reinforced concrete-filled steel tubular short columns incorporating novel confinement model and interaction local buckling. *Engineering Structures*. 2023. 274. Article no. 115168. DOI: 10.1016/j.engstruct.2022.115168
- Almasabha, G., Ramadan, M. Finite Element Modelling of Circular Concrete-Filled Steel Tubular Columns Under Quasi-Static Axial Compression Loading. *Journal of Composites Science*. 2024. 8(11). Article no. 472. DOI: 10.3390/jcs8110472
- Nakahara, H., Uchida, K., Yanai, Y. Test and Analysis for Shearing Behavior of Circular CFST Columns. *Buildings*. 2024. 14(12). Article no. 3871. DOI: 10.3390/buildings14123871
- Yadav, R., Chen, B. Parametric Study on the Axial Behaviour of Concrete Filled Steel Tube (CFST) Columns. *American Journal of Applied Scientific Research*. 2017. 3(4). Pp. 37–41. DOI: 10.11648/j.ajasr.20170304.11
- Manikandan, K.B., Umarani, C. Parametric study of CFST columns by numerical mock-up. *Materials Today: Proceedings*. 2021. 45(7). Pp. 6021–6027. DOI: 10.1016/j.matpr.2020.09.532
- Xu, L., Pan, J., Yang, X. Mechanical performance of self-stressing CFST columns under uniaxial compression. *Journal of Building Engineering*. 2021. 44. Article no. 103366. DOI: 10.1016/j.jobe.2021.103366
- Reddy, G.S.R., Bolla, M., Patton, M.L., Adak, D. Comparative study on structural behaviour of circular and square section-Concrete Filled Steel Tube (CFST) and Reinforced Cement Concrete (RCC) stub column. *Structures*. 2021. 29. Pp. 2067–2081. DOI: 10.1016/j.istruc.2020.12.078
- Erdoğan, A., Güneyisi, E.M., İpek, S. Finite Element Modelling of Ultimate Strength of CFST Column and Its Comparison with Design Codes. *Bilecik Şeyh Edebali Üniversitesi Fen Bilimleri Dergisi*. 2022. 9(1). Pp. 324–339. DOI: 10.35193/bseufbd.1033827
- Hou, C., Zhou, X.G. Strength prediction of circular CFST columns through advanced machine learning methods. *Journal of Building Engineering*. 2022. 51. Article no. 104289. DOI: 10.1016/j.jobe.2022.104289
- Le, T.T. Practical machine learning-based prediction model for axial capacity of square CFST columns. *Mechanics of Advanced Materials and Structures*. 2022. 29(12). Pp. 1782–1797. DOI: 10.1080/15376494.2020.1839608
- Zarringol, M., Thai, H.T. Prediction of the load-shortening curve of CFST columns using ANN-based models. *Journal of Building Engineering*. 2022. 51. Article no. 104279. DOI: 10.1016/j.jobe.2022.104279
- Đorđević, F., Kostić, S.M. Practical ANN prediction models for the axial capacity of square CFST columns. *Journal of Big Data*. 2023. 10(1). Article no. 67. DOI: 10.1186/s40537-023-00739-y
- Chepurmenko, A.S., Turina, V.S., Akopyan, V.F. Artificial Intelligence Model for Predicting the Load-Bearing Capacity of Eccentrically Compressed Short Concrete Filled Steel Tubular Columns. *Construction Materials and Products*. 2024. 7(2). Article no. 2. DOI: 10.58224/2618-7183-2024-7-2-2
- Chepurmenko, A., Yazyev, B., Meskhi, B., Beskopylny, A., Khashkhozhev, K., Chepurmenko, V. Simplified 2D Finite Element Model for Calculation of the Bearing Capacity of Eccentrically Compressed Concrete-Filled Steel Tubular Columns. *Applied Sciences*. 2021. 11(24). Article no. 11645. DOI: 10.3390/app112411645
- Litvinov, S.V., Yazyev, B.M., Kuznetsov, V.V., Belyugin, N.V., Avakov, A.A. Study of the concordance between various concrete deformation models and experimental data for uniaxial compression cases. *Construction Materials and Products*. 2024. 7(6). Article no. 6. DOI: 10.58224/2618-7183-2024-7-5-6
- Uy, B. Strength of short concrete filled high strength steel box columns. *Journal of Constructional Steel Research*. 2001. 57(2). Pp. 113–134. DOI: 10.1016/S0143-974X(00)00014-6

30. Yang, Y.F., Han, L.H. Behaviour of concrete filled steel tubular (CFST) stub columns under eccentric partial compression. *Thin-Walled Structures*. 2011. 49(2). Pp. 379–395. DOI: 10.1016/j.tws.2010.09.024
31. Qu, X., Chen, Z., Sun, G. Experimental study of rectangular CFST columns subjected to eccentric loading. *Thin-Walled Structures*. 2013. 64. Pp. 83–93. DOI: 10.1016/j.tws.2012.12.006

**Information about the authors:**

**Anton Chepurnenko**, Doctor of Technical Sciences

ORCID: <https://orcid.org/0000-0002-9133-8546>

E-mail: [anton\\_chepurnenk@mail.ru](mailto:anton_chepurnenk@mail.ru)

**Batyr Yazyev**, Doctor of Technical Sciences

ORCID: <https://orcid.org/0000-0002-5205-1446>

E-mail: [ps62@yandex.ru](mailto:ps62@yandex.ru)

**Samir Al-Zgul**,

ORCID: <https://orcid.org/0000-0001-6182-786X>

E-mail: [samiralzgulfx@gmail.com](mailto:samiralzgulfx@gmail.com)

**Vasilina Tyurina**, PhD in Technical Sciences

ORCID: <https://orcid.org/0009-0001-6399-401X>

E-mail: [vasilina.93@mail.ru](mailto:vasilina.93@mail.ru)

Received 21.01.2025. Approved after reviewing 23.03.2025. Accepted 23.03.2025.



Research article

UDC 69

DOI: 10.34910/MCE.134.7



## Bending of orthotropic scalene triangle plates: finite difference modeling

M.S. Beketova<sup>1</sup> , Zh. Nuguzhinov<sup>2</sup> , V.I. Travush<sup>3</sup> , N.I. Vatin<sup>4</sup> ,  
S.K. Akhmediyev<sup>1</sup> , I.A. Kurokhtina<sup>1</sup> , R.A. Shagiyeva<sup>5</sup> , V.F. Mikhailov<sup>1</sup> ,  
O. Khabidolda<sup>6</sup>

<sup>1</sup> Abylkas Saginov Karaganda Technical University, Karaganda, Republic of Kazakhstan

<sup>2</sup> Kazakhstan Multidisciplinary Institute of Reconstruction and Development Republican State Enterprise on the Right of Economic Use, Karaganda, Republic of Kazakhstan

<sup>3</sup> GORPROJECT, Moscow, Russian Federation

<sup>4</sup> Peter the Great St. Petersburg Polytechnic University, St. Petersburg, Russian Federation

<sup>5</sup> Toraighyrov University, Pavlodar, Republic of Kazakhstan

<sup>6</sup> Karaganda University named after E.A. Buketov, Karaganda, Republic of Kazakhstan  
 [vatin@mail.ru](mailto:vatin@mail.ru)

**Keywords:** orthotropic material, triangular plate, finite difference method, triangular grid, deflections and forces in the middle surface

**Abstract.** The object of the study is a transversely bent triangular plate made of an orthotropic material, fixed along the edges of the plate, under the action of a uniformly distributed load. The fourth-order differential equilibrium equations with variable orthotropy parameters were used. The equations were approximated by finite differences for a grid of scalene triangles. Such a grid describes well the boundary contour of triangular plates. The boundary conditions for the grid were written taking into account the orthotropy of the plate material. Seven typical finite difference equations were developed taking into account the boundary conditions along three edges of the plate and the presence of three angles of an irregular triangle. A finite difference matrix was obtained. The matrix structure allows calculating a triangular plate at different angles at the base. It is possible to vary the boundary conditions in the form of rigid or hinged support of the triangular plates. The calculation method takes into account the parameters of the orthotropy of the material in two mutually perpendicular planes. The adaptation of the numerical method to the calculation of orthotropic plates of arbitrary shape was described. The relationships for determining the rigidity characteristics of orthotropic materials were given. An algorithm for simple engineering calculation of triangular orthotropic plates was proposed that allowed performing accurate calculations in variant design. The scientific and applied results of the proposed article will find wide application in mechanics of deformable solids in the field of studying two-dimensional thin-walled structures, as well as in calculating plates of complex geometry with non-uniform mechanical characteristics of their materials.

**Funding:** This research was funded by the Ministry of Science and Higher Education of the Russian Federation within the framework of the state assignment No 075-03-2025-256 dated 16 January 2025, Additional agreement No 075-03-2025-256/1 dated 25 March 2025, FSEG-2025-0008

**Citation:** Beketova, M.S., Nuguzhinov, Zh., Travush, V.I., Vatin, N.I., Akhmediyev, S.K., Kurokhtina, I.A., Shagiyeva, R.A., Mikhailov, V.F., Khabidolda, O. Bending of orthotropic scalene triangle plates: finite difference modeling. Magazine of Civil Engineering. 2025. 18(2). Article no. 13407. DOI: 10.34910/MCE.134.7



## 1. Introduction

In various branches of technology (construction, mechanical engineering, aircraft building, and shipbuilding), orthotropic plates are widely used, in which the physical and mechanical characteristics of materials are symmetrical about three mutually perpendicular planes (wood, plywood, reinforced concrete). Many designs also have orthotropic properties, for example, corrugated and ribbed plates. A lot of works are dealing with studying orthotropic plates. Recent works include [1–3].

A study [4] showed that the general anisotropic property and the variable in-plane stiffness property inherent in composites create significant challenges in the static and dynamic analysis of these new types of variable stiffness composite structures. Therefore, it is important to develop mechanical models and calculation methods for composite lamellar-shell structures of variable stiffness to understand their complex mechanical mechanisms and promote their further application in aerospace engineering.

Publications devoted to triangular orthotropic plates appear much less frequently. In one of the first such publications [5], large amplitude oscillations of right triangular anisotropic plates were analyzed based on von Kármán governing equations. Utilizing the Bubnov–Galerkin procedure, a nonlinear second-order differential equation for the unknown time function was drawn. The equation was solved in terms of Jacobian elliptic functions.

Vibration analysis and multi-objective optimization of stiffened triangular plate was done in [6]. The triangular plate included stiffeners (ribs), which were parallel to each other and parallel to one edge of the triangle. The governing equation of transversal deflection of the plate was obtained by considering the effects of orthotropic characteristics and external excitation. The ordinary differential equation for the system's time response was obtained using the Bubnov–Galerkin method. In the next step, a multi-objective optimization was carried out considering two conflicting objective functions, i.e., maximizing the system's nonlinearity and minimizing the amplitude of vibration. Four decision variables were considered, including the plate's thickness, geometry, and the distance of the stiffeners. Finally, the effects of different parameters on the optimal solutions and the distribution of decision variables were investigated.

The buckling analysis of general triangular anisotropic plates with different boundary conditions subjected to combined in-plane loads was considered in [7, 8]. Solutions for plate buckling were obtained using the Rayleigh–Ritz method combined with a variational formulation. The numerical results were obtained for various triangular geometries with isotropic and anisotropic material properties. The effect of transverse-shear deformation was studied for different triangular geometries. The results confirm the importance of including the effect of transverse-shear deformation in the buckling analysis of composite plates. These results were later used in [9, 10] for optimal design of composite grid-stiffened aircraft panels subjected to global and local buckling constraints. The local buckling of aircraft skin segments is assessed with material anisotropy and transverse shear flexibility. The local buckling of stiffener segments was also assessed.

An accurate and simplified solution was provided in [11] for the free vibration problem of simply supported thin general triangular plates. The proposed method applies to thin plates with linear boundaries regardless of their geometrical shapes. The results were compared with previously published data for the isosceles and general triangles. Good agreements were reported. Although the paper deals only with simple support conditions, the article claims that any combination of classical boundary conditions, with or without complicating factors, can be handled.

The  $p$ -Ritz method operates with mathematically complete two-dimensional polynomial functions, and boundary polynomial equations raised to appropriate powers are used to approximate the displacements. In the [12], the  $p$ -Ritz method was used to derive the governing eigenvalue equation for the buckling behavior of triangular plates with both translational and rotational elastic edge constraints. The effect of elastic edge supports on the buckling factors for triangular plates of various vertex angles (aspect ratios) and boundary conditions was examined. The buckling solutions for isosceles and right-angled triangular plates with elastic edge constraints were presented.

The unilateral buckling behavior of point-restrained triangular plates was studied in [13]. The Rayleigh–Ritz method with polynomial-based shape functions was used to study the unilateral buckling behavior of triangular plates with various loading combinations, aspect ratios, boundary conditions, and point restraint configurations. Polynomials and tensionless foundation modeled the displacement functions and restraining medium, respectively. The results were obtained for different boundary conditions, aspect ratios, and various in-plane compressive and shear loadings. Convergence and comparison studies were undertaken to confirm the validity and precision of the solution method.

Free and forced multi-frequency vibrations of stiffened triangular plate with the stiffeners were studied in [14]. The governing motion equation for a triangular plate was developed based on the von Kármán theory. The nonlinear ordinary differential equation of the system using the Bubnov–Galerkin approach was

obtained. Closed-form expressions for the free undamped and large-amplitude vibration of an orthotropic triangular elastic plate were presented using two analytical methods, namely, the energy balance method [15] and the variation approach. It was demonstrated that those two methods were straightforward and reliable techniques for solving those nonlinear differential equations.

A nonlinear vibration of a triangular shape plate with several stiffeners was studied in [16]. The Bubnov–Galerkin method was used to obtain the ordinary differential equation for the system time response. A genetic-based multi-objective optimization was performed to find the geometry and locations of the plate stiffeners.

Three-dimensional structures in the form of triangular plates of thin and medium thickness with homogeneous and inhomogeneous characteristics of materials (isotropic and orthotropic) were considered in [17]. The finite difference method was applied using a grid of scalene triangles as a resolving method. Based on a numerical algorithm and the author's Fortran programs, the leading parameters were obtained from transverse and in-plane loads under various boundary conditions (in bending, buckling, and free oscillations).

In [18], free vibration characteristics of moderately thick composite materials triangular plates under multi-points support boundary conditions were analyzed. An improved Fourier series method was used. Energy equations were established based on the first-order shear deformation theory. The Rayleigh–Ritz technique was adopted to solve unknown coefficients of energy equations with the multi-point support boundary conditions. This study was aimed to simulate real engineering structures with multi-point support. It was shown that the method has a higher accuracy than the finite element method.

In-plane vibration of arbitrary laminated triangular plates with elastic boundary conditions was studied in [19] by the Chebyshev–Ritz method. The coordinate transformation mapped the arbitrarily shaped triangular laminated plate into a square plate to facilitate energy calculation. The displacement functions of the square plate after transformation were expressed as two-dimensional Chebyshev polynomials multiplied by coefficients. The arbitrary elastic boundary conditions of the plate were obtained by changing the stiffness values of each spring with artificial virtual spring technology. The in-plane free vibration characteristics of the triangular laminated plate under different boundary conditions were calculated. The accuracy of this method was verified by comparing with finite element results and experimental results. The comparison shows that the present method has good convergence and satisfactory actuarial accuracy.

The bending of cantilever triangular plates at the same inclination angles of the side edges to the base was investigated in [20]. The finite difference method was applied. Combining the results was applied to solve the problem of an acute angle at the top of the plate. The results of calculating a cantilever bar of variable bending stiffness were combined with similar results of calculating a triangular plate supported along the contour using a reduction factor. This study theoretical provisions and applied results could be partially used to investigate the bending of orthotropic scalene triangle plates supported along the edges.

The frequency and mode of free vibrations of thin isotropic triangular plates with a central hole for different boundary conditions were investigated in [21]. The finite element method was used. Some plates topology of vibration modes was compared to square plates with hinged and clamped edges. The numerical values of the natural frequencies and modes of triangular plates are in good agreement with the experimental results.

The simplistic superposition method was used for analytic free vibration solutions of right triangular plates [22]. The problem was solved by dividing it into three subproblems that were solved by the symplectic techniques via imposing the variable separation on the Hamiltonian-system-based governing equation and symplectic eigen expansion. Then, the analytic frequency and mode shape solutions were obtained by requiring the equivalence between the original problem and the superposition. The comparison with the numerical results for the right triangular plates confirmed the approach's convergence and accuracy.

In this case, the aim of this work is to develop and apply a rarely used and complex type of triangular grid of the finite difference method to plates of complex geometry, in particular for calculating the stress-strain state of triangular orthotropic plates with unequal values of angles at their vertices that has previously been insufficiently studied.

The objective of the study is to evaluate the stress-strain state of triangular orthotropic plates with different boundary conditions under different types of loads, to determine the dependence of the effect of the orthotropy coefficients of boundary conditions, the values of angles at the base on the strength parameters of the bearing capacity of triangular plates.

## 2. Methods

The object of the study is a transversely bent triangular plate made of orthotropic material, fixed along the edges of the plate, under the action of a uniformly distributed load. Fig. 1 shows the computational scheme of the triangular plate.

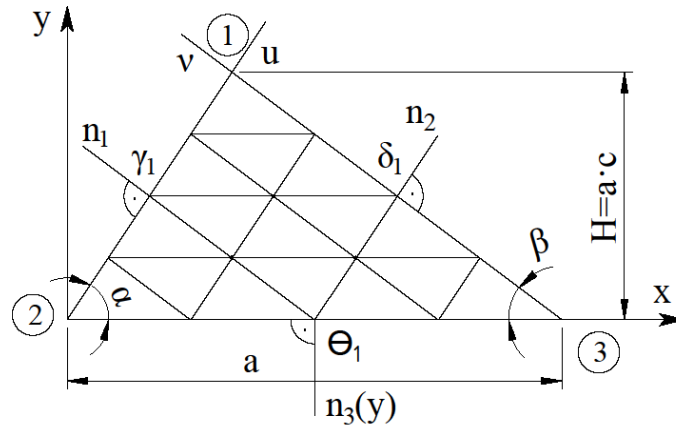


**Figure 1. Computational scheme of the triangular plate.**

The plate configuration is determined by three parameters:  $a$  is the base of the triangle (plate);  $\alpha$ ,  $\beta$  are the angles of inclination of the side edges to the base (in the general case,  $\alpha$  is not equal to  $\beta$ ). The study used the well-known initial differential equation for the bending of orthotropic plates [23–25], which has the form:

$$D_1 \frac{\partial^4 w}{\partial x^4} + 2D_3 \frac{\partial^4 w}{\partial x^2 \partial y^2} + 2D_2 \frac{\partial^4 w}{\partial y^4} = q, \quad (1)$$

where  $w = w(x, y)$  is the sought deflection function;  $q$  is the intensity of the stationary transverse distributed load in the plane of the plate;  $D_1$ ,  $D_2$ ,  $D_3$ ,  $D_k$  is the bending and torsional rigidity of the orthotropic material;  $x$ ,  $y$  are the Cartesian coordinates.

The bending and torsional rigidity of the orthotropic material is determined as follows:

$$D_1 = \frac{E_1 t^3}{12(1 - \nu_1 \nu_2)}; \quad D_2 = \frac{E_2 t^3}{12(1 - \nu_1 \nu_2)}; \quad (2)$$

$$D_3 = D_1 \cdot \nu_2 + 2D_k; \quad D_k = \frac{G t^3}{12}.$$

Here,  $E_1$ ,  $E_2$  is the modulus of elasticity of the material in two mutually perpendicular planes;  $\nu_1$ ,  $\nu_2$  are Poisson ratios in two mutually perpendicular planes;  $G$  is the shear modulus;  $D_k$  is the torsional bending rigidity;  $t$  is the thickness of the plate.

Then, the orthotropy coefficients were introduced:

$$\alpha_0 = \frac{2 \cdot D_3}{D_1}, \quad \beta_0 = \frac{D_2}{D_1}. \quad (3)$$

Equation (1), taking into account the accepted designations of (2) and (3), has the form:

$$\frac{\partial^4 w}{\partial x^4} + 2\alpha_0 \frac{\partial^4 w}{\partial x^2 \partial y^2} + \beta_0 \frac{\partial^4 w}{\partial y^4} = \frac{q}{D_1}. \quad (4)$$

Bending moments  $M_x$ ,  $M_y$  and torsional moment  $M_{xy}$ , taking into account the structure material orthotropy, have the form:

$$M_x = -D_1 \left( \nu_2 \frac{\partial^2 w}{\partial y^2} + \alpha_0 \frac{\partial^2 w}{\partial x^2} \right); \quad M_y = -D_1 \left( \nu_1 \frac{\partial^2 w}{\partial x^2} + \beta_0 \frac{\partial^2 w}{\partial y^2} \right);$$

$$M_{xy} = -D_k \frac{\partial^2 w}{\partial x \partial y}.$$
(5)

The boundary conditions of plates supported at the edges are written in the same way as for bending isotropic plates (with hinged or rigidly fixed plate edges):

$$w_i = 0; \quad M_{n_j} = 0; \quad \partial w_i / \partial n_j = 0,$$
(6)

where  $j$  in the edge number,  $n_j$  is the normal direction to the corresponding plate edges,  $M_{n_j}$  is the bending moment in the normal direction.

### 3. Results and Discussion

It is known that the finite difference method can be a preferred choice for problems on a uniform grid. To apply equation (4) to the bending analysis of a triangular orthotropic plate (Fig. 1), the finite difference method with a grid of scalene triangles is used. The grid of scalene triangles fits well into the oblique contour of the triangular plates. Fig. 2 shows a fragment of the grid of scalene triangles.

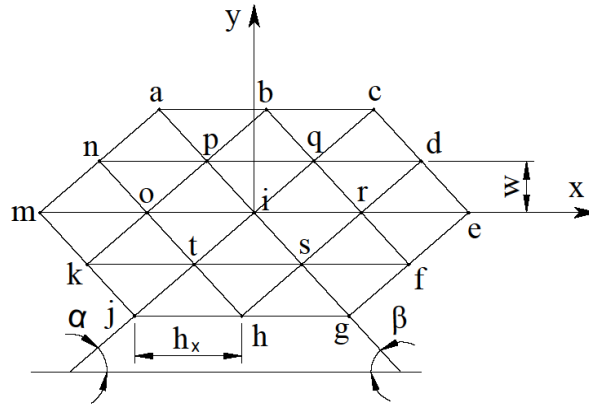


**Figure 2. A grid fragment of scalene triangles.**

To the  $i$ -th node of the grid of scalene triangles, equation (4) will have the form (without taking into account the boundary conditions) that is presented in work [17]:

$$\begin{aligned} & \psi_1 w_i + \psi_2 (w_o + w_r) + \psi_3 (w_p + w_s) + \psi_4 (w_q + w_t) + \\ & + \psi_5 (w_n + w_f) + \psi_6 (w_b + w_h) + \psi_7 (w_d + w_k) + \psi_8 (w_m + w_e) + \\ & + \psi_9 (w_a + w_g) + \psi_{10} (w_c + w_j) = \frac{q h y^4}{D_1}. \end{aligned}$$
(7)

Here, the grid parameters  $\psi_1, \psi_2, \psi_3, \psi_4, \psi_5, \psi_6, \psi_7, \psi_8, \psi_9, \psi_{10}$  are determined in such a way:

$$\begin{aligned} \psi_1 &= 6C^4 + \alpha_0 C^2 (-6AB + 4) + \beta_0 [4(AB - 1)^2 + 2(AB)^2 + 2A^2 + 2B^2]; \\ \psi_2 &= -4C^4 + \alpha_0 C^2 (4AB - 2) + \beta_0 [-4AB(AB - 1) + 2AB]; \\ \psi_3 &= \alpha_0 C^2 (B - 2A) + \beta_0 [4A(AB - 1) - 2A^2 B]; \quad \psi_5 = \alpha_0 C^2 + 2\beta_0 A^2 B; \\ \psi_6 &= 2\beta_0 AB; \quad \psi_7 = \alpha_0 C^2 B - 2\beta_0 AB^2; \quad \psi_8 = C^4 - \alpha_0 C^2 AB + \beta_0 (AB)^2; \\ \psi_9 &= \beta_0 A^2; \quad \psi_{10} = \beta_0 B^2. \end{aligned}$$
(8)



The angles  $\alpha$  and  $\beta$  define the parameters  $A$ ,  $B$ ,  $C$  and  $U$  :

$$A = \frac{\sin \beta \cos \alpha}{\sin(\alpha + \beta)}; \quad B = \frac{\sin \alpha \cos \beta}{\sin(\alpha + \beta)}; \quad C = \frac{\sin \alpha \sin \beta}{\sin(\alpha + \beta)}; \quad (9)$$

$$U = C^2 - AB.$$

The equation in the particular case for an isotropic plate for the  $i$ -th grid node is also written according to [17] in the following form:

$$\begin{aligned} & \varphi_1 w_1 + \varphi_2 (w_o + w_r) + \varphi_3 (w_p + w_s) + \varphi_4 (w_q + w_t) + \\ & + \varphi_5 (w_n + w_f) + \varphi_6 (w_b + w_h) + \varphi_7 (w_d + w_k) + \varphi_8 (w_m + w_e) + \\ & + \varphi_9 (w_a + w_g) + \varphi_{10} (w_c + w_j) = \frac{qhy^4}{D_1}, \end{aligned} \quad (10)$$

where

$$\begin{aligned} \varphi_1 &= 2 \left[ 2(U+1)^2 + A^2 + B^2 + U^2 \right]; \quad \varphi_2 = -2 \left[ 2U(U+1) - AB \right]; \\ \varphi_3 &= -2 \left[ 2A(U+1) - BU \right]; \quad \varphi_4 = -2 \left[ 2B(U+1) - AU \right]; \\ \varphi_5 &= 2AU; \quad \varphi_6 = 2AB; \quad \varphi_7 = 2BU; \quad \varphi_8 = U^2; \quad \varphi_9 = A^2; \quad \varphi_{10} = B^2. \end{aligned} \quad (11)$$

Thus, equations (7), (10) differ only in expressions (8), (11), respectively.

The original equation (1) must be accompanied by the corresponding boundary conditions at the edges of the plate. For continuously supported sides of the plate along the perimeter (Fig. 1), the boundary conditions are as follows:

$$w_i = 0; \quad \partial w_i / \partial n_j = 0; \quad \partial^2 w_i / \partial n_j^2 = 0, \quad (12)$$

where  $w_i$  is the deflection at the  $i$ -th node of the plate contour;  $n_j$  are the normals to the edges of the plate (Fig. 1);  $j = 1, 2$  are the numbers of the plate edges.

Boundary conditions (11) for the  $i$ -th grid node are written in the finite differences in the group form as follows:

- For the left edge of the plate (Fig. 3, a):

$$w_q = w_i = w_t = 0; \quad (\psi_8 w_o + 0.5\psi_7 w_p) = \gamma_1 (\psi_8 w_r + 0.5\psi_7 w_s); \quad (13)$$

- For the right edge of the plate (Fig. 3, b):

$$w_q = w_i = w_s = 0; \quad (\psi_8 w_r + 0.5\psi_5 w_q) = \delta_1 (\psi_8 w_o + 0.5\psi_5 w_t); \quad (14)$$

- For the plate base (Fig. 3, c):

$$w_o = w_i = w_r = 0; \quad (0.5\psi_7 w_s + 0.5\psi_5 w_t) = \theta_1 (0.5\psi_7 w_p + 0.5\psi_5 w_t). \quad (15)$$

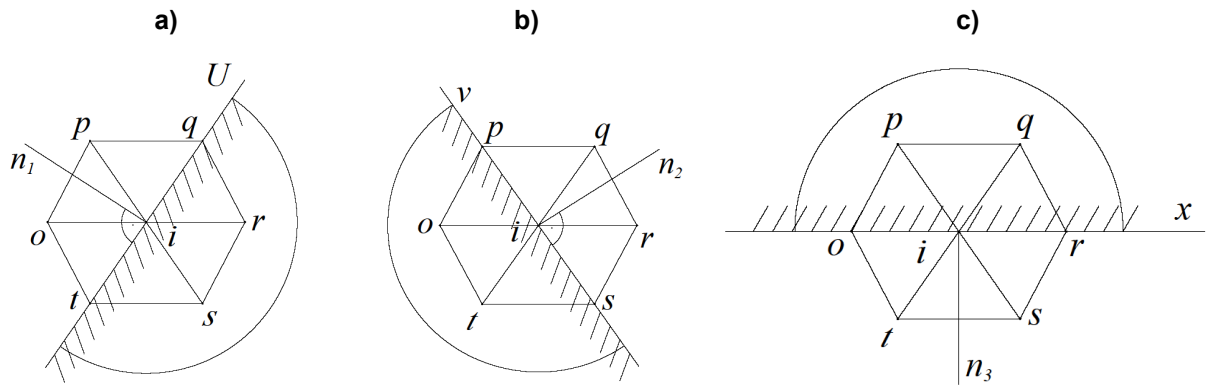


**Figure 3. Definition of boundary conditions: a) the left edge of the plate "1-2"; b) the right edge of the plate "1-3"; c) the base of the plate "2-3".**

The coefficients in expressions (13)–(15) took the following values:  $(\gamma_1 = \delta_1 = \theta_1) = -0.1$  for hinge-support edges of the plate;  $(\gamma_1 = \delta_1 = \theta_1) = +1.0$  for rigid edges of the plate.

Boundary conditions (13)–(15) modify the basic finite difference equation for orthotropic triangular plates (7) taking into account and takes the form of seven typical finite difference equations for seven characteristic grid nodes. Fig. 4 illustrates the numbering of typical grid equations.

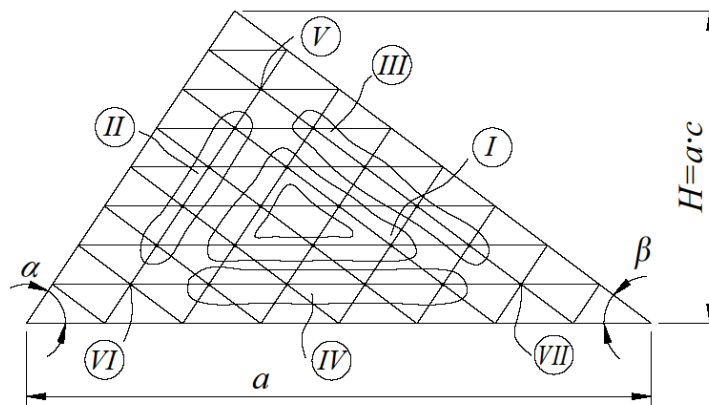


**Figure 4. Numbering of typical grid equations.**

With the triangular plate discretized into  $N$  grid divisions and continuous edge support along the perimeter, 21 calculation (intra-contour) nodes were obtained. Fig. 5 shows the numbering of some calculation nodes.

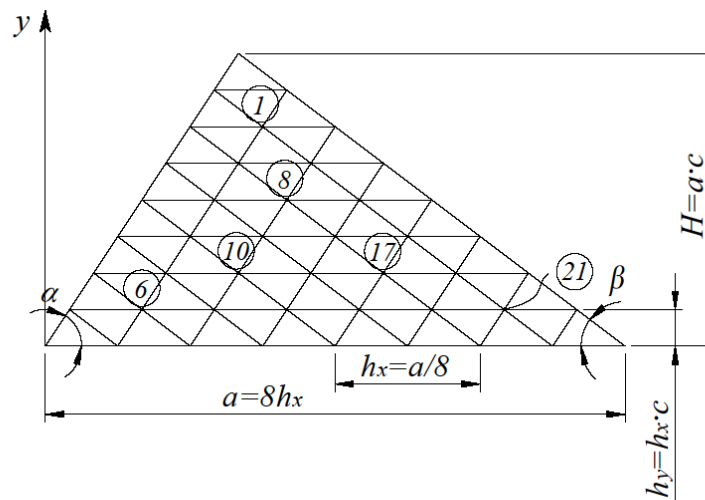


**Figure 5. Numbering of the analysis nodes of the triangular grid.**

The finite difference equations for all 21 computational nodes of the triangular grid (Fig. 5) constitute a system of linear algebraic equations of the 21<sup>st</sup> order, which in matrix form has the form:

$$\mathbf{D}_u \cdot \vec{\mathbf{w}} = \vec{\mathbf{P}}. \quad (16)$$

Here,  $\mathbf{D}_u$  is a square matrix of the 21<sup>st</sup> order;  $\vec{\mathbf{w}} = \{w_1, w_2, \dots, w_{21}\}$  is the vector of the sought deflections;  $\vec{\mathbf{P}} = \{P_1, P_2, \dots, P_{21}\}$  is the vector of free terms, taking into account the transverse load acting on the surface.

With uniform distribution of the intensity of the transverse distributed load  $q$  over the plate, there is:

$$P_i = qh_y^4/D_1, \quad (17)$$

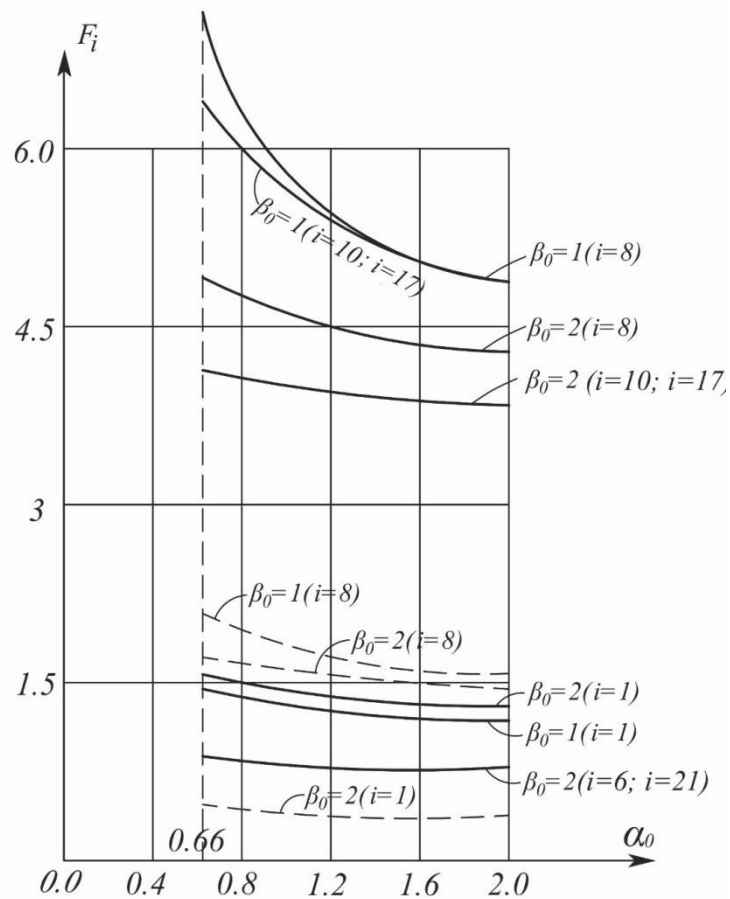
where  $D_1$  is accepted based on expression (3);  $h_y = AC/8$  is a grid step along the  $y$  axis (Fig. 5).

Thus, the algorithm for calculating orthotropic plates proposed by the authors consists of applying expressions (2), (3), (7)–(9), (13)–(15) to implement equation (16).

Using the SMATH Studio program [26, 27], a number of research problems were solved based on expression (16). There was studied the effect of the following:

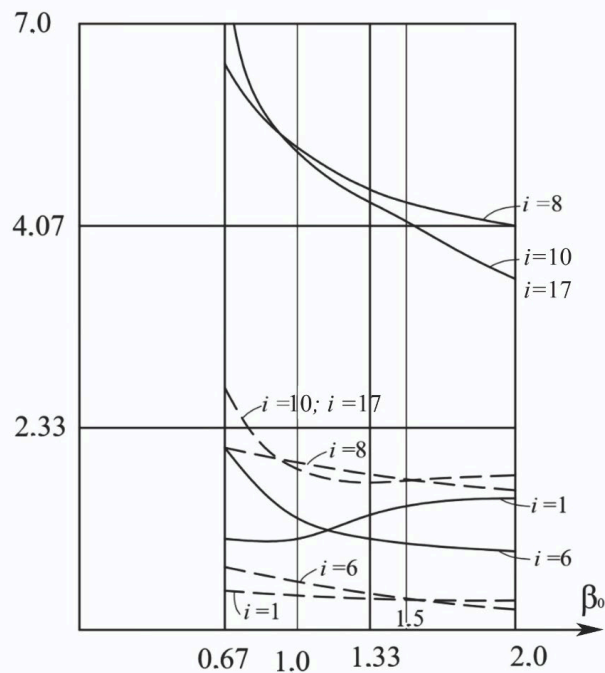
- the type of boundary conditions (using the  $\gamma_1, \delta_1, \theta_1$  coefficients);
- the plate geometry (setting the values of angles  $\alpha$  and  $\beta$  at the base of the plate);
- the orthotropy coefficients  $\alpha_0$  and  $\beta_0$  determined by formula (3), on the value of nodal deflections ( $w_i = 1, 2, \dots, 21$ ).

Figs. 6 and 7 show the graphical dependencies of the deflections at the grid nodes  $\delta = 1, 6, 8, 10, 17, 21$  (Fig. 5) for equilateral ( $\alpha = \beta = 60^\circ$ ) triangular orthotropic plates (with  $\alpha_0 = 0.66; 1; 1.5; 2.0$  and  $\beta_0 = 0.5; 1; 1.5; 2.0$ ) with rigid and hinged edges with the number of grid divisions  $N = 8$ .



— — — — — hinged support of the plate edges, \_ \_ \_ \_ \_ rigid support of the plate edges

Figure 6. Dependence of deflections at the nodes ( $i = 1, 8, 10, 17$ ) of triangular orthotropic plates with changing the orthotropy coefficients  $\alpha_0$ .



— — — — — hinged support of the plate edges, \_ \_ \_ \_ \_ rigid support of the plate edges.

Figure 7. Dependence of deflections at nodes ( $i = 1, 8, 10, 17$ ) of triangular orthotropic plates on the orthotropy coefficient  $\beta_0$  with a constant orthotropy coefficient  $\alpha_0 = 1$ .

Tables 1 and 2 present the results of numerical calculations of equilateral triangular plates with different edge fastening methods.

**Table 1. Deflections of nodes under different boundary conditions and orthotropy coefficients.**

Support type	$\beta_0$	$\alpha_0$	Deflections $\left( w_i \cdot 10^4 \frac{D_1}{qa^4} \right)$ of nodes					
			1	6	21	8	10	17
Hinged support around the perimeter, $\alpha = \beta = 60^\circ$ , $N = 8$	2	0.66	1.537	0.97	0.97	4.97	4.29	4.29
		1	1.44	0.92	0.92	4.68	4.07	4.07
		2	1.21	0.8	0.8	4.0	3.55	3.55
	1	0.66	1.45	1.58	1.58	6.36	6.21	6.21
		1	1.38	1.46	1.46	5.87	5.78	5.78
		1.5	1.288	1.317	1.317	5.28	5.25	5.25
	Isotropic material		2	1.202	1.202	1.202	4.807	4.807
Rigid support around the perimeter, $\alpha = \beta = 60^\circ$ , $N = 8$	2	0.66	0.38	0.22	0.22	1.698	1.33	1.33
		1	0.36	0.21	0.21	1.62	1.29	1.29
		2	0.31	0.18	0.18	1.42	1.17	1.17
	1	0.66	0.35	0.36	0.36	2.1	1.99	1.99
		1	0.33	0.34	0.34	1.98	1.9	1.9
		1.5	0.308	0.309	0.309	1.82	1.78	1.78
	Isotropic material		2	0.29	0.29	0.29	1.68	1.68

**Table 2. Deflections of nodes under different boundary conditions and orthotropy coefficient  $\beta_0$  and constant orthotropy coefficient  $\alpha_0$ .**

	$\beta_0$	$\alpha_0$	Deflections $\left( w_i \cdot 10^4 \frac{D_1}{qa^4} \right)$ of nodes					
			1	6	21	8	10	17
Hinged support around the perimeter, $\alpha = \beta = 60^\circ$ , $N = 8$	0.5	1	1.28	2.14	2.14	6.83	7.7	7.79
	1		1.38	1.46	1.46	5.87	5.78	5.78
	1.5		1.43	1.125	1.125	5.19	4.74	4.74
	2		1.44	0.92	0.92	4.68	4.07	4.07
Rigid support around the perimeter, $\alpha = \beta = 60^\circ$ , $N = 8$	0.5	1	0.3	0.5	0.5	2.21	2.63	2.63
	1		0.33	0.34	0.34	1.98	1.9	1.94
	1.5		0.35	0.257	0.257	1.777	1.526	4.526
	2		0.361	0.21	0.21	1.617	1.289	1.289

Based on the data of Tables 1 and 2, there can be concluded the following:

- with increasing the orthotropy coefficient  $\alpha_0$  (Fig. 6) for different  $\beta_0$  and different boundary conditions, the deflections in the calculated nodes decrease monotonically;
- with increasing the orthotropy coefficient  $\beta_0$  (Fig. 7) for constant values ( $\alpha_0 = 1 \approx \text{const}$ ), the deflections in the plate nodes change according to a complex relationship;
- for an equilateral isotropic triangular plate ( $\alpha_0 = 2$ ,  $\beta_0 = 1$ ), there are three axes of symmetry along its three medians. In this case, there is equality of deflections in nodes 1, 6, and 21;



- for equilateral orthotropic triangular plates, there is only one axis of elastic symmetry. This axis of symmetry is the  $y$ -axis. In this case, the deflections are equal only in nodes 6 and 21 (Figs. 6 and 7, Tables 1 and 2). To evaluate the grid convergence, this problem was solved for two numbers of partitions of the plate sides – 4, 8. The results were as follows:
- for the number of partitions  $N = 4$ , the deflection in the middle of the median of the triangle is 5.96;
- for the number of partitions  $N = 8$ , the deflection in the middle of the median of the triangle is 4.97;
- the resulting convergence graph (Fig. 8) was obtained using the Richardson extrapolation formula [28].

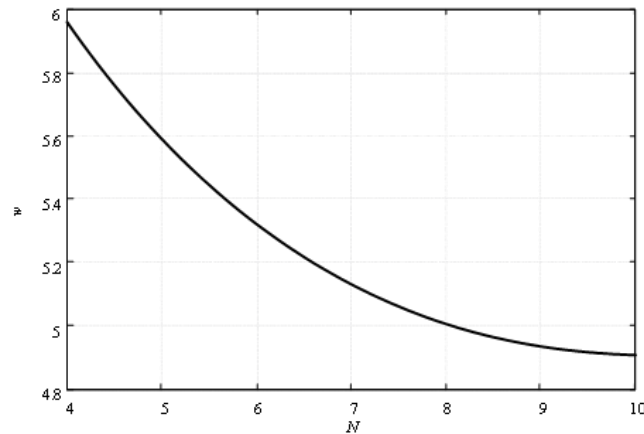


**Figure 8. The grid convergence graph.**

To assess reliability of the presented results, a finite element calculation was performed for an equilateral triangular plate with a hinged support along the perimeter in order to determine the deflection at node 8 (Fig. 5), if  $E_1 = 1.5 \cdot 10^{11}$  Pa,  $E_2 = 1.0 \cdot 10^{11}$  Pa,  $\nu_1 = 0.1$ ,  $\nu_2 = 0.2$ ,  $t = 2.5 \cdot 10^{-3}$  m,  $q = 1.0$  kPa. The following value of  $u = 2.584 \cdot 10^{-3}$  m was obtained. When switching to dimensionless coefficients, the deflection at node at  $\alpha_0 = 0.66$ ,  $\beta_0 = 2$ , is as follows:

$$w_8 = \frac{D_1 \cdot u}{q \cdot a^4} \cdot 10^4 = 5.15.$$

The error with the tabular value (Table 1) is  $\delta = (5.15 - 4.97) / 4.97 \cdot 100\% = 3.6\%$ , which indicates the acceptable accuracy of the described calculation algorithm based on the finite difference method.

It was found that when the values of the orthotropy coefficients approach the values of  $\alpha_0 = 2$  and  $\beta_0 = 1$ , the orthotropy factor of materials can be neglected in the calculations.

To assess the reliability of the presented results, an alternative calculation by the finite element method in the ANSYS program was performed for an orthotropic equilateral triangular plate with hinged support along the perimeter in order to determine the deflection in the vicinity of the node ( $i = 8$ ) (Fig. 11)  $E_1 = 1.5 \cdot 10^{11}$  Pa,  $E_2 = 1.0 \cdot 10^{11}$  Pa,  $\nu_1 = 0.1$ ,  $\nu_2 = 0.2$ ,  $t = 2.5 \cdot 10^{-3}$  m,  $q = 1.0$  kPa. In this case, the following value of  $u = 2.403 \cdot 10^{-3}$  m was obtained.

To verify the reliability of the presented results, an alternative finite element analysis was performed in ANSYS to determine the deflection of an orthotropic equilateral triangular plate with hinged supports along its perimeter. The hinged support was in the vicinity of the node ( $i = 8$ ) with  $E_1 = 1.5 \cdot 10^{11}$  Pa,  $E_2 = 1.0 \cdot 10^{11}$  Pa,  $\nu_1 = 0.1$ ,  $\nu_2 = 0.2$ ,  $t = 2.5 \cdot 10^{-3}$  m,  $q = 1.0$  kPa (Fig. 11). In this case, the following value of  $u = 2.403 \cdot 10^{-3}$  m was obtained.

When switching to dimensionless coefficients, the deflection in the  $\alpha_0 = 0.66$  node with  $\beta_0 = 2$ , is as follows:

$$w_8 = \frac{D_1 \cdot u}{q \cdot a^4} \cdot 10^4 = 4.789.$$

The error with the tabular value (Table 1) is  $\delta = (4.97 - 4.789)/4.789 \cdot 100\% = 3.8\%$ , which indicates the acceptable accuracy of the calculation algorithm based on the finite difference method proposed by the authors of the article.

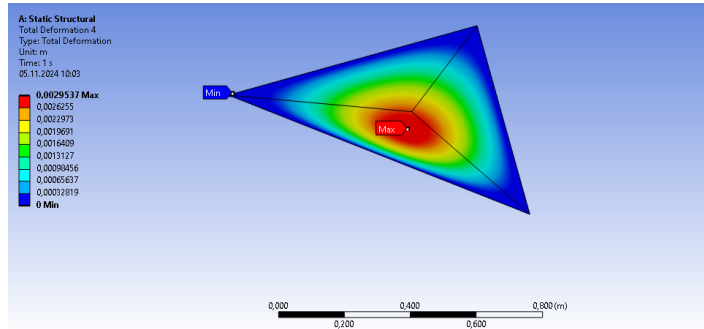


Figure 8. Isolines of deflections of a triangular orthotropic plate under a uniformly distributed load with hinged support of the edges.

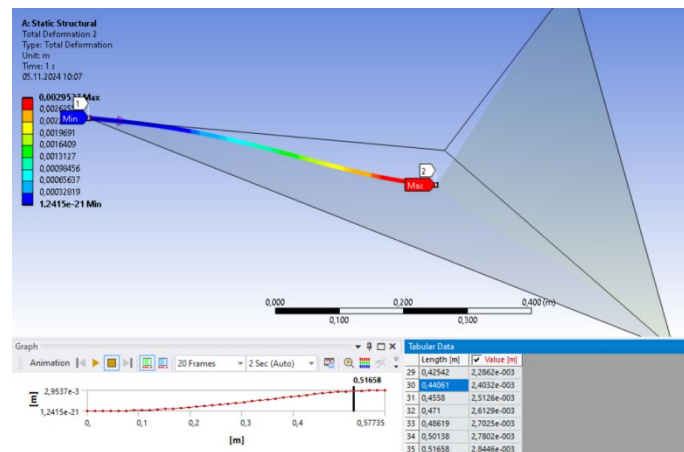


Figure 9. Diagram of deflections in the directions of the median AB.

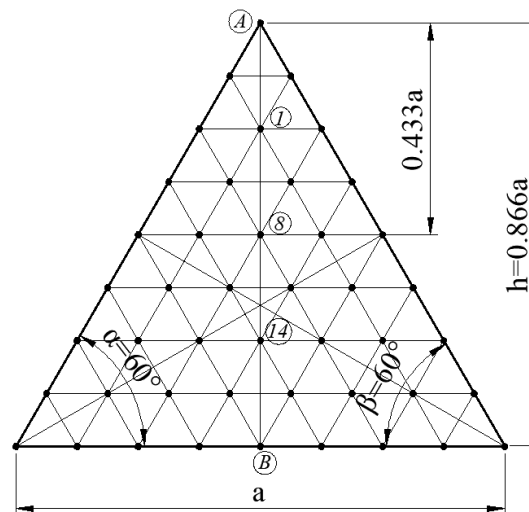


Figure 10. Computational scheme of an orthotropic equilateral plate.

## 4. Conclusion

The object of the study is a transversely bent triangular plate made of orthotropic material, fixed along the edges of the plate, under the action of a uniformly distributed load. An algorithm for a simple engineering calculation of triangular orthotropic plates based on the finite difference method is given, which allows performing manual or machine calculations with sufficient accuracy in variant (or sketch) design. At the same time, the technical problem of boundary conditions for the edges of triangular plates is solved in the form of the idea of paired exclusion of deflections of contour nodes, which occurs when using a grid of scalene triangles; when using a known rectangular grid, such a problem does not arise.

In the proposed research method, the original differential equations of the 4<sup>th</sup> order with variable orthotropy coefficients based on finite difference approximation are replaced by grid equations using a grid of scalene triangles. As a result, a mathematical transition occurs to a system of linear algebraic equations, the solution of which results in deflections at the nodes of the applied grid, and then the corresponding internal forces are calculated.

The results obtained allow drawing the following conclusions.

1. The main and typical finite difference equations for a grid of scalene triangles (Fig. 2) are obtained, taking into account changes in the parameters of the plate geometry (angles  $\alpha$  and  $\beta$ ), boundary conditions (coefficients  $\gamma_1$ ,  $\delta_1$ ,  $\theta_1$ ), material orthotropy (coefficients  $\alpha_0$ ,  $\beta_0$ ), and the number of grid partitions  $N$ .
2. The boundary conditions for a grid of scalene triangles are written in an original group (pair) form, which allows us to take into account the presence of oblique edges of irregular (not equilateral) triangular plates;
3. Calculation of the deflection of equilateral ( $\alpha = \beta = 60^\circ$ ) orthotropic triangular plates (equation (16)). The deflection of equilateral ( $\alpha = \beta = 60^\circ$ ) orthotropic triangular plates was investigated with the number of grid divisions  $N = 8$ , which ensures sufficient engineering accuracy.
4. An alternative calculation of an orthotropic equilateral triangular plate using the finite element method confirmed the reliability of the numerical calculation algorithm proposed by the authors of this article.
5. The results of this study expand the range of problems to be solved for triangular orthotropic plates with their geometric asymmetry (oblique, scalene plates), which is the basis for further theoretical and practical developments in the field of mechanics of thin-walled structures.

## References

1. Eröz, M. Stress analysis of a pre-stretched orthotropic plate with finite dimensions. Transactions of the Canadian Society for Mechanical Engineering. 2021. 45(2). Pp. 346–354. DOI: 10.1139/tcsme-2019-0241
2. Xu, Y., Wu, Z. Exact solutions for rectangular anisotropic plates with four clamped edges. Mechanics of Advanced Materials and Structures. 2022. 29(12). Pp. 1756–1768. DOI: 10.1080/15376494.2020.1838007
3. Yu, Q. A hierarchical wavelet method for nonlinear bending of materially and geometrically anisotropic thin plate. Communications in Nonlinear Science and Numerical Simulation. 2021. 92. Article no. 105498. DOI: 10.1016/j.cnsns.2020.105498
4. Chen, X., Nie, G., Zhong, Z. Research Progress on Static and Dynamic Problems of Variable Angle Tow Composite Plates and Shells. Chinese Quarterly of Mechanics. 2023. 44(1). Pp. 1–14. DOI: 10.15959/j.cnki.0254-0053.2023.01.001
5. Nowinski, J.L., Ismail, I.A. Large oscillations of an anisotropic triangular plate. Journal of the Franklin Institute. 1965. 280(5). Pp. 417–424. DOI: 10.1016/0016-0032(65)90531-4
6. Sathyamoorthy, M. Effects of large amplitude and transverse shear on vibrations of triangular plates. Journal of Sound and Vibration. 1985. 100(3). Pp. 383–391. DOI: 10.1016/0022-460X(85)90294-9
7. Jaunky, N., Knight Jr., N.F., Ambur, D.R. Buckling analysis of general triangular anisotropic plates using polynomials. Collection of Technical Papers – AIAA/ASME/ASCE/AHS/ASC Structures, Structural Dynamics and Materials Conference. 1995. 4. Pp. 2647–2654.
8. Jaunky, Navin, Knight, N.F., Ambur, D.R. Buckling analysis of general triangular anisotropic plates using polynomials. AIAA Journal. 1995. 33(12). Pp. 2414–2417. DOI: 10.2514/3.13000
9. Jaunky, N., Knight Jr., N.F., Ambur, D.R. (). Optimal design of general stiffened composite circular cylinders for global buckling with strength constraints. Composite Structures. 1998. 41(3–4), Pp. 243–252. DOI: 10.1016/S0263-8223(98)00020-8
10. Jaunky, N., Knight Jr. N.F., Ambur, D.R. Optimal design of grid-stiffened composite panels using global and local buckling analyses. 37<sup>th</sup> AIAA/ASME/ASCE/AHS/ASC Structure, Structural Dynamics and Materials Conference. Salt Lake City UT, 1996. Pp. 2315–2325. DOI: 10.2514/6.1996-1581
11. Saliba, H.T. Free vibration of simply supported general triangular thin plates: An accurate simplified solution. Journal of Sound and Vibration. 1996. 196(1). Pp. 45–57. DOI: 10.1006/jsvi.1996.0466

12. Xiang, Y. Buckling of triangular plates with elastic edge constraints. *Acta Mechanica*. 2002. 156(1–2). Pp. 63–77. DOI: 10.1007/BF01188742
13. Dayyani, I., Moore, M., Shahidi, A. Unilateral buckling of point-restrained triangular plates. *Thin-Walled Structures*. 2013. 66. Pp. 1–8. DOI: 10.1016/j.tws.2013.01.007
14. Askari, H., Saadatnia, Z., Esmailzadeh, E., Younesian, D. Multi-frequency excitation of stiffened triangular plates for large amplitude oscillations. *Journal of Sound and Vibration*. 2014. 333(22). Pp. 5817–5835. DOI: 10.1016/j.jsv.2014.06.026
15. Esmailzadeh, E., Younesian, D., Askari, H. Energy Balance Methods. *Solid Mechanics and Its Applications*. 2019. 252. Pp. 73–122. DOI: 10.1007/978-94-024-1542-1\_3
16. Saadatnia, Z., Rahnamayan, S., Esmailzadeh, E. Vibration Analysis and Multi-Objective Optimization of Stiffened Triangular Plate. *Proceedings of the ASME Design Engineering Technical Conference*. Buffalo NY, 2014. Article no. V008T11A033. DOI: 10.1115/DETC2014-35553
17. Akhmediev, S.K., Zhakibekov, M.E., Kurokhtina, I.N., Nuguzhinov, Z.S. Numerical study of the stress-strain state of structures such as thin triangular plates and plates of medium thickness. 2015. 2(259). Pp. 28–33.
18. Wang, Q., Xie, F., Liu, T., Qin, B., Yu, H. Free vibration analysis of moderately thick composite materials arbitrary triangular plates under multi-points support boundary conditions. *International Journal of Mechanical Sciences*. 2020. 184. Article no. 105789. DOI: 10.1016/j.ijmecsci.2020.105789
19. He, D., Liu, T., Qin, B., Wang, Q., Zhai, Z., Shi, D. In-plane modal studies of arbitrary laminated triangular plates with elastic boundary constraints by the Chebyshev-Ritz approach. *Composite Structures*. 2021. 271. Article no. 114138. DOI: 10.1016/j.compstruct.2021.114138
20. Akhmediyev, S.K., Khabidolda, O., Vatin, N.I., Yessenbayeva, G.A., Muratkhon, R. Physical and Mechanical State of Cantiliver Triangular Plates. *Journal of Mathematics, Mechanics and Computer Science*. 2023. 118(2). Pp. 64–73. DOI: 10.26577/JMMCS.2023.v118.i2.07
21. Grigorenko, O.Y., Borisenko, M.Y., Boichuk, O.V., Vasil'eva, L.Y. Free Vibrations of Triangular Plates with a Hole. *International Applied Mechanics*. 2021. 57(5). Pp. 534–542. DOI: 10.1007/s10778-021-01104-3
22. Yang, Y., An, D., Xu, H., Li, P., Wang, B., Li, R. On the symplectic superposition method for analytic free vibration solutions of right triangular plates. *Archive of Applied Mechanics*. 2021. 91(1). Pp. 187–203. DOI: 10.1007/s00419-020-01763-7
23. Ambartsumian, S.A. On the theory of bending of anisotropic plates and shallow shells. *Journal of Applied Mathematics and Mechanics*. 1960. 24(2). Pp. 500–514. DOI: 10.1016/0021-8928(60)90052-6
24. Ambartsumian, S.A. *Membrane Theory of Plates*. Foundations of Engineering Mechanics. Springer. Cham, 2021. Pp. 73–103. DOI: 10.1007/978-3-030-71326-3\_4
25. Poniatovskii, V.V. On the theory of bending of anisotropic plates. *Journal of Applied Mathematics and Mechanics*. 1964. 28(6). Pp. 1247–1254. DOI: 10.1016/0021-8928(64)90036-X
26. Brezinski, C. Some pioneers of extrapolation methods. *The Birth of Numerical Analysis*. World Scientific Publishing Company, 2009. Pp. 1–22. WORLD SCIENTIFIC. DOI: 10.1142/9789812836267\_0001
27. Nuzhdin, L., Mikhailov, V., Rezyapkin, V. Modeling and analysis of the pile cluster foundation in SCAD and SMATH Studio. *Proceedings of 16<sup>th</sup> Asian Regional Conference on Soil Mechanics and Geotechnical Engineering (ARC 2019)*. Taipei, 2020.
28. Zlatev, Z., Dimov, I., Faragó, I., Georgiev, K., Havasi, Á. Stability of the Richardson Extrapolation combined with some implicit Runge–Kutta methods. *Journal of Computational and Applied Mathematics*. 2017. 310. Pp. 224–240. DOI: 10.1016/j.cam.2016.03.018

#### **Information about the authors:**

**Moldir Sailaubekovna Beketova,**

ORCID: <https://orcid.org/0009-0003-2248-312X>

E-mail: [moldir-9292@mail.ru](mailto:moldir-9292@mail.ru)

**Zhmagul Smagulovich Nuguzhinov, Doctor of Technical Sciences**

ORCID: <https://orcid.org/0000-0002-0252-2115>

E-mail: [kazmir@mail.ru](mailto:kazmir@mail.ru)

**Vladimir Ilyich Travush, Doctor of Technical Sciences**

ORCID: <https://orcid.org/0000-0003-1991-7233>

E-mail: [vtravush@mail.ru](mailto:vtravush@mail.ru)

**Nikolai Ivanovich Vatin, Doctor of Technical Sciences**

ORCID: <https://orcid.org/0000-0002-1196-8004>

E-mail: [vatin@mail.ru](mailto:vatin@mail.ru)

**Serik Kabultaevich Akhmediyev, PhD in Technical Sciences**

ORCID: <https://orcid.org/0000-0001-6723-4571>

E-mail: [serik.akhmediyev.50@mail.ru](mailto:serik.akhmediyev.50@mail.ru)

**Irina Alekseevna Kurokhtina,**

ORCID: <https://orcid.org/0000-0002-8367-7636>

E-mail: [kurohtina.ira@mail.ru](mailto:kurohtina.ira@mail.ru)

**Roza Abdullaevna Shagiyeva**, PhD in Technical Sciences

ORCID: <https://orcid.org/0009-0003-1867-7300>

E-mail: [shagieva2008@mail.ru](mailto:shagieva2008@mail.ru)

**Valentin Feliksovich Mikhailov**, PhD in Technical Sciences

ORCID: <https://orcid.org/0000-0002-2588-9438>

E-mail: [v.mikhailov@ktu.edu.kz](mailto:v.mikhailov@ktu.edu.kz)

**Omirkhan Khabidolda**, PhD

ORCID: <https://orcid.org/0000-0001-7909-7201>

E-mail: [oka-kargtu@mail.ru](mailto:oka-kargtu@mail.ru)

*Received 14.01.2025. Approved after reviewing 23.03.2025. Accepted 30.03.2025.*





Research article

UDC 624

DOI: 10.34910/MCE.134.8



## A model study of axially loaded micropiles in layered soils

A.A. Al-Omari  , A. Al-Dabbagh

<sup>1</sup> Department of Civil Engineering, University of Mosul, Mosul, Iraq

✉ [asaad.alomari@uomosul.edu.iq](mailto:asaad.alomari@uomosul.edu.iq)

**Keywords:** physical model, single micropile, group micropile, layered soil, load-settlement curve

**Abstract.** The current research uses a physical model to investigate the role of micropiles as vertical reinforcement of footing when embedded in sandy silty soil from Mosul city – Iraq. The experimental program focused on carrying out several load-settlement tests for the footing with two different reinforcement conditions: by a single micropile and group micropiles. The study is extended to investigate the role of soil homogeneity, weak soil underneath by strong soil layer, in the behavior of load-settlement curves for the reinforced footing. Next, the load settlement tests were, again, conducted using the same model but for the non-reinforced footing (flat footing). The first results indicated that the physical model has succeeded in representing all the studied cases. Also, the results showed a significant improvement in the behavior of the load-settlement curves when the footing was reinforced with micropile, especially using the micropile group, compared with the non-reinforced footing. Also, the degree of improvements in the load-bearing capacity and load-settlement behavior, for the footing reinforced with micropiles embedded in different conditions of soil homogeneity, was examined through two different non-dimensional factors: bearing capacity ratio (BCR) and percent of settlement reduction (PSR). The results indicated that the BCR was increased and the PSR was decreased for the reinforced footing compared to the non-reinforced footing. Moreover, from the test results, we noticed that the homogeneity of the soil has a significant effect on the load-settlement curves behavior of the footing.

**Acknowledgment:** The authors would like to thank the College of Engineering / University of Mosul for its encouragement and incorporeal support to the authors for research publishing.

**Citation:** Al-Omari, A.A., Al-Dabbagh A. A model study of axially loaded micropiles in layered soils. Magazine of Civil Engineering. 2025. 18(2). Article no. 13408. DOI: 10.34910/MCE.134.8

### 1. Introduction

Since ancient times, humans have tried establishing strong buildings that could last for hundreds of years. Many buildings, consisting of stone and light materials, were erected. In nature, soil exists with a wide range of variety in its bearing capacity. Therefore, it was necessary to use different foundation types commensurate with the nature of the soil in the field and with the number of loads transferred to it. Micropiles are considered a modern foundation type that proves successful in the practical field. They were called "Micropiles" due to their small diameter, which ranges from ten to thirty centimeters, and their light weight. Micropiles are usually executed by injection of the cement mixture with or without using steel reinforcement. Recently, technological advances in machinery made it possible to implement micropiles with different small diameters. Whether in the static or dynamic state, the micropiles are a type of foundation that can work, mainly using friction, as an integrated system to transfer the loads from the structures to the layers of the soil. The purpose of micropiles work is to improve the bearing capacity of the soil by increasing the density, increasing the confinement of the soil surrounding the micropile, and consequently creating friction [1].

Micropiles are characterized by the possibility of improving the weak soil layers (i.e. by reinforcing the foundations of existing buildings, especially ancient archaeological buildings). The micropiles also contribute to the consolidation of the foundations of buildings in cramped places that are difficult to reach

by massive machines [2]. Likewise, Micropiles play an decisive role in stabilizing deep excavations for new strategic projects to be implemented in places with limited spaces in crowded cities, and in the case of projects that are difficult to reach using machines for traditional piles, here micropiles must be used [3]. The micropiles are also characterized by their rapid implementation compared to the implementation of traditional piles with large diameters [4]. In addition, because the execution of micropiles does not require the use of large equipment, as is the case in the execution of other traditional foundations, thus the selection of micropiles does not result in destructive and harmful vibrations to neighboring buildings [5]. Due to the distinctive features of micropiles, many projects have adopted using micropiles in unlimited scope and have proven to be functionally successful.

The first use of micropiles was in the mid of the twentieth century when they were invented for the first time in Italy to support the foundations of the Anguilli School in Naples by engineer Fernando Lizzi [6]. In North America, specifically on the East Coast of the United States, micropiles witnessed wide interest in the seventies [7]. In Japan, again, micropiles were used in eighties to support the foundations of a lookout tower [8]. Moreover, the researchers [9] indicated that China used micropiles in the eighties as a new experiment through the study of representing a laboratory model to simulate the reality of the Uu-Qui tower. Furthermore, Hong Kong also paid attention to the first studies on micropiles through the published research of [5], where it was recommended to use micropiles in construction conditions that need as little disturbance as possible for neighboring buildings. Locally, micropiles were used in consolidating the Al-Hadbaa minaret foundation in Mosul city - Iraq, as part of the maintenance work carried out by the Italian company in the early eighties [10, 11], Fig. 1.

Through the efforts made by many researchers, scientific research institutions, and universities, including the Federal Highway Administration of the US Department of Transportation [12] in the field of carrying out, and studying the behavior and design methodologies of the micropiles, therefore the micropiles have been used all over the world with their proven track record of success [13]. Finally, it must be noted that the use of micropiles has taken place in development projects and urban and industrial redevelopment, and here the selection of the characteristics of micropiles (length and diameter of micropile, and the angle of inclination while fixing micropile to the soil) depends on the type of soil, the depth of the foundation, groundwater, and the type of loads (tension or compression).

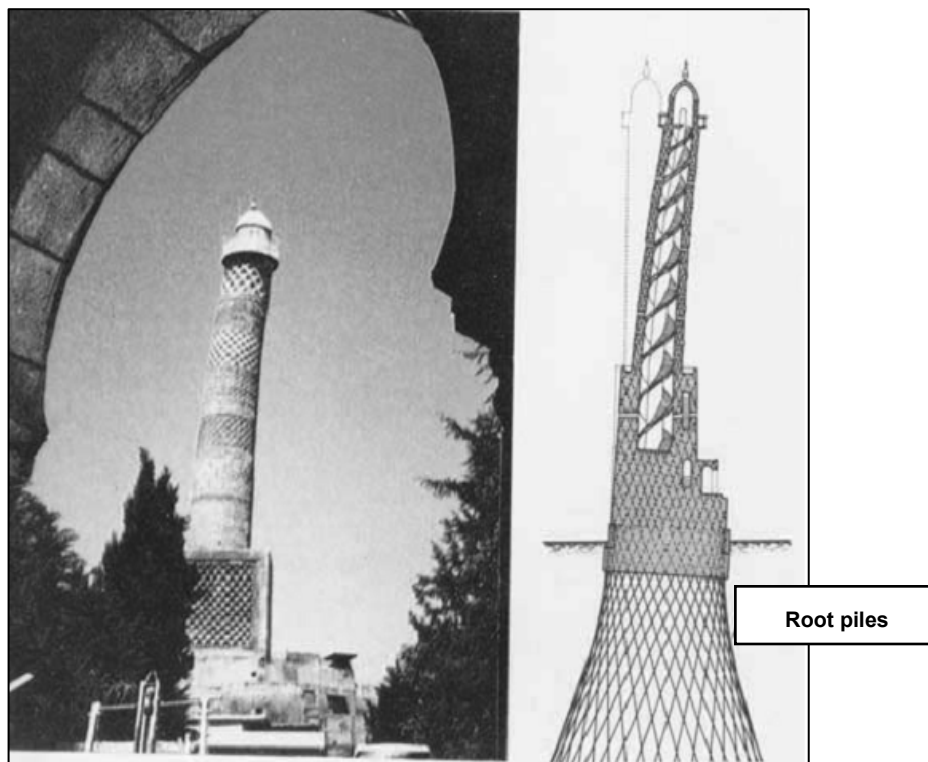


**Figure 1. The use of micropiles in consolidating the Al-Hadbaa minaret foundation, (Lizzi, 1982; 1997).**

Many previous studies focused on studying the behavior of micropiles (bearing capacity and settlement of foundation) and the extent to which they are used, whether in reinforcement and treatments of pre-existing foundations or in the field of using them as a foundation when constructing vital engineering projects.

In [14] the researchers were interested in using a laboratory-physical model to study the possibility of reinforcing fly-ash soil using micropiles. The laboratory model was represented numerically using SIGMA/W of GeoStudio 2016 software. The numerical study was adopted to investigate the bearing capacity and settlement of the foundation with different conditions of micropile length, the distance between micropiles, and the distance of the micropiles extending beyond the foundation edge. The researchers concluded from this study that the bearing capacity increases with the increase of the micropile length. Another conclusion is that, when the distance between the micropiles reduced and the piles extends beyond the edge of the foundation increased, there are increases in the bearing capacity and decreases in the settlement of the foundation.

Away from fly-ash soils, the research work of [1] focused on studying the behavior of the micropiles in the case of sandy soils. Once again, the studied variables are the micropile diameter, length, the distance between the micropiles, and the distance of the micropiles from the edge of the foundation. The laboratory results showed that the foundation increased in its bearing capacity and decreased in its settlement in case of increasing the diameter and the length of the micropile and decreasing both the distance between the micropiles and the micropiles distance to the foundation edge.

The behavior of micropiles in sandy soils was studied extensively by previous research works [15–19]. The laboratory model proposed by [15] revealed the effect of five different parameters (degree of inclination, diameter, length-to-width ratio, spacing between micropile, and the closeness of the micropiles to the footing) on the behavior of micropiles footing. The inclination of micropile was more effective in the case of horizontal loading than vertical loading. The micropile diameter and the length-to-width ratio enhance the bearing capacity of micropile footing. The degree of micropile closeness to the footing and the decrease in the spacing between the micropile increase the bearing capacity of the micropile footing.

In [16] the researchers carried out a series of model tests on group micropiles to reinforce the footing resting on sandy soils with different densities. The study showed that the sandy soil with different degrees of confinement (dense, medium, and loose) led to induce different mechanisms in the behavior of group micropile: the positive dilatant behavior of dense sand led to a significant improvement of the micropile footing.

On the other hand, the mode of failure of the group micropiles implemented in the sand and subjected to vertical or oblique pull-out loads was examined [18]. The most important finding of this study is that micropiles with a high length-to-diameter ratio can fail in two different modes: soil failure and structural failure. The former failure mode belongs to the group of vertically pulled micropile, while the latter mode of failure belongs to the group of micropiles subjected to a load pulling with a high degree of obliquity.

In another aspect, in a study conducted by [19], a laboratory model was used to apply inclined compressive loads on a group of micropiles implemented in sandy soil with different spacing between the micropiles and different length-to-diameter ratios of the micropiles. The study concluded that the lateral capacity of the group micropiles increases with increasing the length of micropiles and the spacing between the micropiles.

After demonstrating the literature review above, it can be said that most of the previous studies attempt to investigate the behavior of micropiles in homogeneous sandy soil. In contrast, the studies of the micropiles in layered soils are rather limited, especially for the silty soil type. Therefore, the current research work adopts the use of a physical model to study the behavior of micropiles in heterogeneous silty soils in two different cases: when the silty soil surrounding the micropiles has a homogeneous layer (the soil density is constant for the entire single soil layer), and the silty soil is two-layered (the soil in the lower layers has a density greater than the soil in the upper layer). Again, the previous studies have not fully addressed the behavior of micropiles that are implemented in layered soils. Moreover, such type of study has not previously covered in the case of micropiles implemented in local soils from Mosul city - Iraq. Therefore, it can be said that the distinctive objectives of this study are:

- Characterization of the local soils from Mosul city near the Tigris River basin, with a particular focus in recent years in the exploitation and investment of lands near the site of the current study area.
- Investigating the possibility of using a physical model to simulate the behavior of micropiles in the field.
- Representation of the soil in the physical model with different states of soil stratification.
- Characterization, in details, the bearing capacity and settlement of the micropiles when implemented in the local soil in two different states: layered and non-layered.
- Determining the ultimate bearing capacity of the foundations by four different graphical methods with comparing the obtained ultimate values.

## 2. Methods

### 2.1. Selection and Properties of Soil

The natural soil samples of this study are brought from Khawaja Khalil village. Khawaja Khalil is located in the alignment of the Tigris River on the left coast of Mosul city – Nineveh Governorate, Iraq, Fig. 2. The excavations were carried out to a depth of approximately 2.5 m. During the field campaign, two types of soil samples were excavated: disturbed and non-disturbed soil samples. These soil samples were wrapped to avoid changes in the moisture content. Later, the soil samples were transferred to the Geotechnical Laboratory at the University of Mosul to conduct some of the physical and mechanical laboratory tests that help us in soil characterization.

Physical tests were conducted on soil samples based on the method adopted by the American Society for Testing and Materials (ASTM). These tests included: natural moisture content, natural dry density, specific gravity, Atterberg limits, and soil grain gradation by both dry and wet analysis.

In light of the Atterberg limits test and the sieve analysis test, one can identify the liquid limits, the plasticity index, and the percent of gravel, sand, silt, and clay materials of the tested soil. Thus, a soil sample can be classified according to the Unified Classification System (USCS). The details of these tests are listed in Table 1. Again, a set of mechanical tests: the standard Proctor compaction test, modified Proctor compaction test, and direct shear test, were performed on soil samples, and the results of these tests are listed in Table 1.

According to the USCS, the data analysis of the physical and mechanical tests proved that the soil in the current study is silty soil with low plasticity (ML) of group name (sandy silt). Also, the soil samples can show good shear strength resistance: the shear strength parameters ranged between 27–34 degrees and 8–13 kPa as the angle of internal friction and the cohesive force, respectively.

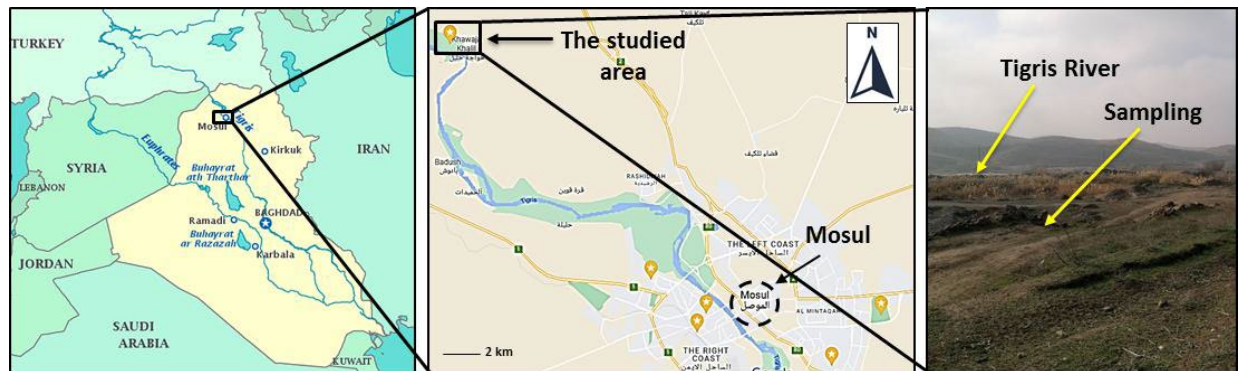


Figure 2. Location of the studied area.

Table 1. Physical and mechanical properties of the studied soil.

Parameter		Values	Test procedure
Natural water content, (%)		9.80	ASTM D 2216, 2010**
Natural moist unit weight, (kN/m <sup>3</sup> )		16.30	ASTM D7263, 2018**
Natural dry unit weight, (kN/m <sup>3</sup> )		14.84	
Specific gravity		2.67	ASTM D854 – 14**
Atterberg limits	Liquid limit, (%)	NP	ASTM D 4318, 2017**
	Plastic limit, (%)	NP	
	Plasticity index, (%)	NP	
Percentage of soil grains	Gravel, (%)	10	ASTM D 6913M – 17** ASTM D7928 – 17**
	Sand, (%)	30	
	Silt, (%)	48	
	Clay, (%)	12	
Soil classification, (USCS)		ML: silt with low plasticity (sandy silt)	ASTM D2487 – 17**

Parameter		Values	Test procedure
Compaction test	SPE*	Max. dry density, (kN/m <sup>3</sup> )	17.0
		Optimum water content, (%)	16.0
	MPE*	Max. dry density, (kN/m <sup>3</sup> )	18.75
		Optimum water content, (%)	12.0
Direct shear test	SPE*	c = 8 kN/m <sup>2</sup>	ASTM D3080M – 11**
		φ = 27°	
	MPE*	c = 13 kN/m <sup>2</sup>	
		φ = 34°	
*SPE: Standard Proctor energy, and MPE: Modified Proctor energy			
** [20]			

## 2.2. Physical Model

Mainly, physical modeling is used to reduce the dimensions of the represented prototype. This reduction saves time, resources, and effort consumption. Also, the physical modeling facilitates the conduct of various tests in the laboratory and the interpretation of their results. Testing the performance of micropile by physical models requires using several tools and devices (soil containment tank, loading plate, micropile foundation, compaction machine, load cell for measuring the applied load, sensors for measuring the induced settlement, and a data logger). In this study, the physical model of the formative parts is described briefly in the following paragraphs.

### 2.2.1. The model tank and loading plate

In this experimental work, a tank made of rigid steel was used. The volume of the tank is suitable to contain a sufficient amount of soil pressed with axial static pressure loads, stress control, or strain control using a hydraulic piston. The used tank is a square cube with internal dimensions of fifty centimeters a side and a height of 60 cm, Fig. 3. The choice of the dimensions of the tank should be taken into account so that the depth of the tank model is more than ten times the diameter of the used micropile. This measure is to avoid the effect of the extension of the micropile stresses and the interaction with the bottom of the tank body while applying the axial loading [21].

The loading plate (square plate) is made of rigid steel with dimensions of ten centimeters a side and a depth of 0.6 cm, Fig. 3. Previous research indicates that choosing the dimensions of the loading plate and the dimensions of the model tank must be compatible so that the experiment is conducted without the tank walls affecting the distributed loads coming from the loading plate, i.e. the boundary effects [14]. This compatibility between the dimensions of the loading plate and the dimensions of the tank requires that the width of the tank be at least five times greater than the width of the loading plate [1, 22]. Moreover, the loading plate was designed with a rough surface enough to represent the actual roughness of the footing [23].

It is worth mentioning that the used tank should be well attached to an iron frame. The purpose of using this framework is to facilitate the implementation of the test at a constant loading rate on the one hand and to collect data correctly without disarrangement on the other hand. Thus, the obtained data can be analyzed accurately and with complete control over the test conditions.

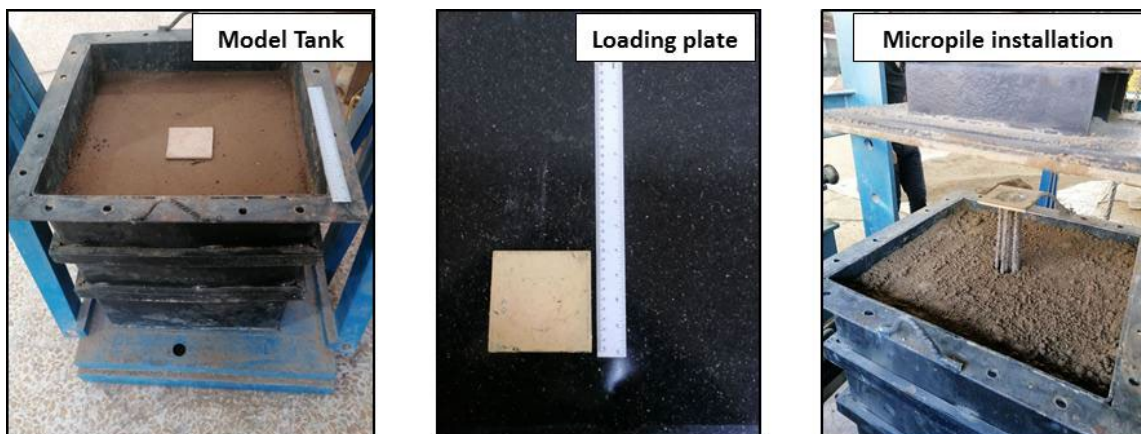


Figure 3. The model tank (left), loading plate used in the physical model (middle), and the process of micropile model installation (right).



### 2.2.2. The micropile foundation

Previous studies indicate that the micropile model was represented experimentally by using micropiles made of different materials; a rod of steel [1, 14, 16, 24–26], a rod of Aluminum [15, 27], a rod of Polyvinyl Chloride (PVC) [16, 28–31], and even rod of Bamboo sticks [32–34]. The foundations used in this study are composed of a loading plate and reinforced with piles (single or group micropiles). The micropile model used in this study with a diameter of 6 mm and a length of 300 mm and is made of stainless steel.

Following the procedure outlined in the work of [24], the micropiles were fastened to the loading plate: the loading plate has been reinforced with micropiles, where the micropiles were welded in the center and perpendicular to the surface of the loading plate to avoid the eccentricity of the loading. Concerning the micropiles group, the mode of reinforcing the loading plate with micropile was done using the honeycomb shape with seven micropiles, Fig. 4. In this case, the distance between the micropiles is even and equal to four times the diameter of the micropile [32]. Choosing the distance between the micropiles of the group four times the diameter of the micropile (greater than three times the diameter) is to ensure avoiding interaction between the micropiles [13]. The smooth surface of the steel rods (micropile model) was coated with a thin layer of sand to make the surface rough (to impose the skin friction) and to represent the condition of the micropiles in the field [15, 16, 28, 31]. Fig. 4 shows the conditions of the micropile model used in the study. Here it is worth noting that the reason for using a honeycomb shape (hexagonal) pattern of micropiles distribution is to make the distance between all micropiles equal (even the diagonal distance between the central micropile and the micropiles located at the ends), and this cannot be achieved in the case of using a pattern of regular micropile distribution such as the square shape or the rectangular shape.

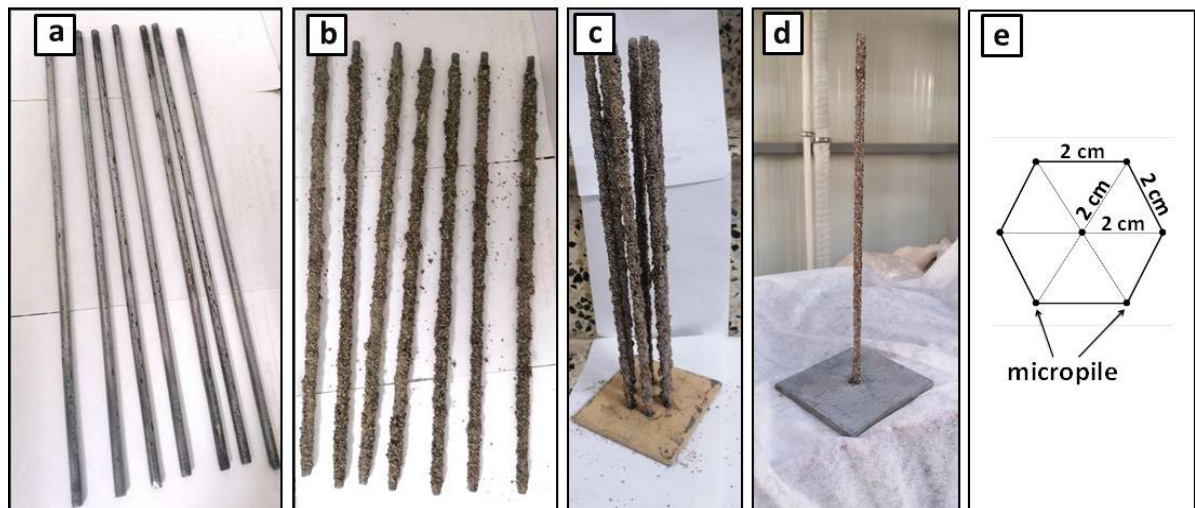


**Figure (4) The stainless steel micropiles model, a) before gluing with sand, b) after gluing with sand, c) group micropiles, d) single micropile, and e) top view of the micropiles model with honeycomb shape.**

### 2.2.3. Soil beds and micropile installation

Before conducting the soil deformation test, the soil layers inside the physical model were prepared with a maximum dry density of standard or modified Proctor compaction test. To this end, a certain amount of water, at optimum water content, was added to the dry soil. Later, a certain weight of pre-mixed moist soil was compacted statically into the tank at a constant rate using an electro-hydraulic press machine. To achieve the requisite soil dry density of 17.0 and 18.75 kN/m<sup>3</sup>, which correspond to the maximum dry densities for the standard and modified Proctor compaction tests, respectively, the soil mixture was compacted in five stages, each lasting 100 mm. After completing the compaction process for each stage, the density of the compacted soil was checked by inserting a small mold inside the compacted soil layers to measure the soil density. At the end of the fourth stage of soil compaction (at a height of 400 mm of soil inside the tank), the micropiles were pushed inside the soil layers during the soil compaction process in the fifth stage [1], as shown in Fig. 3. By following this method, we ensure that the micropiles are well installed inside the soil beds while reducing the disturbance of the soils surrounding the micropile to as little as possible. It is pertinent to note that the electro-hydraulic press machine was utilized to set the micropiles into the soil inside the model tank. The penetration of the micropiles is controlled with a constant penetration rate of 1.0 mm /min.

### 2.3. Loading the Micropile

In this experimental work, the process of applying the loads was done with the help of a rigid loading frame by using a hydraulic jack. Multiplicative increments of loads (0.25, 0.5, 1.0, 2.0, 4.0, ... kN), were applied during the test. The previous studies indicated that the laboratory tests for the physical model are usually done by loading the micropiles and recording the settlement until reaching different values of the settlement ratio ( $S_r = s / b$ ), where ( $s$ ) is the settlement, and ( $b$ ) is the width of the footing. For instance, the recorded settlement ratio is:  $S_r = 13\%$  [15],  $S_r = 16\%$  [24],  $S_r = 25\%$  [25], and even  $S_r$  reaches a high value of about  $70\%$  [28]. In this study, the load increments were applied during the test until the reaching the failure: excessive settlement at a certain load or the maximum settlement of 50 mm (i.e.  $S_r = 50\%$ ). The loads were applied at a constant rate of 1.0 mm/min.

### 2.4. Load and Settlement Recording

Concerning the load and settlement data recording, a set of tools was used for this purpose: the load cell, the displacement gauges, and the data logger. The Z beam load cell with 50 kN capacity was used to measure the applied loads. The range of temperature was from negative thirty to positive seventy centigrade is accepted by using such a type of load cell. The vertical displacement was measured by the linear variable differential transformer-LVDT, with a displacement range of 50 mm. Again, this displacement transducer LVDT is workable at a temperature range from negative ten to positive sixty centigrade. Three LVDTs were utilized to measure the settlement of the loading plate during the test. These three displacement transducer LVDTs are set at an angle of  $120^\circ$  to cover the entire loading plate. The average value is taken from the three LVDTs. Also, the data logger of type TDS-530 was selected to read the data: load and settlement, Fig. 5. This device is capable of reading data from 20 channels simultaneously. By using these tools, the accuracy of measuring the settlement and the applied loads during the experiment was 0.001 mm and 1 kN, respectively. These data were recorded every second to monitor any change that could occur during the progress of the test. The collected data in Excel file format was uploaded to the computer once each test was finished. The recorded data resulted in the analysis of an average of 8,000 rows in the Excel file for each test. Again, Fig. 5 shows a set of tools used in this study and the test setup.

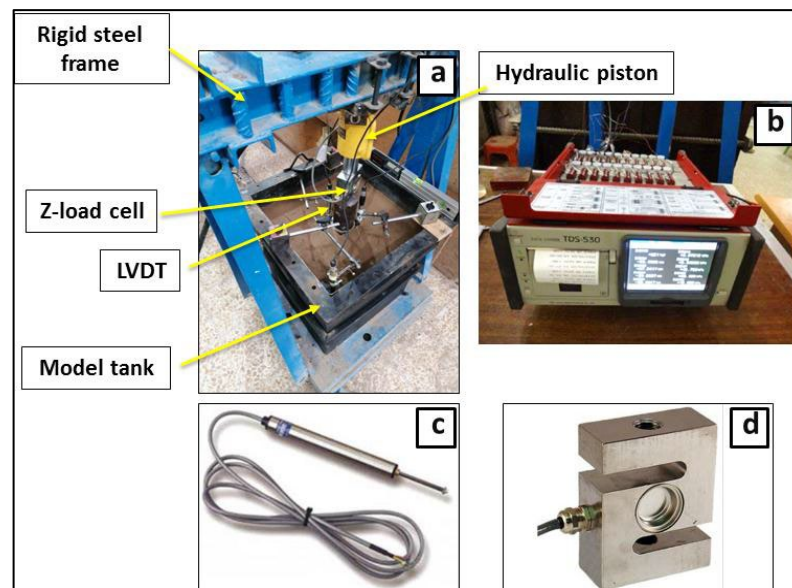


**Figure 5. Set of tools used in the physical model and test setup during the test.**

### 2.5. Test Series

The current experimental work included carrying out the loading tests with two different soil stratification cases: the first case is for the non-stratified soil condition (the whole soil inside the tank prepared with the density of standard Proctor compaction energy). The second one represents the stratified soil condition (the upper soil layers with a thickness of 20 cm inside the tank were prepared with the density of standard Proctor compaction energy, while the lower layers with a thickness of 30 cm were prepared with the density of modified Proctor compaction energy).

Three footing reinforcement scenarios were tested for both types of soil conditions: the first scenario involved reinforcing the footing with a single micropile, while the second scenario involved reinforcing the footing with a group of micropiles. To compare the findings and acquire reference data for the loading-settlement tests, the third scenario was interested in the footing but without reinforcement (flat loading

plate). Six experimental tests were completed as part of this study project using these various soil layer conditions and footing reinforcement scenarios.

### 3. Results and Discussion

The load-settlement test results for the footing with three different reinforcing cases (flat footing, footing reinforced with single micropile, and footing reinforced with group micropiles) are presented and discussed in this section. These tests involved embedding the micropiles in soils that were either homogeneous non-layered or heterogeneous layered.

#### 3.1. Load-settlement Curves for Different Cases of Footing Reinforcement

Fig. 6 shows the load-settlement curves for three cases of footing reinforcement; the non-reinforced footing or flat footing (F), the reinforced footing with a single micropile (S), and the reinforced footing with a group of micropiles (G). For all the cases studied, the footing's load-settlement curves under an axial compressive load are non-linear. Fig. 6-a is interesting for the case of the soil layers inside the tank having a density of standard compaction Proctor energy (non-layered soil, "N L"). Also, Fig. 6-b shows the load-settlement curves for the same different cases of footing reinforcement shown in Fig. 6-a, but when the soil is layered "L", the tank contains soil in the upper layers having a density of standard compaction Proctor energy and the lower soil layers having a density of modified compaction Proctor energy). The difference in the type of footing reinforcement has a significant effect on the behavior of the load-settlement curves. In general, at a certain settlement, it is noted that there is a clear increase in bearing capacity when the footing is reinforced compared to the non-reinforced footing. The same observation can be seen when the footing is reinforced with a single micropile compared to a footing reinforced with a group of micropiles.

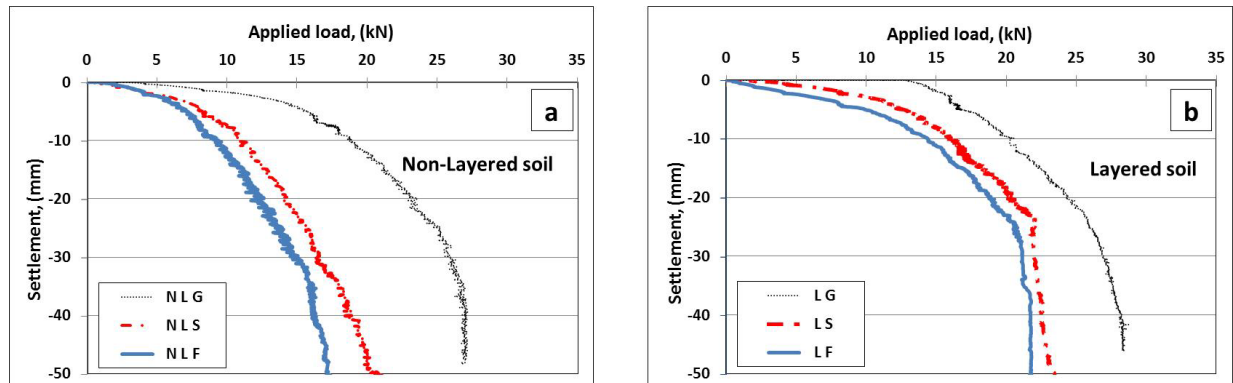


**Figure 6. Load-settlement curves for different cases of footing reinforcement.**

#### 3.2. Load-settlement Curves for Different Cases of Soil Homogeneity

The curves in Fig. 6 show the load-settlement curves in the case of non-reinforced footing (flat footing) in two different cases of soil homogeneity inside the tank: heterogeneous layered soil (LF) and homogeneous layered soil (NLF). Furthermore, Fig. 6 show the effect of soil homogeneity on the behavior of the load-settlement curves in the case of a footing reinforced with a single micropile (LS and NLS) and a group of micropiles (LG and NLG), respectively. Once again, it is noted that there is a clear difference in the behavior of load-settlement curves depending on the case of soil homogeneity.

Regardless of the type of footing (flat footing, footing reinforced with a single micropile, or a group of micropiles), the curves presented in Fig. 6 denote that there is a clear increase in the bearing capacity of the footing or a clear decrease in the settlement at a certain applied loading in the case of layered soil compared to non-layered soil. This occurs due to the improvement of the soil properties in the lower layers inside the tank since these soil layers have been compacted with the modified compaction energy. This, in turn, leads to an increase in the soil shear strength parameters (C and Phi).

On the other hand, in the current research work, the layered soil was made denser than the non-layered soil. This results in a commitment to change the failure mode from the local shear failure state of the non-layered soil to the general shear failure mode of the layered soil. In this case, increasing the density in the lower layers of the soil inside the tank leads to an increase in the frictional resistance between the micropile and the surrounding soil, and this is another reason to justify the increase in bearing capacity of the footing embedded in the layered soil rather than the non-layered soil.

### 3.3. Determination of the Footing Bearing Capacity by Graphical Methods

In the case of shallow footing, the bearing capacity from the load-settlement curve can be easily distinguished, through which three natural bearing capacity failures in the soil can be named: general shear failure, local shear failure, and punching shear failure [35]. This is not the case in micropile footing, where it is difficult to identify the point of failure in the load-settlement curves. The graphical methods are usually used to find the bearing capacity of the micropiles. Below is a brief explanation of the most important of these graphical methods used in previous studies:

#### 3.3.1. Tangent method

This approach involves creating two tangent lines for the load-settlement curve: the first line at the beginning of the curve and the second one at the end of the curve. The intersection of these two tangents can represent the bearing capacity of the micropile, Fig. 7-a.

#### 3.3.2. Butler and Hoy method

In this method, a tangent line with a slope of  $0.127 \text{ mm/kN}$  is drawn to intersect with the initial tangent line of the load-settlement curve. The point of intersection represents the bearing capacity of the micropile [36], Fig. 7-b.

#### 3.3.3. De Beer and Wallays method

This method is the same as the tangent method, but when the load-settlement curve is drawn on a logarithmic scale for both load and settlement axes [37], Fig. 7-c.

#### 3.3.4. Corps of engineering method

This method is concerned with finding three load values from the load-settlement curve. The first load value ( $Q_1$ ) can be found when the settlement is  $6.4 \text{ mm}$ . The second load value ( $Q_2$ ) represents the load value obtained by the tangent method (as mentioned above). The third load value ( $Q_3$ ) represents the value of the load when the line with a slope of  $0.025 \text{ mm/kN}$  touches the load-settlement curve. Finally, the bearing capacity of the micropile could be calculated as the average of these three load values [38], Fig. 7-d.

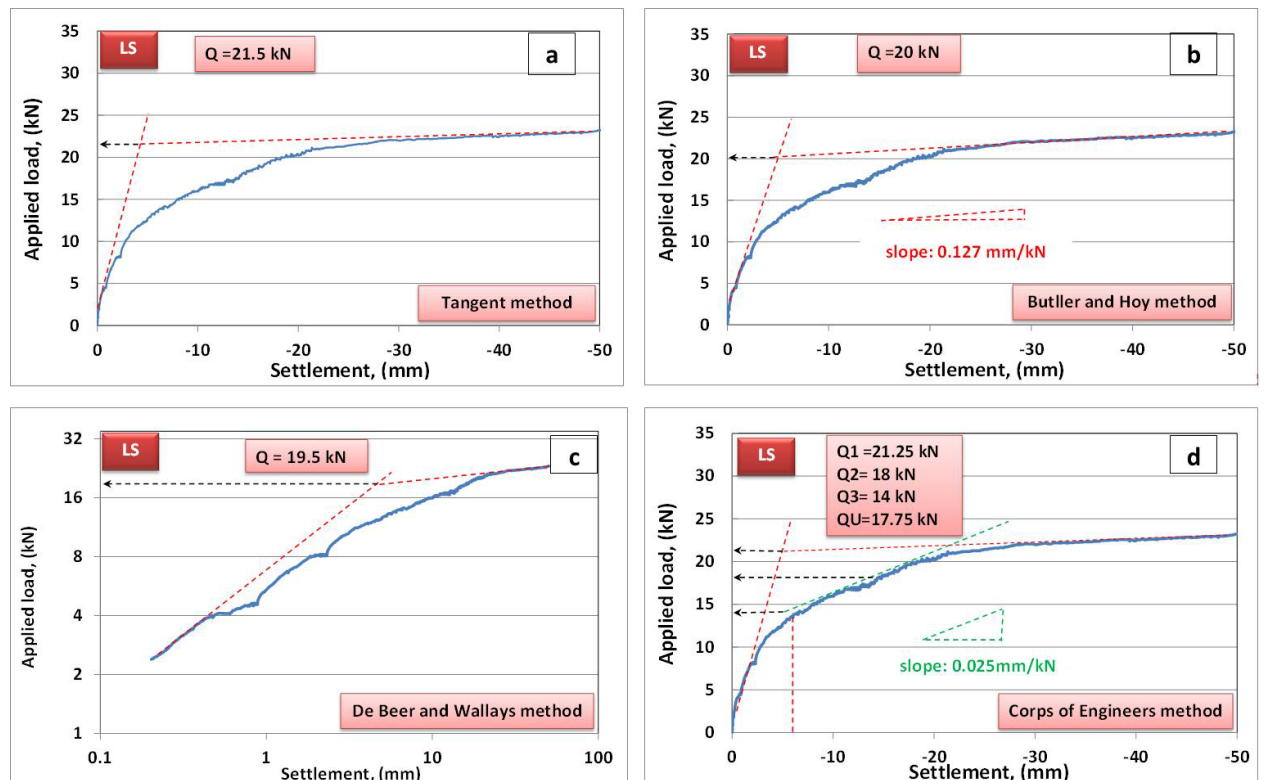


**Figure 7. The use of graphical methods in determining the ultimate bearing capacity for the footing reinforced with single micropile in layered soil condition.**

The ultimate load values at failure for the six loading instances were determined using the four aforementioned graphical methodologies, the results are listed in Table 2. It is observed that these values are differed to each other due to the difference in the methodology used to determine the point of failure for each method. Again, the maximum values of bearing capacity for the different six loading types are those



values obtained from the tangent method followed by the other three methods [36, 37, 38]. The variations in the ultimate capacities between the maximum and the minimum values are 50.0 %, 50.0 %, 35.1 %, 28.4 %, 21.1 %, and 23.5 % for the footing type of NLF, NLS, NLG, LF, LS, and LG, respectively. Therefore, taking the average ultimate load obtained from the four different approaches is the most sensible way to calculate the ultimate capacity. Table 2 lists the average ultimate load for each case. It is clear to notice that these values ranged between 11.25–24.63 kN. Taking into account that the square loading plate with ten centimeters a side, thus the bearing capacity ranges between 1125–2463 kPa. Fig. 8 shows the variation of ultimate bearing capacity for the studied cases. It is well noted that the bearing capacity of the foundation increases when the condition of the non-layered soil changes to the layered one. This finding is attributed to the improvement of the characteristics of the lower soil layers compacted with the modified Proctor energy (denser) compared to the properties of the upper soil layers compacted with the standard Proctor energy. Also, the results presented in Fig. 8 clearly show that the bearing capacity increases when the type of footing reinforced with a single micropile change to the case of a footing reinforced with a group of micropiles.

**Table 2. Failure loads of footing determined by different graphical methods.**

Methods	Footing type					
	NLF*	NLS*	NLG*	LF*	LS*	LG*
Tangent method	13.50	15.75	25.00	20.75	21.50	26.25
Butler and Hoy, 1977	13.00	15.50	24.70	19.50	20.00	25.50
De Beer and Wallays, 1972	9.50	12.50	22.50	18.50	19.50	24.50
U.S. Army Corps of Engineering, 1991	9.00	10.50	18.50	16.16	17.75	21.25
Ave. load value at failure, (kN)	11.25	13.56	22.68	18.73	19.69	24.63

\* Non layered soil with flat footing- NLF  
 Non layered soil with single micropile – NLS  
 Non layered soil with group micropile – NLG  
 Layered soil flat footing – LF  
 Layered soil with single micropile – LS  
 Layered soil with group micropile – LG

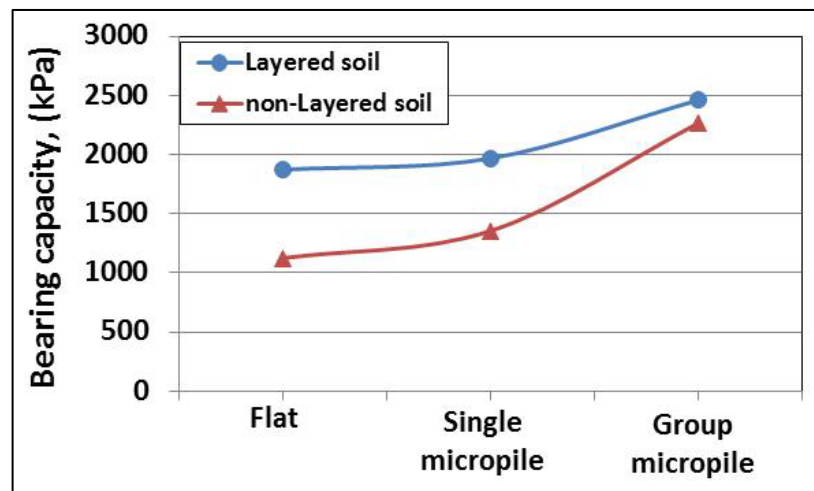


**Figure 8. Ultimate bearing capacity of the loading plate at different conditions.**

The next section deals with the bearing capacity ratio (BCR) and the percent of settlement reduction (PSR) when changing the state of the footing from non-reinforced footing to reinforced footing with a single micropile and/or with a group of micropiles, also when changing the state of the soil condition from non-layered soil to the layered one.

### 3.4. Bearing Capacity Ratio and Percent of Settlement Reduction

The bearing capacity ratio (BCR) is a dimensionless factor that can be used to examine the degree of improvement of the bearing capacity of footing at a certain condition. Equation (1) can be used to determine (BCR):

$$BCR, (\%) = \frac{q_{ult.(reinf.)}}{q_{ult.(non-reinf.)}} 100, \quad (1)$$



where  $q_{ult.(reinf.)}$  is the ultimate bearing capacity of loading plate reinforced with single micropile or group micropiles; while  $q_{ult.(non-reinf.)}$  is the ultimate bearing capacity of non-reinforced loading plate (flat plate).

For example, the (BCR) of single micropile ( $BCR_{S-M}$ ) can be calculated as:

$$BCR_{S-M}, (\%) = \frac{1969}{1873} \times 100, \quad BCR_{S-M}, (\%) = 1.05.$$

The BCRs for varying studied conditions are listed in Table 3. The data analysis shows that the BCR is more than 1 for all studied cases. Furthermore, for a given type of reinforcement, the BCRs decrease remarkably for the layered soil compared to the non-layered soil. Thus, it can be concluded that the BCR is strongly influenced according to soil condition during the test (i.e. layered soil or non-layered soil conditions). Also, the variation in the BCRs is clear when the type of footing reinforcement differs, the higher ratios belong to the footing reinforced with group micropiles.

**Table 3. Calculated values of the bearing capacity ratio, (%).**

Soil condition	Bearing capacity, (kPa)			Bearing capacity ratio, (%)	
	Flat	Single micropile	Group micropile	BCRS-M	BCRG-M
Layered	1873	1969	2463	1.05	1.32
Non-layered	1125	1356	2268	1.21	2.02

Again, the previous results showed that the reinforcement of the loading plate with micropiles reduces the settlement. To investigate these results distinctly, the percentage of settlement reduction (PSR) was calculated for each studied case, as shown in Fig. 9. Equation (2) was used to calculate the PSR:

$$PSR, (\%) = \frac{S_f - S_r}{S_f} 100, \quad (2)$$

where  $S_f$  is the settlement of flat loading plate at a certain applied load while  $S_r$  is the settlement of the loading plate reinforced with micropile (single or group) at the applied load corresponding to  $S_f$  condition.

For the layered soil condition, the PSRs ranged between 35–20 % and 95–60 % for the loading plate reinforced with a single micropile and group micropiles, respectively. While in the case of non-layered soil, the PSR ranged between 30–20 % for the case of a loading plate reinforced with a single micropile. Again, the PSR is around 80 % for the case of a loading plate reinforced with a group of micropiles. It is noted from Fig. 9 that the highest PSR belongs to the layered soil compared to the non-layered soil condition.

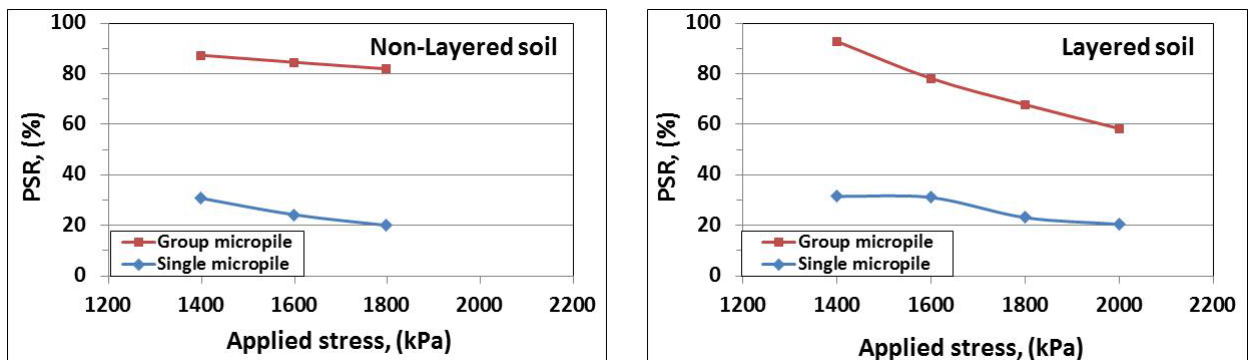


**Figure 9. Percent of settlement reduction for footings tested in different conditions.**

To give a discussion of the overall outcomes above, it can be said that the bearing capacity of the footing increases after being reinforced with a single micropile due to the creation of friction between the micropile and the surrounding soil. Additionally, the soil confinement on the one hand and the increase in the footing's stiffness on the other hand clearly have an impact on the BCR of the footing reinforced with a group of micropiles as opposed to the BCR of the footing reinforced with a single micropile. Another premise for interpreting the results is that the presence of group micropiles is likely to act as a senior pile. Also, the

failure in the soil turns into a block failure type with a perimeter of the senior pile equal to about 15.6 cm (six micropiles  $\times$  "0.6 + 2" the micropile diameter and the spacing between micropile, respectively). In this case, the interaction between this pile and the surrounding soil will increase, and thus the frictional surface area will increase. This, in turn, results in an increase in BCR and a decrease in PSR.

Regarding the effect of soil homogeneity, for the layered soil condition (the lower soil layers have a greater density than the upper soil layers), the results show that there is a clear increase in the footing bearing capacity or an improvement in the behavior of the load-settlement curves. It is very acceptable to explain these findings due to the increase in the angle of internal friction for the lower soil layers of high density compared to the upper soil layers of low soil density. However, it is possible to add to this interpretation the conclusion of [16]: the dense soil results in positive dilatancy during the load-settlement test, whereas the rule of the skin friction of micropile become crucial in the development of footing bearing capacity. On contrary, the soils with medium or low density will be exposed to negative or contractive dilatancy during the load-settlement test, and this will not lead to a significant increase in the bearing capacity of the footing, as is the case of dense soils.

## 4. Conclusions

The purpose of the current study is to investigate the effectiveness of micropiles in strengthening the soil and minimizing footing settlement of structures built on sandy silty soil from the eastern bank of the Tigris River in Mosul city - Iraq. The study is carried out using the experimental program on a laboratory-scaled model. The study was also interested in investigating the role of soil heterogeneity (weaker soil underneath by stronger soil) in the behavior of the load-settlement curves. The study's outcomes are as follows:

1. As a tool, the physical model was successful in identifying and describing the load-settlement curves for the six different loading scenarios performed in this study, including flat footing and footing reinforced with single or group micropiles in two different cases of soil homogeneity (layered and non-layered soil).
2. For all the cases studied, the footing's load settlement behavior under an axial compressive load is non-linear.
3. The use of micropiles as vertical reinforcement of the footing has a significant impact on the behavior of the load-settlement curve; an increase in the bearing capacity or a decrease in the settlement of the footing.
4. The BCR and PSR are two non-dimensional factors that are used to examine the improvement of the footing when reinforced with micropiles.
5. The role of the footing reinforcement in the non-layered soil is more obvious than in the layered soil. The bearing capacity of the footing reinforced with group micropile embedded in non-layered soil is 2268 kPa which is equivalent to BCR = 202 % more than non-reinforced footing. Whilst, the footing reinforced with a group of micropiles but embedded in layered soil has a bearing capacity of 2463 kPa or 132 % more than the footing without reinforcement BCR = 132 %.
6. In contrast to layered soil, the role of footing reinforcement is more noticeable in non-layered soil. The bearing capacity of the footing reinforced with group micropile embedded in non-layered soil is 2268 kPa which is equivalent to 200 % more than non-reinforced footing BCR = 202 %. Whilst, the footing reinforced with a group of micropiles but embedded in layered soil has a bearing capacity of 2463 kPa or 132 % more than the footing without reinforcement BCR = 132 %.
7. In the case of non-layered soil, the presence of the strong soil layers under the weak soil layers increases the bearing capacity from two points of view: the first is that the increase in the density of the strong soil layers increases the angle of internal friction and thus increases the bearing capacity of the footing. The second one is that the presence of the micropiles in the strong soil layers leads to an increase in the confinement of the soil surrounding these micropiles, and thus the occurrence of a positive dilatancy for the soil that has a high density, which increases in the bearing capacity. This is not the case in low-density soil layers which are accompanied by negative or contractive dilatancy during the load-bearing test.

## References

1. Bhattacharjee, A., Mittal, S., Krishna, A. Bearing capacity improvement of square footing by micropiles. *International Journal of Geotechnical Engineering*. 2011. 5(1). Pp. 113–118. DOI: 10.3328/IJGE.2011.05.01.113-118
2. Bruce, D.A., DiMillo, A.F. A primer on micropiles. *Civil Engineering*. 1995. 65(12). Pp. 51–54.
3. Srivastava, A., Kumar, P., Babu, G.S. Stability analyses of 18 m deep excavation using micro piles. *IGC Delhi* 2012.

4. Ma, L., Hu, Y., Gu, D., Jiang, C. Characteristics and Application of Micropiles in Slope Engineering. Proceedings of China-Europe Conference on Geotechnical Engineering: Volume 2. Springer, 2018. Pp. 1504–1507.
5. Bruce, D.A., Yeung, C.K. Minipiling at the Hong Kong country club. Hong Kong Contract. 1983. Pp. 13–18.
6. Bruce, D.A., DiMillio, A.F. Introduction to micropiles: an international perspective. Foundation upgrading and repair for infrastructure improvement. ASCE, Geotechnical Special Publication. 1995. No 50 Pp. 1–26.
7. Bruce, D.A., Nicholson, P.J. The practice and application of pin piling. ASCE Foundation Engineering Conference. Evanston IL, 1989. Pp 1–19.
8. Tsukada, Y., Ichimura, Y. Micropiles in Japan: present status and future prospects. International Workshop of Micropile. 1997. Pp. 265–278.
9. Han, J., Ye, S-L. A field study on the behavior of micropiles in clay under compression or tension. Canadian Geotechnical Journal. 2006. 43(1). Pp. 19–29. DOI: 10.1139/t05-089
10. Lizzi, F. The Static Restoration of Monuments. Sage Publisher, Genoa, Italy. 1982. Pp 146.
11. Lizzi, F. The Pali Radice (Micropiles) for the preservation of monuments and historic sites. Geotechnical Engineering for the Preservation of Monuments and Historic Sites. 1997. Pp. 463–469.
12. Bruce, D.A., DiMillio, A.F., Juran, I. Micropiles: the state of practice part 1: characteristics, definitions and classifications. Proceedings of the Institution of Civil Engineers-Ground Improvement. 1997. 1(1). Pp. 25–35.
13. Bruce, D.A., Cadden, A.W., Sabatini, P.J. Practical advice for foundation design – micropiles for structural support. Proceedings GeoFrontiers: contemporary issues in Foundation Engineering, ASCE. 2005. Pp. 1–25. DOI: 10.1061/40777(156)14
14. Shah, I.A., Zaid, M., Farooqi, M.A., Ali, K. Numerical study on micropile stabilized foundation in flyash. Indian Geotechnical Journal. 2021; 51: Pp. 1099–1106. DOI: 10.1007/s40098-020-00476-6
15. Malik, B.A., Shah, M.Y., Sawant, V.A. Influence of micropile parameters on bearing capacity of footings. Environmental Science and Pollution Research. 2021. 28(35). Pp. 48274–48283. DOI: 10.1007/s11356-021-14062-7
16. Tsukada, Y., Miura, K., Tsubokawa, Y., Otani, Y., You, G-L. Mechanism of bearing capacity of spread footings reinforced with micropiles. Soils and Foundations. 2006. 46(3). Pp. 367–376. DOI: 10.3208/sandf.46.367
17. Sharma, B., Zaheer, S., Hussain, Z. Experimental model for studying the performance of vertical and batter micropiles. Proceedings of Geo-Congress, Geo-characterization and Modeling for Sustainability. Atlanta GA, ASCE. 2014. Pp. 4252–4264. DOI: 10.1061/9780784413272.412
18. Sharma, B., Buragohain, P. Behaviour of micropile groups under oblique pull out loads in sand. Indian Geotechnical Journal. 2014. 44(4). Pp. 400–408. DOI: 10.1007/s40098-013-0091-1
19. Jose, S., Prakash, V.M., Paul, H. A model study on lateral behaviour of micropile under Inclined compressive loads in sand. International Research Journal of Engineering and Technology. 2018. 5(4). Pp. 2946–2950.
20. American Society for Testing and Materials (ASTM). Annual Book of ASTM Standards. 4. Construction. 04.08. Soil and rock (I). West Conshohocken PA, 2005.
21. Poulos, H.G. Some aspects of skin friction of piles in clay under cyclic loading. Geotech Eng ASCE. 1980. 12. Pp. 1–17.
22. Dash, S.K., Sireesh, S., Sitharam, T.G. Model studies on circular footing supported on geocell reinforced sand underlain by soft clay. Geotextiles and Geomembranes. 2003. 21(4). Pp. 197–219. DOI: 10.1016/S0266-1144(03)00017-7
23. Latha, G.M., Dash, S.K., Rajagopal, K. Numerical simulation of the behavior of geocell reinforced sand in foundations. International Journal of Geomechanics. 2009. 9(4). Pp. 143–152. [https://doi.org/10.1061/\(ASCE\)1532-3641\(2009\)9:4\(143\)](https://doi.org/10.1061/(ASCE)1532-3641(2009)9:4(143))
24. Elsaied, A.E. Performance of footing with single side micro-piles adjacent to slopes. Alexandria Engineering Journal. 2014. 53(4). Pp. 903–910. DOI: 10.1016/j.aej.2014.07.004
25. You, G-L, Miura, K. Ishito, M. Behavior of micropile foundations under inclined loads in laboratory tests. Lowland Technology International. 2003. 5. Pp. 16–26.
26. Shah, I.A., Ali, K., Farooqi, M.A. A numerical study on the bearing capacity of fly-ash reinforced with fine micropiles. International Journal of Geosynthetics and Ground Engineering. 2021. DOI: 10.1007/s40891-020-00245-8
27. Hong, W-P., Chim, N. Prediction of uplift capacity of a micropile embedded in soil. KSCE Journal of Civil Engineering. 2015. 19(1). Pp. 116–126. DOI: 10.1007/s12205-013-0357-2
28. Moradi Moghaddam, H., Keramati, M., Ramesh, A., Naderi, R. Experimental evaluation of the effects of structural parameters, installation methods and soil density on the micropile bearing capacity. International Journal of Civil Engineering. 2021. DOI: 10.1007/s40999-021-00629-5
29. Alnuaim, A.M., El Naggar, M.H., El Naggar, H. Numerical investigation of the performance of micropiled rafts in sand. Computers and Geotechnics. 2016. 77. Pp. 91–105. DOI: 10.1016/j.compgeo.2016.04.002
30. Alnuaim, A.M., El Naggar, M.H., El Naggar, H. Performance of micropiled rafts in clay: Numerical investigation. Computers and Geotechnics. 2018. 99. Pp. 42–54. DOI: 10.1016/j.compgeo.2018.02.020
31. Mashhoud, H.J., Yin, J-H., Panah, A.K., Leung, Y.F. Shaking table test study on dynamic behavior of micropiles in loose sand. Soil Dynamics and Earthquake Engineering. 2018. 110(2). Pp. 53–69. DOI: 10.1016/j.soildyn.2018.03.008
32. Ambak, K., Abdullah, N.A.H., Yusoff, M.F., Abidin, M.H.Z. Soft soil improvement for sub-grade layer using hexagonal micropiles layout. Journal of Physics: Conference Series. 2018. DOI: 10.1088/1742-6596/995/1/012020
33. Cheng, Z., Deng, Y. Bearing characteristics of moso bamboo micropile-composite soil nailing system in soft soil areas. Advances in Material Science and Engineering. 2020. DOI: 10.1155/2020/3204285
34. Jha, J.N., Choudhary A.K., Gill K.S. Bearing capacity improvement of soil using bamboo micropiles. International Journal of Plasma Science and Engineering. 2010. 3(1). Pp. 167–176.
35. Das, B.M., Sivakugan, N. Principles of foundation engineering. Cengage Learning, SI Edition. USA. 2018. 944 p.
36. Prakash, S., & Sharma, H. D. Pile foundations in engineering practice. John Wiley & Sons. 1991. 768 p.
37. De Beer, E.E., Wallays, M. Franki piles with overexpanded bases. La Technique des Travaux. 1972. Article no. 333.
38. USACE Engineering and Design Manual. Design of pile foundations, EM 1110-2-2906, US Army Corps of Engineers, Washington, DC. 1991.

**Information about the authors:**

**Asaad Al-Omari, PhD**

ORCID: <https://orcid.org/0000-0003-3032-1334>

E-mail: [asaad.alomari@uomosul.edu.iq](mailto:asaad.alomari@uomosul.edu.iq)

**Ahmed Al-Dabbagh,**

E-mail: [ahmed.20enp109@student.uomosul.edu.iq](mailto:ahmed.20enp109@student.uomosul.edu.iq)

*Received 08.02.2023. Approved after reviewing 19.10.2023. Accepted 20.10.2023.*



Research article

UDC 691.32

DOI: 10.34910/MCE.134.9



## An investigation on the nonlinear dynamic behavior of reinforced concrete shear wall under seismic loading

A. Hasanzadeh<sup>1</sup> , M. Hematibahar<sup>2</sup> , N.I. Vatin<sup>3</sup> , M. Kharun<sup>4</sup> 

<sup>1</sup> Civil Engineering Department, Babol Noshirvani University of Technology, Babol, Iran

<sup>2</sup> ANO SAFAS, Moscow, Russian Federation

<sup>3</sup> Peter the Great St. Petersburg Polytechnic University, St. Petersburg, Russian Federation

<sup>4</sup> Moscow State University of Civil Engineering, Moscow, Russian Federation

✉ [a\\_hasanzade64@yahoo.com](mailto:a_hasanzade64@yahoo.com)

**Keywords:** reinforced concrete, shear wall, nonlinear dynamic analysis, seismic loading, finite element method

**Abstract.** The current research presents a new approach for nonlinear dynamic analysis of reinforced concrete shear wall under seismic loading in ANSYS Mechanical software via adding APDL commands. By applying lateral load, the behavior of reinforced concrete shear wall as a model was analyzed using the proposed method and the maximum bearing load, maximum displacement and the positions of the occurrence of the cracks were determined. Then, this shear wall was analyzed through Response Spectrum Method (RSM) as a linear dynamic method and the results of nonlinear dynamic method were compared with RSM. The results of nonlinear dynamic analysis showed that the maximum loading and its maximum displacement were 276 kN and 2 cm, respectively. However, the maximum displacement obtained by RSM was more than the corresponding value using the proposed nonlinear method, which this is mainly due to the consideration of safety factor in RSM. In addition, the whole capacity of materials is employed in nonlinear analysis, which this issue is not taken into account in RSM.

**Funding:** The research was funded by the Ministry of Science and Higher Education of the Russian Federation as the grant Self-Healing Construction Materials (contract No. 075-15-2021-590 dated 04.06.2021)

**Citation:** Hasanzadeh, A., Hematibahar, M., Vatin, N.I., Kharun, M. An investigation on the nonlinear dynamic behavior of reinforced concrete shear wall under seismic loading. Magazine of Civil Engineering. 2025. 18(2). Article no. 13409. DOI: 10.34910/MCE.134.9

### 1. Introduction

Reinforced concrete (RC) shear wall is a vertical element utilized to withstand lateral loads such as wind and seismic loads acting on a building structure. Many studies have been performed on the modeling of the behavior of the RC shear wall during earthquakes [1–4]. Modeling techniques have been progressively updated during the last two decades, moving from linear static to nonlinear dynamic, enabling more realistic representation of the behavior of structure. Different models have been developed over time, including macro-models, vertical line element models, finite element (FE) models, and multi-layer models. For example, Epackachi et al. [5] developed a FE model to simulate the nonlinear cyclic response of flexure-critical steel-plate concrete (SC) composite shear walls. Each SC wall was constructed with steel faceplates, infill concrete, steel studs and tie rods, and a steel baseplate that was post-tensioned to a RC foundation. They showed that the FE predictions are in good agreement with the measured values. Rafiei et al. [6] presented the development and validation of FE models to simulate the performance of a composite



shear wall system consisting of two skins of profiled steel sheeting and an infill of concrete under in-plane loadings. According to the results, the developed FE models were capable of simulating the behavior of composite walls under in-plane loadings with reasonable degree of accuracy.

Kharun et al. [7] simulated the behavior of shear walls with different material properties (glass fiber, basalt fiber, steel fiber and conventional concrete) under earthquake loading via SAP2000 software. They found that glass fiber and conventional concrete shear walls had higher dissipation energy and showed more suitable responses during earthquake. Rahai and Hatami [8] assessed the behavior of composite steel shear wall (CSSW) under cyclic loadings. They focused on the impact of shear studs spacing variation, middle beam rigidity, and the method of beam to column connection on the CSSW behavior. They reported that the increase of the shear studs spacing can reduce the slope of load–displacement curve and enhance the ductility up to a specific studs' spacing. Najm et al. [9] employed ANSYS software to numerically analyze the behavior of smart composite shear walls under dynamic loading. The results of FE analysis indicated excellent agreement with the experimental test results in terms of the ultimate strength, initial stiffness and ductility. Wang et al. [10] developed FE models to forecast the hysteresis behavior of composite shear walls with stiffened steel plates and in-filled concrete. They found that the web plate contributes between 55 % and 85 % of the total shearing resistance of the wall. Furthermore, the corner of wall mainly resisted the vertical force and the rest of wall resisted the shear force.

Wang et al. [11] studied the seismic performance of shear walls with different coal gangue replacement rates. They found that the stress performance and failure morphology of coal gangue concrete shear walls and conventional concrete shear walls are extremely similar, and the characteristics of the hysteretic and backbone curves are approximately the same. They concluded that with increasing in the coal gangue replacement rate, the stiffness degradation gradually slows. Therefore, it is possible to construct a shear wall using coal gangue concrete instead of conventional concrete. Sijwal et al. [12] used ABAQUS FE software for modeling of the concrete-filled cold-formed steel shear wall (CFCSW) and validated their results with the experimental results. They found that the FE analysis is able to appropriately simulate the overall behavior of CFCSW. In addition, ABAQUS satisfactorily predicted the load carrying capacity of the CFCSW. Liu et al. [13] investigated seismic performance of recycled aggregate concrete (RAC) composite shear walls with different expandable polystyrene (EPS) configurations. They found that the seismic resistance behavior of the EPS module composite performed better than ordinary recycled concrete for shear walls. In addition, shear walls with sandwiched EPS modules had a better seismic performance than those with EPS modules lying outside. Kamgar et al. [14] evaluated the dynamic behavior of steel shear wall (SSW) stiffened with Shape-Memory Alloy (SMA). They indicated that SMA strips are able to limit structural and non-structural damage under earthquakes. Besides, SMA strips can delay the SSW failure. They concluded that their method can be a good retrofitting approach to strengthen existing steel structures against seismic loading.

On the other hand, linear analysis is an analysis, in which there is a linear relationship between applied forces and displacements. Besides, the stresses remain within the linear elastic range. In nonlinear analysis, the applied forces and displacements have non-linear relationship. Nonlinearity effects can be due to geometry (e.g. large deformations), materials (e.g. elasto-plastic materials), or support conditions. A linear analysis mainly requires linear elastic materials and small displacements while a nonlinear analysis considers large displacements and elasto-plastic materials. Thus, the superposition effect cannot be applied. Another important difference is the stiffness matrix. The stiffness matrix remains constant during a linear analysis while it is not constant in the nonlinear analysis. Whenever a material in the model demonstrates a nonlinear stress-strain behavior under the specified loading, nonlinear analysis must be used. ABAQUS is FE software, which is able to simulate linear and nonlinear materials easily, while ANSYS Mechanical is not able to simulate nonlinear material independently. In fact, Advertising Permit and Developer's License (APDL) commands have to be added to ANSYS Mechanical software in order to make it possible to simulate the behavior of nonlinear materials. APDL is a powerful structured scripting language used to interact with the ANSYS Mechanical. The lack of nonlinear definition of the material behavior in ANSYS Mechanical software is a neglected point that makes problems for engineers. Moreover, this software is not able to find cracks on the surface of concrete. To cover these gaps, in this study, the APDL commands have been added to ANSYS Mechanical software for investigation of the nonlinear behavior of reinforced RC shear wall under earthquake loading.

## 2. Methods

The concrete can not be defined as a nonlinear material in the ANSYS Mechanical. To change the behavior of material to the nonlinear behavior, the APDL commands were applied as a text in this study. The APDL text is based on Drucker–Prager theory. First, the isotropic elastic materials were selected in the ANSYS Mechanical (Fig. 1). Next, a displacement was applied as a loading with symmetries in X, Y and Z axis. Finally, the APDL commands were added to the ANSYS Mechanical (Figs. 2 and 3).

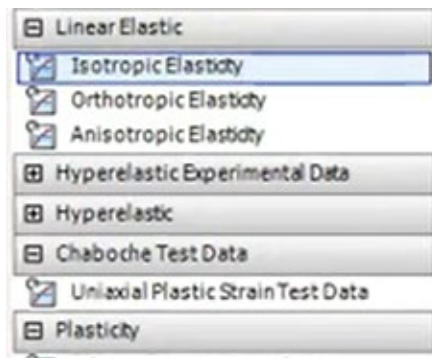


Figure 1. Selection of the material type.

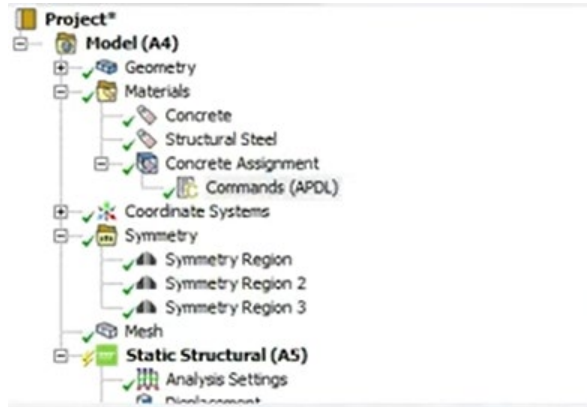


Figure 2. Settings of ANSYS Mechanical.

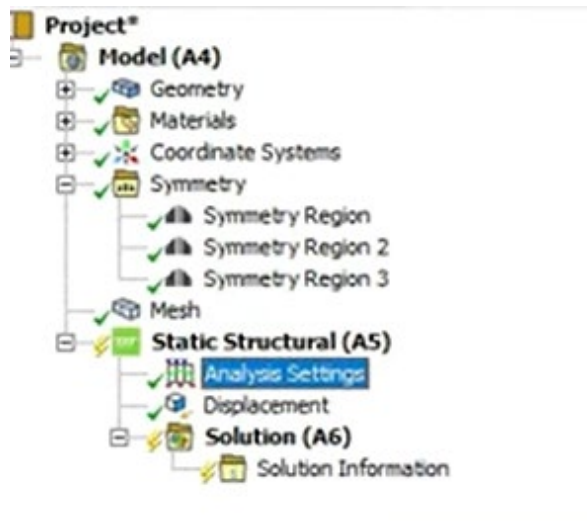
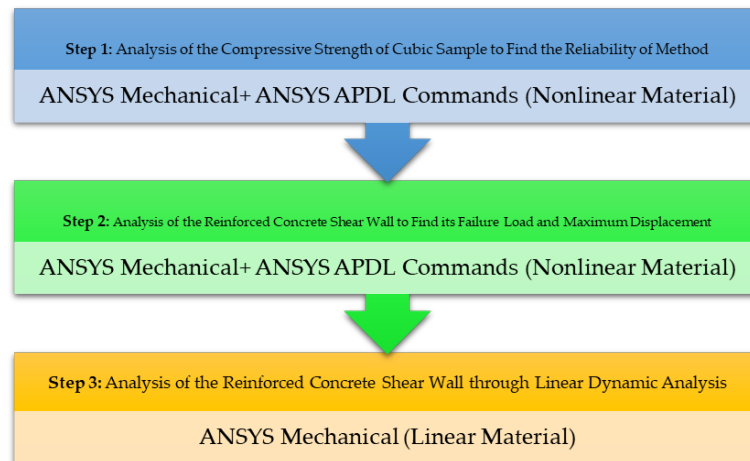


Figure 3. The addition of the APDL commands to the ANSYS Mechanical.

In the APDL command, compressive and tensile strength of concrete, tension cap hardening, compressive hardening constant, compression cap ratio constant, compressive, tensile damage threshold, and the number of quadratic elements were coded. The purpose of adding of these properties is simulating the compressive stress-strain curve of concrete in the ANSYS Mechanical. In fact, ANSYS Mechanical is not able to simulate the hardening and softening parts of stress-strain curve. In this term, the APDL commands help to find a new way to simulate this curve.

The research methodology has three steps, which have been shown in Fig. 4. At the first step, the compressive strength of cubic concrete sample (as a nonlinear material), and its compressive stress-strain curve were assessed using ANSYS Mechanical FE software via adding APDL commands to check the reliability of this software. It should be noted that the APDL commands were added to ANSYS Mechanical to change the behavior of concrete to a nonlinear behavior using the mentioned command. In fact, the first step is the basis for the the second and third steps to find the reliability of the proposed method. At the second step, the lateral load was applied to RC shear wall constructed by reinforced high-performance concrete (as a nonlinear material) and its maximum displacement and failure load were determined using

ANSYS Mechanical and APDL. At the third step, the behavior of RC shear wall was investigated by the Response Spectrum Method (RSM) as a linear dynamic analysis method. Finally, the results obtained by the second and third steps were compared with each other.



**Figure 4. The research methodology.**

### 2.1. Model Reliability

In this study, high-performance concrete with 1.2 % basalt fibers (HPC-12) was selected as the concrete material for the shear wall. Table 1 shows the properties of this concrete. To control the model reliability, the compressive strength and compressive stress-strain curve of a cubic HPC-12 sample were investigated through ANSYS Mechanical via adding the APDL commands. To simulate the cubic concrete sample, the Micro-Plane method was applied. This method has been employed by several researchers [15–18].

**Table 1. Mechanical properties of HPC-12 [19].**

Concrete type	Compressive Strength (MPa)	Tensile Strength (MPa)	Young Modulus (GPa)	Density (kg/m <sup>3</sup> )
HPC-12	94.5	14	33.8	3475

To find the compressive stress-strain curve, three symmetric sides in the cube (A, B, and C) were applied to the opposite sides of each natural coordinate axis (Fig. 5, a). Moreover, the material behavior was defined nonlinear in the software via APDL commands. The loading of 5 kN/mm<sup>2</sup> was applied at the Y- direction (Fig. 5, b).

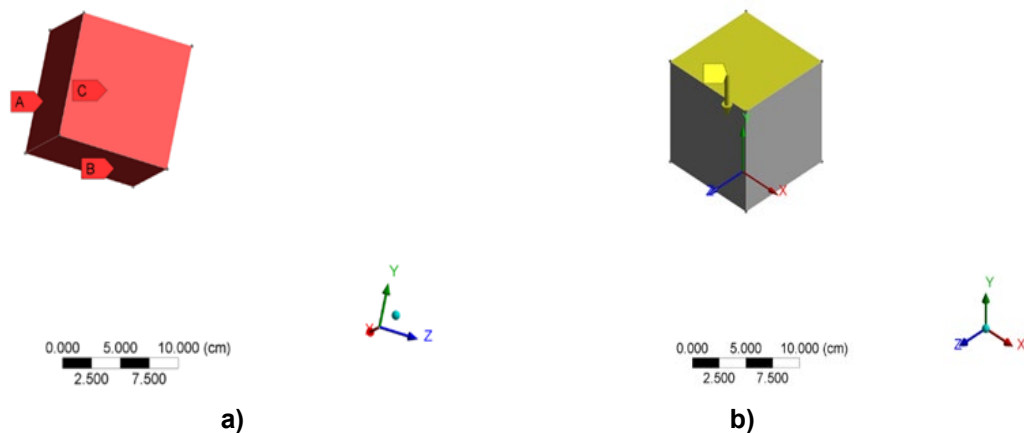


**Figure 5. Concrete cubic simulation: a) the symmetric sides; b) application of load.**

As seen in Table 2, the difference between experimental and numerical values of compressive strength is 0.6 MPa. Moreover, the compressive stress-strain curve was estimated via ANSYS software (Fig. 6). The comparison of the experimental and numerical results shows that the modeling has been performed with high accuracy. The results of the current study show the reliability of coding and APDL commands.

**Table 2. The comparison between experimental and numerical values of compressive strength.**

Experimental value (MPa)	Numerical value (MPa)	Difference (MPa)
94.5	93.9	0.6

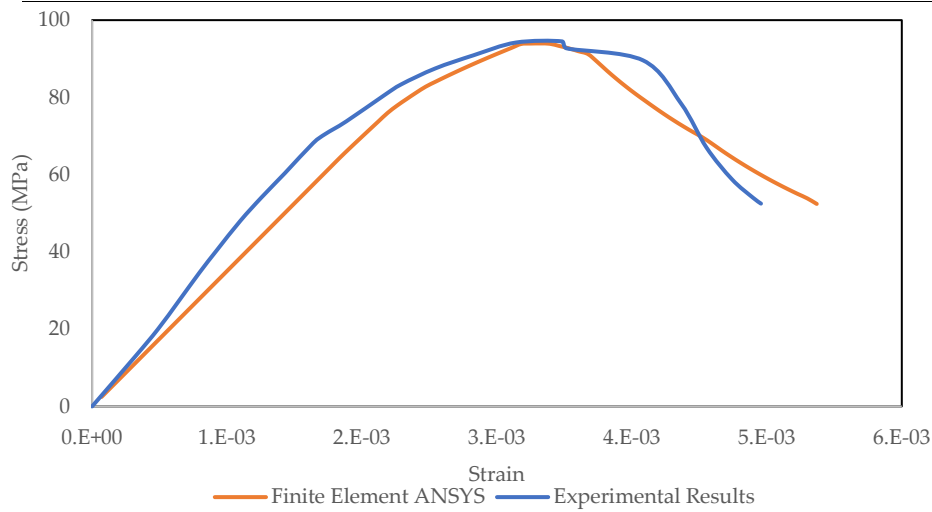


**Figure 6. Comparison between stress-strain curves (experimental and numerical).**

## 2.2. Modeling of RC Shear Wall

For the design of RC shear wall, ACI-318 [20] and Iranian Seismic Design Code [21] were used. According to the type and density of concrete, the shear wall thickness was selected. Then, the ratio of height to length of wall and also the horizontal and vertical reinforcement bars were calculated. The dimensions of shear wall are 500×300×30 cm, the horizontal rebars have a diameter of 16 mm used at every 5 cm, and the vertical rebars have a diameter of 16 mm used at every 41 cm. The foundation of RC shear wall was considered rigid. Shear wall model is shown in Fig. 7.

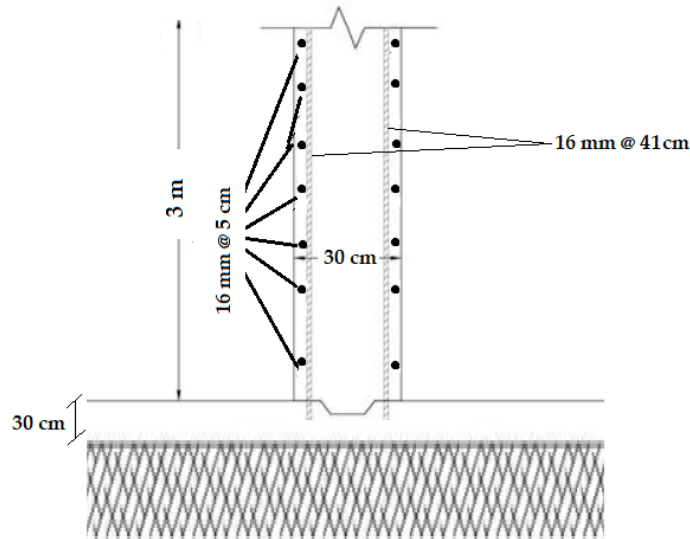


**Figure 7. Shear wall section in the current study.**

For the nonlinear analysis of the RC shear wall, the material was defined as nonlinear using APDL commands in ANSYS Mechanical software. The quadratic elements were used for meshing. Next, the behavior of materials was changed to nonlinear behavior through adding APDL commands to the ANSYS Mechanical. A lateral load of 10 kN/mm<sup>2</sup> at the X-direction was applied on the top of the RC shear wall (Fig. 8) to find the maximum bearing load and displacement of the shear wall in the lateral direction. Fig. 9 shows the position of rebars in RC shear wall model. The fixed supports were used in the current study.

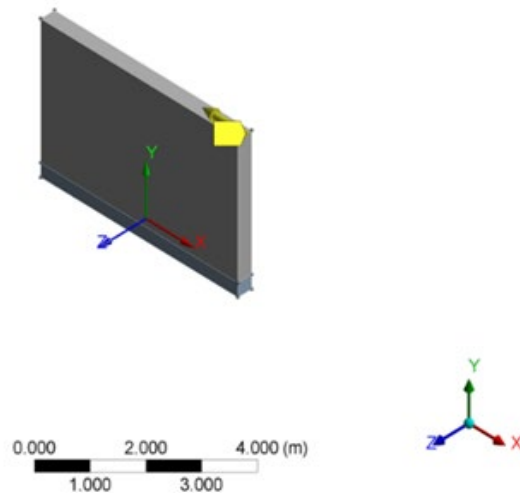


**Figure 8. The position of load application to RC shear wall (yellow spot).**

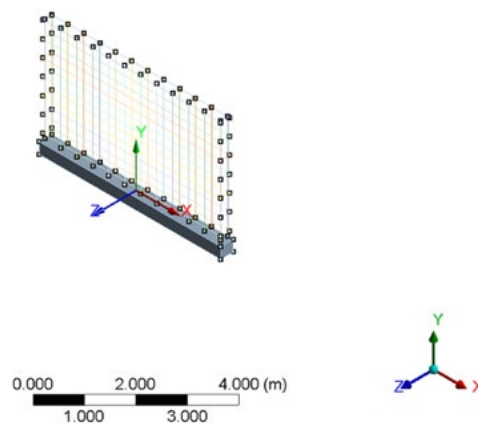


**Figure 9. The arrangement of rebars in RC shear wall model.**

### **2.3. Response Spectrum Method**

In this study, the behavior of RC shear wall under earthquake loading was analyzed using linear dynamic analysis. According to Iranian Seismic Design Code [21], there are two types of linear dynamic methods for analysis of structures under dynamic loads: 1 – RSM; 2 – Time Domain History Method (TDHM). RSM analysis is able to perform a more accurate estimation of the analysis considering the modal effects. TDHM depends on several criteria before applying to the structure while RSM is easier. Thus, in the current study, RSM was used for linear dynamic analysis.

A response spectrum is a plot of the peak or steady-state response (displacement, velocity, or acceleration) of a series of oscillators of varying natural frequencies that are forced into motion by the same base vibration or shock. RSM is a dynamic analysis method, which measures the contribution from each natural mode of vibration to indicate the likely maximum seismic response of an essentially elastic structure. It can be stated that it is a method to estimate the structural response of short, nondeterministic, and transient dynamic events such as earthquakes and shocks. The response-spectrum analysis provides insight into dynamic behavior by measuring pseudo-spectral acceleration, velocity, or displacement as a function of the structural period for a given time history and level of damping. It is practical to envelope response spectra such that a smooth curve represents the peak response for each realization of the structural period. The RSM is performed in the following four basic steps: 1 – modal analysis of the structure; 2 – calculation of the responses of the structure in each vibration mode; 3 – combining the effects of the modes; 4 – modifying the values of the responses of the structure.

In the modal analysis, the structural responses such as the internal forces of the members, displacement, floor shears, and support reactions are obtained separately for each mode. Due to the fact that the periods of vibration of the modes are different from each other, the maximum responses of the structure for various modes do not occur simultaneously, and for this reason, it is not possible to determine the total response of the structure by summing the response of different modes. In spectral analysis, the final response of the structure is obtained using the superposition of its different modes (within the frequency



domain). In fact, the response of the structure is a combination of various mode shapes. For each considered mode, based on the frequency and mass of the mode, the response of that mode is extracted from the design spectrum and then, is combined with the response of other modes to obtain the overall response of the structure. Combination methods include the following: 1 – Square Root Sum of Squares (SRSS); 2 – Complete Quadratic Combination (CQC), which is a modified method of SRSS for close modes. It is well-known that the application of the SRSS in seismic analysis for combining modals can cause significant errors.

The Peak Ground Acceleration (PGA) is computed according to the factored spectral response diagram. Three different earthquake pulses including Bam, Iran (2003), Mount Borrego, USA (1968), and Northern California, USA (1941) were selected to determine the Factorized Response Spectrum (FRS) diagram. FRS is called a spectrum, which is scaled to the standard design spectrum in Code with applying a coefficient factor. Fig. 7 shows the Time-Acceleration graphs of these earthquakes. The applied loads to RC shear wall in RSM are illustrated in Fig. 10.

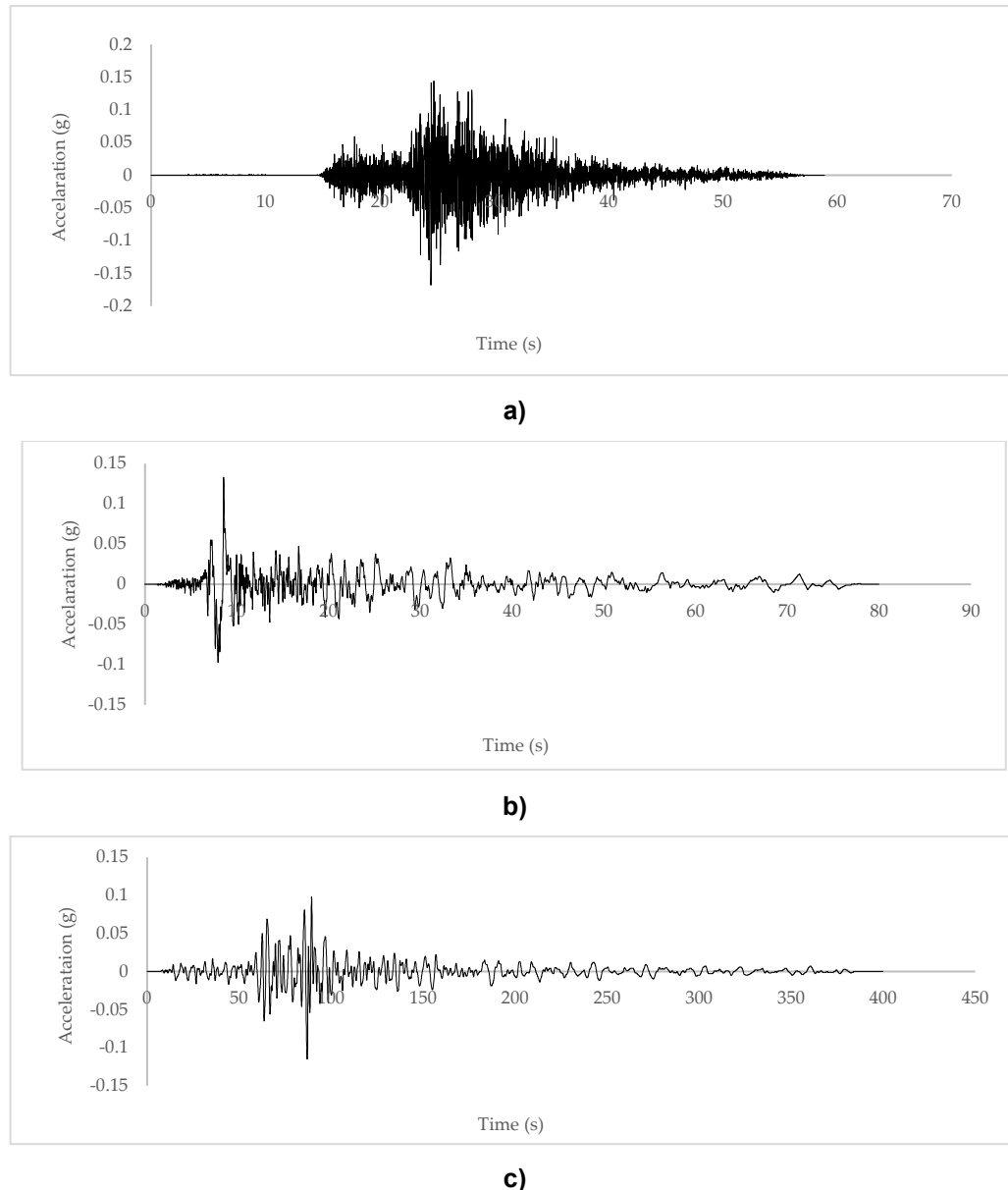


**Figure 10. The Time-Acceleration graphs for: a) Bam, Iran (2003); b) Borrego Mountain, USA (1968); c) Northern California, USA (1941).**

As seen, Bam and Northern California earthquakes have the highest and lowest frequency content, respectively. Northern California earthquake has the highest period and Bam has the lowest one. Earthquake records with low and high frequency have a greater effect on tall and short structures, respectively, due to the phenomenon of resonance. Moreover, amplitude of the earthquake record is the highest in Bam earthquake. The FRS diagram is shown in Fig. 11. The SRSS and CQC are recommended to plot the FRS

diagram. In this research, the SRSS used a damping ratio of 5 % of the structure weight as recommend by Iranian Seismic Design Code [21].

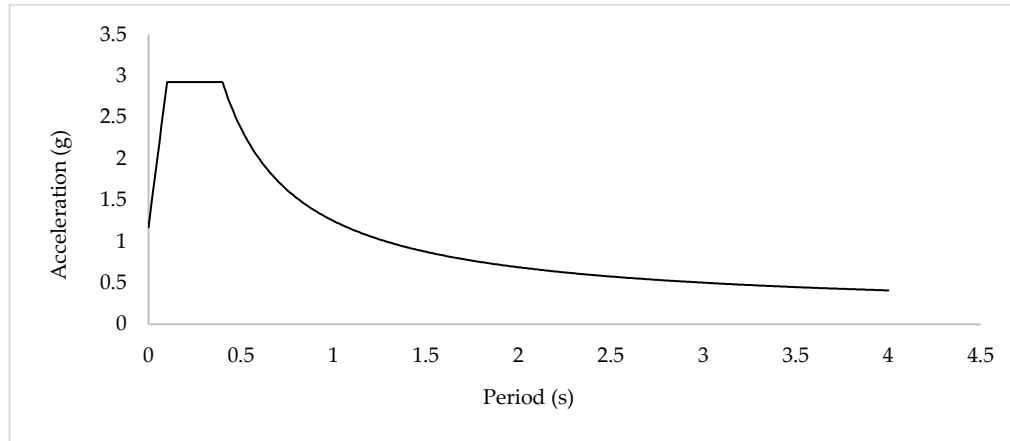


**Figure 11. The FRS diagram of three mentioned earthquakes.**

### **3. Results and Discussion**

#### **3.1. Results of Nonlinear Analysis**

Fig. 12 shows the load–displacement graph of RC shear wall using nonlinear analysis. As seen, the maximum load that RC shear wall can bear and its corresponding displacement are 276 kN and 2 cm, respectively. The shear wall under loading has three phases. The first step is the softening behavior, in which the displacement is lower than 0.39 cm and the loading is less than 118 kN. This section is the linear phase of the shear wall under lateral loading. The second stage is the hardening stage until the maximum bearing loading of 276 kN and displacement of 2 cm. The third stage is the shear wall failure, in which the displacement will be maximum and the load gets near to zero.

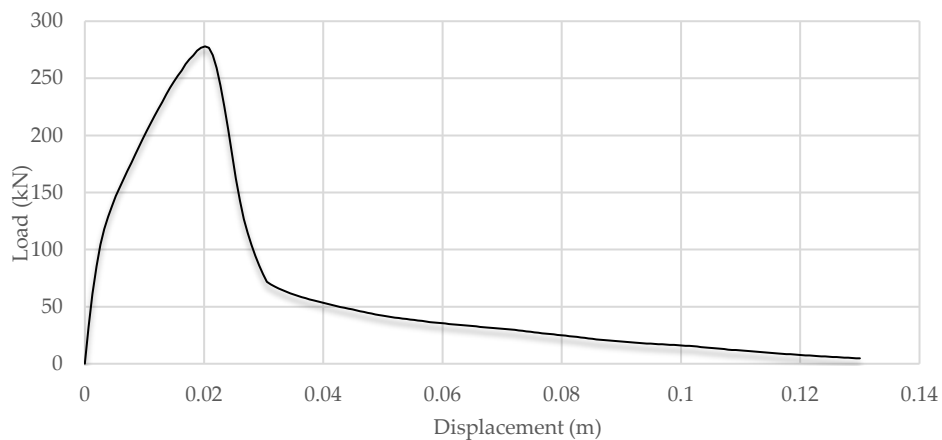


**Figure 12. Load–displacement graph of RC shear wall.**

Figs. 13 and 14 illustrate the values of displacements in RC shear wall on the concrete and rebar parts, respectively. As seen, the maximum displacement of RC shear wall occurs on its top. Table 3 presents the values of maximum bearing load, maximum linear load, and displacement at the maximum load.

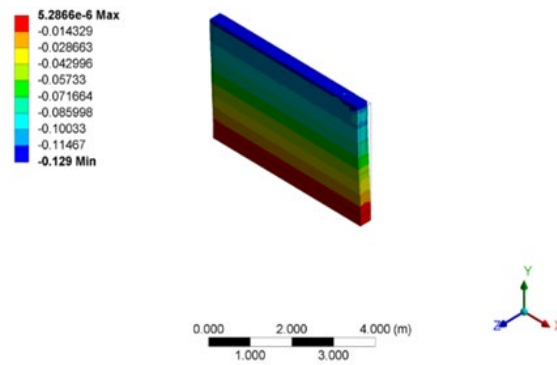


Figure 13. The displacement values in the RC shear wall.

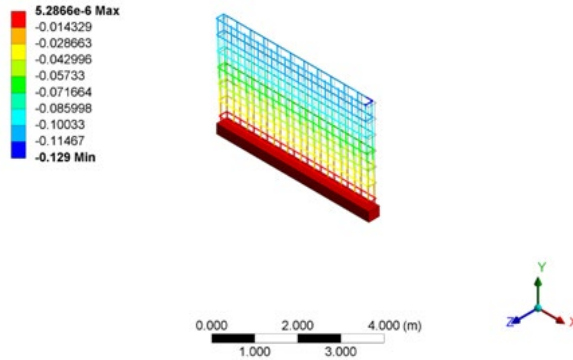


Figure 14. The displacement values in the rebars of RC shear wall.

Table 3. The comparison of the results.

Maximum load (kN)	Maximum linear load (kN)	Displacement at the maximum load (m)
276	118	0.0206

According to the results of the analysis, the joint of the shear wall with the foundation corners and also the middle of shear wall are critical zones in which cracks were occurred (Fig. 15). The maximum shear force likely occurs at these positions due to the stress concentration. Therefore, cracks have been generated near the edges of the shear wall and on its middle. ANSYS Mechanical is not able to show the cracks while the addition of APDL commands has made it possible to reveal the crack zones.



Figure 15. The cracks on the RC shear wall found by nonlinear analysis.

### 3.2. Results of Linear Dynamic Modal Analysis

The lateral behavior of any building can be written by a linear combination of the vibration modes of that building. Oscillating modes of every building are different forms of vibrations that can be formed at the structure height. Some modes of the structure are easily excited, in other words, with the lowest level of energy entering the building, those modes can be excited in the building. These modes have the highest vibration period. The highest vibration period and the lowest frequency in a building are related to the first

vibration mode of that building. Due to the high excitability of the first mode, the largest displacement contribution for a specific vibration is related to this mode. By moving towards higher vibration modes, more energy will be required to excite the modes and the vibrational period of the modes will be decreased. Sometimes, the stimulation of higher modes is difficult (requires high energy) that the Codes assume them as non-sense modes and do not include them in the calculations because the contribution of these modes in the lateral behavior of the structure is insignificant. For the simplicity of modal calculations, it is possible to assume an equivalent single degree of freedom structure for each of the vibration modes of the building, and the jump of that single degree of freedom structure is equal to the vibration jump of the investigated mode in the building.

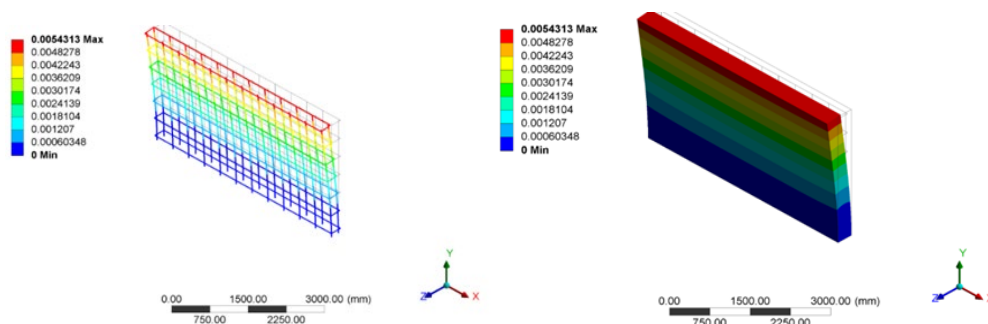
The linear dynamic analysis is investigated by dynamic section of ANSYS Mechanical. In order to analyze RC shear wall through RSM, six natural modals were evaluated by ANSYS Mechanical. According to Iranian Seismic Design Code [21], the cumulative mass up to the modes must be larger than 80 ~ 90 % of the total mass. Moreover, in each of the two orthogonal extensions of the building, all oscillation modes that their total effective masses are more than 90 % of the total mass of the structure should be considered. Thus, six modes were taken into account in this study. Table 4 illustrates the six natural modal data such as natural frequencies, mass participation factor, and effective mass.

**Table 4. The modal analysis results.**

Modal No.	Frequency [Hz]	Mass participation factor X-direction	Effective mass X-direction (g)
1	25.233	1.40E-12	1.97E-24
2	43.621	9.42E-13	8.88E-25
3	91.126	2.68E-12	7.18E-24
4	151.83	2.85E-11	8.13E-22
5	170.28	9.61E-11	9.37E-20
6	173.15	4.34E-10	1.89E-19

As expected, with the increase in the vibration modes of the structure, the vibration frequency increases. Therefore, the first mode has the lowest frequency and highest period while the sixth mode has the highest frequency and lowest period. Mass participation factors are scalars that measure the interaction between the modes and the directional excitation in a given reference frame. Larger values of mass participation factors indicate a stronger contribution to the dynamic response. Hence, the sixth mode has the highest contribution. The effective mass factors associated with each mode represents the amount of system mass participating in that mode in a given excitation direction. This value is given as a percentage of the total system mass. Therefore, a mode with a large effective mass will be a significant contributor to the system response in the given excitation direction. A common rule of thumb for linear dynamic analysis is that a mode should be included if it contributes more than 1–2 % of the total effective mass. As expected, the sixth mode has the maximum value in effective mass.

Fig. 16 illustrates six modal shapes of the RC shear wall. As seen, if the structure vibrates in a lower mode, it needs less energy while in higher modes, more energy is required. At the sixth mode, the RC shear wall has the most intricate deformity among others modes. Moreover, displacements are high at the top of the shear wall. It can be said that the first mode has the simplest oscillation and moves along the z-axis. As the mode goes higher, the probability of fluctuation in this mode decreases. In the second mode, the shear wall oscillates in the direction perpendicular to the first mode and in the direction of the x-axis. In the third mode, the oscillation bends in-plane around the z-axis at the corner of the wall. In the fourth mode, oscillation moves towards the z-axis. In the fifth mode, the oscillation is around the z-axis and the maximum bending is in the middle of the shear wall. Finally, the sixth mode has the lowest probability of occurrence and represents a kind of twisting deformation.



a)

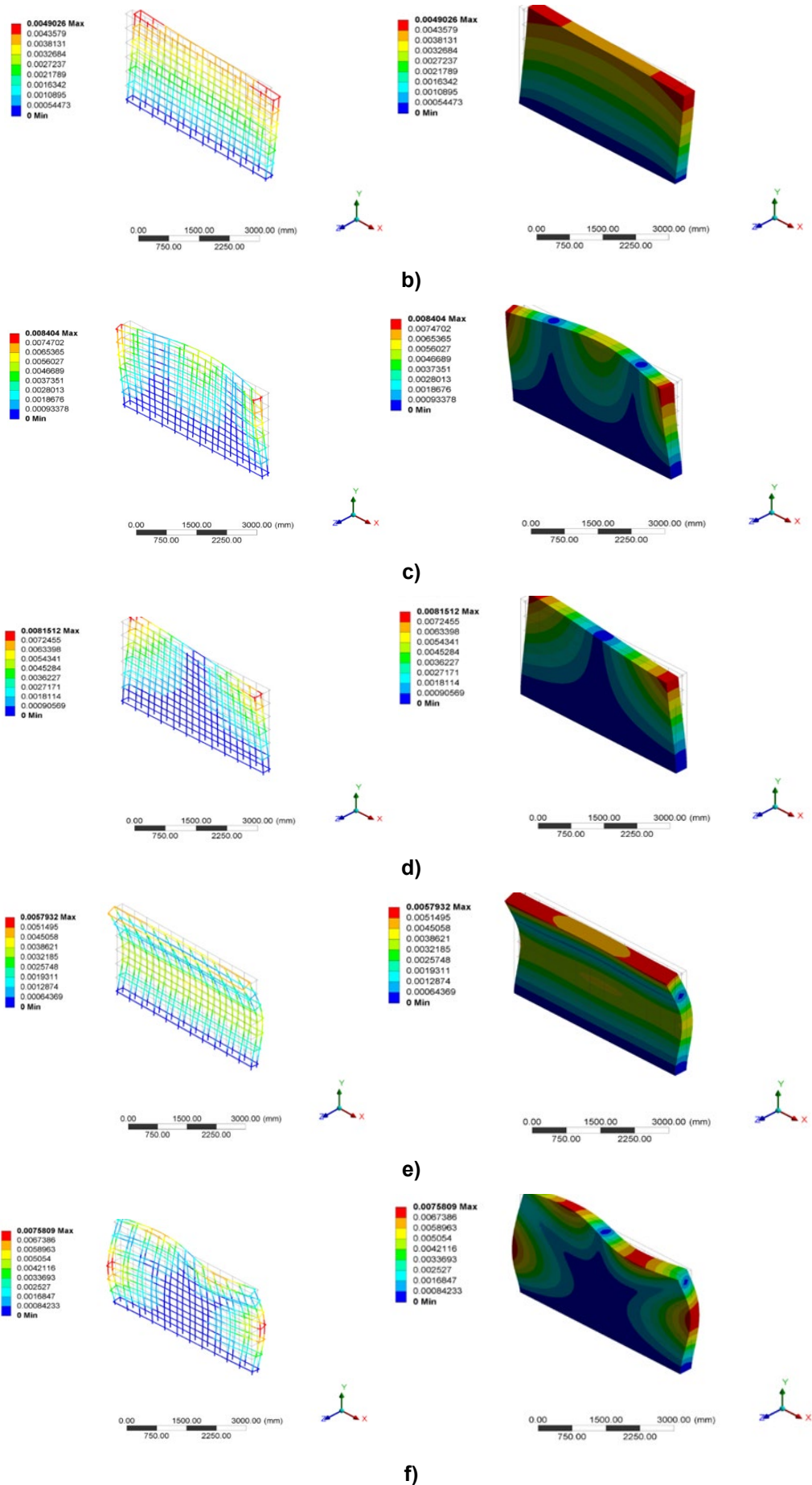


**Figure 16. The natural modal analysis for rebar, and shear wall: a) First Mode; b) Second Mode; c) Third Mode; d) Fourth Mode; e) Fifth Mode; f) Sixth Mode.**



Fig. 17 shows variation of displacement with period in RC shear wall via RSM. As seen, the maximum displacement of RC shear wall is more than 5 cm while the RC shear wall displacement was 2 cm in non-linear analysis. In fact, due to application of the safety factor to the structure, the maximum displacement obtained via RSM is greater than the maximum displacement found through nonlinear dynamic analysis. Table 5 shows the comparison of displacements. The results of nonlinear analysis are more acceptable than linear analysis. This is related to the usage of the whole capacity of material properties in nonlinear analysis.

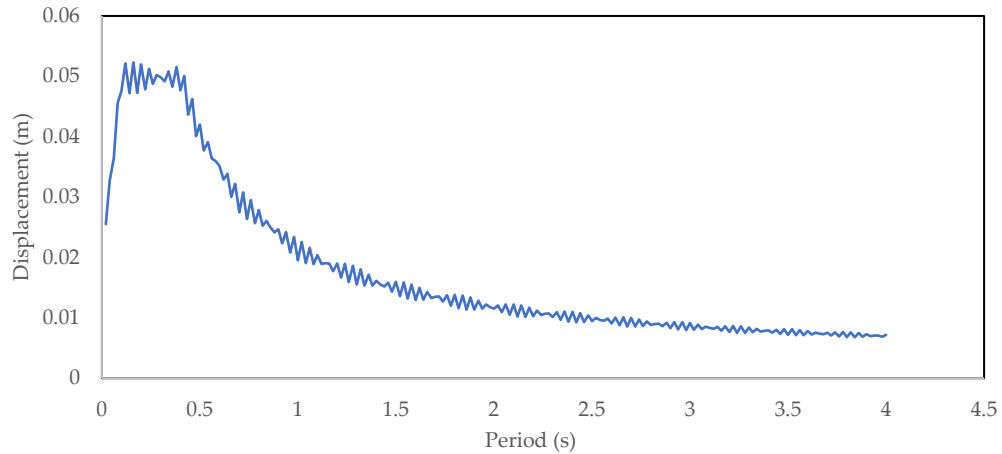


**Figure 17. Variation of displacement with period in RC shear wall.**

**Table 5. Comparison of displacements.**

Maximum displacement obtained via RSM (cm)	Maximum displacement obtained via nonlinear analysis (cm)
5.23	2

Based on the von-Mises (VM) failure theory, when principal stress is less than VM stress, the structure tends to fail. In another words, in this theory, a material will fail if the VM or effective stress of the material under load is equal to or greater than the yield strength of the same material under a simple uniaxial tensile test [22, 23]. In fact, when principal stress values increase more than VM stress, the RC shear wall starts cracking. Fig. 18 shows VM theory definition, where  $\sigma_1$  and  $\sigma_2$  are the principal stresses.

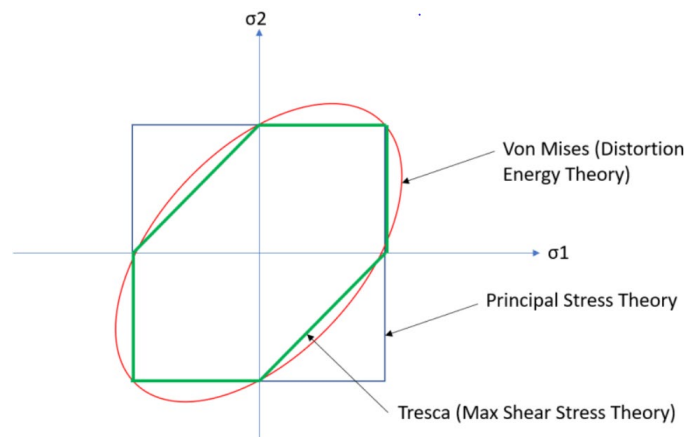


**Figure 18. Von-Mises theory definition.**

In the present study, the cracks, which occurred based on VM theory, were called “critical crack zones”, which were illustrated by the circle in Fig. 19. As observed, the VM stress is less than principal stress at the fixed supports. Therefore, according to the VM theory, these zones will be possibly cracked. Fig. 20 shows the position of critical zones and probability of cracking on the concrete part of the RC shear wall. As seen, the small cracks have been continued to the middle of RC shear wall. The critical crack zones have been formed in these positions with the angle of about 30° to 45° with respect to the horizontal axis, which is mainly due to the existence of diagonal tension as a result of shear stress. Fig. 21 depicts

the VM and principal stresses for rebar part of RC shear wall. As seen, rebars play as the tensile elements and do not allow the total failure of the shear wall.

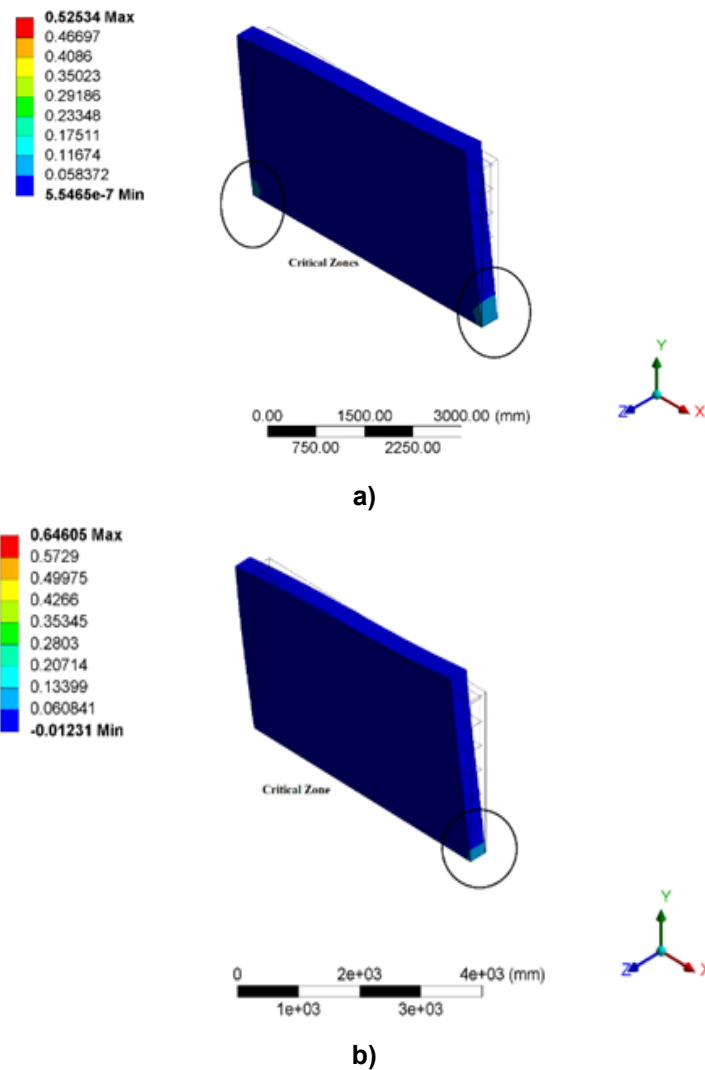


Figure 19. The concrete part of RC shear wall: a) VM Stress; b) Principal Stress.

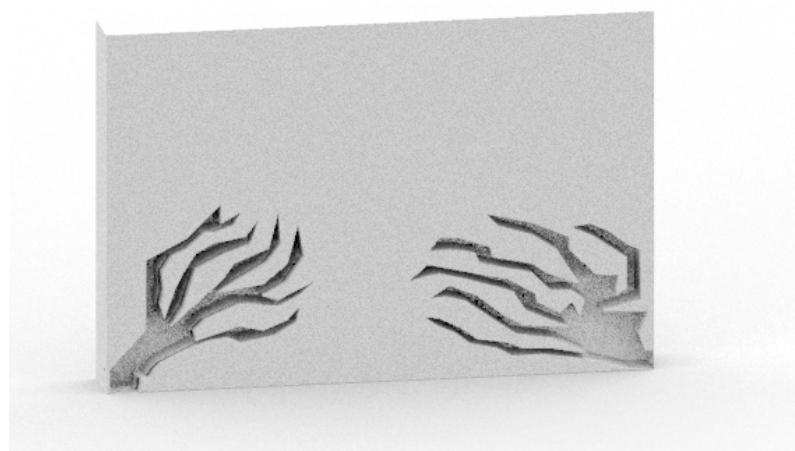
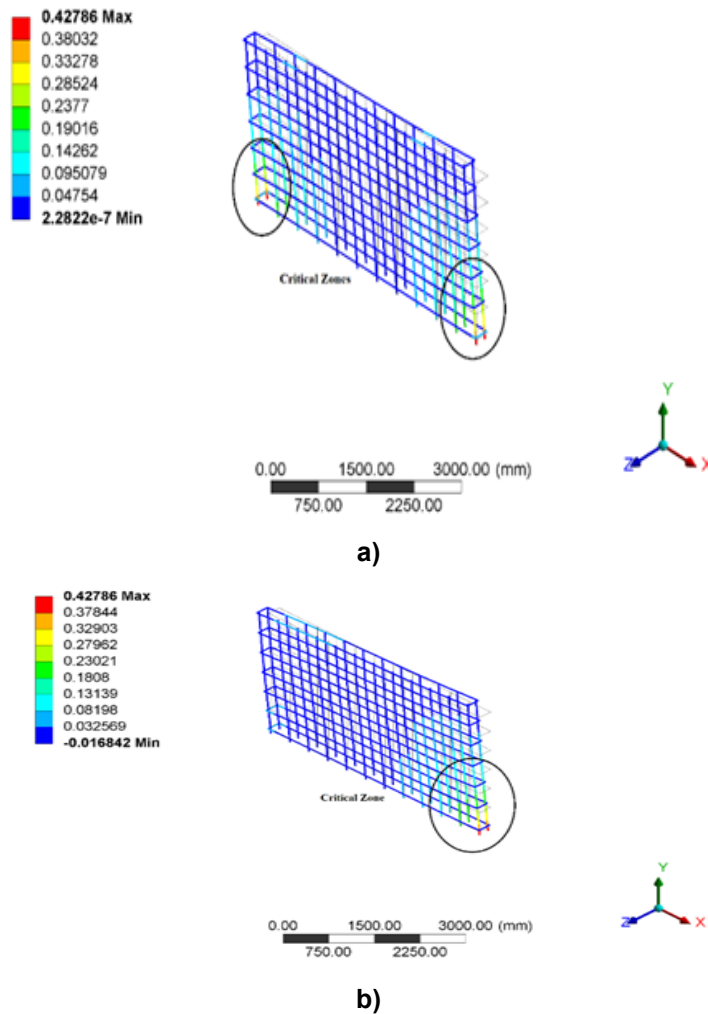


Figure 20. The critical crack zones in RC shear wall via RSM.



**Figure 21. The rebar part of RC shear wall: a) VM Stress; b) Principal Stress.**

### 3.3. Discussion

The present approach for evaluating the displacement of the shear wall needs to be compared with other results obtained in other related papers. The comparison of the results is a way to ensure the reliability of the proposed method in this study. Greifenhagen and Lestuzzi [24] studied the strength and deformation capacity of lightly RC shear walls under cyclic loading. The test series included four lightly RC shear walls in 1:3 scale, for which the horizontal reinforcement, axial force ratio, and concrete compressive strength are varied. For these four samples and under different shear forces, the maximum displacement values were reported. The maximum loading values were 140, 156, 134, and 101 kN, and the maximum displacements were 1.88, 2.88, 3.2, and 2.8 mm, respectively. In this paper, the maximum load bearing of the RC shear wall was 276 kN, and the maximum displacement of the shear wall was 2 cm in the lateral direction. The results showed that the current RC shear wall was able to bear more loads. This difference can be related to the fact that they used light materials that is far from high performance concrete material in this study. Another point is that they applied cyclic loading but in the present paper, nonlinear and RSM analyses were carried out.

Kharun et al. [7] investigated nonlinear behavior of shear walls against seismic wave by using conventional and fiber RC in SAP 2000. They studied the behavior of different sets of fiber RCs such as glass fiber RC, basalt RC, and steel fiber RC. Their research and the present paper both try to estimate displacement value for the shear wall via nonlinear analysis. SAP 2000 is not able to find the crack and also the nonlinear behavior of material can not be defined in this software. However, the nonlinear behavior of materials can be defined in ANSYS through APDL commands. In fact, the ANSYS APDL is able to cover the gap of the material nonlinearity through adding commands.

Al Agha and Umamaheswari [25] studied irregular RC building with shear wall and dual framed-shear wall system by using equivalent static and RSMs. For all nine modes, they reported top story displacement through RSM as 4, 3, 5.5, 6.5, 2, 7, 4, 2.5, and 4.5 cm. In the present paper, RSM analysis for all six modes showed the maximum displacement was 5, 4, 8, 8, 5, and 7 cm. They used the ETABS FE software while the ANSYS Mechanical was used in this study. Obviously, the current analysis method by ANSYS had

better results than ETABS. Softwares such as ETABS and SAP2000 do not focus on the determinants and are not able to define the non-linearity of concrete and steel. In the current study, the APDL commands and ANSYS Mechanical have solved this problem in the material definition of ETABS and SAP2000.

Kisa et al [26] explored the effect of hysteric behavior of concrete shear walls with steel sheets. They applied the lateral loads to the shear wall to find the maximum load and displacement. Their results showed that maximum bearing load and displacement was 200 kN and 40 mm, respectively. Zhang et al. [27] examined the seismic behavior of steel fiber-reinforced high-strength concrete shear wall with steel bracing. They found that the maximum displacement and loading was 2 cm and 450 kN, respectively. The reason for the less bearing load in this study (276 kN) is due to the lack of steel bracing. The types of cracks in their study were similar to the results of nonlinear analysis in this research. Zhang et al. [28] assessed the seismic performance of RAC shear wall. They applied the horizontal cyclic load to RC shear wall to find the maximum displacement and loading. Their results depicted that the maximum loading and displacement was 250 kN and 20 mm, respectively. The comparison of the obtained results in this study with the experimental results (Fig. 22) show that the results of this study are similar to them. In addition, the shear wall in this study has been able to bear more load than Kisa et al. [26] and Zhang et al. [28].

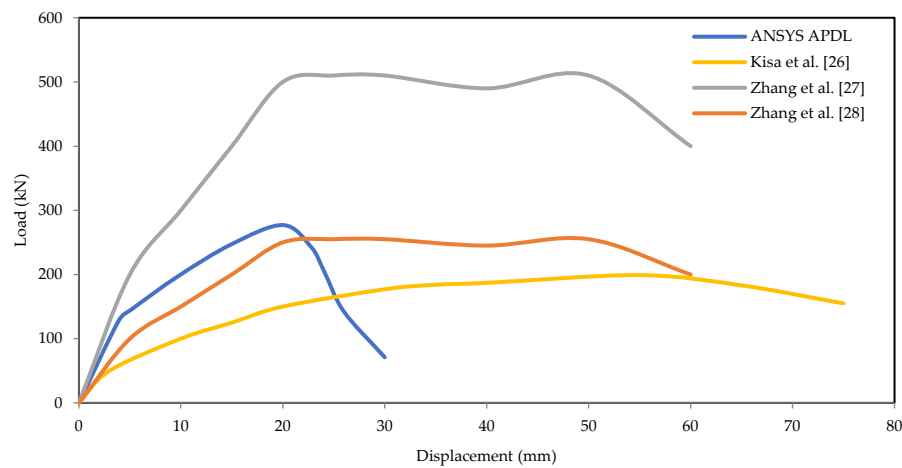


**Figure 22. Comparison of the obtained results in this investigation with other studies.**

#### 4. Conclusions

The weakness of ANSYS Mechanical software in performing dynamic analysis has led us to use a new approach for this purpose. The present method covers this gap in ANSYS Mechanical by adding APDL commands. The following results can be achieved from this study:

1. ANSYS Mechanical is not able to show the crack while the addition of APDL commands has made it possible to reveal the crack zones.
2. Due to the consideration of safety factor in RSM, the maximum displacement was more than 5 cm, which was higher than the nonlinear dynamic analysis result (2 cm).
3. The current study presented a new method to analyze nonlinear behavior of RC shear wall using ANSYS Mechanical via adding APDL commands. It can be concluded that the nonlinear analysis in this study is able to find the maximum load bearing and displacement similar to the experimental results.

#### References

1. Jeong, S.H., Jang, W.S. Modeling of RC shear walls using shear spring and fiber elements for seismic performance assessment. *Journal of Vibroengineering*. 2016. 18. Pp.1052–1059. DOI: 10.21595/jve.2015.16757
2. Fu, W. Modeling and Simulation of Reinforced Concrete Shear Wall under Bidirectional Earthquake Action. *IOP Conference Series: Materials Science and Engineering*. 2018. 394(3). Article no. 032109. DOI: 10.1088/1757-899X/394/3/032109
3. Galal, K., El-Sokkary, H. Advacement in modeling of RC shear walls. *The 14<sup>th</sup> World Conference on Earthquake Engineering*. Beijing, 2008.
4. El-Kashif, K.F.O., Adly, A.K., Abdalla, H.A. Finite element modeling of RC shear walls strengthened with CFRP subjected to cyclic loading. *Alexandria Engineering Journal*. 2019. 58. Pp. 189–205. DOI: 10.1016/j.aej.2019.03.003
5. Epackachi, S., Whittaker, A.S., Varma, A.H., Kurt, E.G. Finite element modeling of steel-plate concrete composite wall piers. *Engineering Structures*. 2015. 100. Pp. 369–384. DOI: 10.1016/j.engstruct.2015.06.023
6. Rafiei, S., Hossain, K.M.A., Lachemi, M., Behdian, K., Anwar, M.S. Finite element modeling of double skin profiled composite shear wall system under in-plane loadings. *Engineering Structures*. 2013. 56. Pp. 46–57. DOI: 10.1016/j.engstruct.2013.04.014

7. Kharun, M., Koroteev, D.D., Hemati Bahar, M., Huang, J., Kamrunnaher, M. Behavior of conventional and fibered concrete shear walls during earthquake, an analytical simulation in SAP2000. *Journal of Physics: Conference Series*. 2020. 1678. Article no. 012033. DOI: 10.1088/1742-6596/1687/1/012033
8. Rahai, A., Hatami, F. Evaluation of composite shear wall behavior under cyclic loadings. *Journal of Constructional Steel Research*. 2009. 65(7). Pp.1528–1537. DOI: 10.1016/j.jcsr.2009.03.011
9. Najm, H.N., Ibrahim, A.M., Sabri, M.M.S., Hassan, A., Morkhade, S., Mashaan, N.S., Eldirderi, M.M.A., Khedher, K.M. Evaluation and Numerical Investigations of the Cyclic Behavior of Smart Composite Steel–Concrete Shear Wall: Comprehensive Study of Finite Element Model. *Materials*. 2022. 15(13). Article no. 4496. DOI: 10.3390/ma15134496
10. Wang, K., Zhang, W., Chen, Y., Ding, Y. Seismic Analysis and Design of Composite Shear Wall with Stiffened Steel Plate and Infilled Concrete. *Materials*. 2022. 15(1). Article no. 182. DOI: 10.3390/ma15010182
11. Wang, S., Liu, H., Wang, Y., Qiao, Y., Wang, L., Bai, J., Tse, K. T.T., Li, C.Y., Fu, Y. Experimental Study on the Seismic Performance of Shear Walls with Different Coal Gangue Replacement Rates. *Applied Sciences*. 2022. 12(20). Article no. 10622. DOI: 10.3390/app122010622
12. Sijwal, G., Man Pradhan, P., Phuvoravan, K. Lateral Load Carrying Capacity of Concrete-filled Cold-formed Steel Shear Wall. *International Journal of Engineering*. 2022. 35(1). Pp. 161–171. DOI: 10.5829/ije.2022.35.01a.15
13. Liu, W., Cao, W., Zhang, J., Qiao, Q., Ma, H. Seismic Performance of Composite Shear Walls Constructed Using Recycled Aggregate Concrete and Different Expandable Polystyrene Configurations. *Materials*. 2016. 9(3). Article no. 148. DOI: 10.3390/ma9030148
14. Kamgar, R., Heidarzadeh, H., Babadaei Samani, M. R. Evaluation of buckling load and dynamic performance of steel shear wall retrofitted with strips made of shape memory alloy. *Scientia Iranica*. 2021. 28(3). Pp. 1096–1108. DOI: 10.24200/sci.2020.52994.2991
15. Carol, I., Jirásek, M., Bažant, Z.A. A thermodynamically consistent approach to microplane theory. Part I. Free energy and consistent microplane stresses. *International Journal of Solids and Structures*. 2001. 38(17). Pp. 2921–2931. DOI: 10.1016/S0020-7683(00)00212-2
16. Zreid, I., Kaliske, M.A. Gradient enhanced plasticity–damage microplane model for concrete. *Computational Mechanics*. 2018. 62. Pp. 1239–1257. DOI: 10.1007/s00466-018-1561-1
17. Zreid, I., Kaliske, M. An implicit gradient formulation for microplane drucker-prager plasticity. *International Journal of Plasticity*. 2016. 83. Pp. 252–272. DOI: 10.1016/j.ijplas.2016.04.013
18. Zreid, I., Kaliske, M. Regularization of microplane damage models using an implicit gradient enhancement. *International Journal of Solids and Structures*. 2014. 51(19–20). Pp. 3480–3489. DOI: 10.1016/j.ijsolstr.2014.06.020
19. Hasanzadeh, A., Vatin, N.I., Hematibahar, M., Kharun, M., Shooshpasha, I. Prediction of the Mechanical Properties of Basalt Fiber Reinforced High-Performance Concrete Using Machine Learning Techniques. *Materials*. 2022. 15(20). Article no. 7165. DOI: 10.3390/ma15207165
20. ACI Committee 318. Building Code Requirements for Structural Concrete (ACI 318-11) and Commentary. American Concrete Institute. Farmington Hills MI, 2011. 509 p.
21. Iranian Seismic Design Code. Standard No. 2800. Iranian Building and Housing Research Center. Ministry of Housing and Urban, 2014.
22. Kala, Z. Stability of Von-Misses Truss with Initial Random Imperfections. *Procedia Engineering*. 2017. 172. Pp. 473–480. DOI: 10.1016/j.proeng.2017.02.055
23. Theocaris, P., Kolokolis, S., Andriasopoulos, N. The von Mises plastically deformed enclave as heat source for running cracks. *International Journal of Pressure Vessels and Piping*. 1994. 57(3). Pp. 359–363. DOI: 10.1016/0308-0161(94)90042-6
24. Greifenhagen, C., Lestuzzi, P. Static cyclic tests on lightly reinforced concrete shear walls. *Engineering Structures*. 2005. 27(11). Pp. 1703–1712. DOI:10.1016/j.engstruct.2005.06.008
25. Al Agha, W., Umamaheswari, N. Analytical study of irregular reinforced concrete building with shear wall and dual Framed-Shear wall system by using Equivalent Static and Response Spectrum Method. *Materials Today: Proceedings*. 2021. 43(2). Pp. 2232–2241. DOI: 10.1016/j.matpr.2020.12.525
26. Kisa, H., Yuksel, S., Caglar, N. Experimental study on hysteric behavior of composite shear walls with steel sheet. *Journal of Building Engineering*. 2020. 33. Article no. 101570. DOI: 10.1016/j.jobe.2020.101570
27. Zhang, J., Li, X., Cao, W. Seismic behavior of steel fiber-reinforced high-strength concrete mid-rise shear walls with high-strength steel rebar. *Journal of Building Engineering*. 2021. 42. Article no. 102462. DOI: 10.1016/j.jobe.2021.102462
28. Zhang, J., Zhao, Y., Li, X., Li, Y., Dong, H. Experimental study on seismic performance of recycled aggregate concrete shear wall with high-strength steel bars. *Structures*. 2021. 33. Pp. 1457–1472. DOI: 10.1016/j.istruc.2021.05.033

#### **Information about the authors:**

**Ali Hasanzadeh, PhD**

ORCID: <https://orcid.org/0000-0001-5546-0950>

E-mail: [a\\_hasanzade64@yahoo.com](mailto:a_hasanzade64@yahoo.com)

**Mohammad Hematibahar,**

ORCID: <https://orcid.org/0000-0002-0090-5745>

E-mail: [eng.m.hematibahar1994@gmail.com](mailto:eng.m.hematibahar1994@gmail.com)

**Nikolai Ivanovich Vatin, Doctor of Technical Sciences**

ORCID: <https://orcid.org/0000-0002-1196-8004>

E-mail: [vatin@mail.ru](mailto:vatin@mail.ru)



**Makhmud Kharun**, PhD in Technical Sciences

ORCID: <https://orcid.org/0000-0002-2773-4114>

E-mail: [miharun@yandex.ru](mailto:miharun@yandex.ru)

*Received 28.08.2023. Approved after reviewing 15.01.2025. Accepted 18.01.2025.*



Research article

UDC 624

DOI: 10.34910/MCE.134.10



## Experimental study on the behavior of multilayer geosynthetic-reinforced sandy embankments

H.A. Al-Salamy, M.A. Al-Naddaf , R.A. Almuhanha

The University of Kerbala, Karbala, Iraq

✉ [mahdi.a@uokerbala.edu.iq](mailto:mahdi.a@uokerbala.edu.iq)

**Keywords:** geosynthetic reinforcement, laboratory model, plate loading test, sandy embankment.

**Abstract.** A significant number of transportation embankments fail before their design life due to poor quality of construction materials, inadequate compaction, embankment construction, and overloading. To overcome this issue, increasing the strength and rigidity of the embankment layers is necessary to lower the stresses on the sub-layers. This paper aims to advance the knowledge of using multilayer geosynthetic reinforcements to improve the performance of sandy embankments. Four laboratory model tests with reinforced and unreinforced embankment were conducted in a box of inner dimensions of 2.40(L)×1.15(W)×1.20(H) m. Local poorly graded sand (A3 soil) was used as fill material to construct a 450 mm high embankment with a 1:1 side slope resting on a 300 mm high of sandy subgrade soil. In the reinforced embankments, three layers with 150 mm vertical spacing of either geotextile, geogrid, or geocomposite (i.e., geotextile sheet over geogrid) were utilized in each model test. Several non-destructive tests, e.g., lightweight deflectometer, dynamic cone penetration, and field California bearing ratio tests, were performed during the embankment construction. In each test, two static plate loading tests were conducted to evaluate the embankment performance and the benefit of geosynthetic reinforcement. The study showed that geosynthetic reinforcement significantly decreased surface settlement and increased load-carrying capacity. The results indicate that the load-carrying capacity near the embankment side slope can be significantly increased by the inclusion of geosynthetic layers and that the magnitude of capacity increase depends greatly on the geosynthetic type. The results also demonstrate that geogrid lateral restraint and confinement were more effective alternatives to sublayer improvement than geotextile or geocomposite.

**Citation:** Al-Salamy, H.A., Al-Naddaf, M.A., Almuhanha, R.A. Experimental study on the behavior of multilayer geosynthetic-reinforced sandy embankments. Magazine of Civil Engineering. 2025. 18(2). Article no. 13410. DOI: 10.34910/MCE.134.10

### 1. Introduction

Since the highway transportation network has grown significantly in recent years, designers have begun to decrease route lengths and trip times. Geosynthetics have long been used to improve soft soil conditions for projects, such as highway embankments, seawalls, and building foundations, as well as to cover excavated and backfilled trenches. Geosynthetics, such as geotextiles (GTs) and geogrids (GGs), have been widely employed in geotechnical engineering for a variety of applications. Reinforcement, filtration, separation, drainage, protection, and fluid barriers are all common uses for geosynthetics [1].

Roadways were built to pass through locations with a variety of tough terrains, necessitating the development of constructions, such as steep embankments. Controlling the stability and settling of embankments under various loading circumstances has always been a difficult task for designers [2]. In general, ground improvement techniques, such as vibro stone columns, are utilized to reinforced embankment bases in soft soils. The use of geosynthetic reinforcements to improve the stability of

embankments has become popular recently. Improving the engineering qualities of soil by using reinforcement layers is a valuable option. The beneficial effect of geosynthetic material as reinforcement is largely determined by the form in which it is applied. When the same geosynthetic material is utilized in planar layers (e.g., geogrids or geotextiles), three dimensional (e.g., geocells), or discrete fibers, they would yield distinct strength gains in different forms. This disparity in strengthening the soil is mostly due to differences in failure mechanisms in soil reinforced with geosynthetic material in various forms. Friction and interlocking between soil and reinforcement improve the strength of horizontal geosynthetic layers, whereas friction and coiling around soil particles improve the strength of randomly oriented fibers [3].

Much research has been carried out to understand the beneficial effects of planar form of reinforcement in sand using geosynthetic layers, such as those discussed in [4–7]. Several studies are also available on the use of randomly oriented discrete geosynthetic fibers to reinforce sand, such as those discussed in [8–14]. Some studies are also available on sand reinforced with 3D inclusions made of galvanized iron sheet and hard plastic sheet [15]. In addition, the concept of cellular geosynthetic reinforcement is studied in several previous studies [16–19].

In the past two decades, some laboratory and field research projects have been conducted to investigate the performance of the geogrid-supported embankments on soft subgrades. Geocomposite (GC) reinforcements are now successfully utilized for different geotechnical structures like sloped embankment. A review on the literature suggests that geosynthetics have been abundantly used in road and railway projects during the recent years. Most of these projects are based on placing geosynthetic layers as reinforcement in superstructure layers of roads and railways [2]. An extensive range of studies have been carried out on geogrid inclusion under foundation to evaluate the bearing capacity of geogrid-reinforced soil using laboratory model tests. On the other hand, geotextile provides separation and filtration functions, preventing the intermixing of granular layers and the ingress of fines. Their use ensures an improved performance and design life of the materials layers in several application [20].

The present study aims to find the effect of geotextile, geogrid, and geocomposite reinforcement in sandy soil embankment and evaluate their behavior in comparison with unreinforced (UR) case. In addition, evaluating the reinforcement benefits in sliding control of embankment slopes and decreasing the surface settlement under loading are of great interest.

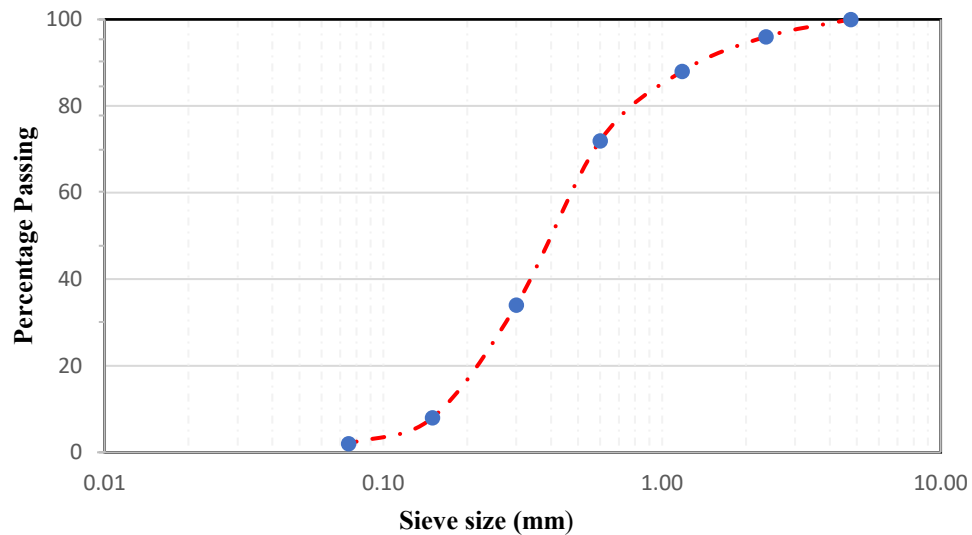
## 2. Methods and Materials

### 2.1. Physical and Chemical Properties of Embankment Soil

As illustrated in Fig. 1(a), the soil was collected from the site of Karbala Airport. It was classified as (A-3) soil and poorly graded sand (SP) according to the American Association of State Highway and Transportation Officials (AASHTO M145-91, 2012) and the American Society for Testing and Materials (ASTM D 2487), respectively. Fig. 1(b) depicts the grain size distribution of this soil. The main tests were done to determine the basic characteristics of soil that will be utilized in the physical model tests. These tests are the modified Proctor test (ASTM D 1557) to obtain the maximum dry density of the soil and the optimum moisture content, particle size distribution (ASTM D2487) to classify the soil, specific gravity (ASTM D854), and California bearing ratio (CBR) test (ASTM D1883). The parameters of the sand utilized in the investigation are listed in Table 1. As a subgrade and embankment material, sand is employed.



(a)



(b)

Figure 1. (a) Soil of Kerbala Airport; (b) Grain Size Distribution of Soil.

Table 1. Physical and Chemical Characteristics of Sandy Soil.

Property	Tests Result	Specification
AASHTO Classification	A-3	AASHTO M145
USCS Classification	Poorly Graded Sand (SP)	ASTM D 2487
Max. Dry Unit Weight (g/cm <sup>3</sup> )	1.925	ASTM D 1557
CBR at 95 %	22 %	
OMC	11 %	ASTM D 1557
D10	0.14	ASTM D 2487
D30	0.3	ASTM D 2487
D60	0.6	ASTM D 2487
Specific Gravity	2.57	ASTM D 854
Uniformity Coefficient (Cu)	4.28	ASTM D 2487
Curvature Coefficient (Cc)	1.07	ASTM D 2487
Chemical Characteristics		
SO <sub>3</sub>	9.9	B.S Part 3
Gypsum	21.3	B.S Part 3
PH	7.9	B.S Part 3
CL	79.9	B.S Part 3

## 2.2. Geosynthetic Reinforcement

Biaxial geogrid of 30 mm aperture size is used in this study. The properties of the geogrid used are shown in Table 2. Polypropylene non-woven geotextile (A401) having mass per unit area of 300 g/m<sup>2</sup> is used in the present study. Table 3 shows the various properties of geotextile.

Table 2. Specification of Geogrid.

Property	Type or Value
Standard Color	Black
Polymer Type	Polypropylene
Aperture Size (mm)	30
Weight (g/m <sup>2</sup> )	370
Peak Tensile Strength (MPa)	30
Beak Extension (kN/m)	L=15, W=11

**Table 3. Properties of Non-Woven Polypropylene Geotextile.**

Particulars	Test Method	Value
Tensile Strength (CD) (KN/m)	EN ISO 10319	17
Tensile Strength (MD) (KN/m)	EN ISO 10319	11.2
CBR Puncture (N)	EN ISO 12236	2380
Permeability ( $10^3 \text{ms}^{-1}$ )	EN ISO 111058	55
Tensile Elongation (%)	EN ISO 10319	55/66
Mass / Unit Area ( $\text{g/m}^2$ )	EN ISO 10319	300
Thickness (mm) under 2Kpa	EN ISO 9863-1	2.8
Color		White

For the application of load on the embankment, a loading chamber with specified dimensions must be modelled. After proper scaling, four series of embankments should also be modelled.

### 2.3. Subgrade Preparation

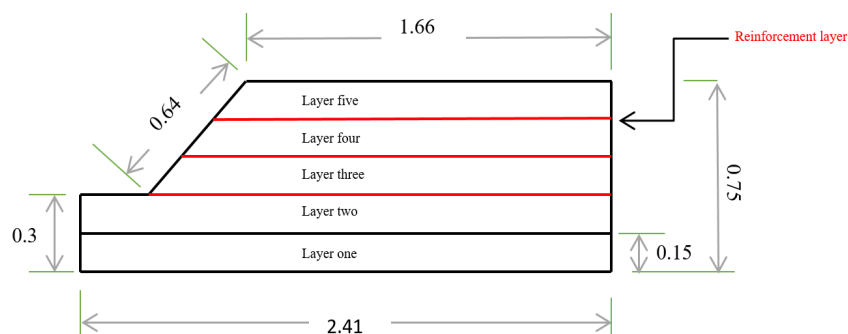
The embankment is built with a height of 0.45 m over a 0.30 m thick subgrade in the loading chamber, taking into account the height of the loading chamber. Subgrade material was poor graded (PW) sand with a uniformity coefficient ( $C_u$ ) of 4.2857 and a curvature coefficient ( $C_c$ ) of 1.0714. The dirt was compacted with optimum wetness in 15 cm layers using suitable roller weights up to a height of 0.30 m from the chamber's foundation to create the subgrade.

### 2.4. Embankment Modelling

In this study, a 0.45 m height embankment with a side slope of 1:1 is selected as the reference embankment. The scaling law was applied on the aforementioned embankment with a scale of 1:4 for the laboratory test programmer. A side slope of 1:1 is selected for laboratory model. The poor graded (PW) sand with uniformity coefficient ( $C_u$ ) of 4.2857 and curvature coefficient ( $C_c$ ) of 1.0714 was adopted as the embankment material. The maximum dry density of this soil has been obtained equal to  $1.925 \text{ g/cm}^3$  in the optimum moisture 11 %. The dimensions of the laboratory model are given in Table 4. Fig. 2 shows the schematic diagram of the model embankment.

**Table 4. The Dimensions of the Laboratory Model.**

Parameter	Laboratory Embankment
Embankment Length (m)	2.41
Embankment Height (m)	0.45
Subgrade Height (m)	0.30
Width of Bed Side (m)	0.30

**Figure 2. The Schematic Diagram of the Model Embankment.**

### 2.5. Model Preparation and Test Procedure

A steel box with dimensions of length = 2.4 m, height = 1.2 m, width = 1.2 m was utilized to approximate in-situ subgrade conditions. The steel box's purpose was to represent the subgrade and embankment layers so that compaction and other tests could be performed. Four series of models were constructed one without reinforcement and three with reinforcement with geogrid, with geotextile and with a composite of them. Each model was built to represent a cross-section of a railway. The model contains two layers to represent the subgrade with a height of 15 cm for each layer and contains three layers to



represent the embankment with a height of 15 cm for each layer. Three layers of reinforcement were placed between the layers of the embankments and between the second layer of the subgrade and the first layer of the embankment.

The preparation of the model involves several steps to improve the density of the subgrade and embankment samples, each layer was compacted. The compacted effort was achieved with 8 passes for subgrade and 10 passes for embankments on each layer using a compaction unit. During the creation of the model layers, Table 5 illustrated a number of field tests that were carried out for each of the model layers as plate loading test (PLT), CBR, lightweight deflectometer (LWD), sand replacement method (SRM), and dynamic cone penetration (DCP) tests as shown in Fig. 3.

**Table 5. Type of Layer Tests.**

No. of Layer	Description	Type and Number of Tests			
1	Subgrade	3 SRM			
2	Subgrade	3 SRM	3 LWD	3 DCP	
3	Embankment	3 SRM	3 LWD	3 DCP	
4	Embankment	3 SRM	3 LWD	3 DCP	3 CBR
5	Embankment	3 SRM	3 LWD	3 DCP	2 PLT

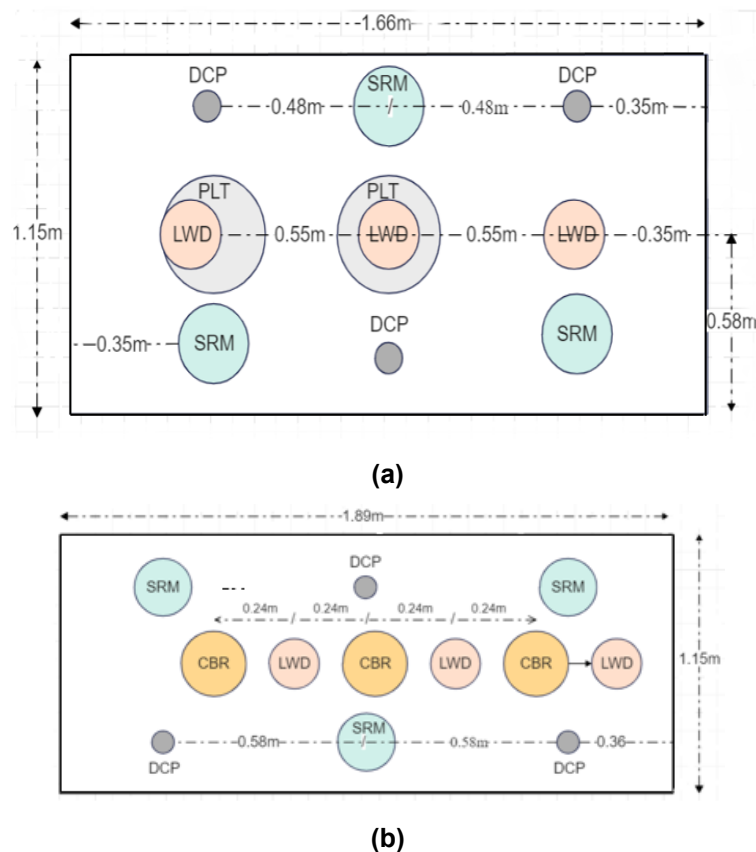


**Figure 3. Location of Field Tests: (a) Layer 4 ;(b) Layer 5.**

### 3. Results and Discussion

#### 3.1. Results of SRM Test

As a quality control test of the construction process for all model tests, SRM test was performed in this experimental work in accordance with ASTM D155. The compaction efforts were achieved by applying different number of passes using a vibratory compactor on the top of each layer of the subgrade and the embankment in all model tests. Three SRM test points were selected and performed on the top of each layer of subgrade and embankment, and then an average value is calculated and reported. Table 5 summarizes the results of the moisture content, dry density, and relative compaction of the subgrade and the embankment layers. The results show that the average relative compaction results of subgrade soil are in the range from 88 to 92 %, and those of the embankment ranged from 91 to 92 %. This indicates an acceptable level of quality and consistency for all model tests.

**Table 5. Summarizes the Results of SRM and the Relative Compaction.**

Model Types				No. of Passes	Unreinforced Test (URT)	Geotextile- Reinforced Test (RT-GT)	Geogrid- Reinforced Test (RT-GG)	Geocomposite- Reinforced Test (RT-GC)
					Average of Three Test Points			
Subgrade	Layer 1	W.C%	8	11.33	10.31	10.42	8.35	
		Dry Density		1.68	1.76	1.77	1.81	
		R.C%		87	91	92	94	
	Layer 2	W.C%	8	9.94	11.7	11.32	10.2	
		Dry Density		1.71	1.79	1.77	1.74	
		R.C%		89	93	92	90	
	Avg.	W.C%		10.64	10.87	10.87	10.1	
		Dry Density		1.70	1.77	1.77	1.78	
		R.C%		88	92	92	92	
	Embankment	Layer 3	W.C%	10	9.93	10.09	8.62	10.29
Dry Density			1.77		1.76	1.79	1.72	
R.C%			92		91	93	89	
Layer 4		W.C%	10	10.26	12.11	10.29	10.15	
		Dry Density		1.75	1.74	1.75	1.75	
		R.C%		91	91	91	91	
Layer 5		W.C%	10	8.41	9.477	8.78	9.36	
		Dry Density		1.72	1.81	1.76	1.78	
		R.C%		90	94	92	93	
Avg.		W.C%		9.53	9.23	9.23	9.93	
		Dry Density		1.74	1.77	1.77	1.75	
		R.C%		91	92	92	91	

### 3.2. Results of DCP Test

Depending on the obtained data of the DCP test, the in-site CBR values for each subgrade layer (i.e., Layers 1 and 2) and embankment layer (i.e., Layers 3, 4, and 5) were estimated by using the empirical relation shown in Eq. 1 (21).

$$CBR = \frac{292}{DCPI^{1.12}} \quad (1)$$

Table 6 presents the CBR results for the unreinforced and geosynthetic-reinforced (i.e., geotextile-, geogrid-, and geocomposite-reinforced) embankments Eq. 4-1.

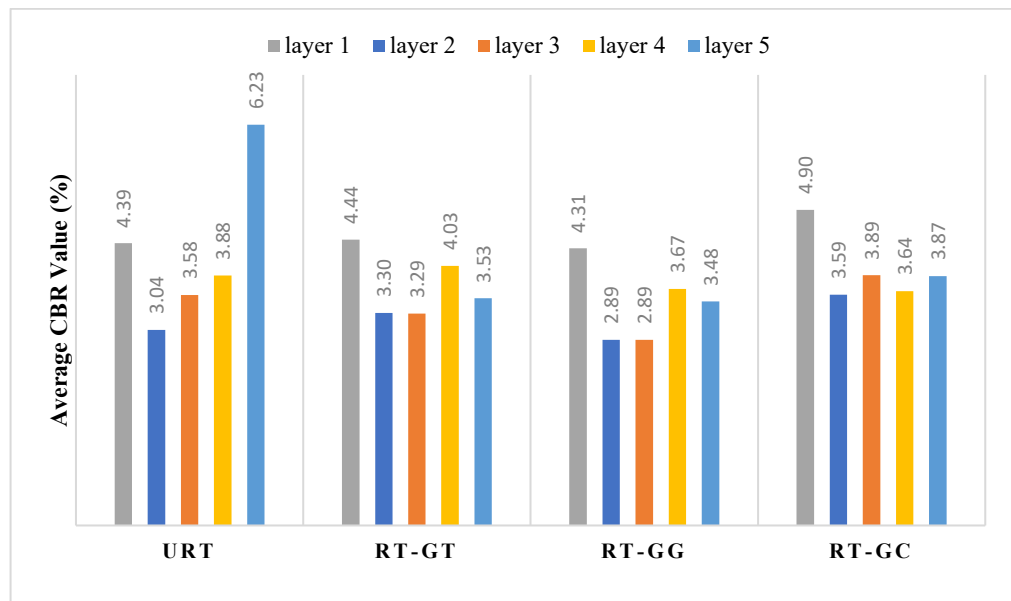
Furthermore, the elastic modulus ( $E$ ) was determined based on the obtained data of the DCP test and the CBR value using Eq. 4-2 (22).

$$E = 17.6 * CBR^{0.64} \quad (2)$$

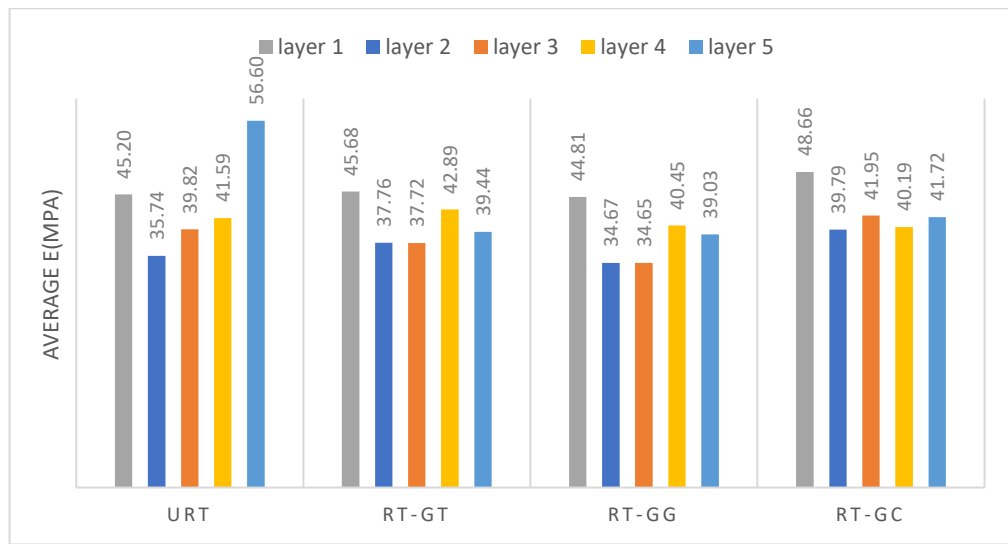
In summary, and even though there is some variation in the obtained results for the CBR values for all model test, the embankment layer constructed with geosynthetic reinforcement shows a higher value of CBR than the unreinforced model except for layer five. When comparing the geotextile-reinforced embankment to the geogrid-reinforced embankment, the CBR values have shown that the geotextile-reinforced model has a higher value than the geogrid-reinforced one, which agrees with the results of M. M. Singh et al. [22]; and that the geocomposite-reinforced model has the most significant value as shown in Fig. 4. This is related to the type of reinforcement and the condition of the DCP test. The DCP cone needs higher energy to penetrate through the geotextile layer within the soil mass in both RT-GT and RT-GC, however, less energy is required in the RT-GG due to the existence of its aperture opening.

**Table 6. Result of CBR Value and Value of E from DCP Test.**

No. of Layer	No. of Point	The Value of CBR (%)			
		URT	RT-GT	RT-GG	RT-GC
1	1	5.40	4.10	4.45	5.24
	2	3.84	4.406	4.26	4.71
	3	3.92	4.82	4.21	4.76
	Average	4.39	4.44	4.31	4.90
2	1	3.73	2.95	2.80	4.24
	2	2.70	3.30	2.76	3.28
	3	2.69	3.66	3.10	3.24
	Average	3.04	3.30	2.89	3.59
3	1	3.56	3.12	3.17	3.66
	2	3.50	3.50	2.52	3.88
	3	3.68	3.26	2.97	4.13
	Average	3.58	3.29	2.89	3.89
4	1	3.74	3.77	3.49	4.14
	2	2.68	3.67	3.45	3.19
	3	5.23	4.66	4.09	3.59
	Average	3.88	4.03	3.67	3.64
5	1	6.73	3.72	3.15	3.38
	2	4.98	3.47	3.30	4.87
	3	6.97	3.40	3.98	3.37
	Average	6.23	3.53	3.48	3.87



(a)



(b)

Figure 4. (a) Value of CBR from DCP Test, (b) Value of E from DCP Test.

### 3.3. Results of LWD Test

Three LWD tests were performed on the top of the Layers 2, 3, 4, and 5 in all physical models; these tests were distributed at three different locations on the top of each layer in the unreinforced and geosynthetic-reinforced models. Table 7 shows the results of these LWD tests. The dynamic modulus values ( $E_{vd}$ ) ranged from 13.8 to 14.5 MPa for all subgrade soil in all model tests, which show a consistent construction. In addition, the  $E_{vd}$  values were from 14.3 to 15.0 MPa along embankment layers of the unreinforced model. Lower values were obtained in the geotextile-reinforced and geocomposite-reinforced model tests; the  $E_{vd}$  values ranged from 8.94 to 11.1 MPa, and from 9.8 to 12.6 MPa, respectively for RT-GT and RT-GC. However, much higher dynamic modulus was obtained for the RT-GG (i.e., 15.5–25.1 MPa).

In addition, Fig. 5 shows the value of dynamic modulus graphically for each layer in all model tests. The results indicate that  $E_{vd}$  slightly increased for the unreinforced embankment layers due to the accumulative compaction efforts on each layer, while it gradually decreases for the geotextile and geocomposite models from the third to the fifth layer. This is due to the use of geotextile in these two cases, which allowed the soil to move easily over the geotextile layer and decreased the frictional resistance between the layers. On the other hand, it was observed, in the case of geogrid reinforcement, the dynamic modulus significantly increased as the embankment layer increased. This is due to a better interlocking action and confinement between the embankment layers provided by the geogrid reinforcement layers.

Table 7. Result of Modules from LWD Test.

No.of Layer	No. of Point	Tests			
		URT	RT-GT	RT-GG	RT-GC
		$E_{vd}$ (MPa)	$E_{vd}$ (MPa)	$E_{vd}$ (MPa)	$E_{vd}$ (MPa)
2	1	14.00	14.20	14.20	13.50
	2	15.37	14.90	15.36	14.98
	3	13.68	13.80	13.79	12.90
	Average	14.35	14.30	14.45	13.79
3	1	12.90	11.56	17.25	13.26
	2	15.60	11.70	15.26	11.62
	3	14.30	10.20	14.04	12.84
	Average	14.27	11.15	15.52	12.57
4	1	14.90	11.34	14.27	10.73
	2	15.00	10.72	22.70	8.96
	3	14.30	10.23	29.11	8.97

No. of Layer	No. of Point	Tests			
		URT	RT-GT	RT-GG	RT-GC
		$E_{vd}$ (MPa)	$E_{vd}$ (MPa)	$E_{vd}$ (MPa)	$E_{vd}$ (MPa)
5	Average	14.73	10.76	22.03	9.55
	1	15.13	8.33	18.50	11.14
	2	15.16	9.00	25.80	9.57
	3	14.70	9.50	31.08	8.85
	Average	15.00	8.94	25.13	9.85

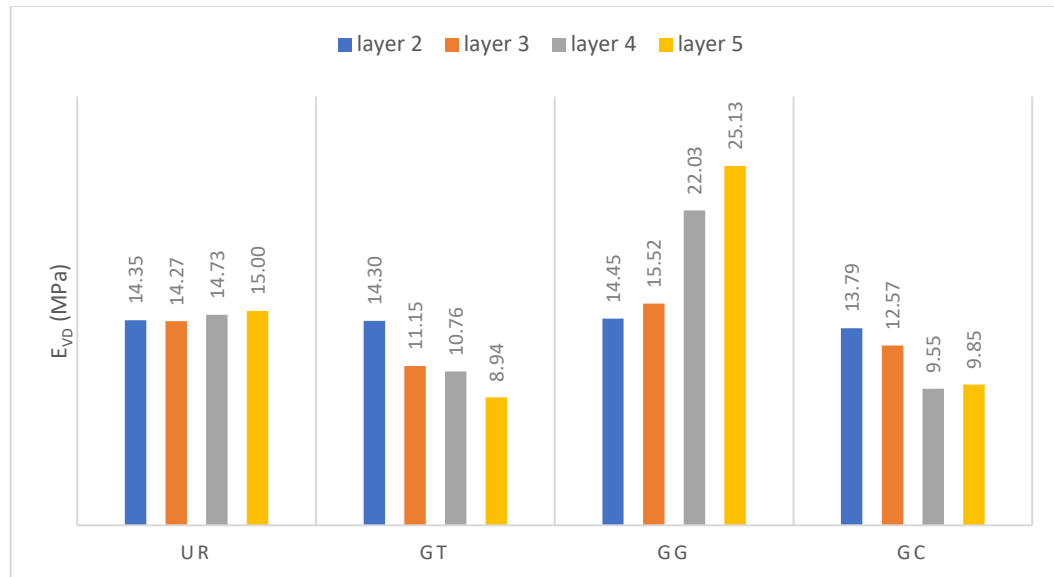


Figure 5. Value of Dynamic Modulus ( $E_{vd}$ ) from LWD Test.

### 3.4. Results of CBR Test

The CBR test was used to determine the field CBR value of the sandy soils. There were twelve CBR tests completed during the experimental study period (i.e., three for each model test) including the geogrid-reinforced model test, but unfortunately, the data logger software did not function appropriately and the data was lost. The other nine tests were performed as follows; three tests were performed in the unreinforced model and the remaining six tests were conducted in the geotextile- and geocomposite-reinforced models. Table 8 and Fig. 6 present the results for these models, which shows that the average CBR value varies from 6.78 % for the unreinforced embankment and from 13.56 % and 14.35 % for the geotextile- and geocomposite-reinforced embankments, respectively. The increase in the CBR values for the geotextile and geocomposite model tests can be related to bearing zone underneath the CBR piston, and the tension membrane effect of the geosynthetic reinforcement.

Table 8. The Result of the CBR Field Test.

Model Name	No. of Point	CBR %
Unreinforced test (URT)	1	8.41
	2	5.80
	3	6.09
	Average	6.76
Reinforced with geotextile (RT-GT)	1	17.25
	2	11.74
	3	11.67
	Average	13.56
Reinforced with composite (RT-GG)	1	14.50
	2	14.21
	3	13.92
	Average	14.35



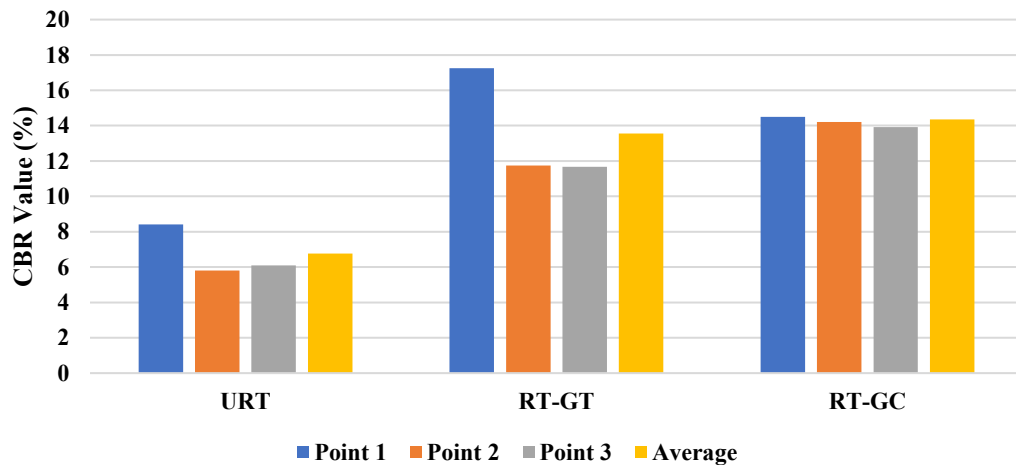


**Figure 6. Comparison the Results of CBR Value for Different Models.**

**Point 1:** it is the point near the wall of the box.

**Point 2:** it is the point in the center of layer four.

**Point 3:** it is the point near the edge of the slope.

A significant difference was observed between field CBR values and CBR values acquired from DCP test data as shown in Fig. 7. This figure shows that the value of CBR is approximately various from 3.88 % to 6.76 % in the unreinforced model, while it was changed from 4.03 % to 13.56 % in the geotextile-reinforced model and from 3.64 % to 14.35 % in the geocomposite-reinforced model. Keeping in mind that the CBR calculated from the DCP test are based on an empirical equation that have not adequately represented the CBR value, while those calculated from the field CBR test are much closer to the laboratory CBR value of the soil.

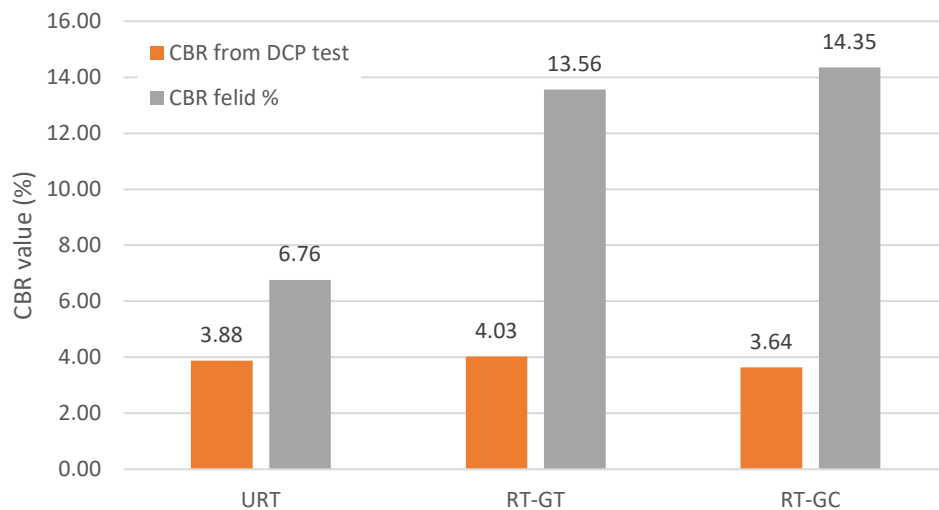


**Figure 7. Compares the Value of CBR in Field and the CBR Value from DCP Test.**

### 3.5. Results of PLT

Static PLTs were performed in all model tests to assess the load carrying capacity and calculate the subgrade modulus for the unreinforced and geosynthetic-reinforced embankments, as well as evaluating the benefits of using different geosynthetic products. Two points were selected to perform the PLT in each model test, one at the center of the embankment width (i.e., this represents a point under the railway track for the embankment configuration/dimension chosen in this study) and the other point near the slope to assess the benefit of geosynthetic reinforcement in stabilizing the slope.

#### 3.5.1. Load-Settlement Results

Fig. 8 presents the load (stress)-settlement curve for the PLTs at the mid-point of all model tests. As shown in this figure, the unreinforced embankment has the highest settlement as compared to the

geosynthetic-reinforced model tests. However, the RT-GG has the lowest settlement or the highest bearing capacity, followed by the RT-GT and the RT-GC, respectively. For comparisons, at an applied vertical stress of 1000 kPa, the soil surface settlements under the plate were 8.0, 6.5, 5.3, and 1.7 mm for the URT, RT-GC, RT-GT, and RT-GG, respectively. This corresponding to a reduction in the surface settlement of 19, 34, and 79 % for the geocomposite, geotextile, and geogrid reinforcement, respectively, as compared to the unreinforced condition. Similarly, for the PLTs at the edge-point, the RT-GG performed the best followed by the RT-GT and RT-GC as compared to the URT as shown in Fig. 9. This can be attributed to the shearing resistance and the tensioned membrane effects of the geosynthetic under the plate.

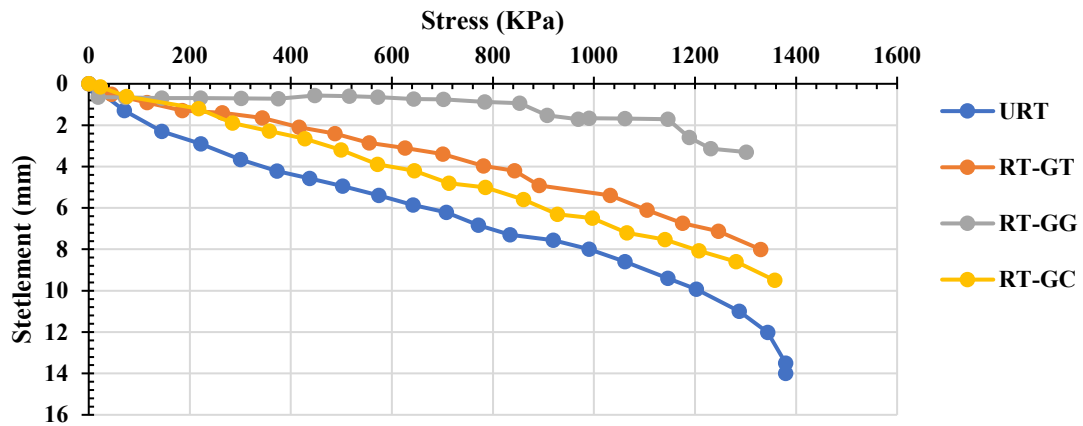


Figure 8. Stress-Settlement Curves of the PLT in URT, RT-GT, RT-GG, and RT-GC at the Embankment Mid-Point.

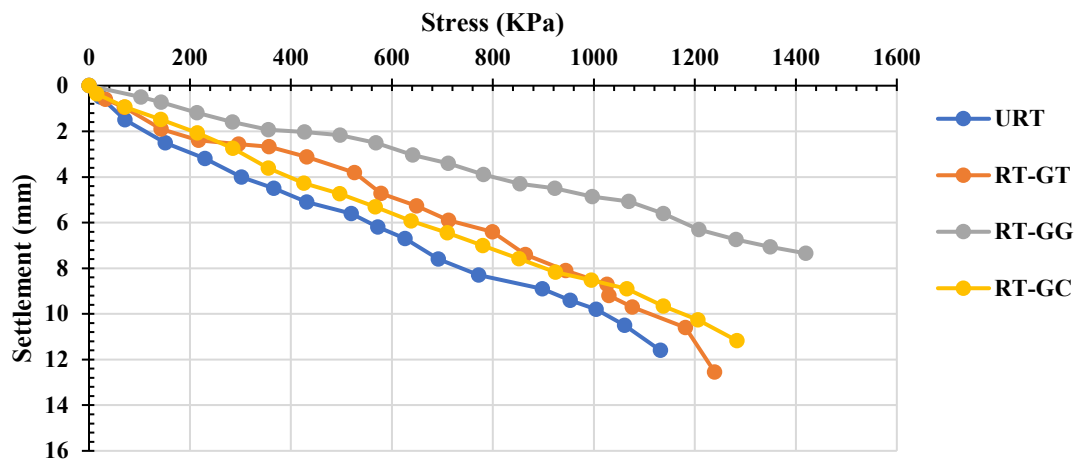


Figure 9. Stress-Settlement Curves of the PLT in URT, RT-GT, RT-GG, and RT-GC at the Embankment Edge-Point.

The subgrade reaction modulus ( $K_s$ ) and  $E$  for all model tests are listed in Table 9. It was noted that the value of  $K_s$  calculated from actual curve in the PLT at the mid-point equal to 53.08 kPa/mm for unreinforced model, which is in agreement with (24) finding, while the  $K_s$  value was equal to 111.29, 115.00, and 173.33 kPa/mm for the models reinforced with geotextile, geogrid, and geocomposite, respectively. Whereas the  $K_s$  value obtained from the corrected curve varied from 38.25 kPa/mm for unreinforced model to 181.58, 575.00, and 73.33 kPa/mm for the models reinforced with geotextile, geogrid, and geocomposite, respectively. The value of  $E$  changed from 17.59 MPa in unreinforced model to 44.17, 38.58, and 33.43 MPa in the models reinforced with geotextile, geogrid, and geocomposite, respectively. On the other hand, it was noted in Table 9 for the results of the PLTs at the edge-point that there is an apparent change in the test results when compared with the middle point test. Values changed significantly due to the proximity of the test point to the edge of the embankment slope.

**Table 9. The Result of PLT.**

Model Type	Test Location					
	Mid-Point			Edge-Point		
	$K_s$ (kPa/mm) of Actual Curve	$K_s$ (kPa/mm) of Corrected Curve	$E$ (MPa)	$K_s$ (kPa/mm) from Actual Curve	$K_s$ (kPa/mm) of Corrected Curve	$E$ (MPa)
UR	53.08	115	17.59	46.31	98.57	19.52
GT	111.29	181.58	44.16	71.88	115.00	25.04
GG	102	575.00	84.56	191.67	191.67	41.43
GC	173.33	173.33	33.43	75.00	75.00	24.10

### 3.5.2. Failure Mechanism of the Physical Models

The sliding surface covers more than half of the embankment in the unreinforced model. The sliding surface gradually moves towards the higher part of the reinforced region and at the interface between reinforcing layers and soil as the geosynthetic layers are positioned in the embankment. Failure is identified as cracks only in the upper half when reinforced with layers of geosynthetic as clear in RT-GT, due to the presence of the geotextile reinforcement layers, which have the property of separating between the layers and it provides the process of sliding between the layers. While the lines of failure were clear along the layers in the URT. However, the line of failure slightly appeared lowest in RT-GG, which may be the result of the skin friction and interlocking between geogrid and soil particles. Fig. 10 depicts the failure pattern of geosynthetics-reinforced laboratory embankments.

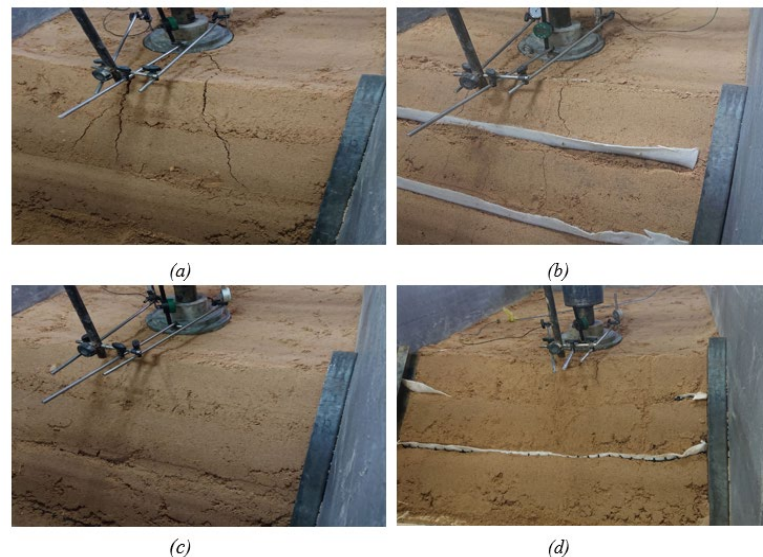


**Figure 10. Failure Mechanism in the Embankments:**  
(a) URT, (b) RT-GT, (c) RT-GG, and (d) RT-GC.

## 4. Conclusions

Depending on the results of the experimental that were obtained, the following conclusions are summarized:

1. The results of SRM show that the average relative compaction results of subgrade soil were in the range from 88 to 92 %, and those of the embankment ranged from 91 to 92 %, which led to an acceptable level of quality and consistency for all model tests.
2. Even though there is some variation in the obtained results for the CBR values for all model test, the embankment layer constructed with geosynthetic reinforcement show a higher value of CBR than the unreinforced model except for layer five. The CBR values have shown that the RT-GT model has a higher value than the RT-GG one; and that the RT-GC model has the most significant value.

3. The  $E_{vd}$  ranged from 13.8 to 14.5 MPa for all subgrade soil in all model tests, which show a consistent construction. In addition, the  $E_{vd}$  were from 14.3 to 15.0 MPa along the embankment layers of the unreinforced model test. Lower values were obtained in the geotextile and geogrid model tests; the  $E_{vd}$  ranged from 8.94 to 11.1 MPa, and 9.8 to 12.6 MPa for RT-GT and RT-GC, respectively. However, a much higher dynamic modulus was obtained for RT-GG (i.e., 15.5–25.1 MPa).
4. In addition, the results indicate that  $E_{vd}$  slightly increased for the unreinforced embankment layers due to the accumulative compaction efforts on each layer, while it gradually decreases for the RT-GT and RT-GC models from the third to the fifth layer. On the other hand, it was observed, in RT-GG, the dynamic modulus significantly increased as the embankment layer increased.
5. The results for the CBR of these models showed that the average CBR value varies from 6.78 % for URT and from 13.56 % and 14.35 % for the RT-GT and RT-GC, respectively. The increase in the CBR values for the geotextile and geocomposite model tests can be related to the bearing zone underneath the CBR piston and the tension membrane effect of the geosynthetic reinforcement.
6. In the PLT, the results showed that RT-GG gave the best values for  $K_s$  and  $E$  as compared to other models. As well as there is less vertical settlement in it compared with the unreinforced model.
7. The result showed that the unreinforced embankment has the highest settlement as compared to the geosynthetic reinforced model tests. However, RT-GG has the lowest settlement or the highest bearing capacity, followed by RT-GT and RT-GC, respectively. Similarly, for the PLTs at the edge point, RT-GG performed the best followed by RT-GT and RT-GC as compared to URT. This can be attributed to the shearing resistance and the tensioned membrane effects of the geosynthetic under the plate.

## References

1. Shukla, S.K. Handbook of Geosynthetic Engineering: Geosynthetics and their applications. ICE. London. 2012. 409 p. DOI: 10.1680/hge.41752
2. Esmaeili, M., Naderi, B., Neyestanaki, H.K., Khodaverdian, A. Investigating the effect of geogrid on stabilization of high railway embankments. *Soils and Foundations*. 2018. 58(2). Pp. 319–332. DOI: 10.1016/j.sandf.2018.02.005
3. Chandrasekaran, B., Broms, B.B., Wong K.S. Strength of fabric reinforced sand under axisymmetric loading. *Geotextiles and Geomembranes*. 1989. 8(4). Pp. 293–310. DOI: 10.1016/0266-1144(89)90013-7
4. Krishnaswamy, N.R., Isaac, N.T. Liquefaction potential of reinforced sand. *Geotextiles and Geomembranes*. 1994. 13(1). Pp. 23–41.
5. Haeri, S.M., Noorzad, R., Oskoorouchi, A.M. Effect of geotextile reinforcement on the mechanical behavior of sand. *Geotextiles and Geomembranes*. 2000. 18(6). Pp. 385–402. DOI: 10.1016/S0266-1144(00)00005-4
6. Rao, V.G., Dutta, R.K., Ujwala, D. Strength characteristics of sand reinforced with coir fibers and coir geotextiles. *Electronic Journal Of Geotechnical Engineering*. 2005. 10 G.
7. Gray, D.H., Ohashi, H. Mechanics of fiber reinforcement in sand. *Journal of Geotechnical Engineering*. 1983. 1109(3). Pp. 335–353.
8. Gray, D.H., Al-Refeai, T. Behavior of Fabric-Versus Fiber-Reinforced Sand. *Journal of Geotechnical Engineering*. 1986. 112(8). Pp. 804–820. DOI: 10.1061/(ASCE)0733-9410(1986)112:8(804)
9. Al-Refeai, T.O. Behavior of granular soils reinforced with discrete randomly oriented inclusions. *Geotextiles and Geomembranes*. 1991. 10(4). Pp. 319–333. DOI: 10.1016/0266-1144(91)90009-L
10. Ranjan, G., Vasan, R.M., Charan, H.D. Behaviour of plastic-fibre-reinforced sand. *Geotextiles and Geomembranes*. 1994. 13(8). Pp. 555–565. DOI: 10.1016/0266-1144(94)90019-1
11. Kaniraj, S.R., Gayathri, V. Geotechnical behavior of fly ash mixed with randomly oriented fiber inclusions. *Geotextiles and Geomembranes*. 2003. 21(3). Pp. 123–149. DOI: 10.1016/S0266-1144(03)00005-0
12. Yetimoglu, T., Salbas, O. A study on shear strength of sands reinforced with randomly distributed discrete fibers. *Geotextiles and Geomembranes*. 2003. 21(2). Pp. 103–110. DOI: 10.1016/S0266-1144(03)00003-7
13. Park, T., Tan, S.A. Enhanced performance of reinforced soil walls by the inclusion of short fiber. *Geotextiles and Geomembranes*. 2005. 23(4). Pp. 348–361. DOI: 10.1016/j.geotextmem.2004.12.002
14. Zhang, M.X., Javadi, A.A., Min, X. Triaxial tests of sand reinforced with 3D inclusions. *Geotextiles and Geomembranes*. 2006. 24(4). Pp. 201–209. DOI: 10.1016/j.geotextmem.2006.03.004
15. Bathurst, R.J., Karpurapu, R. Large-Scale Triaxial Compression Testing of Geocell-Reinforced Granular Soils. *Geotechnical Testing Journal*. 1993. 16(3). Pp. 296–303. DOI: 10.1520/GTJ10050J
16. Rajagopal, K., Krishnaswamy, N.R., Latha, G.M. Behaviour of sand confined with single and multiple geocells. 1999. 17(3). DOI: 10.1016/S0266-1144(98)00034-X.
17. Madhavi Latha, G. Investigations on the behaviour of geocell supported embankments. Ph.D. Thesis. Indian Institute of Technology Madras. Chennai, 2000.
18. Dash, S.K., Rajagopal, K., Krishnaswamy, N.R. Performance of different geosynthetic reinforcement materials in sand foundations. *Geosynthetics International*. 2004. 11(1). Pp. 35–42. DOI: 10.1680/gein.2004.11.1.35

19. Lawson, C.R. Subgrade Stabilisation with Geotextiles. *Geosynthetics International*. 1995. 2(4). Pp. 741–763. DOI: 10.1680/gein.2.0034
20. Webster, S.L., Grau, R.H., Williams, T.P. Description and Application of Dual Mass Dynamic Cone Penetrometer. US Army Corps of Engineering. Washington DC, 1992. 52 p.
21. Powell, W.D., Potter, J.F., Mayhew, H.C., Nunn, M.E. The Structural Design of Bituminous Roads. TRRL Report LR 1132. Transport and Road Research Laboratory, 1984. 62 p.
22. Singh, M., Trivedi, A., Shukla, S.K. Influence of geosynthetic reinforcement on unpaved roads based on CBR, and static and dynamic cone penetration tests. *International Journal of Geosynthetics and Ground Engineering*. 2020. 6(2). Article no. 13. DOI: 10.1007/s40891-020-00196-0
23. Ahela, A.J. Assessment of Modulus of Subgrade Reaction of Stabilized Soils Using Light Weight Deflectometer. Master's Thesis. Department of Civil Engineering. University of Kerbala, 2017. 163 p.

***Information about the authors:***

***Howaidah Al-Salamy,***

*E-mail:* [howidah.f@s.uokerbala.edu.iq](mailto:howidah.f@s.uokerbala.edu.iq)

***Mahdi Al-Naddaf, PhD***

*ORCID:* <https://orcid.org/0000-0002-6643-8449>

*E-mail:* [mahdi.a@uokerbala.edu.iq](mailto:mahdi.a@uokerbala.edu.iq)

***Raid Almuhanha, PhD***

*E-mail:* [raidr@uokerbala.edu.iq](mailto:raidr@uokerbala.edu.iq)

*Received 15.02.2023. Approved after reviewing 29.08.2023. Accepted 29.03.2024.*



